Modelling the Effect of Minority Components in Biominerals via Biomimetic Mineralisation

Modellierung des Effektes von Spurenelementen in Biomineralien durch biomimetische Synthese

Benedikt Demmert
Department of Earth and Environmental Sciences
Macquarie University

&

Department of Materials Science and Engineering
Friedrich-Alexander-University Erlangen-Nürnberg

For the degree of
Doctor of Philosophy
&
Dr. – Ing.
(Cotutelle program)

Principal Supervisors:
Prof. Dr. Dorrit E. Jacob, PD Dr. Stephan E. Wolf

October 2020

MACQUARIE University
SYDNEY·AUSTRALIA

FRIEDRICH-ALEXANDER UNIVERSITÄT ERLANGEN-NÜRNBERG

…dedicated to my son, my wife, and my parents

STATEMENT OF ORIGINALITY

This thesis is being submitted to Macquarie University and Friedrich-Alexander University Erlangen-Nürnberg in accordance with the Cotutelle agreement dated 03/05/2017.

To the best of my knowledge and belief, the thesis contains no material previously published or written by another person except where due reference is made in the thesis itself.

Benedikt Demmert
October 17, 2020

ABSTRACT

This work aims to determine whether the different crystallisation pathways of amorphous calcium carbonate (ACC) have an impact on the element and oxygen isotope partitioning of the final crystalline phase. In this study, special emphasis is placed on the sparsely investigated pathway of the so-called *pseudomorphic transformation*, which is a crystallisation process that preserves the disequilibrium morphology of the amorphous precursor. Since it is shown that the composition of ACC can be preserved under pseudomorphic conditions, the influence of a range of synthesis parameters and conditions on the material properties and chemical composition of ACC was scrutinised.

While solid-state transformation retains the chemical composition of doped ACC during crystallisation, the chemical composition is altered during dissolution-reprecipitation pathways. An alternative crystallisation pathway, namely the shape-preserving pseudomorphic transformation, is induced by additives such as poly(acrylic acid), polyaspartic acid and trace amounts of phosphate. Since ACC crystallisation in biominerals occurs in the presence of these or similar additives – especially aspartate-rich domains were found in unusually acidic biomineralisation proteins – a thorough mechanistic understanding of the pseudomorphic transformation is of importance for paleoclimate reconstructions. This work revealed that the pseudomorphic transformation not only preserves the morphology of the amorphous precursor, but also retains the partition coefficients, *e.g.*, in case of Sr-doped ACC. Furthermore, the influence of the pseudomorphic transformation on the oxygen isotope composition demonstrated that this transformation is a quasi-solid to solid phase transformation process, although it takes place in aqueous solutions. Mechanistically, it seems that the presence of certain surface-active additives limits diffusional exchange with the surrounding liquid environment so that pseudomorphic transformation preserves the partition coefficients of ACC even in the final crystalline product.

As the pseudomorphic transformation preserves the composition of the amorphous precursor, it is necessary to understand how the formation of ACC and its partitioning coefficients, as well as its material properties, is influenced by the synthesis conditions. For instance, it was recently shown that it is possible to precipitate ACC with distinct short-range order by simply altering the pH slightly. Therefore, it is of high significance to analyse the influence of the synthesis conditions on ACC. In this thesis, three different approaches were conducted to achieve a better understanding of the structural and compositional synthesis dependence of ACC:

#1 The influence of the synthesis procedures revealed that material properties such as particle size, level of hydration, crystallisation temperature, and density are sensitive to simple changes in the synthesis conditions, which have much less effect on the chemical composition of ACC. Notably, density measurements indicated that synthesis-dependent microstructures

of ACC structures exist. Furthermore, a microfluidic setup allowed for ACC synthesis at an exceptionally low pH (pH 7.5) by using ethanol as anti-solvent. Under these conditions, synthesis of ACC at varying pH revealed a significant increase of barium incorporation by decreasing pH.

#2 The influence of the mixing kinetics on the element partition was analysed by precipitating magnesium-, strontium-, and barium-doped ACC under varying flow rates. While less magnesium was incorporated at increasing flow rates, increasing partition coefficients were determined for Sr-doped ACC by increasing flow rates. Notably, no flow rate influence was determined for Ba-doped ACC. These results demonstrate that element partitioning is highly sensitive to changing mixing kinetics, which indicates that prenucleation clusters play a role during ACC formation and control element partitioning to a certain extent.

#3 To mimic ACC formation in a natural environment, ACC was synthesised in artificial seawater under varying synthesis conditions as flow rate, temperature, and pH, which resulted in multiple-doped ACC. Besides material properties such as particle size, the chemical composition was also affected by the synthesis conditions. A significant influence of the flow rate and temperature on magnesium and sulphur partitioning was determined. While less magnesium was incorporated by increasing flow rates, increasing sulphur incorporation was detected. Furthermore, both additives were better incorporated at enhanced temperatures. Notably, increasing concentrations of all dopants were determined with increasing pH.

In the final chapter, a feasibility study was conducted to assess whether a flow-through synthesis enables the synthesis of the fundamental building blocks of calcareous biominerals, namely calcium carbonate nanograins coated with organic matrices. This study demonstrated that the precipitation of Mg-doped ACC particles coated with negatively charged polyelectrolytes, such as polyacrylates or polystyrene sulfonate, is possible by using a flow-through synthesis.

KURZFASSUNG

Diese Arbeit befasst sich mit dem Einfluss der verschiedenen Kristallisationspfade auf die Einbauraten von Ionen und Sauerstoffisotopen in amorphem Kalziumkarbonat (ACC). Besonderes Augenmerk liegt dabei auf dem Einfluss der wenig untersuchten und sogenannten pseudomorphen Umwandlung (*pseudomorphic transformation*), welche die Morphologie während der Kristallisation nicht verändert. Da in dieser Arbeit gezeigt wird, dass unter pseudomorphen Bedingungen auch die chemische Zusammensetzung erhalten werden kann, untersucht diese Arbeit zudem den Einfluss der Synthesebedingungen auf die Materialeigenschaften und die chemische Zusammensetzung von ACC.

Während eine sogenannte Festphasenumwandlung (*solid-state transformation*) die chemische Zusammensetzung von dotiertem ACC während der Kristallisation nicht verändert, wird diese bei einem Kristallisationspfad verändert, bei welchem ACC sich auflöst und neugebildetes kristallines Kalziumkarbonat ausfällt (*dissolution-reprecipitation*). Jedoch gibt es einen weiteren Kristallisationspfad, die sogenannte pseudomorphe Umwandlung, welche sich dadurch auszeichnet, dass die Nichtgleichgewichtsmorphologie des amorphen Vorläufers während der Kristallisation erhalten wird. Dieser Kristallisationspfad wird durch die Präsenz von Additiven wie Polyacrylsäure, Polyasparaginsäure und sogar von Spurenelementen von Phosphat induziert, wie in dieser Arbeit gezeigt wird. Aufgrund der Tatsache, dass die Kristallisation von ACC in Biomineralien unter der Anwesenheit dieser Additive abläuft – besonders Asparaginsäure ist ein Bestandteil von ungewöhnlich sauren Biomineralisationsproteinen – ist ein tiefergehendes Verständnis der pseudomorphen Umwandlung von Bedeutung für die Paläoklimatik. Diese Arbeit weist erstmals nach, dass die pseudomorphe Umwandlung sogar die Verteilungskoeffizienten während der Kristallisation bewahrt, nachweisbar insbesondere für die Einbauraten von Strontium in ACC. Weiterhin zeigt sich im Einfluss der pseudomorphen Umwandlung auf die Sauerstoffisotopie, dass es sich quasi um eine Festphasenumwandlung handelt, obwohl die Reaktion in Lösung stattfindet. Oberflächenaktive Substanzen scheinen den diffusiven Austausch mit der umgebenden Lösung zu hemmen, sodass die Verteilungskoeffizienten der amorphen Phase dem des kristallinen Endproduktes unerwarteterweise entsprechen.

Aufgrund der Tatsache, dass die pseudomorphe Umwandlung die chemische Zusammensetzung der amorphen Vorphase erhält, ist ein fundierter Kenntnisstand über den Einbau von Dotierelementen in ACC und der Einfluss der Synthesebedingungen auf die Materialeigenschaften und die chemische Zusammensetzung notwendig. Da vor kurzem demonstriert wurde, dass durch eine Veränderung des pH-Wertes unterschiedliche ACC-Nahstrukturen hergestellt werden können, ist eine Untersuchung des Syntheseeinflusses auf ACC von zusätzlicher Bedeutung. Um ein tiefergehendes Verständnis zu erreichen, wurden drei verschiedene Ansätze verfolgt:

#1 Untersuchungen zum Einfluss der Synthesen verdeutlichten, dass Materialeigenschaften wie die Partikelgröße, die Hydratisierung der Proben, die Kristallisationstemperatur und die Dichte durch eine einfache Veränderung der angewendeten Synthese beeinflusst werden können. Im Gegensatz hierzu wird die chemische Zusammensetzung durch die Anwendung einer anderen Synthese nur geringfügig beeinflusst. Dichtemessungen der Pulver deuteten auf die beachtenswerten Möglichkeiten hin, verschiedene ACC-Microstrukturen über die Auswahl der Synthesemethode herstellen zu können. Weiterhin war es durch einen mikrofluidischen Ansatz möglich, Ethanol als Ausfällungsmittel zu verwenden, was eine Synthese von ACC bei pH 7,5 erlaubte. Eine Synthese von ACC bei verschiedenen pH-Werten zeigte einen verstärkten Einbau von Barium in ACC bei verringertem pH.

#2 Um den Einfluss der Kinetik auf den Einbau von Ionen zu untersuchen, wurde mit Magnesium, Strontium und Barium dotiertes ACC bei verschiedenen Fließraten hergestellt. Während bei höheren Fließraten weniger Magnesium eingebaut wurde, wurde das Gegenteil für den Einbau von Strontium festgestellt. Beachtenswert ist, dass der Einbau von Barium nicht von der Fließrate beeinflusst wurde. Diese Ergebnisse verdeutlichen, dass der Einbau von Ionen sehr sensitiv gegenüber veränderten Herstellungsbedingungen ist, was darauf hinweist, dass sogenannte Pränukleationscluster (PNCs) eine gewichtige Rolle während der Bildung von ACC spielen. Weiterhin deutet dies darauf hin, dass PNCs in einem gewissen Rahmen den Einbau von Ionen in ACC kontrollieren.

#3 Um die Herstellung von ACC unter natürlichen Umweltbedingungen zu simulieren, wurde ACC in künstlichem Meerwasser ausgefällt, was in der Bildung von mehrfachdotiertem ACC resultierte. Zusätzlich wurden während der Synthese Bedingungen wie die Fließrate, die Temperatur und der pH-Wert systematisch verändert. Diese Veränderungen beeinflussen nicht nur Materialeigenschaften wie die Partikelgröße, sondern ebenfalls die chemische Zusammensetzung von ACC. So wurde ein deutlicher Einfluss der Fließrate und der Temperatur auf die Einbauraten von Magnesium und Schwefel festgestellt. Während steigende Fließraten zu einer Verringerung des Einbaus von Magnesium führten, erreichten sie einen verstärkten Einbau von Schwefel. Eine Erhöhung der Temperatur führte zu einem erhöhten Einbau beider Ionen. Beachtenswert war der verstärkte Einbau aller Ionen bei steigendem pH-Wert.

Im abschließenden Kapitel des experimentellen Teils dieser Arbeit wurde eine Machtbarkeitsstudie durchgeführt, die aufzeigen soll, ob es mit Hilfe einer sogenannten Flow-through Synthese möglich ist, die fundamentalen Bauteile von kalkhaltigen Biomineralien herzustellen. Diese Bauteile bestehen aus nanogranulärem Kalziumkarbonat, welches mit einer organischen Matrix beschichtet ist. Diese Machtbarkeitsstudie verdeutlichte, dass eine

Herstellung von mit Magnesium dotiertem ACC, welches mit negativ geladenen Polyelektrolyten wie Polyacrylsäure oder Polystyrolsulfonat beschichtet wurde, möglich ist.

TABLE OF CONTENTS

LIST OF FIGURES

LIST OF TABLES

LIST OF SUPPLEMENTARY FIGURES

LIST OF SUPPLEMENTARY TABLES

LIST OF PUBLICATIONS

Publications during the Ph.D. candidature:

1. Wolf, S. E.; Böhm, C. F., Harris, J.; **Demmert, B.**; Jacob, D. E.; Mondeshki, M.; Ruiz-Agudo, E.; Rodríguez-Navarro, C.: *Nonclassical crystallization in vivo et in vitro (I): Process-structure-property relationships of nanogranular biominerals*. Journal of Structural Biology; 196(2):244-259 (2016).
2. **Demmert, B.**; Schinzel, F.; Schüßler, M.; Mondeshki, M.; Kaschta, J.; Schubert, D. W.; Jacob, D. E., Wolf, S. E.: *Polymer-Functionalised Nanograins of Mg-Doped Amorphous Calcium Carbonate via a Flow-Chemistry Approach*. Materials, 12(11):1818 (2019). [Chapter 6].
3. Wolf, S. E.; Schüßler, M.; Böhm, C. F.; **Demmert, B.**: *Frontiers in Bio-Inspired Mineralization: Addressing the Mimesis of the Four-Dimensional, Hierarchical and Nonclassical Growth Characteristics of Biominerals.* Frontiers in Biomaterials (Bentham e-Books), 6 (2019).
4. Myszka, B.; Schüßler, M.; Hurle, K.; **Demmert, B.**; Detsch, R.; Boccaccini, A. R.; Wolf, S. E.: *Phase-specific bioactivity and altered Ostwald ripening pathways of calcium carbonate polymorphs in simulated body fluid.* RSC Advances, 9:18232-18244 (2019).
5. Myszka, B.; Schodder, P. I.; Leupold, S.; Barr, M. K. S.; Hurle, K.; Schüßler, M.; **Demmert, B.**; Biggemann, J.; Fey, T.; Boccaccini, A. R.; Wolf, S. E.: *Shape Matters: Crystal Morphology and Surface Topography Alter Bioactivity of Bioceramics in Simulated Body Fluid.* Advanced Engineering Materials, 22(9):2000044 (2019).
6. Trinh, T. T. H.; Schodder, P. I.; **Demmert, B.**; Nguyen, A.-T.: *Crystallization of l-glutamic acid under microfluidic conditions and levitation.* Chemical Engineering Research and Design, 169:176-188 (2021).

PARTS OF THE THESIS

Chapter 2 is a manuscript in preparation for Advanced Engineering Materials:

Demmert, B.; Schüßler, M.; Schodder, P.I.; Joachimski, M.; van Geldern, R.; Mario, C.; Cheong, S.; Khansur, N.H.; Jacob, D.E. and Wolf, S.E.: Shape-preserving phase transformations of ACC affect element and isotope partitioning.

Chapter 3 is a manuscript in preparation for RSC Advances:

Demmert, B.; Schüßler, M.; Schodder, P.I.; Jacob, D.E. and Wolf, S.E.: Synthesis-dependent properties and composition of undoped and doped ACC.

Chapter 4 is a manuscript in preparation for Materials:

Demmert, B.; Schüßler, M.; Schodder, P.I.; Jacob, D.E. and Wolf, S.E.: Foreign element partition rates change in ACC with mixing conditions.

Chapter 5 is a manuscript in preparation for Scientific Reports:

Demmert, B.; Schodder, P.I.; Schüßler, M.; Jacob, D.E. and Wolf, S.E.: Multiple doping of ACC in an artificial seawater environment under varying synthesis conditions.

Chapter 6 is published in Materials (2019):

Demmert, B.; Schinzel, F.; Schüßler, M.; Mondeshki, M.; Kaschta, J.; Schubert, D.W.; Jacob, D.E. and Wolf, S.E.: Polymer-Functionalized nanograins of Mg-doped amorphous calcium carbonate via a flow chemistry approach. Materials 2019, 12(11):1818; https://doi.org/10.3390/ma12111818.

ACKNOWLEDGEMENTS

Firstly, I want to thank my two supervisors PD Dr. Stephan E. Wolf and Prof. Dr. Dorrit E. Jacob who gave me the opportunity to conduct a binational Ph. D. between the Friedrich-Alexander University Erlangen-Nürnberg and the Macquarie University in Sydney, Australia. Thank you for your support during these past years.

Furthermore, I want to thank Prof. Dr. Michael Joachimski and PD Dr. Robert van Geldern, GeoZentrum Nordbayern, Friedrich-Alexander University Erlangen-Nürnberg, for the collaboration in the context of this thesis, and especially for conducting the oxygen isotope measurements.

Thank you to all the members of the Institute of Glass and Ceramics, Department of Materials Science and Engineering, Friedrich-Alexander University Erlangen-Nürnberg. Special thanks to Evelyn Gruber, Heike Reinfelder and Sabine Fiedler for their technical support. It has always been a pleasure to work in the chemical lab.

Thank you to all the members of the Department of Earth and Environmental Sciences at Macquarie University, Sydney, and especially Prof. Dr. Simon Clark for his input and discussions. Thank you to Dr. Tom Lawson, and Peter Wieland, who introduced me to conducting ICP-MS measurements. Another thank you to all the Ph.D. students for their warm welcome at Macquarie University, especially Kui Han, Thusitha Nimalsiri, Dilmi Herath, Sarath Patabendigedara. I enjoyed working with you!

Thank you to all former and current members of the Biomimetics Group at the Institute of Glass and Ceramics, Department of Materials Science and Engineering, Friedrich-Alexander University Erlangen-Nürnberg. It was always a pleasure working with you. Thank you to Martina Schüßler, Philipp Schodder, Barbara Myzska, Simon Leupold and Corinna Böhm for all the discussions and encouragement you offered me these past years.

Finally, thank you to my family and friends, who always supported and encouraged me these past years, especially when the Covid-19 pandemic complicated the completion period of this thesis. Thank you to my chemistry teacher Dr. Udo Niederreuther who awakened my interest in chemistry. Thank you to my parents, Hannelore and Oskar Demmert, for their support throughout my life. You have my deepest gratitude. Thank you to my brothers and their families, especially to Katja and Christoph Demmert for their CorelDraw advice. Thank you to my wife's family, for their support in the final phase of the thesis. At last, thank you to my wife Sabine Sältzer, and to our son Hugo, without whom this past year would not have been possible.

1. THEORETICAL BACKGROUND

1.1 Introduction

Biominerals are minerals produced by organisms, which are composite materials consisting of mineral and organic components[1]. They not only provide protection in the form of armour or weaponry, but they can also serve in more complex functions, *e.g.*, as sensors for vision, or magnetic and gravity fields. Because of their vital importance to the producing organism, biominerals developed highly optimized structures which are organized across several length scales from nanometre to millimetre over millions of years of evolution. Biominerals show complex design that provides outstanding mechanical properties, despite being composed of weak constituents[2–4]. Nacre, which consists of aragonite platelets jointed by a few per cent of organics (1 – 5 %)[5], shows a fracture toughness which by far exceeds pure aragonite and features an exceptionally high strength, rooted in its nanoscale organization increasing flaw tolerance[6,7]. Furthermore, biomineralising organisms have achieved the ability to shape the morphology of biominerals, seemingly ignoring crystallographic limits, and are capable of exerting exact local control over the polymorph selection[8,9].

Many disciplines participate in the quest of revealing how nature achieves this superior control over mineralisation and crystallisation. Based on these insights, new synthesis approaches for solid-state materials or new materials design principles can be derived, a venture which is subsumed under the notion of biomimesis or bionics[10]. Inspired by nature, the ultimate goal of biomimetic research is the implementation of new routes towards outstanding functional materials or the invention of newly-designed materials which can induce a higher sustainability due to their higher reusability[6,11,12].

Calcareous biominerals are ubiquitous in the biosphere; their evolutionary development dates back to the Cambrian explosion. Because of its biological dominance, the calcium carbonate system is thus often chosen as a model system, and not only because of its industrial importance[13–17]. Calcium carbonate is also crucial for climatology and paleoclimatology, mainly because fossilised calcitic and aragonitic biominerals serve as proxy archives of past climates[18–20]. For reconstructing past climates from biomineralised archives of the past, it is clear that a profound and thorough understanding of the processes that drive calcium carbonate formation is needed under biologically and geologically relevant conditions.

1.2 Motivation and aim of the thesis

While the influence of the so-called *solid-state transformation* and *dissolution-reprecipitation crystallisation* on the chemical composition of ACC are known (Chapter 1.6.3)[21], the influence of the so-called *pseudomorphic transformation*, which retains the morphology during crystallisation, on the partition coefficients is enigmatic. Deciphering the influence of the

pseudomorphic transformation is crucial, as it was demonstrated that this crystallisation pathway is inducible by additives present in biominerals[22,23]. Furthermore, the question how environmental conditions are recorded by a biomineral formed by ACC intermediates is of vital importance for paleoclimate reconstructions. Accordingly, the influence of the pseudomorphic transformation on the chemical composition was analysed in Chapter 2.

As the precipitation of ACC with distinct short-range order by changing the pH value was recently demonstrated[24], the question arises whether the synthesis, or rather the synthesis conditions, affect the precipitated ACC. A positive answer to this important question would have far-reaching implications, especially because a range of different ACC synthesis procedures are currently in use. In fact, such a finding would question whether studies employing different synthesis strategies are actually comparable. Three different approaches were applied to decipher this question: Firstly, the influence of the synthesis on ACC was investigated by using a batch mixing method and two flow-through methods (Chapter 3). Secondly, ACC was precipitated under varying flow rates to determine the influence of the mixing kinetics on element partitioning (Chapter 4). Thirdly, ACC was synthesised in artificial seawater under varying synthesis conditions such as flow rate, temperature, and pH to determine their influence on the material properties and chemical composition of multi-doped ACC (Chapter 5).

Calcareous biominerals are composed of fundamental building blocks of calcium carbonate nanograins coated with organic matrices. Therefore, it is necessary to establish a reliable synthesis which mimics the structure of biominerals, resulting in more advanced models to describe biominerals. Accordingly, a feasibility study was conducted in Chapter 6 to establish if it is possible to mimic the biomineral structure by synthesising doped ACC coated with a polymer-functionalised layer.

In summary, this work mainly focusses on the following aspects:

1. Investigation of how the pseudomorphic transformation influences the partition coefficients of trace elements and the oxygen isotope fractionation during crystallisation.
2. Evaluation of whether the synthesis can affect the material properties and chemical composition of ACC.
3. Determination of how experimental parameters, such as the flow rate, affect ACC.

1.3 Biomineralisation

Biomineralisation, which encompasses all kinds of mineral formation guided or induced by living organisms, is a vibrant field of research. Depending on the field of research different definitions exists, *e.g.,* sedimentologists and paleoclimatologists differentiate between

biomineralisation and organomineralisation[25], though as the focus of this work is rather on the chemical aspects of biomineralisation, the common definition of biomineralisation stated by Weiner and Dove (Chapter 1.1) will be used here[1].

Biominerals blend simple constituents of low mechanical performance, such as phosphate, and carbonate with organic matrices, such as biopolymers like proteins and proteoglycans, chitin, collagen, or keratin[6,26], to produce hybrid materials with superior material properties[1,6,27–29]. Material scientists often focus their research to the field of biomineralisation because of the unparalleled spatial, structural, and chemical control over the mineralisation exerted by the living organism[30].

Biominerals usually consist of an inorganic mineral phase and a pliable organic phase moulded into complex and hierarchically organised structures which range from the atom level, over the nano- to macroscale[2,3,6,31].

Depending on the extent of control, biomineralisation can be divided into two different modes: biologically induced and biologically controlled[32]. Biologically-induced mineralisation describes the less controlled extracellular mineralisation processes. In many cases, the mineral deposition is triggered by the organism's metabolic products which react with the ions in the surrounding environment. As a consequence of the weak mineralisation control, the resulting minerals are often characterized by low crystallinity and the absence of intricate morphologies[33].

In contrast, numerous organisms, such as vertebrates and mollusc, regulate all aspects of mineralisation, from nucleation, via growth and morphology through to the composition of the biologically produced mineral. This pathway of biologically controlled mineralisation offers an exceptional degree of control over the mineralisation, and the minerals formed in this way are characterized by complex structures which are optimized for function[1,33].

More recently, Dupraz *et al.*[25] summarized biologically influenced mineralisation and biologically induced mineralisation to the umbrella term *organomineralisation*.

Biomineralisation processes can be further classified into extra-, inter-, or intracellular processes, depending on the mineralisation site. However, biomineral formation can also take place in different locations. For example, mineral formation can begin intracellularly and then proceed extracellularly[1].

1.4 Calcium carbonate polymorphs

Calcium carbonate is known to have several polymorphs: Three anhydrous crystalline forms (calcite, aragonite, and vaterite), three hydrous forms (calcium carbonate hexahydrate also known as ikaite, calcium carbonate monohydrate, and hemihydrate calcium carbonate), and amorphous calcium carbonate (ACC)[34–36].

The anhydrous polymorphs of calcium carbonate differ in their crystal structure. Calcite, which is the most stable polymorph, has a trigonal crystal structure. An orthorhombic one is present for aragonite which is less stable than calcite at ambient pressures and temperatures. However, it is known that the presence of magnesium favours aragonite formation, *e.g.,* in cave deposits at ambient conditions[37]. Calcite and aragonite are widely present in biominerals[2–4,31,38]. After years of debate, a complex hexagonal crystal structure was revealed for vaterite[39–42]. Even though vaterite is relatively unstable compared to calcite, it is found in biogenic minerals such as foraminifera, eggshells, and freshwater cultured pearls[43–45]. Furthermore, vaterite can be found in cave deposits[46]. Calcium carbonate monohydrate possesses a trigonal crystal structure, ikaite and hemihydrate calcium carbonate have monoclinic ones[35,47,48].

Amorphous calcium carbonate, described as early as 1916, is widely present in biominerals[49–56]. Amorphous calcium carbonate occurs in a range of hydration states. In biominerals mainly two states were identified: monohydrous and anhydrous amorphous calcium carbonate[52]. Hydrated ACC contains water bound in different ways, namely weakly bound with restricted mobility and strongly bound rigid water[57,58]. As the crystallisation of ACC is accompanied and probably driven by water released due to dehydration[59,60], trace elements with high hydration energy, such as magnesium stabilise amorphous calcium carbonate[61–66]. Recently, it was demonstrated that ACC with distinct short-range ordered structures could be precipitated by changing the pH value during synthesis[24]. Accordingly, ACC is considered to be polyamorphous as it occurs in distinct amorphous structures[67]. Although various synthesis routes are known that partially impact on its near-range order[22,63,68–77], it is still unclear how changing synthesis conditions may further impact on ACC, *e.g.*, concerning its chemical composition.

1.5 Nucleation theories

The formation of a nucleus represents the formation of a new solid phase and is thus of utmost importance for appropriate control over (bio-)mineralisation. A thorough understanding of the various mechanisms involved in nucleation processes is thus indispensable in biomineralisation research.

The concept of nucleation essentially describes a phase separation process, *i.e.*, the appearance of a new phase originating from a parent phase whose formation is driven by the decrease of the free energy of the entire system[78].

Although nucleation of a new phase and its subsequent growth are often introduced in one go, they are distinct processes. As this work focuses on the formation of ACC rather than particle growth, only fundamental concepts of nucleation are introduced here.

1.5.1 Classical nucleation theory (CNT)

1.5.1.1 Binodal phase separation

In the 1930s, scientists developed classical nucleation theory (CNT) based on the ground-breaking works of Gibbs[79–82]. In CNT, it is believed that a nucleus forms by the stochastic clustering of ions, atoms, or molecules. This nucleation cluster, whose internal structure is assumed to be identical to the forming phase, is only stable if the nucleus reaches a critical size. This critical size is another representation of the nucleation energy barrier, which results from the interplay of interfacial free energy (Δg_s) and free bulk energy (Δg_b) of the emerging phase. The surface energy is positive, as it destabilises the nucleus, because energy must be spent to create new interfaces. In contrast, the bulk energy stabilises the nucleus as the new phase has lower free energy than the homogenous parental phase. When a critical size is exceeded, the sum of all free energies is decreasing by the addition of further atoms, ions, or molecules, and accordingly, the nucleus grows. The overall change in free energy for a spherical nucleus can be described by the following equation, assuming a spherical shape of the nucleus (where γ stands for the specific surface energy, *r* describes the radius of the nucleus and Δg_{for} is the gain of energy per volume).

$$\Delta g = \Delta g_s + \Delta g_b = 4\pi\gamma r^2 - \frac{4}{3}\pi r^3 \Delta g_{for} \qquad (1.1)$$

As the nucleation is influenced by supersaturation and solution chemistry, higher supersaturations or a smaller interfacial energies shift the critical radius to lower values[78,82]. Heterogeneous nucleation is often triggered by a foreign surface (*e.g.,* dust, air bubbles) that often reduces the surface energy penalty for creating a new interface. As this interfacial contribution is of special importance for nucleation rates, nucleation occurs preferentially at interfaces.

1.5.1.2 Spinodal decomposition

Nucleation, whether homogenous or heterogeneous, is a binodal phase separation process which occurs in metastable parental phases. In the case of unstable parental phases, spinodal decomposition occurs. Under the assumption that a liquid-condensed calcium carbonate phase exists, as shown by Wolf *et al.*[83], a speculative phase diagram of calcium carbonate-water phase diagram was suggested by Wallace *et al.*[84]. It locates the binodal and the spinodal line as a function of temperature and supersaturation (Figure 1.1): In the bluish area of Figure 1.1, the homogenous solution is undersaturated with respect to crystalline calcium carbonate polymorphs and thus stable. Following the green horizontal line in Figure 1.1 rightwards (black arrow), the solubility line (SL) is crossed. In the yellow-ochre region, the nucleation of solid calcium carbonate is possible, however rarely occurs due to the high thermodynamic barrier. By further increasing the concentration, the binodal line of the liquid phase is crossed at point L-L (liquid-liquid coexistence line); beyond this line a liquid-condensed calcium carbonate phase can form via nucleation. At higher concentrations, the

spinodal line (SP) is reached. In the following yellow region, the solution is thermodynamically unstable. Thus, phase separation is inevitable and is spontaneously induced by even minor concentration fluctuations. However, spinodal decomposition can only take place when the binodal region is crossed quickly enough so that no prior phase separation takes place, *e.g.*, by nucleation. Contrary to binodal phase separation, in which nucleation takes place only locally, spinodal decomposition occurs simultaneously in the entire parental phase. Due to boundary conditions, early stages of spinodal decomposition exhibit a characteristic bi-continuous network similar to a reticulate and sponge-like mesh[84–87].

It should be noted that spinodal decomposition is rarely reported for liquid solutions, but it is often reported for the case of solid solutions. According to recent reports, it seems that spinodal decomposition even takes place in the solid-amorphous precursor phase of some biominerals, *e.g.*, in the brittle star *Ophiocoma wendtii,* and provides a toughening mechanism by inducing compressive stresses. This prestressed material exhibits improved hardness and fracture toughness[88,89]*.* Prestressing is achieved by the spinodal decomposition of Mg-doped ACC which produces Mg-rich nanoparticles and an Mg-depleted amorphous matrix. Crystallisation of ACC results in Mg-rich calcite nanoparticles which are embedded coherently in the calcite matrix in a layered fashion[88].

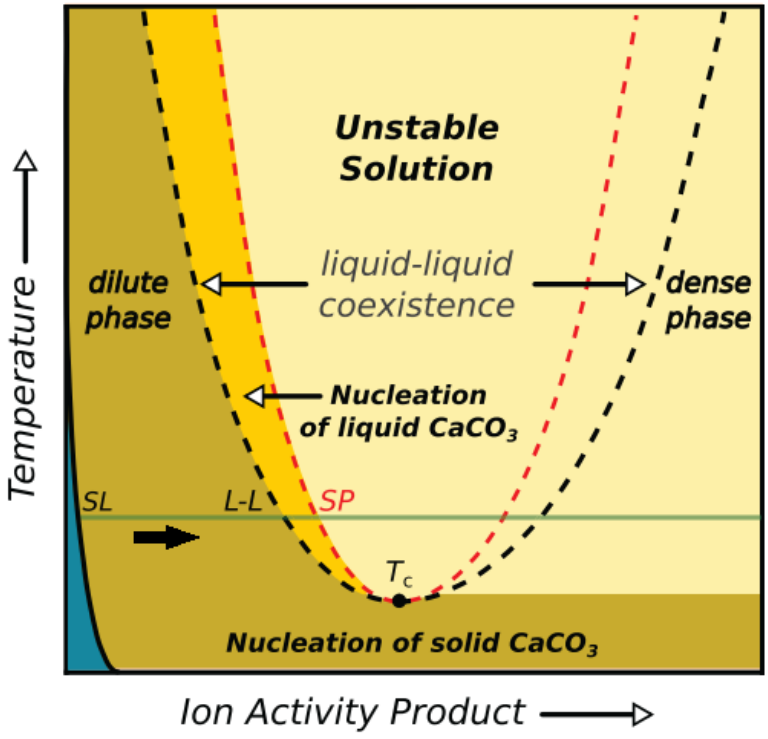

Figure 1.1. Schematic phase diagram of the calcium carbonate-water system. The black and red dashed lines represent the binodal line and the spinodal line, respectively. The green line represents an increasing ion activity product at a constant temperature[84]. [From Wallace, A. F. *et al.* Microscopic evidence for liquid-liquid separation in supersaturated $CaCO_3$ solutions. *Science*. **341**, 885–889 (2013). Reprinted with permission from AAAS.]

1.5.1.3 Kinetic effects in classical crystallisation processes

In a polymorphic system, the rate of nucleation determines which polymorphs are formed first. Since the interfacial energy of polymorphs often correlates with their thermodynamic stability, the most unstable form is formed first. According to the Ostwald-Lussac law of stages, it is possible to retrieve metastable polymorphs if a kinetic reaction control is applied, *e.g.,* by short reaction times. When applying a thermodynamic reaction control, *i.e.*, in case of long reaction times, the thermodynamically stable product is synthesised.

Accordingly, if the reaction time is kept short, it is possible to produce less stable calcium carbonate polymorphs such as ACC and vaterite. Fully in accordance with the Ostwald-Lussac rule of stages, these metastable polymorphs may readily transform into stable calcite if exposed to humid environments[90,91].

1.5.2 Nonclassical nucleation theory

Nonclassical nucleation is a concept of nucleation and growth alternative to *classical nucleation*[92]. The concept has been put forward by Gebauer and Cölfen and rests on the observation that so-called *stable prenucleation clusters* (PNC) exist[93,94]. Mineralisation via PNC was discovered by a combination of Ca^{2+} activity measurements in LaMer-type experiments, which were coupled with particle size determination based on analytical ultracentrifugation. The titration experiments, in which the formation of calcium carbonate was monitored under pH-constant conditions, revealed that an unexpectedly high number of calcium ions were bound in carbonate-containing buffer solutions. Mere ion-pairing could not account for this high loss in Ca^{2+} activity. Additionally, nanosized clusters were found by means of analytical ultracentrifugation in metastable supersaturated solutions. These findings conflict with the predictions of CNT, and Gebauer *et al.*[95] suggested that this difference was caused by the formation of stable prenucleation clusters via ion association. Subsequently Pouget *et al.*[96] provided evidence for the existence of the prenucleation clusters. The structure of these clusters was initially unclear[96,97], until computer simulation suggested that PNCs are solutes with no clear interphase which exhibit a dynamic structure with chain-like motifs that partially cross-link. In this study, PNCs were defined as dynamically-ordered liquid-like oxyanion polymers (DOLLOPs)[94,98,99].

In stark contrast to classical concepts, in which the critical size and energy balance of the nucleus defines the point of nucleation, cluster dynamics is the crucial point for the PNC pathway (Figure 1.2)[84,100]. It has been suggested that upon a loss of cluster dynamics, PNCs/DOLLOPs merge and coalesce to give a liquid-condensed phase in the form of nano-droplets. These droplets then separate from the parental phase[84,101].

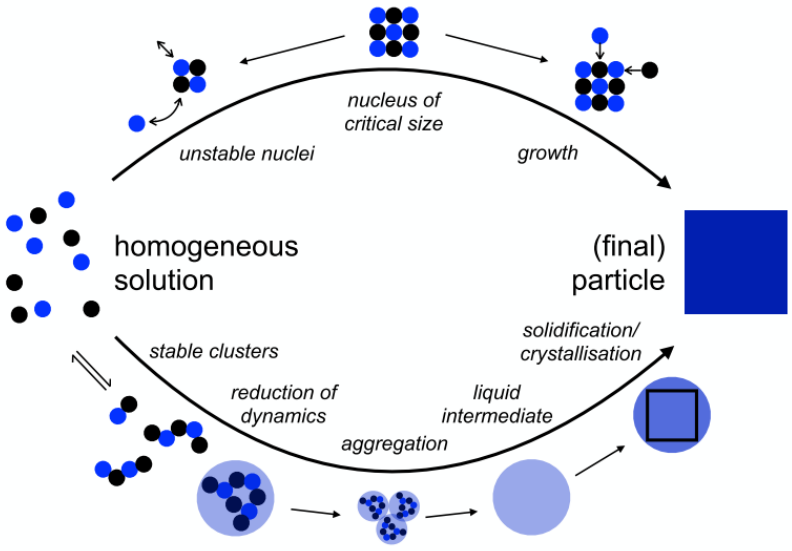

Figure 1.2. Schematic illustration of the classical nucleation theory (CNT, top) and the prenucleation clusters (PNC, bottom). While for the CNT, the nucleus size plays an essential role, the cluster dynamics are the key factor for the PNC. [Reprinted without changes from Gebauer[101] (CC BY 4.0).]

To reduce the interfacial energy, the nano-droplets aggregate into a liquid intermediate which subsequently transforms to amorphous mediates like amorphous calcium carbonate. The subsequent crystallisation of these amorphous mediates proceeds via dissolution-reprecipitation processes (Ostwald ripening).

Nonclassical nucleation theory was criticised in numerous publications which essentially deny the existence of these very clusters and posit that the whole concept can be described by CNT[102–104]. For example, Smeets *et al.*[102] combined experimental and computational approaches to evidence that calcium carbonate formation can be explained in classical terms. In turn, Gebauer *et al.*[100] harshly criticised these results, stating that “no sustainable scientific evidence against the PNC pathway has in fact been reported“. Today, both contrasting views persist, and the PNC concept is still strongly debated[98,105] but there is a growing consensus that PNCs exist at least as solutes in solution[99].

1.6 Crystal Growth

1.6.1 Classical crystallisation

Following classical crystallisation theory, crystal growth occurs via attachment of atoms, ions, and molecules similar to the already existing crystal, *e.g.*, to a stable nucleus. After attaching to the crystal surface, these components are not directly integrated into the crystal. They will migrate within the so-called *adsorption layer* to energetically preferred positions, such as kinks or steps[106,107], resulting in a layer-by-layer assembling of the crystal facet[108,109].

At lower supersaturation, crystal growth is mainly facilitated by screw dislocations[110]. Screw dislocations are topological defects that are always present in macroscopic crystals lattice,

resulting in a shift of the lattice plane by at least one layer similar to a spiral staircase[111]. The final crystal facet is predictable by Wulff rule, as the crystal facet is governed by a reduction of the surface energies[112]. Following Wulff`s rule, fast-growing facets will vanish, due to their high surface energies, and slow-growing facets will be preserved, due to their low surface energies, defining final crystal morphology[108,113].

However, discrepancies to Wulff`s rule are possible, as the crystal facets are often kinetically dominated[107]. Furthermore, additives influence crystal growth, as they can block kinks, resulting in a changed appearance. It is known that the attachment of strontium, barium, and magnesium to calcitic kink sites can block their propagation. Furthermore, the incorporation of such ions causes a straining in the local crystal lattice, which increases the solubility of calcite[114].

1.6.2 Nonclassical crystallisation

In the classical picture, the formation of crystals is entirely driven by attaching monomers in the form of single ions, atoms, or molecules (the grey arrow in Figure 1.3). However, if reaction conditions are suited to stabilise nanoscale intermediates, such as crystalline or amorphous nanoparticles, these nanoparticles may start to interact, in full accordance with the DLVO theory, which states that electrostatic forces and van der Waals forces are independent and can therefore superimpose. It has been repeatedly reported that such nanoparticle accretion mechanisms also can lead to crystals, even to single crystals. Depending on the character of the nanoparticle, a variety of different nonclassical crystallisation pathways open up (the black arrows in Figure 1.3).

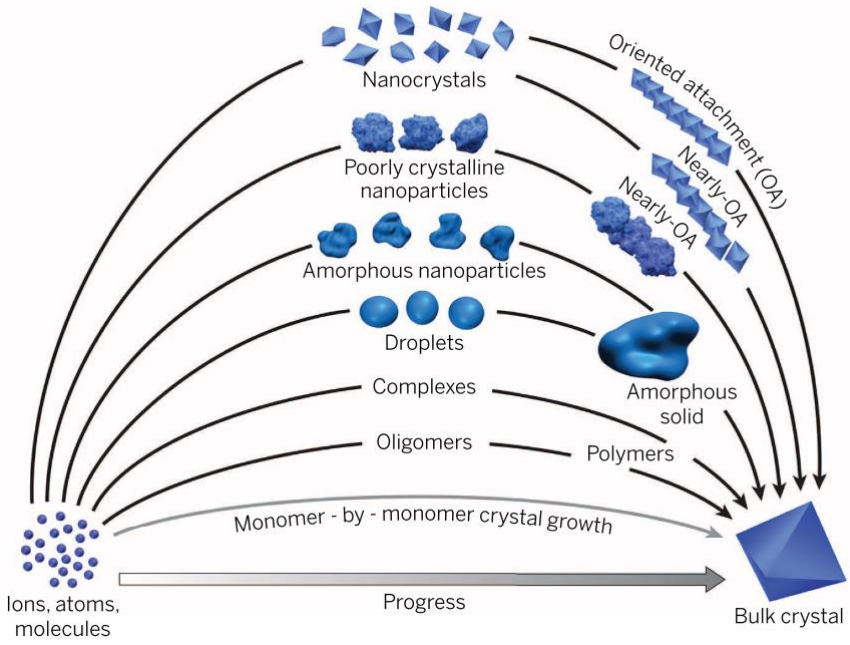

Figure 1.3. Scheme of classical and nonclassical crystallisation. In contrast to the attachment of atoms, ions, and molecules which drives the classical crystallisation (grey arrow at the bottom of the graph), nonclassical crystallisation pathways are characterized by the attachment of higher order species such

as multi-ion complexes or nanocrystals[115]. [From De Yoreo, J. J. *et al.* Crystallization by particle attachment in synthetic, biogenic, and geologic environments. *Science*. **349**, (2015). Reprinted with permission from AAAS.]

Nonclassical crystallisation is characterized by the attachment of higher-order species, *i.e.*, of oligomers and nanoparticles which comprise more than one ion, atom, or molecule. The process of oriented attachment (OA) is typical and the most prominent representative of nonclassical crystallisation processes. In OA, crystal growth occurs via the crystallographically-controlled self-assembly of crystalline particles yielding a crystalline superstructure which features either aligned crystal lattices twin boundary or stacking fault at the interparticle boundaries[115,116].

The superstructures formed are so-called *mesocrystals*, *i.e.*, mesoscopically ordered crystals, which consist of nanocrystals with co-aligned crystal lattices and, consequently, can exhibit a diffraction pattern indicative of a single crystal[117–120]. It has been shown that mesocrystals are present, *i.a.*, in sea urchin spines or aragonitic tablets of nacre[121,122]. Mesocrystals can form via various pathways, such as alignment of organic matrixes, physical forces (*e.g.,* dipole forces, van der Waals forces), and oriented attachment (Figure 1.4). The occurrence of mesocrystals in biomineralised bodies is insofar remarkable, as they form from amorphous calcium carbonate precursors, which are widely present in biominerals[4,54,55,123], and not from the self-assembly of nanocrystals. Thus, another pathway exists to mesocrystal formation which is less prominent.

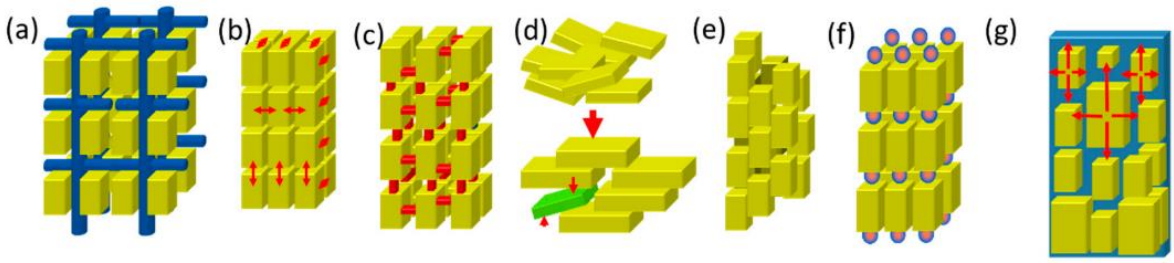

Figure 1.4. Scheme of the main mesocrystal formation pathways. Mesocrystals can develop by the alignment of (a) organic matrices, (b) physical forces, (c) secondary nucleation, (d) spatial limitations, (e) oriented attachment, (f) molecules which are face-selective and (g) solid-phase transformation. [Reprinted without changes from Sturm & Cölfen[120] (CC BY 4.0).]

1.6.3 ACC-mediated crystal formation

Gower and Tirrel[124] revealed that non-equilibrium crystalline calcium carbonate morphologies could form under the presence of polypeptides such as poly(aspartate). It was later shown that a liquid-liquid phase separation enabled the formation of these morphologies as poly(aspartate) stabilised the liquid calcium carbonate phase. By deposition and coalescence, this liquid-condensed phase forms a coating which solidifies into calcitic films and tablets. Due

to the presence of a polymer, which is needed to initiate this crystallisation pathway, the mechanism is referred to as the *polymer induced liquid-precursor process* (PILP)[76].

Harris *et al.*[22] demonstrated that by using the PILP, under the presence of poly(acrylic acid) sodium salt (PAA), it is possible to achieve an ACC transformation into complex calcite spherulites. Harris *et al.* designated this transformation as *pseudomorphic transformation* due to the retained morphology, which yielded in the formation of crystalline calcium carbonate in non-equilibrium morphologies. In this thesis, the definition of the pseudomorphic transformation is slightly modified in accordance with the work of Harris *et al.*[22]: The pseudomorphic transformation is a shape-preserving crystallisation in solution, which is induced by inorganic or organic additives, yielding to the formation of crystalline calcium carbonate in non-equilibrium morphologies.

By using liquid-phase TEM, Liu *et al.*[23] revealed that trace amounts of magnesium could induce a pseudomorphic transformation of calcium carbonate, however, they referred to it as *shape-preserving amorphous-to-crystalline transformation*. Furthermore, they analysed the ability of sodium citrate and PAA to induce a pseudomorphic transformation. Contrary to the work of Harris *et al.*[22], PAA did not induce a pseudomorphic transformation in their experiments.

Despite the knowledge of how to induce the pseudomorphic transformation and that the formation of crystalline calcium carbonate in non-equilibrium morphologies is possible, the pseudomorphic transformation is still enigmatic. In particular, the influence of the pseudomorphic transformation on the number of incorporated ions is unclear. Contrary to that, the influence of the other typical ACC crystallisations, namely the solid-state transformation and the dissolution-reprecipitation pathway, on the incorporated dopants is known. The former crystallisation pathway, in which ACC dehydrates and the crystallisation occurs by structural rearrangement via atomic diffusion, retains the number of incorporated ions during crystallisation. In the latter crystallisation pathway, in which ACC dissolves and is precipitated from the resulting solution, the number of incorporated ions is altered during crystallisation[21].

1.7 Partition coefficients to quantify trace element incorporation into ACC

As the presence of an amorphous phase facilitates the trace element incorporation, a wide variety of literature uses ACC for trace element incorporation[23,63,65,71,72,125–127]. Furthermore, the incorporation of trace elements is of vital importance for paleoclimate reconstructions, as environmental conditions, such as temperature and salinity, cannot be determined directly. As these conditions affected the biology of species or chemistry of minerals, proxies can be used reflecting environmental conditions[18–20,128–131]. For example, strontium incorporation into aragonitic bivalves is used as a temperature proxy, due to the lower strontium incorporation

with increasing temperature[132]. However, incorporation of trace elements into biominerals is often biologically or kinetically controlled, which impedes the usage of proxies[18,130,132–134].

To exploit proxies for paleoclimate reconstruction, the partition coefficients have to be calculated. Depending on the experimental conditions, two different ways of calculating the partition coefficients exist. On the one hand, the Henderson-Kracek model exists, which is applied when the composition of the solution is unaffected by the precipitation[135]. On the other hand, the Doerner-Hoskins model is used when the composition of the solution changes during precipitation[136]. In this work, the Henderson-Kracek model is applied to calculate non-thermodynamic partition coefficients and it bases on the trace element to calcium ratio in the solid divided by the trace element to calcium ratio in the liquid[134,137]. The trace element is designated as X in Equation 1.2.

$$K_D = \frac{(\frac{X^{2+}}{Ca^{2+}})_S}{(\frac{X^{2+}}{Ca^{2+}})_L} \tag{1.2}$$

The Henderson-Kracek model is also suitable to determine the rare earth element (REE) incorporation into calcite[138]. However, Terakado and Masuda[139] suggested modification of the Henderson-Kracek model to take potential REE complexation into account.

1.8 References

1. Weiner, S. & Dove, P. M. An Overview of Biomineralization Processes and the Problem of the Vital Effect. *Rev. Mineral. Geochemistry* **54**, 1–29 (2003).

2. Böhm, C. F. *et al.* Structural commonalities and deviations in the hierarchical organization of crossed-lamellar shells: A case study on the shell of the bivalve *Glycymeris glycymeris*. *J. Mater. Res.* **31**, 536–546 (2016).

3. Agbaje, O. B. A. *et al.* Architecture of crossed-lamellar bivalve shells: the southern giant clam (*Tridacna derasa*, Röding, 1798). *R. Soc. Open Sci.* **4**, 170622 (2017).

4. Killian, C. E. *et al.* Mechanism of calcite co-orientation in the sea urchin tooth. *J. Am. Chem. Soc.* **131**, 18404–18409 (2009).

5. Blank, S. *et al.* The nacre protein perlucin nucleates growth of calcium carbonate crystals. *J. Microsc.* **212**, 280–291 (2003).

6. Wegst, U. G. K., Bai, H., Saiz, E., Tomsia, A. P. & Ritchie, R. O. Bioinspired structural materials. *Nat. Mater.* **14**, 23–36 (2015).

7. Gao, H., Ji, B., Jäger, I. L., Arzt, E. & Fratzl, P. Materials become insensitive to flaws at nanoscale: Lessons from nature. *Proc. Natl. Acad. Sci. U. S. A.* **100**, 5597–5600 (2003).

8. Nudelman, F. & Sommerdijk, N. A. J. M. Biomineralization as an inspiration for materials chemistry. *Angew. Chemie - Int. Ed.* **51**, 6582–6596 (2012).

9. Meldrum, F. C. & Cölfen, H. Controlling mineral morphologies and structures in biological and synthetic systems. *Chem. Rev.* **108**, 4332–4432 (2008).

10. Vincent, J. F. V, Bogatyreva, O. A., Bogatyrev, N. R., Bowyer, A. & Pahl, A. Biomimetics: its practice and theory. *J. R. Soc. Interface* **3**, 471–482 (2006).

11. Wang, S. S. & Xu, A. W. Amorphous calcium carbonate stabilized by a flexible biomimetic polymer inspired by marine mussels. *Cryst. Growth Des.* **13**, 1937–1942 (2013).

12. Barthelat, F. & Zhu, D. A novel biomimetic material duplicating the structure and mechanics of natural nacre. *J. Mater. Res.* **26**, 1203–1215 (2011).

13. He, M., Cho, B. U. & Won, J. M. Effect of precipitated calcium carbonate - Cellulose nanofibrils composite filler on paper properties. *Carbohydr. Polym.* **136**, 820–825 (2016).

14. Boyjoo, Y., Pareek, V. K. & Liu, J. Synthesis of micro and nano-sized calcium carbonate particles and their applications. *J. Mater. Chem. A* **2**, 14270–14288 (2014).

15. Arp, G., Reimer, A. & Reitner, J. Photosynthesis-induced biofilm calcification and calcium concentrations in phanerozoic oceans. *Science.* **292**, 1701–1704 (2001).

16. Matschei, T., Lothenbach, B. & Glasser, F. P. The role of calcium carbonate in cement hydration. *Cem. Concr. Res.* **37**, 551–558 (2007).

17. Ueno, Y., Futagawa, H., Takagi, Y., Ueno, A. & Mizushima, Y. Drug-incorporating calcium carbonate nanoparticles for a new delivery system. *J. Control. Release* **103**, 93–98 (2005).

18. Katz, A. The interaction of magnesium with calcite during crystal growth at 25-90°C and one atmosphere. *Geochim. Cosmochim. Acta* **37**, 1563–1586 (1973).

19. Lorens, R. B. Sr, Cd, Mn and Co distribution coefficients in calcite as a function of calcite precipitation rate. *Geochim. Cosmochim. Acta* **45**, 553–561 (1981).

20. Wassenburg, J. A. *et al.* Determination of aragonite trace element distribution coefficients from speleothem calcite–aragonite transitions. *Geochim. Cosmochim. Acta* **190**, 347–367 (2016).

21. Giuffre, A. J., Gagnon, A. C., De Yoreo, J. J. & Dove, P. M. Isotopic tracer evidence for the amorphous calcium carbonate to calcite transformation by dissolution-reprecipitation. *Geochim. Cosmochim. Acta* **165**, 407–417 (2015).

22. Harris, J., Mey, I., Hajir, M., Mondeshki, M. & Wolf, S. E. Pseudomorphic transformation of amorphous calcium carbonate films follows spherulitic growth mechanisms and can give rise to crystal lattice tilting. *CrystEngComm* **17**, 6831–6837 (2015).

23. Liu, Z. *et al.* Shape-preserving amorphous-to-crystalline transformation of $CaCO_3$ revealed by in situ TEM. *Proc. Natl. Acad. Sci. U. S. A.* **117**, 3397–3404 (2020).

24. Gebauer, D. *et al.* Proto-calcite and proto-vaterite in amorphous calcium carbonates. *Angew. Chemie - Int. Ed.* **122**, 9073–9075 (2010).

25. Dupraz, C. *et al.* Processes of carbonate precipitation in modern microbial mats. *Earth-Science Rev.* **96**, 141–162 (2009).

26. Agbaje, O. B. A., Ben Shir, I., Zax, D. B., Schmidt, A. & Jacob, D. E. Biomacromolecules within bivalve shells: Is chitin abundant? *Acta Biomater.* **80**, 176–187 (2018).

27. Meyers, M. A., Chen, P. Y., Lin, A. Y. M. & Seki, Y. Biological materials: Structure and mechanical properties. *Prog. Mater. Sci.* **53**, 1–206 (2008).

28. Espinosa, H. D., Rim, J. E., Barthelat, F. & Buehler, M. J. Merger of structure and material in nacre and bone - Perspectives on de novo biomimetic materials. *Progress in Materials Science* **54**, 1059–1100 (2009).

29. Barthelat, F., Li, C. M., Comi, C. & Espinosa, H. D. Mechanical properties of nacre constituents and their impact on mechanical performance. *J. Mater. Res.* **21**, 1977–1986 (2006).

30. Gower, L. B. Biomimetic Model Systems for Investigating the Amorphous Precursor Pathway and Its Role in Biomineralization. *Chem. Rev.* **108**, 4551–4627 (2008).

31. Otter, L. M. *et al.* Insights into architecture, growth dynamics, and biomineralization from pulsed Sr-labelled *Katelysia rhytiphora* shells (Mollusca, Bivalvia). *Biogeosciences* **16**, 3439–3455 (2019).

32. Lowenstam, H. A. Minerals formed by weathering. *Science.* **211**, 1126–1131 (1981).

33. Frankel, R. B. & Bazylinski, D. A. Biologically Induced Mineralization by Bacteria. *Rev. Mineral. Geochemistry* **54**, 95–114 (2003).

34. Kawano, J., Shimobayashi, N., Miyake, A. & Kitamura, M. Precipitation diagram of calcium carbonate polymorphs: Its construction and significance. *J. Phys. Condens. Matter* **21**, (2009).

35. Zou, Z. *et al.* A hydrated crystalline calcium carbonate phase: Calcium carbonate hemihydrate. *Science.* **363**, 396–400 (2019).

36. Kralj, D. & Brečević, L. Dissolution kinetics and solubility of calcium carbonate monohydrate. *Colloids Surfaces A Physicochem. Eng. Asp.* **96**, 287–293 (1995).

37. Murray, J. W. The Deposition of Calcite and Aragonite in Caves. *J. Geol.* **62**, 481–492 (1954).

38. Lee, M. R., Hodson, M. E. & Langworthy, G. N. Crystallization of calcite from amorphous calcium carbonate: earthworms show the way. *Mineral. Mag.* **72**, 257–261 (2008).

39. Christy, A. G. A Review of the Structures of Vaterite : The Impossible, the Possible, and the Likely. *Cryst. Growth Des.* **17**, 3567−3578 (2017).

40. Kabalah-Amitai, L. *et al.* Vaterite crystals contain two interspersed crystal structures. *Science.* **340**, 454–457 (2013).

41. Falini, G., Fermani, S., Reggi, M., Džakula, B. N. & Kralj, D. Evidence of structural variability among synthetic and biogenic vaterite. *Chem. Commun.* **50**, 15370–15373 (2014).

42. Makovicky, E. Vaterite: Interpretation in terms of OD theory and its next of kin. *Am. Mineral.* **101**, 1636–1641 (2016).

43. Jacob, D. E., Wirth, R., Agbaje, O. B. A., Branson, O. & Eggins, S. M. Planktic foraminifera form their shells via metastable carbonate phases.

Nat. Commun. **8**, (2017).

44. Tullett, S. G., Board, R. G., Love, G., Perrott, H. R. & Scott, V. D. Vaterite Deposition During Eggshell Formation in the Cormorant, Gannet and Shag, and in 'Shell-less' Eggs of the Domestic Fowl. *Acta Zool.* **57**, 79–87 (1976).

45. Wehrmeister, U., Soldati, A. L., Jacob, D. E., Häger, T. & Hofmeister, W. Raman spectroscopy of synthetic, geological and biological vaterite: A Raman spectroscopic study. *J. Raman Spectrosc.* **41**, 193–201 (2010).

46. Frisia, S., Borsato, A. & Hellstrom, J. High spatial resolution investigation of nucleation, growth and early diagenesis in speleothems as exemplar for sedimentary carbonates. *Earth-Science Rev.* **178**, 68–91 (2018).

47. Effenberger, H. Kristallstruktur und Infrarot-Absorptionsspektrum von synthetischem Monohydrocalcit, $CaCO_3 \cdot H_2O$. *Monatshefte für Chemie* **112**, 899–909 (1981).

48. Hesse, K.-F., Küppers, H. & Suess, E. Refinement of the structure of Ikaite, $CaCO_3 \cdot 6H_2O$. *Zeitschrift für Krist. - Cryst. Mater.* **163**, 227–231 (1983).

49. Habraken, W. J. E. M. *et al.* Layered growth of crayfish gastrolith: About the stability of amorphous calcium carbonate and role of additives. *J. Struct. Biol.* **189**, 28–36 (2015).

50. Jacob, D. E., Wirth, R., Soldati, A. L., Wehrmeister, U. & Schreiber, A. Amorphous calcium carbonate in the shells of adult *Unionoida*. *J. Struct. Biol.* **173**, 241–249 (2011).

51. Wolf, S. E. *et al.* Merging models of biomineralisation with concepts of nonclassical crystallisation: Is a liquid amorphous precursor involved in the formation of the prismatic layer of the Mediterranean Fan Mussel *Pinna nobilis*? *Faraday Discuss.* **159**, 433–448 (2012).

52. Mass, T. *et al.* Amorphous calcium carbonate particles form coral skeletons. *Proc. Natl. Acad. Sci. U. S. A.* **114**, E7670–E7678 (2017).

53. Bentov, S. *et al.* Enamel-like apatite crown covering amorphous mineral in a crayfish mandible. *Nat. Commun.* **3**, 839 (2012).

54. Politi, Y., Arad, T., Klein, E., Weiner, S. & Addadi, L. Sea Urchin Spine Calcite Forms via a Transient Amorphous Calcium Carbonate Phase. *Science.* **306**, 1161–1164 (2004).

55. Weiss, I. M., Tuross, N., Addadi, L. & Weiner, S. Mollusc larval shell formation: Amorphous calcium carbonate is a precursor phase for aragonite. *J. Exp. Zool.* **293**, 478–491 (2002).

56. Johnston, J., Merwin, H. E. & Williamson, E. D. The several forms of calcium carbonate.

American Journal of Science **41**, 473–512 (1916).

57. Radha, A. V. & Navrotsky, A. Direct experimental measurement of water interaction energetics in amorphous carbonates MCO_3 (M = Ca, Mn, and Mg) and implications for carbonate crystal growth. *Cryst. Growth Des.* **15**, 70–78 (2015).

58. Schmidt, M. P., Ilott, A. J., Phillips, B. L. & Reeder, R. J. Structural Changes upon Dehydration of Amorphous Calcium Carbonate. *Cryst. Growth Des.* **14**, 938–951 (2014).

59. Bushuev, Y. G., Finney, A. R. & Rodger, P. M. Stability and Structure of Hydrated Amorphous Calcium Carbonate. *Cryst. Growth Des.* **15**, 5269–5279 (2015).

60. Ihli, J. *et al.* Dehydration and crystallization of amorphous calcium carbonate in solution and in air. *CrystEngComm* **5**, 3169 (2014).

61. Zhang, J., Zhou, X., Dong, C., Sun, Y. & Yu, J. Investigation of Amorphous Calcium Carbonate's Formation under High Concentration of Magnesium: the prenucleation cluster pathway. *J. Cryst. Growth* **494**, 8–16 (2018).

62. Politi, Y. *et al.* Role of magnesium ion in the stabilization of biogenic amorphous calcium carbonate: A structure-function investigation. *Chem. Mater.* **22**, 161–166 (2010).

63. Demmert, B. *et al.* Polymer-Functionalised Nanograins of Mg-Doped Amorphous Calcium Carbonate via a Flow-Chemistry Approach. *Materials.* **12**, 1818 (2019).

64. Jensen, A. C. S., Rodriguez, I., Habraken, W. J. E. M., Fratzl, P. & Bertinetti, L. Mobility of hydrous species in amorphous calcium/magnesium carbonates. *Phys. Chem. Chem. Phys.* **20**, 19682–19688 (2018).

65. Loste, E., Wilson, R. M., Seshadri, R. & Meldrum, F. C. The role of magnesium in stabilising amorphous calcium carbonate and controlling calcite morphologies. *J. Cryst. Growth* **254**, 206–218 (2003).

66. Rodriguez-Blanco, J. D., Shaw, S., Bots, P., Roncal-Herrero, T. & Benning, L. G. The role of pH and Mg on the stability and crystallization of amorphous calcium carbonate. *J. Alloys Compd.* **536S**, S477– S479 (2012).

67. Cartwright, J. H. E., Checa, A. G., Gale, J. D., Gebauer, D. & Sainz-Diaz, C. I. Calcium Carbonate Polyamorphism and Its Role in Biomineralization: How Many Amorphous Calcium Carbonates Are There? *Angew. Chem. Int. Ed* **51**, 11960–11970 (2012).

68. Du, H. *et al.* Amorphous $CaCO_3$: Influence of the Formation Time on Its Degree of Hydration and Stability. *J. Am. Chem. Soc.* **140**, 14289−14299 Article (2018).

69. Rodriguez-Navarro, C., Kudłacz, K., Cizer, Ö. & Ruiz-Agudo, E. Formation of

amorphous calcium carbonate and its transformation into mesostructured calcite. *CrystEngComm* **17**, 58–72 (2015).

70. Bots, P., Benning, L. G., Rodriguez-Blanco, J. D., Roncal-Herrero, T. & Shaw, S. Mechanistic insights into the crystallization of amorphous calcium carbonate (ACC). *Cryst. Growth Des.* **12**, 3806–3814 (2012).

71. Myszka, B. *et al.* Phase-specific bioactivity and altered Ostwald ripening pathways of calcium carbonate polymorphs in simulated body fluid. *RSC Adv.* **9**, 18232–18244 (2019).

72. Ihli, J., Kim, Y.-Y., Noel, E. H. & Meldrum, F. C. The effect of additives on amorphous calcium carbonate (ACC): Janus behavior in solution and the solid state. *Adv. Funct. Mater.* **23**, 1575–1585 (2013).

73. Wang, H.-W. *et al.* Synthesis and structure of synthetically pure and deuterated amorphous (basic) calcium carbonates. *Chem. Commun.* **53**, 2942–2945 (2017).

74. Loste, E., Park, R. J., Warren, J. & Meldrum, F. C. Precipitation of calcium carbonate in confinement. *Adv. Funct. Mater.* **14**, 1211–1220 (2004).

75. Tester, C. C. *et al.* In vitro synthesis and stabilization of amorphous calcium carbonate (ACC) nanoparticles within liposomes. *CrystEngComm* **13**, 3975–3978 (2011).

76. Gower, L. B. & Odom, D. J. Deposition of calcium carbonate films by a polymer-induced liquid-precursor (PILP) process. *J. Cryst. Growth* **210**, 719–734 (2000).

77. Smeets, P. J. M., Cho, K. R., Kempen, R. G. E., Sommerdijk, N. A. J. M. & De Yoreo, J. J. Calcium carbonate nucleation driven by ion binding in a biomimetic matrix revealed by in situ electron microscopy. *Nat. Mater.* **14**, 394–399 (2015).

78. De Yoreo, J. J. & Vekilov, P. G. Principles of Crystal Nucleation and Growth. *Rev. Mineral. Geochemistry* **54**, 57–93 (2003).

79. Gibbs, J. W. On the equilibrium of heterogeneous substances. *Am. J. Sci.* **96**, 441–458 (1878).

80. Volmer, M. & Weber, A. Keimbildung in übersättigten Gebilden. *Zeitschrift für Phys. Chemie* **119**, 277–301 (1926).

81. Farkas, L. Keimbildungsgeschwindigkeit in übersättigten Dämpfen. *Zeitschrift für Physikalische Chemie* **125**, 236–242 (1927).

82. Becker, R. & Döring, W. Kinetische Behandlung der Keimbildung in übersättigten Dämpfen. *Ann. Phys.* **416**, 719–752 (1935).

83. Wolf, S. E., Leiterer, J., Kappl, M., Emmerling, F. & Tremel, W. Early Homogenous

Amorphous Precursor Stages of Calcium Carbonate and Subsequent Crystal Growth in Levitated Droplets. *J. Am. Chem. Soc.* **130**, 12342–12347 (2008).

84. Wallace, A. F. *et al.* Microscopic evidence for liquid-liquid separation in supersaturated $CaCO_3$ solutions. *Science.* **341**, 885–889 (2013).

85. Zou, Z. *et al.* On the Phase Diagram of Calcium Carbonate Solutions. *Adv. Mater. Interfaces* **4**, 1600076 (2017).

86. Cahn, J. W. Phase separation by spinodal decomposition in isotropic systems. *J. Chem. Phys.* **42**, 93–99 (1965).

87. Binder, K. & Fratzl, P. Phase Transformations in Materials - Spinodal Decomposition. in *Wiley-VCH, Weinheim, New York, Chichester* 409–480 (2001). doi:10.1002/352760264X

88. Seknazi, E. *et al.* From spinodal decomposition to alternating layered structure within single crystals of biogenic magnesium calcite. *Nat. Commun.* **10**, (2019).

89. Polishchuk, I. *et al.* Coherently aligned nanoparticles within a biogenic single crystal: A biological prestressing strategy. *Science.* **358**, 1294–1298 (2017).

90. Ostwald, W. Studien über die Bildung und Umwandlung fester Körper. *Zeitschrift für Phys. Chemie* **22U**, 289–330 (1897).

91. Cölfen, H. & Mann, S. Higher-order organization by mesoscale self-assembly and transformation of hybrid nanostructures. *Angew. Chemie - Int. Ed.* **42**, 2350–2365 (2003).

92. Gránásy, L. & James, P. F. Non-classical theory of crystal nucleation: Application to oxide glasses: Review. *J. Non. Cryst. Solids* **253**, 210–230 (1999).

93. Gebauer, D. & Cölfen, H. Prenucleation clusters and non-classical nucleation. *Nano Today* **6**, 564–584 (2011).

94. Gebauer, D., Kellermeier, M., Gale, J. D., Bergström, L. & Cölfen, H. Pre-nucleation clusters as solute precursors in crystallisation. *Chem. Soc. Rev.* **43**, 2348–2371 (2014).

95. Gebauer, D., Völkel, A. & Cölfen, H. Stable Prenucleation Calcium Carbonate Clusters. *Science.* **322**, 1819–1822 (2008).

96. Pouget, E. M. *et al.* The Initial Stages of Template-Controlled $CaCO_3$ Formation Revealed by Cryo-TEM. *Science.* **323**, 1455–1458 (2009).

97. Meldrum, F. C. & Sear, R. P. Now You See Them. *Science.* **322**, 1802–1803 (2008).

98. Demichelis, R., Raiteri, P., Gale, J. D., Quigley, D. & Gebauer, D. Stable prenucleation

mineral clusters are liquid-like ionic polymers. *Nat. Commun.* **2**, (2011).

99. Finney, A. R. & Rodger, P. M. Probing the structure and stability of calcium carbonate pre-nucleation clusters. *Faraday Discuss.* **159**, 47–60 (2012).

100. Gebauer, D., Raiteri, P., Gale, J. D. & Cölfen, H. On classical and non-classical views on nucleation. *Am. J. Sci.* **318**, 969–988 (2018).

101. Gebauer, D. How can additives control the early stages of mineralisation? *Minerals* **8**, 179 (2018).

102. Smeets, P. J. M. *et al.* A classical view on nonclassical nucleation. *Proc. Natl. Acad. Sci. U. S. A.* **114**, E7882–E7890 (2017).

103. Henzler, K. *et al.* Supersaturated calcium carbonate solutions are classical. *Sci. Adv.* **4** (2018).

104. Carino, A. *et al.* Thermodynamic-Kinetic Precipitation Modeling. A Case Study: The Amorphous Calcium Carbonate (ACC) Precipitation Pathway Unravelled. *Cryst. Growth Des.* **17**, 2006–2015 (2017).

105. Avaro, J. T., Wolf, S. L. P., Hauser, K. & Gebauer, D. Stable Prenucleation Calcium Carbonate Clusters Define Liquid–Liquid Phase Separation. *Angew. Chemie - Int. Ed.* **59**, 6155–6159 (2020).

106. Kossel, W. Zur Energetik von Oberflächenvorgängen. *Ann. Phys.* **413**, 457–480 (1934).

107. Cölfen, H. & Antonietti, M. Mesocrystals and Nonclassical Crystallization. Mesocrystals and Nonclassical Crystallization (2008). doi:10.1002/9780470994603

108. Bahrig, L., Hickey, S. G. & Eychmüller, A. Mesocrystalline materials and the involvement of oriented attachment-a review. *CrystEngComm* **16**, 9408–9424 (2014).

109. Volmer, M. Kinetik der Phasenbildung. *Steinkopff* (Dresden, 1939).

110. Frank, F. C. The influence of dislocations on crystal growth. *Discuss. Faraday Soc.* **5**, 48–54 (1949).

111. Uwaha, M. Growth Kinetics: Basics of Crystal Growth Mechanisms. Handbook of Crystal Growth: Second Edition (Elsevier B.V., 2015).doi:10.1016/B978-0-444-56369-9.00008-3

112. Wulff, G. XXV. Zur Frage der Geschwindigkeit des Wachsthums und der Auflösung der Krystallflächen. *Zeitschrift Für Krist. - Cryst. Mater.* **34**, 449–530 (1901).

113. Yu, S. H. & Cölfen, H. Bio-inspired crystal morphogenesis by hydrophilic polymers. *J. Mater. Chem.* **14**, 2124–2147 (2004).

114. Nielsen, L. C., De Yoreo, J. J. & DePaolo, D. J. General model for calcite growth kinetics in the presence of impurity ions. *Geochim. Cosmochim. Acta* **115**, 100–114 (2013).

115. De Yoreo, J. J. *et al.* Crystallization by particle attachment in synthetic, biogenic, and geologic environments. *Science.* **349**, (2015).

116. Penn, R. L. & Banfield, J. F. Imperfect Oriented Attachment: Dislocation Generation in Defect-Free Nanocrystals. *Science.* **281**, 969–971 (1998).

117. Niederberger, M. & Cölfen, H. Oriented attachment and mesocrystals: Non-classical crystallization mechanisms based on nanoparticle assembly. *Phys. Chem. Chem. Phys.* **8**, 3271–3287 (2006).

118. Cölfen, H. & Antonietti, M. Mesocrystals: Inorganic superstructures made by highly parallel crystallization and controlled alignment. *Angew. Chemie - Int. Ed.* **44**, 5576–5591 (2005).

119. Bergström, L., Sturm (née Rosseeva), E. V., Salazar-Alvarez, G. & Cölfen, H. Mesocrystals in biominerals and colloidal arrays. *Acc. Chem. Res.* **48**, 1391–1402 (2015).

120. Sturm, E. V. & Cölfen, H. Mesocrystals: Past, presence, future. *Crystals* **7**, (2017).

121. Oaki, Y. & Imai, H. The hierarchical architecture of nacre and its mimetic material. *Angew. Chemie - Int. Ed.* **44**, 6571–6575 (2005).

122. Oaki, Y. & Imai, H. Nanoengineering in echinoderms: The emergence of morphology from nanobricks. *Small* **2**, 66–70 (2006).

123. Beniash, E., Aizenberg, J., Addadi, L. & Weiner, S. Amorphous calcium carbonate transforms into calcite during sea urchin larval spicule growth. *Proc. R. Soc. B Biol. Sci.* **264**, 461–465 (1997).

124. Gower, L. A. & Tirrell, D. A. Calcium carbonate films and helices grown in solutions of poly(aspartate). *J. Cryst. Growth* **191**, 153–160 (1998).

125. Purgstaller, B., Mavromatis, V., Immenhauser, A. & Dietzel, M. Transformation of Mg-bearing amorphous calcium carbonate to Mg-calcite - In situ monitoring. *Geochim. Cosmochim. Acta* **174**, 180–195 (2016).

126. Littlewood, J. L. *et al.* Mechanism of enhanced strontium uptake into calcite via an amorphous calcium carbonate (ACC) crystallisation pathway. *Cryst. Growth Des.* **17**, 1214–1223 (2017).

127. Koishi, A. *et al.* Role of Impurities in the Kinetic Persistence of Amorphous Calcium Carbonate: A Nanoscopic Dynamics View. *J. Phys. Chem. C* **122**, 16983–16991 (2018).

128. Gaetani, G. A. & Cohen, A. L. Element partitioning during precipitation of aragonite from seawater: A framework for understanding paleoproxies. *Geochim. Cosmochim. Acta* **70**, 4617–4634 (2006).

129. Henderson, G. M. New oceanic proxies for paleoclimate. *Earth Planet. Sci. Lett.* **203**, 1–13 (2002).

130. Gabitov, R. I. & Watson, E. B. Partitioning of strontium between calcite and fluid. *Geochemistry, Geophys. Geosystems* **7**, (2006).

131. Tesoriero, A. J. & Pankow, J. F. Solid solution partitioning of Sr^{2+}, Ba^{2+}, and Cd^{2+} to calcite. *Geochim. Cosmochim. Acta* **60**, 1053–1063 (1996).

132. Füllenbach, C. S., Schöne, B. R. & Mertz-Kraus, R. Strontium/lithium ratio in aragonitic shells of *Cerastoderma edule* (Bivalvia) - A new potential temperature proxy for brackish environments. *Chem. Geol.* **417**, 341–355 (2015).

133. Gascoyne, M. Trace-element partition coefficients in the calcite-water system and their paleoclimatic significance in cave studies. *J. Hydrol.* **61**, 213–222 (1983).

134. Morse, J. W. & Bender, M. L. Partition coefficients in calcite: Examination of factors influencing the validity of experimental results and their application to natural systems. *Chem. Geol.* **82**, 265–277 (1990).

135. Henderson, L. M. & Kracek, F. C. The fractional precipitation of barium and radium chromates. *J. Am. Chem. Soc.* **49**, 738–749 (1927).

136. Doerner, H. A. & Hoskins, W. M. Co-precipitation of radium and barium sulfates. *J. Am. Chem. Soc.* **47**, 662–675 (1925).

137. Blue, C. R. & Dove, P. M. Chemical controls on the magnesium content of amorphous calcium carbonate. *Geochim. Cosmochim. Acta* **148**, 23–33 (2015).

138. Voigt, M., Mavromatis, V. & Oelkers, E. H. The experimental determination of REE partition coefficients in the water-calcite system. *Chem. Geol.* **462**, 30–43 (2017).

139. Terakado, Y. & Masuda, A. The coprecipitation of rare-earth elements with calcite and aragonite. *Chem. Geol.* **69**, 103–110 (1988).

2. SHAPE-PRESERVING PHASE TRANSFORMATIONS OF ACC AFFECT ELEMENT PARTITIONING AND ISOTOPE FRACTIONATION

Demmert, B.[1,2]; Schüßler, M.[1]; Schodder, P. I.[1]; Joachimski, M.[3]; van Gelder, R.[3]; Khansur, N.H.[1]; Jacob, D. E.[2] and Wolf, S. E.[1,4]

[1]Department of Materials Science and Engineering, Institute of Glass and Ceramics (WW3), Friedrich-Alexander University Erlangen-Nürnberg, 90158 Erlangen, Germany.

[2]Department of Earth and Environmental Sciences, Macquarie University, NSW 2109, Australia.

[3]GeoCentre North-Bavaria, Friedrich-Alexander University Erlangen-Nürnberg, 90154 Erlangen, Germany

[4]Interdisciplinary Center for Functional Particle Systems, Friedrich-Alexander University Erlangen-Nürnberg, 91058 Erlangen, Germany.

The author's contribution to the publication is as follows: BD and SEW designed the study, BD conducted the experiments, BD performed SEM, and ICP-OES measurements. BD supported XRD measurements. BD interpreted the data and drafted the manuscript.

Abstract

A detailed understanding of the crystallisation of amorphous calcium carbonate (ACC) is of high importance, especially in paleoclimate reconstructions since calcifying organisms, which rely on ACC as a mineral precursor, are important proxy archives. So far, two different crystallisation pathways are recognised in the literature: Firstly, dissolution-reprecipitation crystallisation in which ACC redissolves and the subsequent crystalline phase is formed from the solution. Secondly, solid-state transformation, in which no redissolution takes place and crystallisation proceeds via diffusional reorganisation processes on the atomic scale. In the latter case, the trace chemical composition of the crystalline product will reflect that of the ACC precursor; thus, the observed incorporation rates are those of the precursor and not of the crystalline phase. In contrast, the dissolution-reprecipitation pathway modifies incorporation rates and thus, the crystal reflects the conditions of its formation reflected by its equilibrium partitioning coefficients. However, in biominerals, a third pathway also seems to exist. Based on biomimetic crystallisation experiments, this pathway was described as a *pseudomorphic transformation*, a phase transformation in which the morphology is retained, but a change in the mineral phase is observed. The mechanism of this pathway, sometimes also simply paraphrased as a *shape-preserving phase transformation*, is still not fully clear. However, it was shown that poly(aspartate) and trace amounts of magnesium can induce this crystallisation pathway. In this work, doped ACC was synthesised by using a flow-through synthesis. Subsequently, ACC was crystallised under various conditions to determine the influence of these three different crystallisation pathways on the partition coefficients. The presented data revealed that the composition of Sr-doped ACC was preserved during a pseudomorphic transformation to the extent that this is comparable to a solid-state transformation whereas under recrystallisation partition coefficients changed drastically. It is shown further that such shape-preserving transformations can be triggered by a range of additives, *e.g.*, by poly(acrylic acid), polyaspartic acid, and phosphate anions.

2.1 Introduction

Calcareous biominerals are used as proxy archives of past climates with excellent success[1–7]. Their biosynthesis is complex, and often their chemical composition deviates from the expected values as predicted by their equilibrium partition coefficients. Most biomineralising organisms employ amorphous calcium carbonate as a precursor to their later crystalline biominerals. The occurrence of an amorphous precursor phase raises questions since it is unclear by which mechanism the phase transformation of ACC under biological control takes place and how important the initial composition of the amorphous phase for that of the final mineral phase is. Generally, two different crystallisation pathways are usually discussed for phase ripening processes of minerals, here, for ACC. On the one hand, there is solid-state crystallisation, where ACC dehydrates and structural rearrangements by atomic diffusion occur

during the transformation process, which is often induced by dry heat[8–10]. Typically for this crystallisation pathway is a retention of the morphology and the chemical composition of the prescursor[11], which means that the trace element concentrations in the crystalline mineral reflect those of the ACC precursor. On the other hand, phase transformation occurs by dissolution-reprecipitation as ACC dissolves and new crystalline calcium carbonate is precipitated from the resulting solution[12–14]. As ACC dissolves, both the morphology and the composition are modified and reflect the equilibrium partition coefficients for the new phase.

Partition coefficients and isotope fractionation are thermodynamic equilibrium parameters that predict the exchange of chemical elements and isotopes between two phases depending on external environmental parameters such as temperature, pH, salinity etc. Paleoclimatic and Paleo-environmental reconstructions based on biocarbonates have, up to date, assumed classical crystallisation and thermodynamic equilibrium, thus have been using the chemical and isotopic composition of the carbonate crystal to reflect certain environmental parameters, such as temperature, quantitatively[11,15]. In light of the recent findings that many calcifying organisms crystallise their skeletal hard parts via amorphous and other metastable precursor phases, the question arises is whether the chemical composition of the final phase is affected by the presence of a preceding precursor phase. In principle, this should not be the case, since classical crystallisation theory predicts that phase ripening, *e.g.*, according to Ostwald rule of stages, is a dissolution-reprecipitation process and thus, the crystal does not bear any "memory" of its earlier amorphous state. But is the phase transformation process in biominerals correctly described as a dissolution-reprecipitation process? In fact, calcareous biominerals form via a shape-preserving transformation process which is rather comparable to a solid-to-solid transformation process as the non-equilibrium morphologies and internal nanogranular structure of these biominerals is preserved in their final crystalline state. On the other hand, it seems unreasonable that a mineral body composed of a highly soluble amorphous precursor undergoes a solid-state transformation when exposed to an aqueous solution. It seems that combinations of these end-member crystallisation pathways are possible, which may complicate appropriate interpretation and analysis[11,16,17].

Based on their biomimetic experiments, Gower and Tirrel[18] described a third pathway and defined it as *pseudomorphic*[19,20]. It is characterised by the retention of the precursor morphology. It proceeds in an aqueous environment, mimicking well various features of biominerals[18]. Liu *et al.*[21] analysed the ability of inorganic and organic additives to induce this type of crystallisation by applying liquid phase-TEM. They revealed that trace amounts of magnesium could induce this crystallisation pathway. It becomes clear that the enigmatic pathway of pseudomorphic transformation strongly differs from a diffusive solid-state transformation, which happens by a rearrangement of ions in solid, even though the latter can also result in non-equilibrium morphologies[22,23].

In this highly complex context, which bears important implications for carbonate biominerals-based paleoclimate research, the first question that should be answered is: Which phase transformation pathway do calcareous biominerals follow? The second question, which is even more pressing for the field of paleoclimate research, is whether this shape-preserving process preserves some memory of the precursor, *i.e.*, is affected by the amorphous precursor's composition – given the existence of various hydrous and anhydrous ACC polyamorphs[13,24,25]. If this is the case, which properties of the parent solution and environment of formation are recorded by the partition coefficients and fractionation factors of the final crystalline mineral? Do the measured partition coefficients reflect the conditions when ACC was formed, or are they re-equilibrated to reflect those of the newly formed phase(s) during the crystallisation of ACC?

In order to take the first and tentative steps towards answering the above questions, this chapter is divided into three parts. To synthesise ACC, a flow-through method was used, which enables comparable mixing conditions, *e.g.,* by adjusting the same flow rate. In the first part, the effect of the three crystallisation pathways, namely solid-state crystallisation, dissolution-reprecipitation, and pseudomorphic transformation, on the chemical composition of strontium-, magnesium-, and barium-doped ACC is analysed. These results show for the first time that pseudomorphic transformation has a significant and unanticipated impact on the partitioning of trace elements, and results in incorporation rates comparable to that of solid-state transformation. In the light of this important finding, the second part assesses those inorganic and organic additives which are common impurities capable of inducing pseudomorphic transformation. In the third part, the influence of the dissolution-reprecipitation pathway and the pseudomorphic transformation on the fractionation of oxygen isotopes are assessed. These crystallisation pathways show pronounced dependency, which provide further insights into the molecular mechanisms of the pseudomorphic phase transformation processes so relevant to biomineralisation.

2.2 Materials and methods

Ultrapure water (Milli-Q Direct 8 with UV photooxidation, Merck Millipore, Burlington, MA, USA, 18.2 MΩ cm^{-1}) was employed in all experiments. However, for the oxygen isotope partitioning, purified groundwater was additionally used (Chapter 2.2.3). All chemical reagents were supplied by Sigma-Aldrich (St. Louis, MO, USA) and employed without further purification. Calcium carbonate was synthesised by utilizing a “µ-Slide III 3in1” microfluidic chip (MFC) which allowed merging three separately fed liquids into one channel (ibidi GmbH, Gräfelfing, Germany; layout is given in Figure 2.1A). Fluid dynamic simulations of the microfluidic chip at a flow rate of 30 mL/min indicated a laminar flow profile in the middle part of the chip, and a turbulent flow with thorough mixing at the orifice (Figure 2.1B). The simulation was conducted by using the software ANSYS AIM, Release 19.0[26]. A peristaltic pump (MA1 70-7000R,

Harvard Apparatus, Holliston, MA, USA) connected to the MFC with standard tubes (tube size 2.79 mm) was applied to maintain the flow rate at 30 mL/min during the syntheses.

2.2.1 Synthesis of doped ACC powders and crystallisation via different pathways

Prior to the synthesis of doped ACC, calcium chloride powder was mixed with the respective additive powder, namely strontium chloride, barium chloride and magnesium chloride to achieve the following dopant concentration in the 40 mM calcium chloride solutions: strontium chloride (4 mM, 6 mM, or 8 mM), barium chloride (4 mM) and magnesium chloride (120 mM). Subsequently, 25 mL of the 40 mM calcium chloride/additive solutions were mixed with 25 mL of a 40 mM sodium carbonate solution. The mixing of the calcium chloride and sodium carbonate solutions occurred in a y-piece which was placed one centimetre in front of the microfluidic chip (Figure 2.1C). The distance between the y-piece and the microfluidic chip has to be as short as possible to ensure that the additives were added before ACC started to crystallise.

Table 2.1. Overview of the applied sample types and the experimental procedure.

Sample type	Solvent	Procedure
ACC	EtOH	Immediate filtration
Annealed	EtOH	Immediate filtration – annealing (400 °C/2h)
Additive	PAA	24 hours of stirring – filtration
Control	H_2O	24 hours of stirring – filtration

Independent of the applied ions, four different sample types were synthesised which differed in the experimental procedure, *i.e.*, “ACC Samples”, “Annealed Samples”, “Additive Samples”, and “Control Samples” – see Table 2.1.

For generating **“ACC Samples”**, 50 mL of ethanol were added to quench the amorphous phase. Afterwards, the mixtures were immediately filtered (nitrocellulose membranes; GVS North America), the residues were washed with ethanol and dried in a desiccator with silica-gel.

For **“Annealed samples”**, dried “ACC Samples” were subsequently annealed in an oven at 400 °C for 2h.

For **“Additive Samples”**, 50 mL of a of 400 µg/mL poly(acrylic acid) sodium salt (PAA, M_w = 5100 g·mol^{-1}) solution was added in the MFC. At the outlet, the mixture was collected in a beaker covered with Parafilm (Bemis Company, Neenah, WI, USA) and stirred for 24 hours.

The suspension was then filtered, the residues were washed with ethanol, and dried in a desiccator over silica-gel.

In case of **"Control Samples",** 50 mL of water was added in the MFC chip. Like in case of the "Additive Samples", the mixture at the outlet was collected in a beaker covered with Parafilm (Bemis Company, Neenah, WI, USA) and also stirred for 24 hours which ensures complete crystallisation via dissolution-reprecipitation. The suspension was then filtered, the residues were washed with ethanol, and dried in a desiccator over silica-gel until dryness.

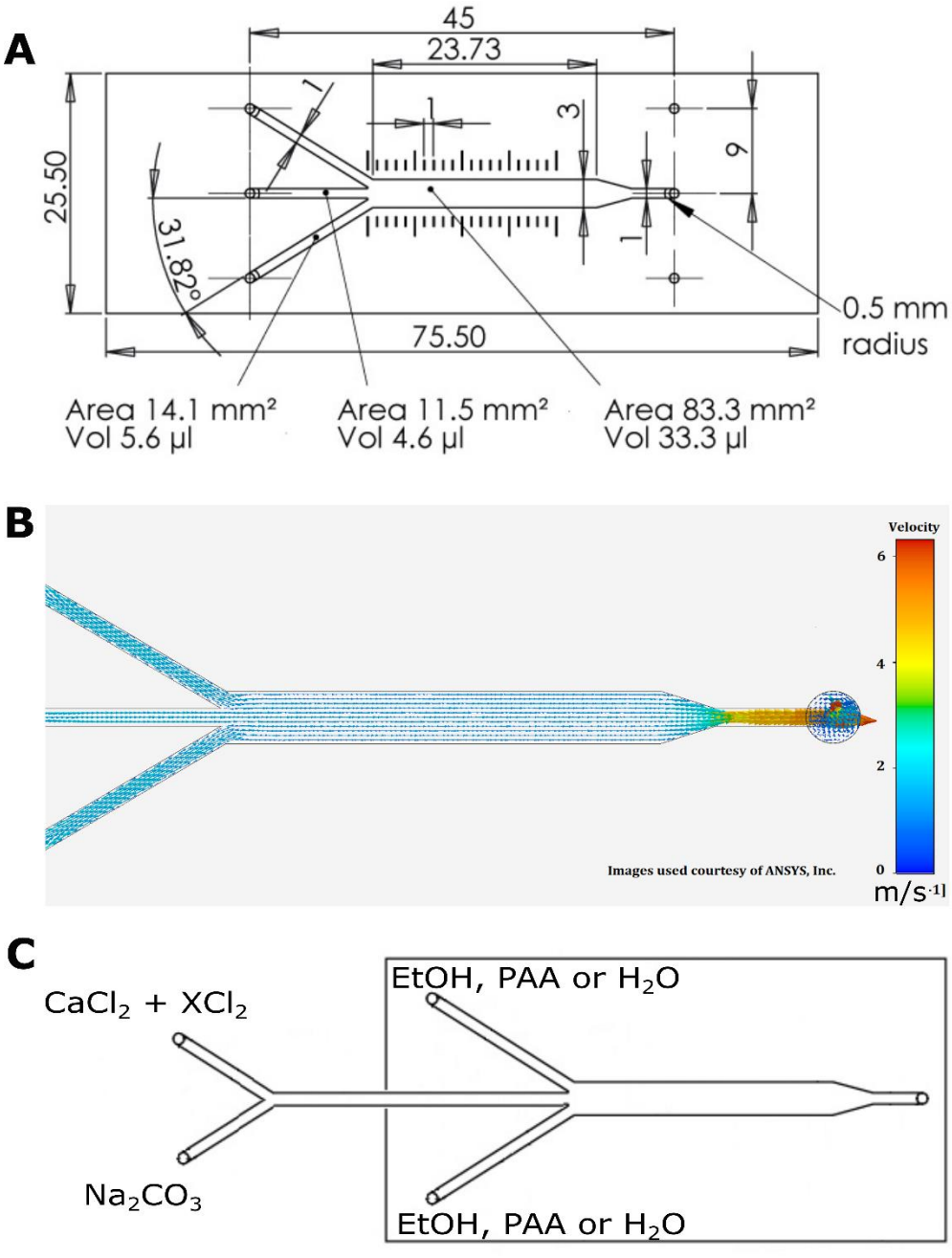

Figure 2.1. (A) Layout of applied microfluidic chip (ibidi GmbH, Gräfelfing, Germany), image courtesy of ibidi GmbH. **(B)** Fluid dynamic simulations in the microfluidic chip, image used by courtesy of ANSYS, Inc. (Canonsburg, PA, USA). **(C)** Experimental setup of the microfluidic chip (MFC) to synthesise doped calcium carbonate. The doped calcium chloride solution (X = Sr, Mg and Ba) and sodium carbonate

solutions were mixed in a y-piece situated in front of the MFC. Ethanol was added in the MFC for “ACC Samples” and “Annealed Samples”, “Additive Samples” received admixture of a 400 µg/mL PAA solution while water was added to “Control Samples”.

Powder X-ray diffraction (D8 Advance Eco, Bruker, Karlsruhe, Germany; Cu Kα radiation with λ = 1.5406 Å) measurements were conducted in Bragg-Brentano geometry with the following parameters: 2θ range between 20° and 70°, step size of 0.05° and a dwell time of 0.3 s. As different calcium carbonate polymorphs were detected for “Additive Samples”, Rietveld refinement was carried out to obtain the phase distribution. Full pattern structural refinements were performed by using the program TOPAS Version 5 (Bruker, Karlsruhe, Germany). An instrumental resolution file was used to describe the instrumental contribution to the profile function. The peak profile shape was described by a Thompson-Cox-Hastings function. Backgrounds of the diffraction patterns were modelled using Chebyshev type polynomial. Lattice parameters, scale factor, atomic parameters, zero angular shift, and microstructural parameters were varied during the refinement.

Particle morphologies were observed by scanning electron microscopy (SEM, GeminiSEM 500, Carl Zeiss, Oberkochen, Germany) on samples mounted on a SEM stub and sputtered with gold (thickness of gold layer 5 – 10 nm), by using an accelerating voltage 1.0 kV and with a working distance of 6.5 mm.

Element concentrations in the powders were measured by inductively coupled plasma optical emission spectroscopy (ICP-OES, Genesis FES, Spectro Analytical Instruments, Kleve, Germany) using external reference materials (Merck, Darmstadt, Germany). Each sample was measured in quintuplicate, each time using 30 mg of powder dissolved in nitric acid (1 M). Following the definition in Chapter 1.7, partition coefficients were calculated by dividing the trace element concentration to calcium concentration given in the solid by the same ratio in the liquid. The precision of the measurements were 0.01 weight percent.

2.2.2 Application of various inorganic and organic additives during pseudomorphic transformation

In addition to PAA, the ability of other inorganic and organic additives to induce a pseudomorphic transformation were tested with the same experimental setup as in Chapter 2.2.1. In these cases, only 4 mM of strontium chloride were used to dope ACC. After synthesising the powders, the mixtures were stirred for 24 hours, similar to the “Additive Samples” in Chapter 2.2.1. Subsequently, they were filtered, the residues were washed with ethanol, dried in a desiccator with silica-gel, and analysed.

An overview of the additives, their concentrations and molecular weights is given in Table 2.2. While 5 mM of phosphate and orthosilicate were applied as inorganic additives in solution, polyaspartic acid sodium salt (PAsp), poly(4-styrenesulfonic acid sodium salt) (PSS), and

poly(allylamine hydrochloride) (PAH) were applied besides PAA as organic additives. For the organic additives 400 µg/mL were employed.

Table 2.2. Inorganic and organic additives used in the experiments with their molecular weights (M_W) and concentrations. Inorganic additives were phosphate and orthosilicate. The organic additives were poly(acrylic acid) sodium salt (PAA), polyaspartic acid sodium salt (PAsp), poly(4-styrenesulfonic acid sodium salt) (PSS), and poly(allylamine hydrochloride) (PAH).

Additive	PAA	PAsp	PSS	PAH	PO_4^{3-}	SiO_4^{4-}
M_w (g·mol^{-1})	5100	2000 - 11000	8000	17500	---	---
Amount	400 µg/mL	400 µg/mL	400 µg/mL	400 µg/mL	5 mM	5 mM

2.2.3 Synthesising calcium carbonate with waters of different oxygen isotopic compositions

Waters with different oxygen isotopic compositions (expressed as $\delta^{18}O$ values) were used to gain better understanding of the effects of the pseudomorphic transformation mechanisms on oxygen isotope fractionation. The $\delta^{18}O$ values are defined as the permil difference in $^{18}O/^{16}O$ ratios (R) compared to a reference material[27]:

$$\delta^{18}O = \left(\frac{R_{Sample}}{R_{Reference}} - 1\right) * 1000 \quad (2.1)$$

Vienna Standard Mean Ocean Water (VSMOW) was used for the waters, and Vienna Pee Dee Belemnite (V-PDB) was used for the calcium carbonate samples.

The applied high-purity waters stem either from Germany (tap water purified by MilliQ) or from Estonian groundwaters (purified by a rotary evaporator). The former water is designated as "Lab Water" (L-water; $\delta^{18}O$ = -9.7 ‰), while the latter is termed "Estonian Groundwater" (E-water; $\delta^{18}O$ = -23.5 ‰). Furthermore, a 1:1 mixture of both waters (M-water; calculated $\delta^{18}O$ = -16.6 ‰) was produced. "Estonian Groundwater" was used as it has a distinctively different $\delta^{18}O$ value compared to tap water from Germany.

Oxygen isotopic compositions of "E-water" and "L-water" samples were analysed by an automated equilibration unit (Gasbench 2; Thermo Fisher Scientific, Bremen, Germany) in continuous flow mode coupled to a Delta *plus* XP isotope ratio mass spectrometer (Thermo Fisher Scientific, Bremen, Germany) using the following procedure:

0.5 mL of each sample was transferred into 12 mL Labco Exetainers™ (Labco Ltd. Lampeter, U.K) and subsequently flushed with 0.3 % CO_2 in helium for CO_2 equilibration. Equilibration time was 24 hours at 25 °C. All samples were measured in triplicate and the results were averaged. All values are reported in the standard delta notation in per mil (‰) vs. VSMOW.

The data sets were corrected for instrumental drift during the run and normalized to the VSMOW/SLAP (Standard Light Antarctic Precipitation) scale by assigning a value of 0 ‰ and –55.5 ‰ ($\delta^{18}O$ value) to VSMOW2 and SLAP2, respectively[28]. External reproducibility based on repeated analyses of a control sample was better than 0.05 ‰ (±1 sigma) for $\delta^{18}O$ value[29,30].

To synthesise the powders, 6 mL of a 40 mM calcium chloride solution was mixed with 6 mL of a 40 mM sodium carbonate solution in the same experimental setup as in Chapter 2.2.1 (Figure 2.2). After synthesising calcium carbonate in the y-piece (position 1), either 12 mL of a 400 µg/mL PAA solution or 12 mL of water were added as solvents in the MFC (position 2). Given the list of experiments and solvents in Table 2.3, the synthesis of "LE-PAA" is described as an example: Calcium chloride and sodium carbonate, each dissolved in Lab-Water, were mixed at position 1, while at position 2 PAA dissolved in Estonian groundwater was added.

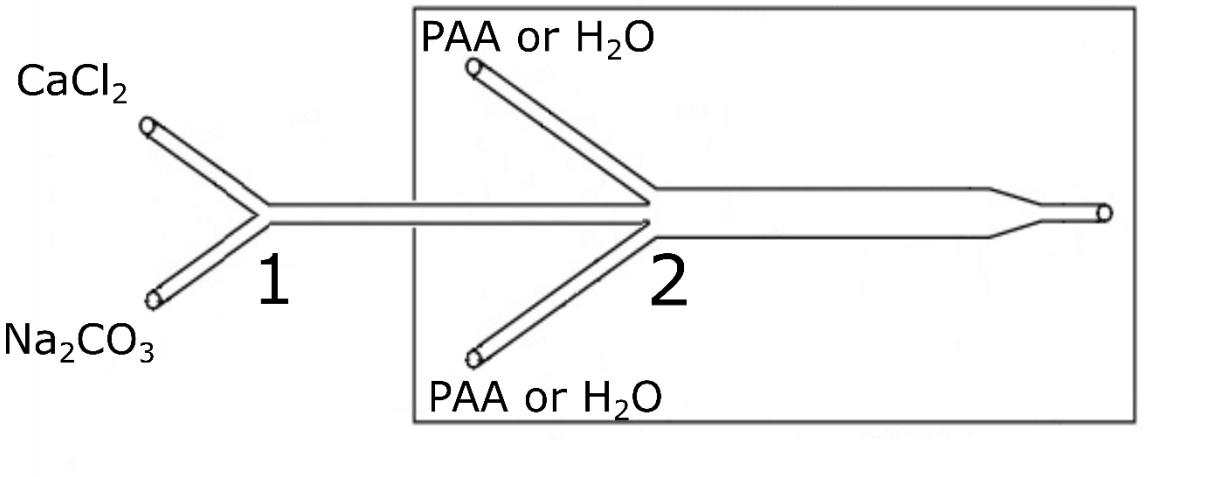

Figure 2.2. Waters with different $\delta^{18}O$ values were used to synthesise ACC. Therefore, calcium chloride and sodium carbonate were mixed in the y-piece (position 1) suited in front of the MFC (position 2). As solvents either a 400 µg/mL PAA solution or water were added at position 2.

"L-ACC", "M-ACC", and "E-ACC" samples were immediately filtered after the synthesis, the residues were washed with acetonitrile, and dried with silica-gel. Acetonitrile was used instead of ethanol to avoid contamination by oxygen isotopes present in ethanol. Similar to the "Additive Samples", all samples – except for the ACC ones – were stirred for 24 hours.

Table 2.3. Sample description with the employed solvent and the types of water. Position 1 and Position 2 refer to the numbered inlets in Figure 2.2.

Designation	Solvent in MFC	Position 1	Position 2
L-ACC	H_2O	L-water	L-water
LE-PAA	PAA	L-water	E-water
LE-H_2O	H_2O	L-water	E-water
M-ACC	H_2O	M-water	M-water
MM-PAA	PAA	M-water	M-water
MM-H_2O	H_2O	M-water	M-water
E-ACC	H_2O	E-water	E-water
EL-PAA	PAA	E-water	L-water
EL-H_2O	H_2O	E-water	L-water

However, in contrast to the “Additive Samples”, the samples were stirred in snap cap vials to prevent evaporation and were stored in an oven at 30 °C to achieve a constant temperature during crystallisation. Subsequently, the mixtures were filtered, the residues washed with acetonitrile, and dried. X-ray diffraction (D8 Advance Eco, Bruker Corporation, Billerica, MA, USA; Cu Kα source) phase analysis was conducted following the procedure outlined in Chapter 2.2.1.

The dried samples were reacted with 100 % phosphoric acid at 70 °C using a Gasbench II connected to a Thermo Fisher Delta V Plus mass spectrometer to analyse $\delta^{18}O$ values of the calcium carbonate samples. All values were reported in per mil relative to V-PDB. Reproducibility and accuracy were monitored by replicate analysis of laboratory standards calibrated by assigning $\delta^{13}C$ values of +1.95 ‰ to NBS19 and -46.6 ‰ to LSVEC and $\delta^{18}O$ values of -2.20 ‰ to NBS19 and -23.2 ‰ to NBS18. The reproducibility for $\delta^{13}C$ and $\delta^{18}O$ value was ±0.0x and ±0.0y, respectively[31].

Given the fact that different reference materials were used for waters (VSMOW) and carbonates (VPDB), the following equation was applied to recalculate the results[32]:

$$\delta^{18}O_{VSMOW} = 1.03092 * \delta^{18}O_{VPDB} + 30.92\ ‰ \quad (2.2)$$

2.3 Results and Discussion

2.3.1 Impact of phase transformation pathways on element partitioning

To analyse the influence of the different phase transformation processes on the element partitioning, strontium-, magnesium-, and barium-doped ACC was synthesised. Subsequent to the syntheses, as well as after the phase transformation experiments, powder morphology, phase and elemental compositions were determined.

2.3.1.1 Sr-doped calcium carbonate with various Sr concentrations

X-ray diffraction patterns demonstrate that the synthesis of Sr-doped ACC successfully yielded amorphous calcium carbonate, irrespective of the strontium chloride concentrations (Figure 2.3 and Supplementary Figure 2.1). As control experiments, these powders were exposed to water and, after Ostwald ripening, only calcite was found for all ACC samples doped with Sr. Annealing of these Sr-doped ACC powders for 2h at 400 °C also resulted in the transformation to calcite for all samples (Figure 2.3 and Supplementary Figure 2.1). In the presence of an additive, either vaterite/calcite mixtures or additional signals of strontianite were observed in case of Sr-doped ACC synthesised with 4 to 6 mM or 8 mM strontium chloride, respectively (Figure 2.3 and Supplementary Figure 2.1). The results of a Rietveld refinement are provided in Table 2.4.

Table 2.4. Phase distribution determined via Rietvield refinement for “Additive Samples”.

Dopant concentration	Vaterite	Calcite	Strontianite
4 mM $SrCl_2$	32 %	68 %	---
6 mM $SrCl_2$	60 %	40 %	---
8 mM $SrCl_2$	34 %	62 %	4 %

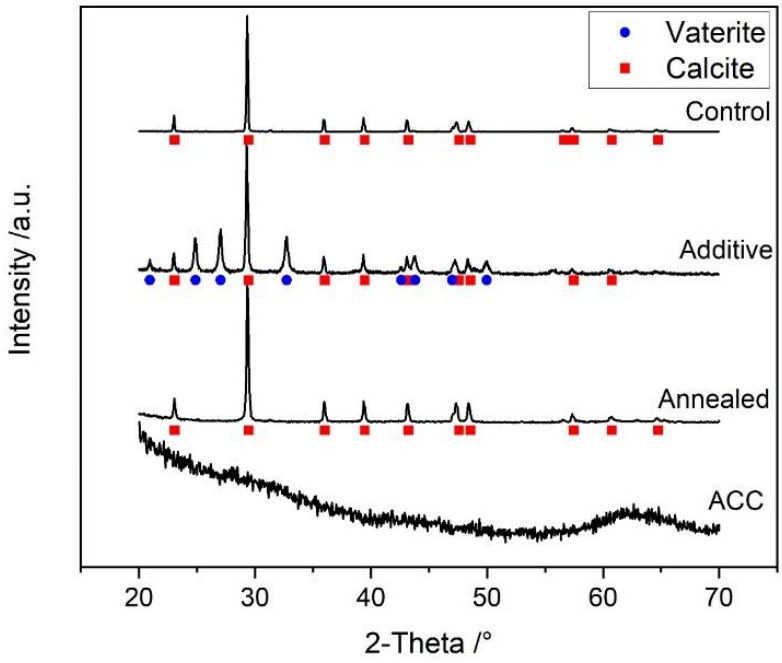

Figure 2.3. Phase analysis of calcium carbonate samples doped with 4 mM $SrCl_2$ before and after crystallisation.

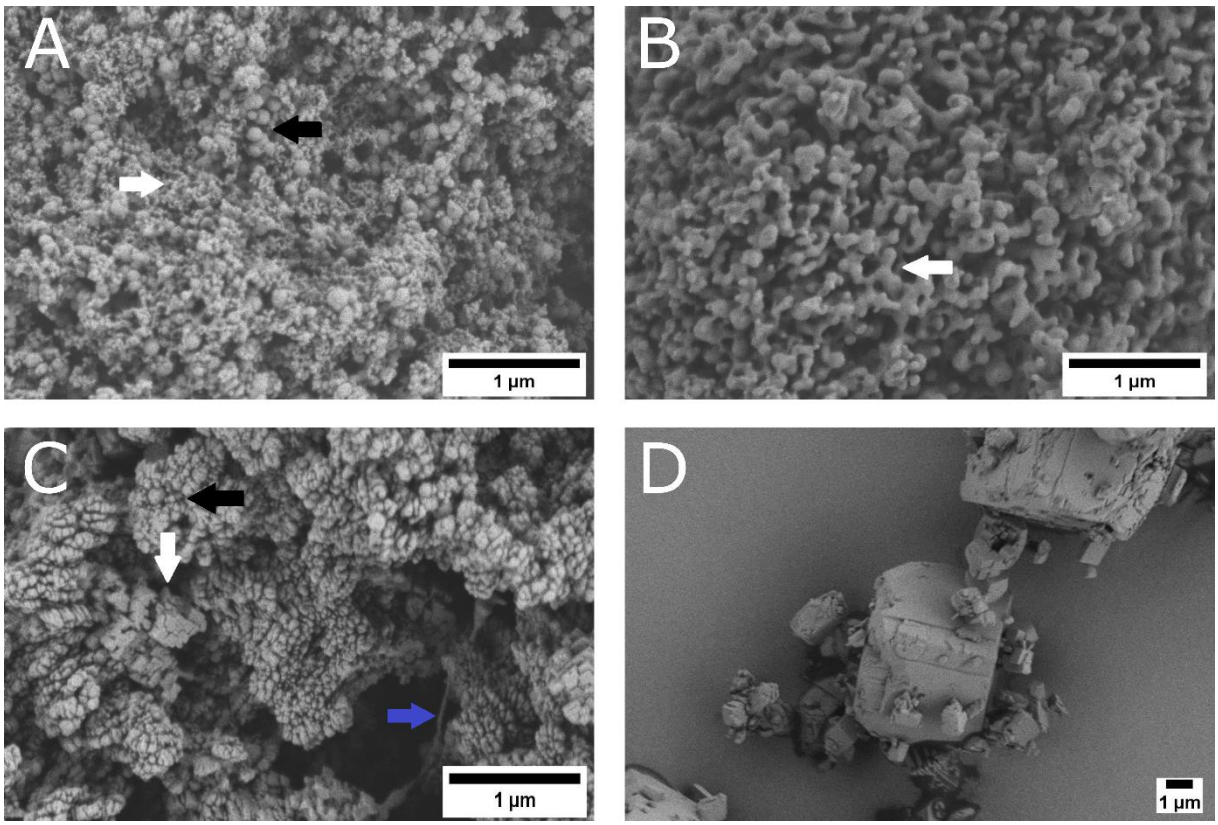

Figure 2.4. Scanning electron micrographs (SEM) of Sr-doped **(A)** "ACC Samples", **(B)** "Annealed Samples", **(C)** "Additive Samples" and **(D)** "Control Samples" (doping concentration 4 mM).

Scanning electron micrographs (Figure 2.4) show that the morphology of the “ACC Samples” have the typical ACC morphology, *i.e.*, spherical particles. Particle sizes range from 30 nm (white arrow in Figure 2.4A) to over 100 nm (black arrow in Figure 2.4A), overlapping with sizes reported in the literature of between 80 nm to 100 nm[33].

After two hours at 400 °C, the “Annealed Samples” showed spherical particles with minor necking (white arrow in Figure 2.4B). However, the overall ACC morphology was retained during crystallisation (Figure 2.3). Therefore, it can be concluded that in the case of the “Annealed Samples” a temperature-induced solid-state transformation was successfully triggered (Figure 2.4B)[14,23].

Despite being more elongated than the spherical particles of the “ACC Samples”, both, the “ACC Samples” and the “Additive Samples” have a fine-grained structure. As shown by the XRD pattern (Figure 2.3), a small proportion of rhombic calcite crystals (white arrow in Figure 2.4C) and hexagonal vaterite crystals (black arrow in Figure 2.4C) were part of the crystallised samples. Furthermore, the addition of PAA resulted in the formation of some filamentous structures (blue arrow in Figure 2.4C). As crystallisation took place in solution under the participation of an organic additive (PAA) and yielded a non-equilibrium morphology of crystalline calcium carbonate, this process can be described as a shape-preserving pseudomorphic phase transformation. It should be noted that Liu *et al.*[21] did not observe a shape-preserving transformation, although they used similar PAA concentrations. Instead, they reported a dissolution-reprecipitation crystallisation pathway. It is possible that this contradictory behaviour was caused by using PAA with different chain lengths, which is known to be of critical importance[34]. Unfortunately, no information about the chain length was provided in the work of Liu *et al.*[21].

The “Control Samples”, which were formed under identical conditions but in absence of PAA, featured the classical rhombic shape of calcite crystals, suggesting a dissolution-reprecipitation process with the spherical particles converted into facetted particles (Figure 2.4D).

In summary, a solid-state crystallisation was successfully induced in the case of “Annealed Samples”, a shape-preserving and pseudomorphic transformation in the “Additive Samples”, and a dissolution-reprecipitation for the “Control Samples”. Applying higher strontium chloride concentrations of 6 mM (Figure 2.5) and 8 mM $SrCl_2$ (Figure 2.6) resulted in very similar powder morphologies as for the 4 mM samples, indicating that the same crystallisation pathways took place. Notably, with increasing strontium chloride concentrations, the calcite crystals became more curved and pores were detectable (white arrow in Figure 2.6D). This suggests that the increasing strontium chloride concentrations affected the crystallisation process.

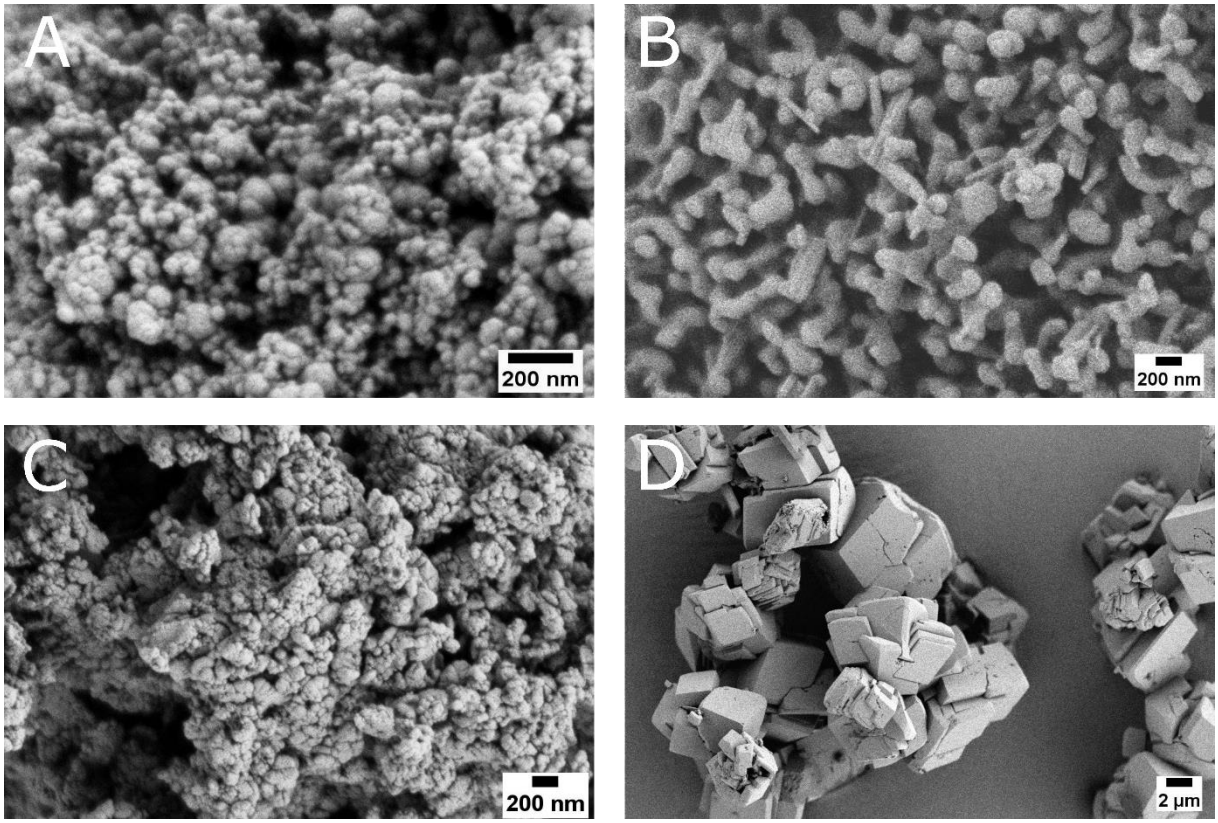

Figure 2.5. SEM images of **(A)** “ACC Samples”, **(B)** “Annealed Samples”, **(C)** “Additives Samples” and **(D)** “Control Samples” doped with 6 mM of strontium chloride.

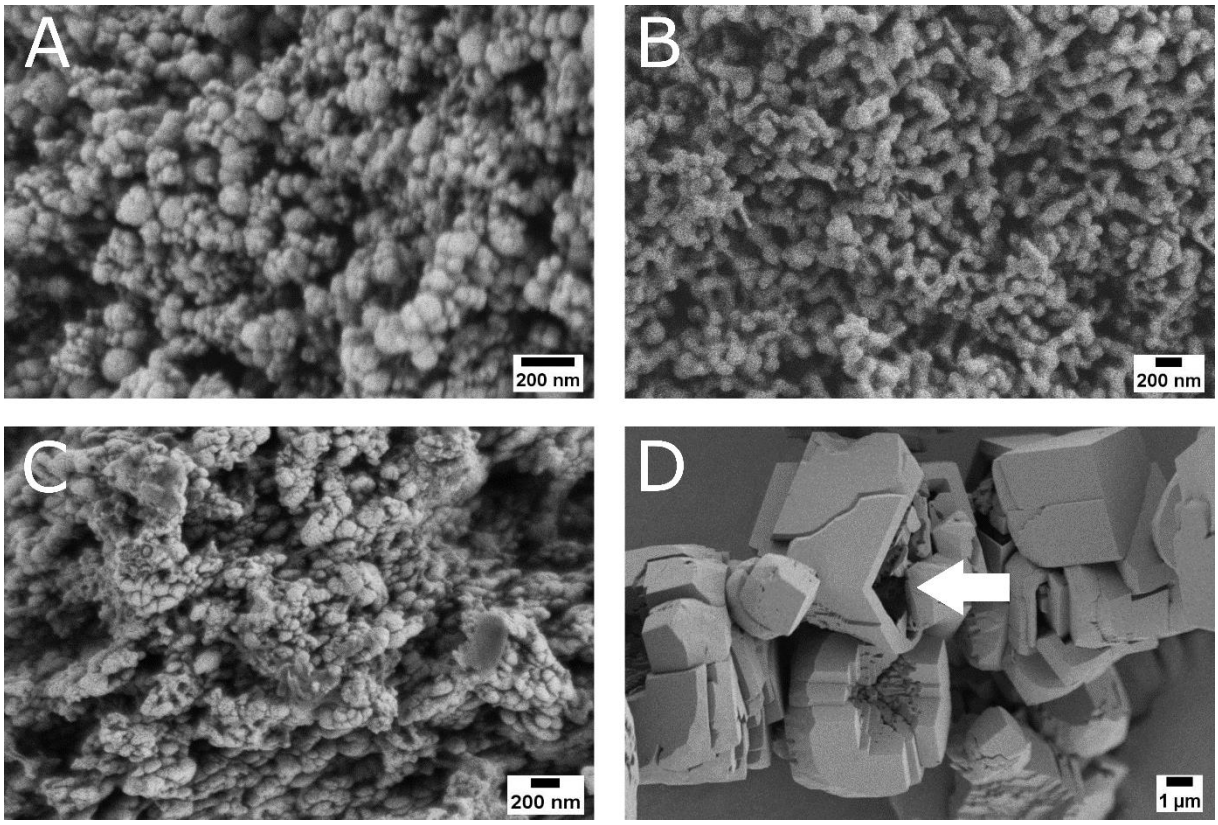

Figure 2.6. Scanning electron micrographs of **(A)** “ACC Samples”, **(B)** “Annealed Samples”, **(C)** “Additives Samples” and **(D)** “Control Samples” doped with 8 mM of strontium chloride.

The influence of the different crystallisation pathways on the chemical composition of the final crystalline phase was explored by ICP-OES measurements to determine calcium and strontium concentrations (Figure 2.7). Independent of the doping concentrations, the chemical composition of the "ACC Samples", "Annealed samples", and – most remarkably – of the "Additive Samples" were similar (Figure 2.7 and Table 2.5). Preservation of the chemical composition is typical for a solid-state transformation and thus expected in case of "Annealed Samples"[11]. However, it is shown here for the first time that the pseudomorphic transformation also preserves the composition, as "Additive Samples" are chemically comparable to "ACC Samples" (Table 2.5). Only a small decrease of the chemical composition was observed, which is negligible in comparison to the partitioning coefficients of the "Control Samples". This minor drop can be explained by the formation of small amounts of rhombic calcite and hexagonal vaterite besides the majority of non-equilibrium shape particles.

Table 2.5. Influence of the crystallisation pathways on the calculated partition coefficients of Sr-doped calcium carbonate, including standard deviations (n=5).

Dopant concentration	ACC	Annealed	Additive	Control
4 mM $SrCl_2$	0.91 ± 0.01	0.92 ± 0.01	0.87 ± 0.01	0.59 ± 0.02
6 mM $SrCl_2$	0.92 ± 0.02	0.91 ± 0.01	0.91 ± 0.02	0.49 ± 0.02
8 mM $SrCl_2$	0.84 ± 0.01	0.85 ± 0.02	0.82 ± 0.01	0.47 ± 0.01

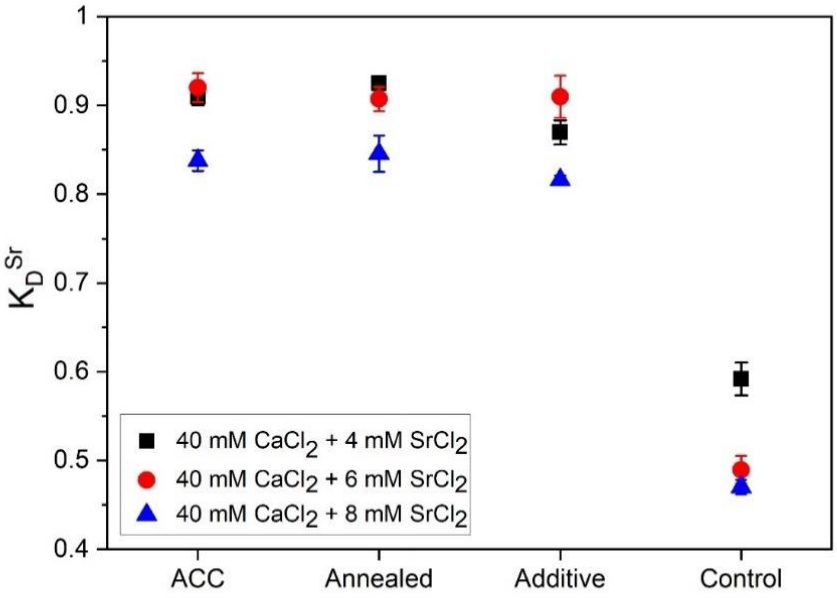

Figure 2.7. Influence of the crystallisation pathways on the calculated partition coefficients of Sr-doped ACC. Note that some error bars are smaller than the symbols.

For the “Control Samples” transformed by dissolution-reprecipitation, a strong decrease of the apparent partition coefficients was detected, which is explained by the dissolution of amorphous calcium carbonate and subsequent reprecipitation of calcite (Figure 2.7). The newly precipitated phase contained much less strontium, which is in good agreement with the reported partitioning coefficients determined by Gabitov and Watson at high growth rates (10 nm/s and above)[2]. Notably, Lorens and Tesoriero and Pankow determined lower partition coefficients in their studies (0.04 – 0.1 respectively 0.02 – 0.14)[3,5], but their growth rates were significantly lower (at maximum 0.1 nm/s) than those of Gabitov and Watson. Accordingly, Gabitov and Watson assumed a strontium enrichment on the crystal surface as diffusive equilibration was prevented at fast growth rates. As no detailed investigations were conducted in this work to reveal the strontium distribution within the crystals, more research is needed to determine if strontium surface enrichment caused the high partition coefficients compared to the works of Lorens and Tesoriero and Pankow.

The ability of PAA to induce a pseudomorphic transformation may have an impact on many scientific areas, as similar organic matrices, such as proteins rich in aspartic acid, are present in biominerals. According to the results presented above, this crystallisation pathway affects the chemical composition of the crystalline endproduct[11,14,35–39]. For calcium carbonate crystallised via solid-state transformation and shape-preserving pseudomorphic transformation, the measured partition coefficients of the crystalline endproduct may deviate significantly from the experimentally determined equilibrium partition coefficients and would therefore result in erroneous reconstructions of quantitative environmental parameters, such as temperature. Instead, for dissolution-reprecipitation in the presence of significant amounts of water (*i.e.* without micron-scale confinement), the newly formed phase can re-equilibrate and impact partition coefficients as well as isotope fractionation factors[11]. As Martignier *et al.*[40] have recently found strontium rich ACC micropearls in algae, which possess a significantly different strontium concentration compared to the surrounding water and growth medium, a detailed reinvestigation of the biominerals used for paleoclimate reconstructions became even more essential.

Other scientific fields may also be impacted by these findings as the pseudomorphic transformation offers, *i.e.*, a low-cost method to synthesise highly doped crystalline calcium carbonate at ambient temperatures. Furthermore, if a pseudomorphic transformation is possible to generate other crystalline phases, this would allow for a way to incorporate dopants and to retain the incorporation rates using an amorphous precursor phase.

2.3.1.2 Mg-doped calcium carbonate

Mg-doped ACC was successfully synthesised, according to diffraction analysis (Figure 2.8). After crystallisation through annealing, only calcite was present. As magnesium and PAA stabilises the amorphous phase[41–43], additive samples did not crystallised, but some showed

two small peaks indicative for vaterite at 42.5° and 43.5°. Thus, Mg-doped powders offered only a limited significance to analyse the influence of the pseudomorphic transformation on the chemical composition. For the “Control Samples”, mainly aragonite was present after crystallisation. This can be explained as Mg suppresses calcite growth, which is an effect well-described in the literature[25,44]. Furthermore, two peaks were detected which can be assigned to vaterite.

The morphology of the “Annealed Samples” and “Additive Samples” were similar to those of the “ACC Samples” (Figure 2.9A-C). Therefore, a solid-state transformation can be assumed for the “Annealed Samples”. As the “Additive Samples” were still amorphous, the unchanged morphology was primarily caused by the unsuccessful crystallisation. The “Control Samples” consisted of mainly of aragonite crystals (Figure 2.9D).

As the Mg-doped powders had only limited significance for this study, the partition coefficients are only summarized here for completeness (Figure 2.10 and Table 2.6). “Annealed Samples” (0.110 ± 0.002) had similar calculated partition coefficients to the “ACC Samples” (0.110 ± 0.003), which is due to a solid-state crystallisation. The calculated partition coefficients for the “Additive Samples” increased to 0.13 ± 0.01, which suggests that the presence of PAA increases Mg incorporation into crystalline calcium carbonate. Crystallisation via the dissolution-reprecipitation pathway resulted in very low calculated partition coefficients in agreement with the incompatibility of magnesium in aragonite. In accordance with the “Control Samples”, Mavromatis *et al.*[15] described a change of the magnesium isotope composition during the crystallisation of Mg-doped ACC.

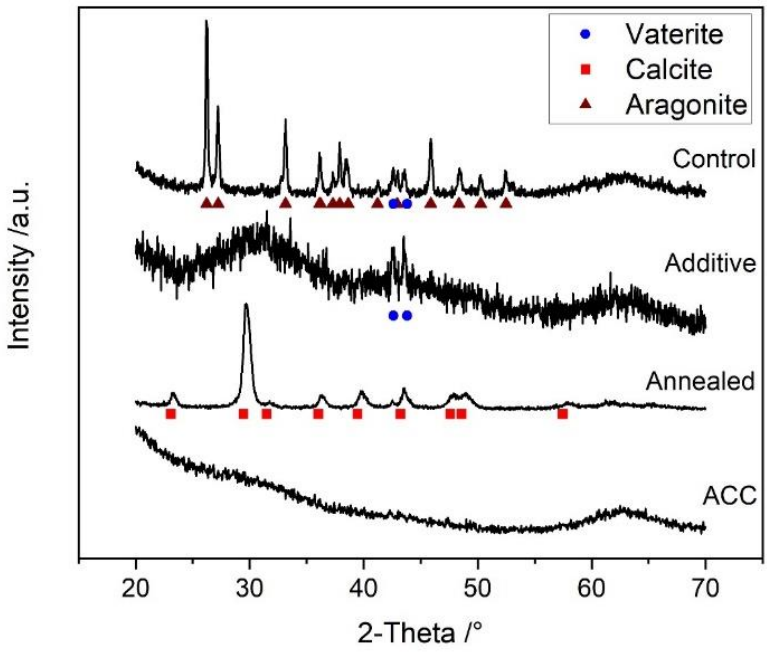

Figure 2.8. Phase analysis of Mg-doped calcium carbonate before and after crystallisation.

Table 2.6. Calculated partition coefficients of Mg-doped calcium carbonate including standard deviations (n=5).

ACC	Annealed	Additive	Control
0.11 ± 0.003	0.11 ± 0.002	0.13 ± 0.008	$0.005 \pm 3 \cdot 10^{-4}$

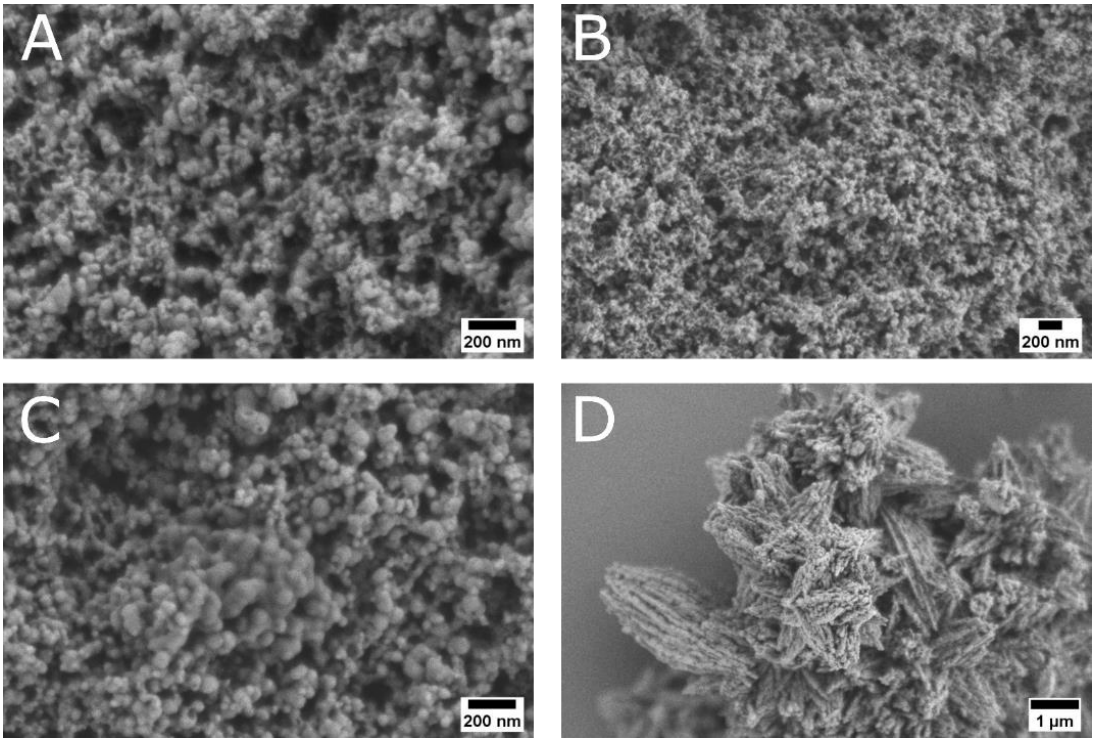

Figure 2.9. SEM micrographs of the Mg-doped **(A)** "ACC Samples", **(B)** "Annealed Samples", **(C)** "Additives Samples" and **(D)** "Control Samples" before and after the crystallisation.

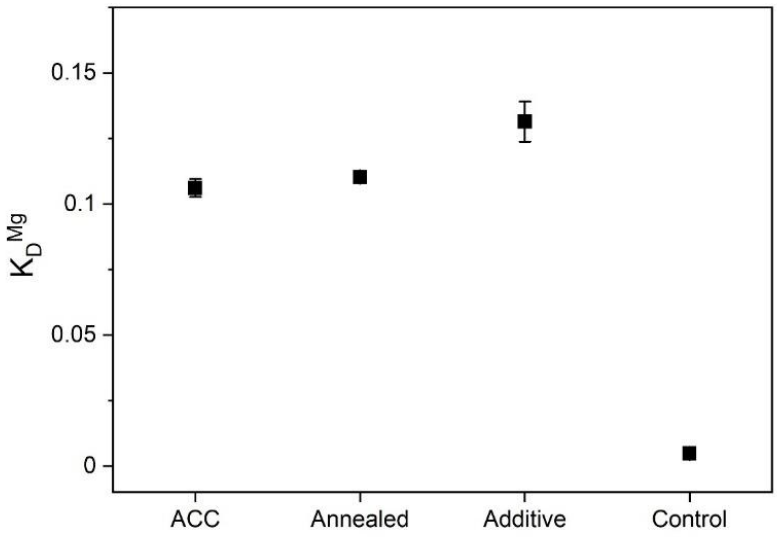

Figure 2.10. Influence of the crystallisation pathways on the calculated partition coefficients of Mg-doped calcium carbonate. Note that some error bars are smaller than the symbols.

2.3.1.3 Barium doped calcium carbonate

Ba-doped ACC was successfully synthesised as shown by XRD (Figure 2.11). The “Annealed Samples” consisted only of calcite. After 24 hours of stirring, the “Additive Samples” were still amorphous and only minor vaterite peaks were detectable in XRD patterns. As the “Additive Samples” derived from Sr-doped ACC crystallised despite the ACC-stabilising effect of PAA[43], this suggests that barium inhibited the formation of crystalline calcium carbonate due to its larger ionic radius[45]. Combined with the stabilising effect of PAA, the crystallisation of “Additive Samples” was delayed, and 24 hours of stirring was not sufficient to achieve complete crystallisation of the powders. Hence, the Ba-doped samples do not allow study of the impact of pseudomorphic transformation on partition coefficients. For the “Control Samples”, only vaterite was present as barium blocks the calcitic growth sides[46].

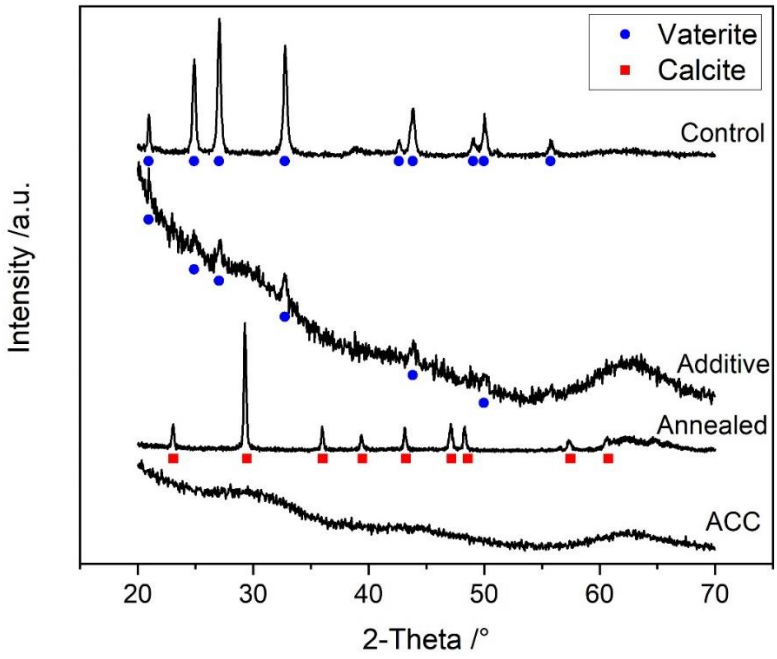

Figure 2.11. Phase analysis of Ba-doped calcium carbonate before and after crystallisation.

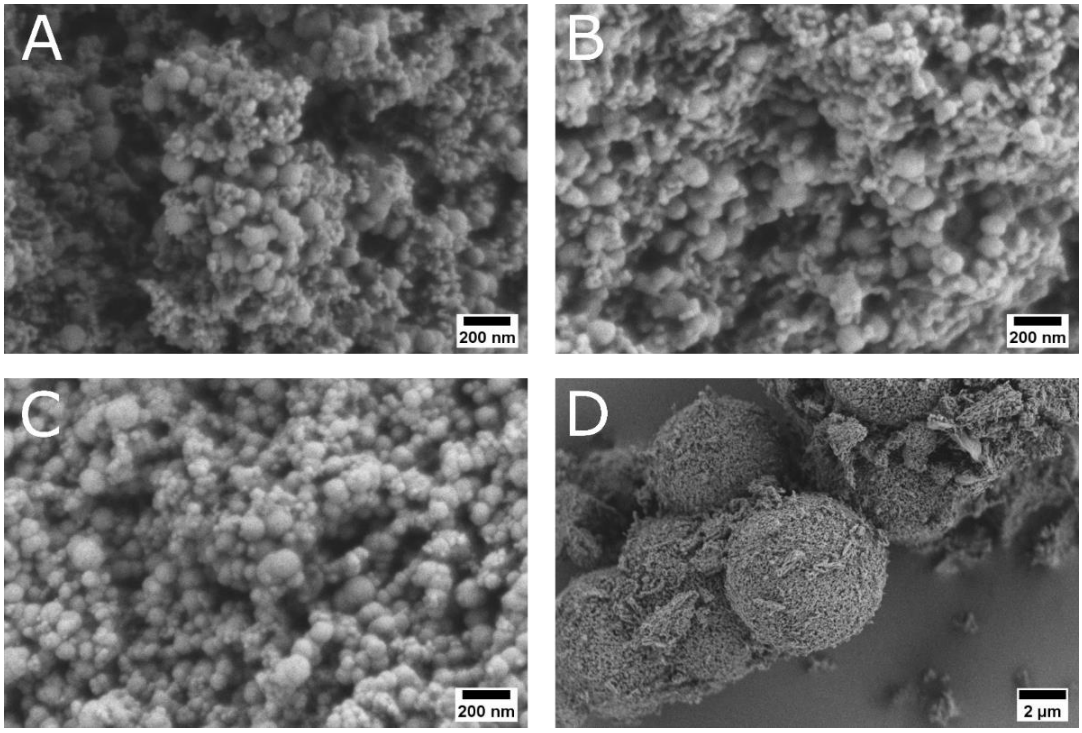

Figure 2.12. SEM images of the Ba-doped **(A)** “ACC Samples”, **(B)** “Annealed Samples”, **(C)** “Additives Samples” and **(D)** “Control Samples” before and after inducing crystallisation.

With the exception of the control experiments, the “Annealed Samples” and “Additives Samples” exhibited a comparable morphology to the “ACC Samples” (Figure 2.12A-C). Therefore, a solid-state crystallisation can be assumed for the “Annealed Samples”, similar to the Sr-doped case. The retention of the morphology for the “Additive Samples” was caused by

an incomplete crystallisation and not by pseudomorphic transformation. Due to the expected dissolution-reprecipitation process, the morphology of the “Control Samples” changed to spherical vaterite particles with particle sizes of 10 µm (Figure 2.12D). Partition coefficients were calculated, revealing that the Ba/Ca ratio was higher in the solid than in the solution (Figure 2.13 and Table 2.7). While the calculated partition coefficients of the “ACC Samples” (1.14 ± 0.03) and the “Annealed Samples” (1.09 ± 0.04) were comparable, the “Additive Samples” exhibited high calculated partition coefficients of 1.2 ± 0.04. Therefore, PAA might promote barium uptake, similar to the case of Mg. The calculated partition coefficients of the “Control Samples” were only 0.22 ± 0.02.

Table 2.7. Calculated partition coefficients of Ba-doped calcium carbonate including standard deviations (n=5).

ACC	Annealed	Additive	Control
1.14 ± 0.03	1.09 ± 0.04	1.2 ± 0.04	0.22 ± 0.02

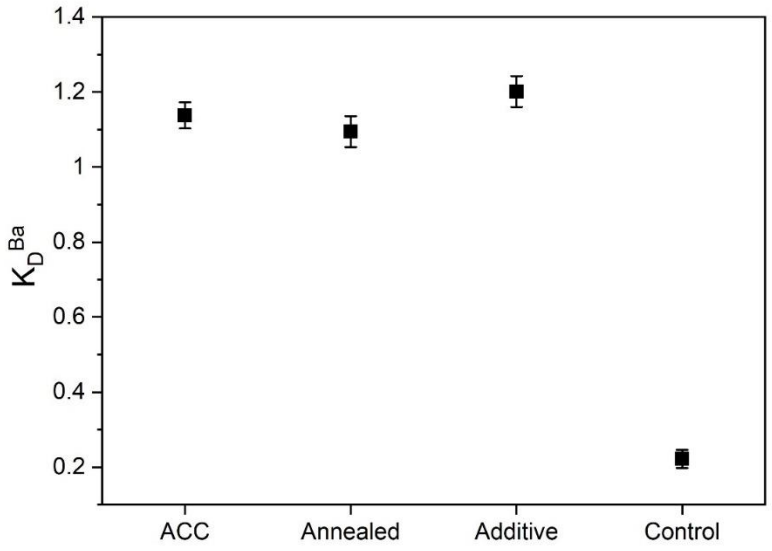

Figure 2.13. Influence of the different crystallisation pathways on the calculated partition coefficients of Ba-doped ACC. Note that some error bars are smaller than the symbols.

2.3.2 Analysing the ability of additives to induce a pseudomorphic transformation

The ability of other inorganic and organic additives than PAA to trigger a pseudomorphic transformation of Sr-doped ACC was explored. For this task, 5 mM of phosphate and orthosilicate were applied, and solutions of polyaspartic acid sodium salt (PAsp), poly(4-styrenesulfonic acid sodium salt; PSS), and poly(allylamine hydrochloride; PAH) were

used. The selected additives were chosen because they are either present in biominerals or are used in the laboratory to mimic the organic matrix in biominerals (Chapter 6)[43,47–50].

2.3.2.1 Inorganic additives

After allowing for crystallisation by stirring the solution for 24 hours, only calcite was present, irrespective whether phosphate or orthosilicate was added (Figure 2.14). A small silicate peak was also detected at 26.6°, which can be explained by the conditions of the experiment reaching the solubility limit of orthosilicate.

SEM micrographs demonstrated that addition of phosphate retained the ACC morphology during crystallisation (Figure 2.14A). This agrees with the literature in which a solid-state transformation was suggested for phosphate doped ACC due to an increase in ACC stability by this additive[51]. Following the definition (above), this crystallisation is rather described as a pseudomorphic transformation here as it took place in solution under participation of an additive and resulted in a non-equilibrium morphology.

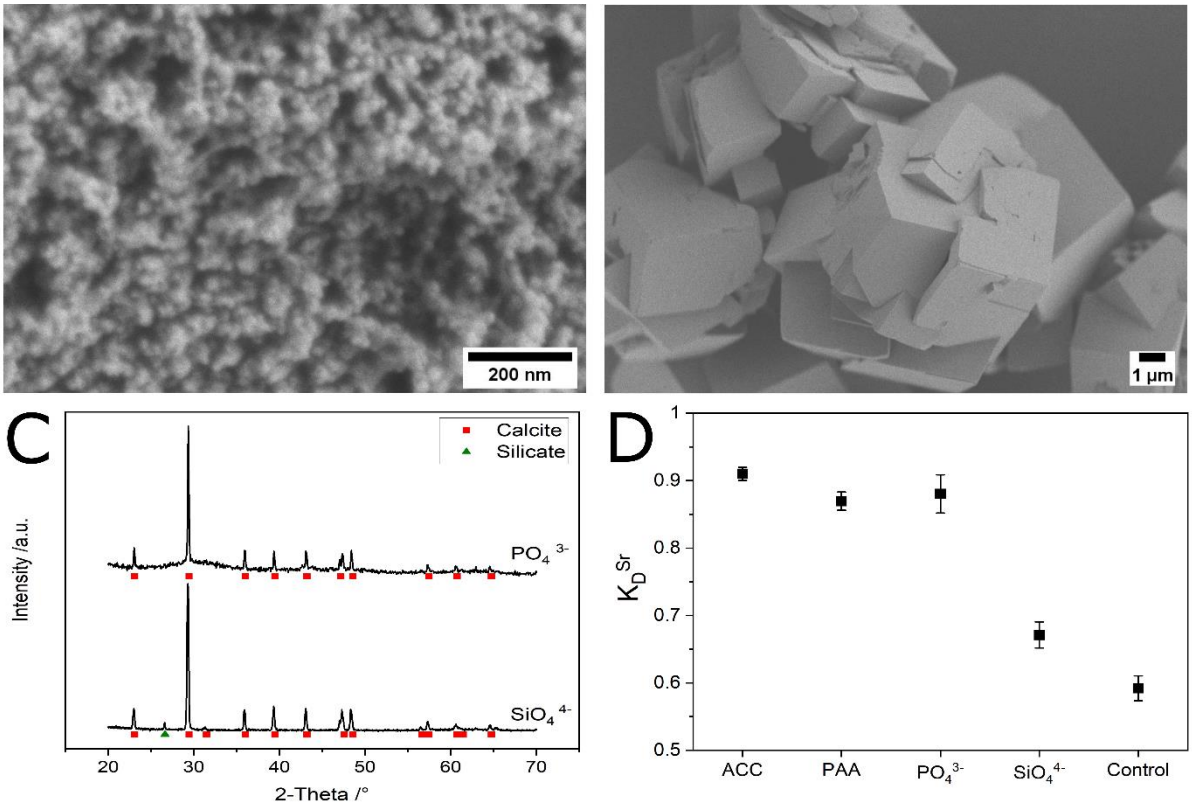

Figure 2.14. Effect of phosphate and orthosilicate on the ACC crystallisation. Scanning electron micrographs of calcium carbonate powders synthesised in the presence of **(A)** phosphate and **(B)** orthosilicate. **(C)** Phase analysis of the precipitated calcium carbonate powders. **(D)** Comparison of the calculated partition coefficients of strontium doped calcium carbonate.

Table 2.8. Calculated strontium partition coefficients for the application of phosphate and orthosilicate as inorganic additives including standard deviations (n=5).

ACC	PAA	Phosphate	Orthosilicate	Control
0.91 ± 0.01	0.87 ± 0.01	0.88 ± 0.03	0.67 ± 0.02	0.59 ± 0.02

In accordance with the observed morphologies indicative for a pseudomorphic phase transformation process, calculated strontium partition coefficients were also retained when phosphate was applied. Thus phosphate ions have a similar effect as PAA on ACC crystallisation. However, the large standard deviation indicated a large variation across the experiments. This suggests that phosphate is not as reliable in triggering the pseudomorphic transformation compared to PAA (Table 2.8). Phosphate is often present in biominerals[52,53], so their ability to induce such a pseudomorphic transformation may have an impact on the trace element concentrations of ACC during crystallisation.

Applying orthosilicate resulted in a decrease of the calculated partition coefficients to 0.67 ± 0.02 (Figure 2.14D). Furthermore, the presence of calcite morphologies (Figure 2.14B) indicated the occurrence of a dissolution-reprecipitation crystallisation.

2.3.2.2 Organic additives

The ability of the polyelectrolytes PAsp, PSS and PAH to trigger a pseudomorphic transformation was evaluated in a similar way to what was done in Chapter 2.3.2.1. After 24 hours of stirring, all samples had crystallised, albeit not completely as shown by the low peak intensity of the PAsp sample, which implied that a significant amount of the sample was still amorphous (Figure 2.15A). Application of PAsp and PSS resulted in the formation of calcite as the only phase. In comparison, a mixture of calcite and vaterite formed when PAH was added (Figure 2.15A).

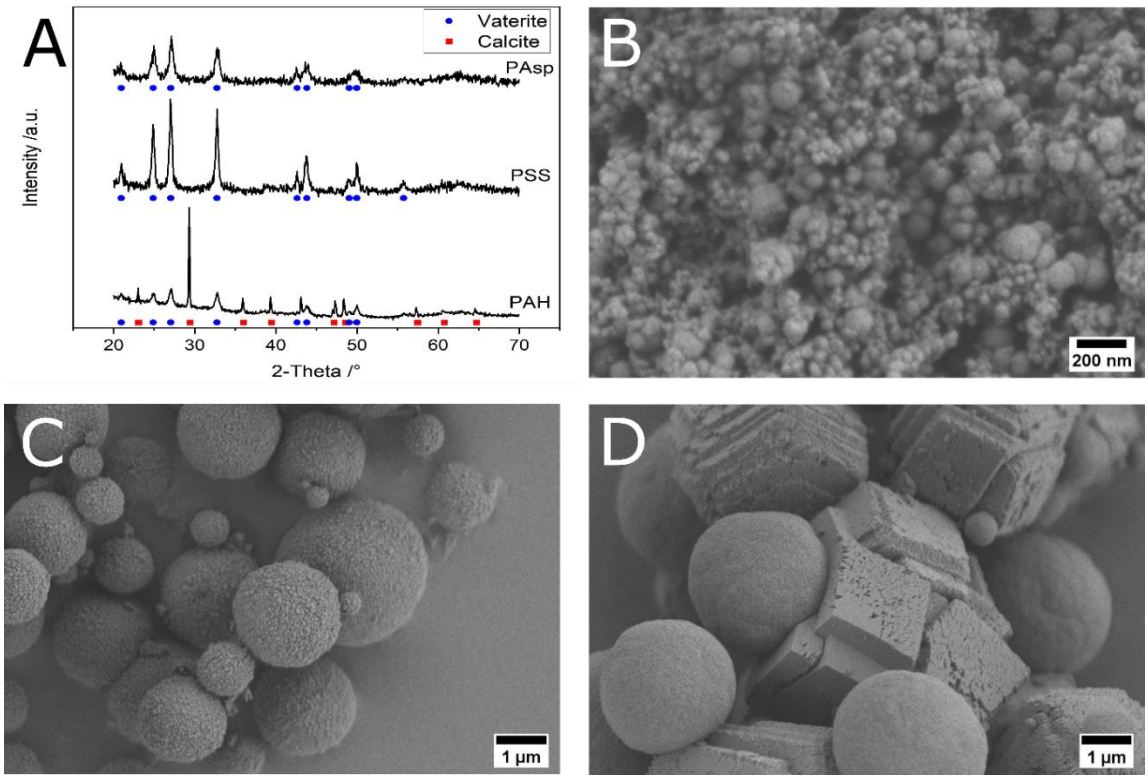

Figure 2.15. Investigating the ability of PAsp, PSS and PAH to induce the pseudomorphic transformation. **(A)** Phase analysis of the synthesised calcium carbonate powders. SEM images of samples synthesised in the presence **(B)** PAsp, **(C)** PSS and **(D)** PAH.

While PAsp retained the morphology during crystallisation (Figure 2.15B), the morphologies of the PSS and PAH samples changed (Figure 2.15C,D). In accordance with XRD measurements, vaterite morphologies were detected for the PSS samples and a mixture of calcite and vaterite morphologies for the PAH samples.

The calculated partition coefficients exhibited a similar behaviour, namely preservation of the calculated partition coefficients of the “ACC Samples” when PAsp was added and a significant decrease when PSS or PAH was added (Figure 2.16 and Table 2.9). Interestingly, using PAsp instead of PAA resulted in better preservation of the calculated partition coefficients. This leads to the assumption that PAsp achieved a better particle coverage compared to PAA, therefore it seems to be more effective in the suppression of redissolution. However, a better crystallisation has to be achieved for the PAsp samples in the future to confirm this assumption, *e.g.*, by increasing the time of stirring considerably.

The addition of PSS and PAH resulted in an even stronger decrease of calculated partition coefficients for strontium (0.41 ± 0.02 and 0.46 ± 0.01) than in the “Control Samples”. However, as these polymers are often used during calcium carbonate precipitation experiments, this effect has to be further analysed, as it is beyond the scope of this work[14,43,48,54–56].

Table 2.9. Calculated partition coefficients for the application of PAsp, PSS, and PAH as further organic additives including standard deviations (n=5).

ACC	PAA	PAsp	PSS	PAH	Control
0.91 ± 0.01	0.87 ± 0.01	0.91 ± 0.02	0.41 ± 0.02	0.46 ± 0.01	0.59 ± 0.02

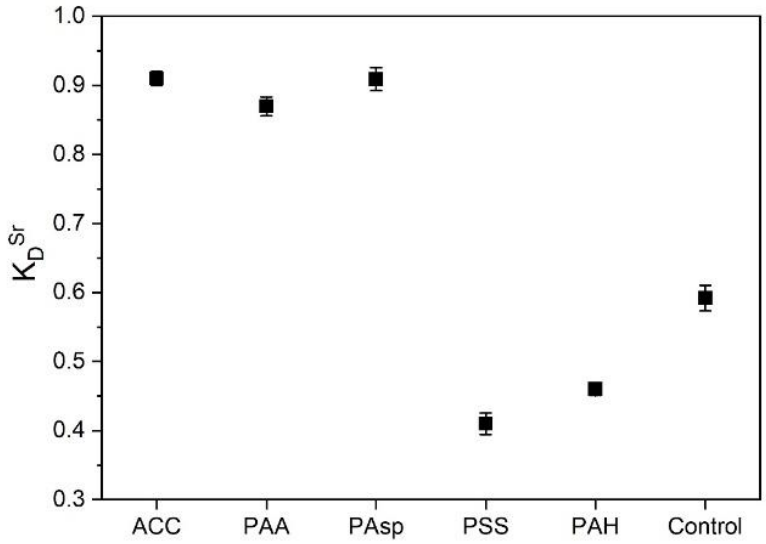

Figure 2.16. Determination of the organic additive influence on the calculated strontium partition coefficients during crystallisation.

2.3.3 The influence of phase transformation pathways on oxygen isotope fractionation

In addition to element partitioning, the influence of pseudomorphic transformation on isotope fractionation was analysed. Oxygen isotopes were used because of their high reactivity and larger fractionation effects compared to heavy metal isotopes. As oxygen isotopic ratios of seawater are different in different eons of Earth history[57], they can be used to determine the age of biological and/or geological paleoclimate archives. Waters differing in $\delta^{18}O$ value were used for the synthesis of amorphous calcium carbonate in order to assess the influence of the crystallisation on the oxygen isotopic system in carbonates.

Phase analysis of the experimental products revealed that the “L-ACC”, “M-ACC”, and “E-ACC” samples were amorphous with no peaks were present. All PAA and H_2O samples crystallised to calcite, independent of the water type and the applied water sequence (Supplementary Figure 2.2-2.4).

Mass spectrometry demonstrated that fractionation between the waters differing in their $\delta^{18}O$ values and ACC as the synthesised ACC samples varied in their $\delta^{18}O$ values (black bars in Figure 2.17 and Table 2.10). This shows that this experimental setup allows the synthesis of calcium carbonate with varying $\delta^{18}O$ values with a high confidence level and reproducibility.

Table 2.10. Overview of the determined $\delta^{18}O$ values for the calcium carbonate powders including standard deviations (n=2).

Sample name	$\delta^{18}O$ (‰)
L-ACC	20.27 ± 0.02
LE-PAA	16.04 ± 0.01
LE-H_2O	13.61 ± 0.01
M-ACC	15.11 ± 0.01
MM-PAA	15.91 ± 0.05
MM-H_2O	13.36 ± 0.01
E-ACC	11.1 ± 0.04
EL-PAA	15.78 ± 0.09
EL-H_2O	13.15 ± 0.01

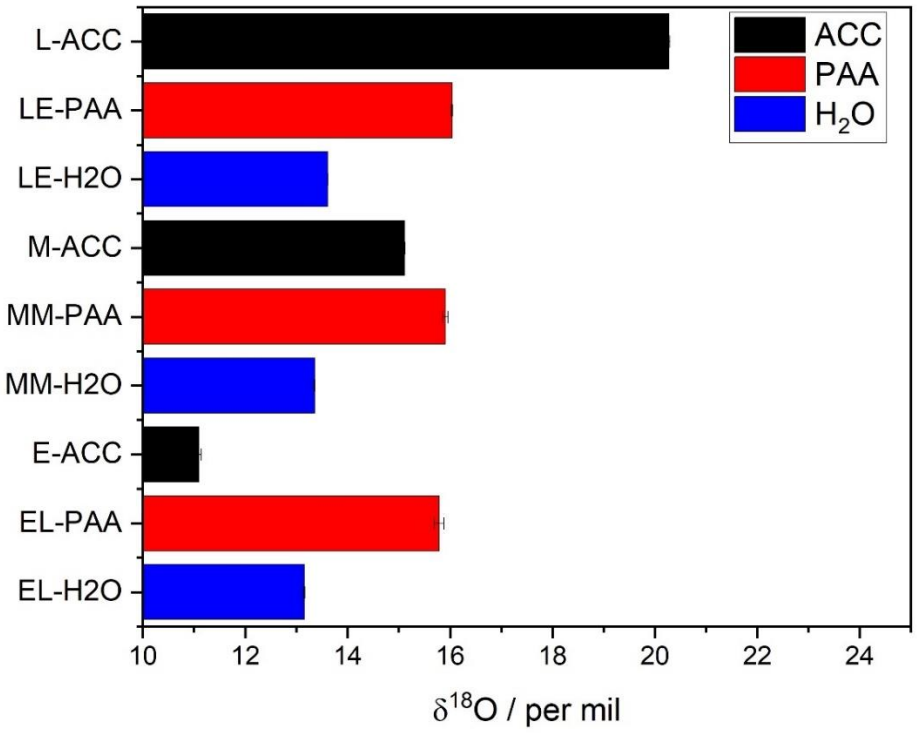

Figure 2.17. Analysing the effect of the pseudomorphic transformation and the dissolution-reprecipitation crystallisation on the $\delta^{18}O$ values in carbonate.

Table 2.11. $\delta^{18}O$ values of the filtrates show no influence on the results (n=1). VSMOW reference material was used.

Filtrates	$\delta^{18}O$ (‰)	Position 1	Position 2
LE-PAA	-15.38	L-water	E-water
LE-H_2O	-15.34	L-water	E-water
MM-PAA	-15.89	M-water	M-water
MM-H_2O	-15.95	M-water	M-water
EL-PAA	-15.8	E-water	L-water
EL-H_2O	-15.88	E-water	L-water

On this basis, the influence of the pseudomorphic transformation and the dissolution-reprecipitation pathway on the $\delta^{18}O$ values could be analysed (Figure 2.17).

Water type and application sequence of the waters had only a minor effect on the $\delta^{18}O$ values. For the PAA samples, an averaged $\delta^{18}O$ value of 15.91 ± 0.13 ‰ was measured (red bars in

Figure 2.17), while the averaged $\delta^{18}O$ value for the H_2O samples was 13.37 ± 0.23 ‰ (blue bars in Figure 2.17). Hence, the observed $\delta^{18}O$ value shift was caused by the “additive” addition, *i.e.*, the addition of PAA or water.

To exclude that a mixing effect caused the shift between PAA and H_2O samples, the $\delta^{18}O$ values of the filtrates were measured after the calcium carbonate precipitate was collected (Table 2.11). Irrespective whether PAA or H_2O was applied, the $\delta^{18}O$ values of the filtrate resulting from the same mixing sequence were compared. The largest $\delta^{18}O$ value difference of only 0.08 ‰ was detected for the “EL” setup, a value which is within the typical measuring inaccuracies. Therefore, mixing issues were not responsible for the $\delta^{18}O$ value shift between PAA and H_2O samples.

Because PAA contains exchangeable oxygens, the addition of PAA might also affect the $\delta^{18}O$ values. The exact influence of the polymer addition was estimated with the following consideration: During the 24 hours of stirring, the volume of the mixture was 24 mL, in which 0.0048 g of PAA was dissolved, which corresponded to 0.0021 g of oxygen ions. If the 24 mL of the mixture were considered as pure water, around 21 g were present as oxygen ions as a part of water molecules. Hence, following this rough calculation around 0.1 ‰ of the total oxygen presence was related to the PAA. Consequently, the influence of the PAA addition on the $\delta^{18}O$ value is negligible.

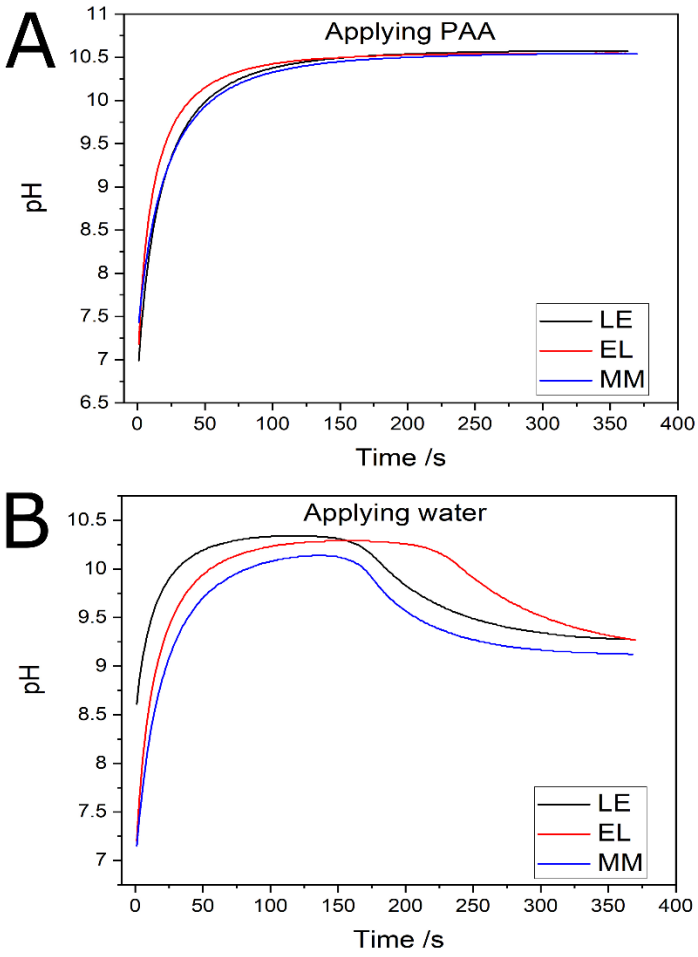

Figure 2.18. Curves of the pH versus crystallisation time for **(A)** PAA samples and **(B)** H_2O samples.

As the pH can also affect the $\delta^{18}O$ value, it was monitored at the beginning of the crystallisation. All PAA samples exhibited an increase in the pH, which flattened after 30 seconds and remained constant after circa 150 seconds (Figure 2.18). For the H_2O samples, a similar pH behaviour was measured with a pH decrease after 150 seconds. This pH decrease is typical for dissolution-reprecipitation crystallisation[58]. Precipitation of calcite decreased the carbonate amount in solution, therefore leading to bicarbonate to carbonate transformation due to the carbonate equilibrium, which explains the decrease of the pH in the H_2O samples. After 360 seconds, a pH difference of around one was observed between the PAA and H_2O samples. To determine if this pH difference is able of inducing the observed $\delta^{18}O$ value shift, the oxygen isotope fractionation factors (ε in ‰) were calculated for pH 10.5 (PAA samples) and pH 9.5 (H_2O samples) by using Equation 2.3[59]. Firstly, it was necessary to determine the pH-dependent isotope fractionation factor ($\alpha_{DIC\text{-}H2O}$). Using the spreadsheet by Zeebe[60], it was possible to determine the oxygen isotope fractionation factor between the "dissolved inorganic carbon" (DIC) – *i.e.* Dissolved Inorganic Carbonate – and H_2O.

$$\varepsilon_{18_{O\,DIC-H_2O}} = \left(\alpha_{18_{O\,DIC-H_2O}} - 1\right) * 1000‰ \approx \delta_{18_{O\,DIC}} - \delta_{18_{O\,H_2O}} \qquad (2.3)$$

The oxygen isotope fractionation factors obtained in this way were then used to calculate the oxygen isotope fractionation factors at pH 9.5 (29.56 ‰) and pH 10.5 (26.22 ‰). Equation 2.3 demonstrates that the oxygen isotope fractionation factor can also be determined by measuring the $\delta^{18}O$ value difference between the PAA and H_2O samples (Table 2.10). The averaged difference between both sample types was 2.54 ± 0.26 ‰ and thus, smaller than the difference determined by calculation (3.34 ‰). The reason for this difference remains enigmatic.

The absence of a pH change in the case of PAA samples and the resulting difference in pH profiles between the PAA and H_2O samples is sufficient to explain the observed shift in $\delta^{18}O$. It indicates that the pseudomorphic transformation is not a veritable solid-solid state transformation, which would preserve the $\delta^{18}O$ values of the initial ACC phase. It rather seems that an extensive exchange of oxygen occurred, which implies exchange with the solution. Thus, pseudomorphic phase transformation is a quasi-solid-state transformation in solution which is “catalysed” by water. A reasonable explanation of the results presented in this chapter would be that certain additives are capable of shielding the calcium carbonate from the surrounding solution by acting as a protective capping agent which act as a diffusional barrier for larger ions but allow for the passage of smaller entities and to a certain extent also water exchange with the surrounding parental liquid. Currently, ToF-SIMS is being conducted to confirm this assumption of a protective adsorbed layer of additives.

2.4 Conclusion

While solid-state and dissolution-reprecipitation crystallisation of ACC has been thoroughly investigated, the biologically relevant, shape-preserving, pseudomorphic phase transformation has to date remained largely unexplored.

In this chapter, it was shown that the pseudomorphic transformation, as introduced by Gower and Tirrell[18], retained not only the morphology, but also the partition coefficients of Sr-doped ACC upon crystallisation. Furthermore, it was shown that pseudomorphic transformation is induced by a variety of inorganic and organic additives, such as phosphate, PAA and PAsp. As aspartic acid is widely present in unusually acidic proteins found in biominerals[61,62], the relevance of these findings in biomineralisation-related research is emphasised.

Expanding the study to the oxygen isotope fractionation revealed that pseudomorphic transformation is a quasi-solid-state transformation which occurs in solution. In this transformation pathway, the additives inhibit large scale redissolution but allow for the involvement of water during the recrystallisation process in a confined space. This explains not only the shape preservation in pseudomorphic transformation, but also has far-reaching implications for bioinspired material synthesis and paleoclimatology.

In conclusion, this chapter revealed that simple additives occurring in natural systems could alter the chemical composition of the crystalline phase by partially or fully preserving the composition of the precursor. Therefore, a different element partitioning, and isotope fractionation has to be expected when different pathways are travelled. A third “transitional” pseudomorphic transformation has to be added to the well-studied dissolution-reprecipitation and solid-state transformation. Due to its relevance in biomineralisation, its impact on chemical and isotopic composition has to be scrutinised in the future.

As the pseudomorphic transformation retains the observed partition coefficients of ACC intermediates, it is necessary to achieve a thorough knowledge of partitioning into ACC and whether synthesis conditions influence the dopant incorporation. To address these issues, the influence of the ACC synthesis on the material properties and chemical composition was analysed in Chapter 3. Furthermore, the influence of mixing conditions on the element partitioning was investigated in Chapter 4. Lastly, the influence of synthesis conditions such as flow rate, temperature, and pH on multi-doped ACC, which was synthesised in artificial seawater, were examined in Chapter 5.

2.5 References

1. Henderson, G. M. New oceanic proxies for paleoclimate. *Earth Planet. Sci. Lett.* **203**, 1–13 (2002).

2. Gabitov, R. I. & Watson, E. B. Partitioning of strontium between calcite and fluid. *Geochemistry, Geophys. Geosystems* **7**, (2006).

3. Lorens, R. B. Sr, Cd, Mn and Co distribution coefficients in calcite as a function of calcite precipitation rate. *Geochim. Cosmochim. Acta* **45**, 553–561 (1981).

4. Katz, A. The interaction of magnesium with calcite during crystal growth at 25-90°C and one atmosphere. *Geochim. Cosmochim. Acta* **37**, 1563–1586 (1973).

5. Tesoriero, A. J. & Pankow, J. F. Solid solution partitioning of Sr^{2+}, Ba^{2+}, and Cd^{2+} to calcite. *Geochim. Cosmochim. Acta* **60**, 1053–1063 (1996).

6. Gaetani, G. A. & Cohen, A. L. Element partitioning during precipitation of aragonite from seawater: A framework for understanding paleoproxies. *Geochim. Cosmochim. Acta* **70**, 4617–4634 (2006).

7. Wassenburg, J. A. *et al.* Determination of aragonite trace element distribution coefficients from speleothem calcite–aragonite transitions. *Geochim. Cosmochim. Acta* **190**, 347–367 (2016).

8. Beniash, E., Addadi, L. & Weiner, S. Cellular Control Over Spicule Formation in Sea Urchin Embryos: A Structural Approach. *J. Struct. Biol.* **125**, 50–62 (1999).

9. Politi, Y. *et al.* Transformation mechanism of amorphous calcium carbonate into calcite in the sea urchin larval spicule. *Proc. Natl. Acad. Sci. U. S. A.* **105**, 17362–17366 (2008).

10. Gal, A. *et al.* Calcite crystal growth by a solid-state transformation of stabilized amorphous calcium carbonate nanospheres in a hydrogel. *Angew. Chemie Int. Ed.* **52**, 4867–4870 (2013).

11. Giuffre, A. J., Gagnon, A. C., De Yoreo, J. J. & Dove, P. M. Isotopic tracer evidence for the amorphous calcium carbonate to calcite transformation by dissolution-reprecipitation. *Geochim. Cosmochim. Acta* **165**, 407–417 (2015).

12. Wolf, S. E., Leiterer, J., Kappl, M., Emmerling, F. & Tremel, W. Early Homogenous Amorphous Precursor Stages of Calcium Carbonate and Subsequent Crystal Growth in Levitated Droplets. *J. Am. Chem. Soc.* **130**, 12342–12347 (2008).

13. Bots, P., Benning, L. G., Rodriguez-Blanco, J. D., Roncal-Herrero, T. & Shaw, S. Mechanistic insights into the crystallization of amorphous calcium carbonate (ACC). *Cryst. Growth Des.* **12**, 3806–3814 (2012).

14. Ihli, J., Kim, Y.-Y., Noel, E. H. & Meldrum, F. C. The effect of additives on amorphous calcium carbonate (ACC): Janus behavior in solution and the solid state. *Adv. Funct. Mater.* **23**, 1575–1585 (2013).

15. Mavromatis, V. *et al.* Impact of amorphous precursor phases on magnesium isotope signatures of Mg-calcite. *Earth Planet. Sci. Lett.* **464**, 227–236 (2017).

16. Ihli, J. *et al.* Dehydration and crystallization of amorphous calcium carbonate in solution and in air. *CrystEngComm* **5**, 3169 (2014).

17. Nielsen, M. H., Aloni, S. & De Yoreo, J. J. In situ TEM imaging of $CaCO_3$ nucleation reveals coexistence of direct and indirect pathways. *Science.* **345**, 1158–1162 (2014).

18. Gower, L. A. & Tirrell, D. A. Calcium carbonate films and helices grown in solutions of poly(aspartate). *J. Cryst. Growth* **191**, 153–160 (1998).

19. Gower, L. B. Biomimetic Model Systems for Investigating the Amorphous Precursor Pathway and Its Role in Biomineralization. *Chem. Rev.* **108**, 4551–4627 (2008).

20. Harris, J., Mey, I., Hajir, M., Mondeshki, M. & Wolf, S. E. Pseudomorphic transformation of amorphous calcium carbonate films follows spherulitic growth mechanisms and can give rise to crystal lattice tilting. *CrystEngComm* **17**, 6831–6837 (2015).

21. Liu, Z. *et al.* Shape-preserving amorphous-to-crystalline transformation of $CaCO_3$ revealed by in situ TEM. *Proc. Natl. Acad. Sci. U. S. A.* **117**, 3397–3404 (2020).

22. Rodriguez-Navarro, C., Kudłacz, K., Cizer, Ö. & Ruiz-Agudo, E. Formation of amorphous calcium carbonate and its transformation into mesostructured calcite. *CrystEngComm* **17**, 58–72 (2015).

23. Konrad, F., Gallien, F., Gerard, D. E. & Dietzel, M. Transformation of Amorphous Calcium Carbonate in Air. *Cryst. Growth Des.* **16**, 6310–6317 (2016).

24. Radha, A. V., Forbes, T. Z., Killian, C. E., Gilbert, P. U. P. A. & Navrotsky, A. Transformation and crystallization energetics of synthetic and biogenic amorphous calcium carbonate. *Proc. Natl. Acad. Sci. U. S. A.* **107**, 16438–16443 (2010).

25. Myszka, B. *et al.* Phase-specific bioactivity and altered Ostwald ripening pathways of calcium carbonate polymorphs in simulated body fluid. *RSC Adv.* **9**, 18232–18244 (2019).

26. Schinzel, F. Powder Synthesis of Amorphous Calcium Carbonate with Inorganic and Organic Dopants. (2018).

27. Coplen, T. B. Guidelines and recommended terms for expression of stable-isotope-ratio and gas-ratio measurement results. *Rapid Commun. Mass Spectrom.* **25**,

2538–2560 (2011).

28. Brand, W. A., Coplen, T. B., Vogl, J., Rosner, M. & Prohaska, T. Assessment of international reference materials for isotope-ratio analysis (IUPAC technical report). *Pure Appl. Chem.* **86**, 425–467 (2014).

29. Chen, B., Joachimski, M. M., Sun, Y., Shen, S. & Lai, X. Carbon and conodont apatite oxygen isotope records of Guadalupian-Lopingian boundary sections: Climatic or sea-level signal? *Palaeogeogr. Palaeoclimatol. Palaeoecol.* **311**, 145–153 (2011).

30. Korte, C. *et al.* Carbon, sulfur, oxygen and strontium isotope records, organic geochemistry and biostratigraphy across the Permian/Triassic boundary in Abadeh, Iran. *Int. J. Earth Sci.* **93**, 565–581 (2004).

31. van Geldern, R. *et al.* Stable isotope geochemistry of pore waters and marine sediments from the New Jersey shelf: Methane formation and fluid origin. *Geosphere* **9**, 96–112 (2013).

32. Kim, S. T., Coplen, T. B. & Horita, J. Normalization of stable isotope data for carbonate minerals: Implementation of IUPAC guidelines. *Geochim. Cosmochim. Acta* **158**, 276–289 (2015).

33. Pai, R. K. & Pillai, S. Nanoparticles of amorphous calcium carbonate by miniemulsion: Synthesis and mechanism. *CrystEngComm* **10**, 865–872 (2008).

34. Trinh, H. T. T. & Wolf, S. E. In preparation.

35. Böhm, C. F. *et al.* Structural commonalities and deviations in the hierarchical organization of crossed-lamellar shells: A case study on the shell of the bivalve *Glycymeris glycymeris*. *J. Mater. Res.* **31**, 536–546 (2016).

36. Wolf, S. E. *et al.* Nonclassical crystallization in vivo et in vitro (I): Process-structure-property relationships of nanogranular biominerals. *J. Struct. Biol.* **196**, 244–259 (2016).

37. Wolf, S. E. *et al.* Single Nanogranules Preserve Intracrystalline Amorphicity in Biominerals. *Key Eng. Mater.* **672**, 47–59 (2016).

38. Jacob, D. E., Wirth, R., Soldati, A. L., Wehrmeister, U. & Schreiber, A. Amorphous calcium carbonate in the shells of adult *Unionoida*. *J. Struct. Biol.* **173**, 241–249 (2011).

39. Gebauer, D., Cölfen, H., Verch, A. & Antonietti, M. The multiple roles of additives in $CaCO_3$ crystallization: A quantitative case study. *Adv. Mater.* **21**, 435–439 (2009).

40. Martignier, A. *et al.* Marine and freshwater micropearls: Biomineralization producing strontium-rich amorphous calcium carbonate inclusions is widespread in the genus *Tetraselmis* (Chlorophyta). *Biogeosciences* **15**, 6591–6605 (2018).

41. Loste, E., Wilson, R. M., Seshadri, R. & Meldrum, F. C. The role of magnesium in stabilising amorphous calcium carbonate and controlling calcite morphologies. *J. Cryst. Growth* **254**, 206–218 (2003).

42. Jiang, J. *et al.* Confined crystallization of polycrystalline high-magnesium calcite from compact Mg-ACC precursor tablets and its biological implications. *CrystEngComm* **13**, 952–956 (2011).

43. Xu, X. *et al.* The roles of water and polyelectrolytes in the phase transformation of amorphous calcium carbonate. *J. Cryst. Growth* **310**, 3779–3787 (2008).

44. Davis, K. J., Dove, P. M. & De Yoreo, J. J. The Role of Mg^{2+} as an Impurity in Calcite Growth. *Science.* **290**, 1134–1137 (2010).

45. Saito, A. *et al.* Incorporation of Incompatible Strontium and Barium Ions into Calcite ($CaCO_3$) through Amorphous Calcium Carbonate. *Minerals* **10**, 270 (2020).

46. Astilleros, J. M., Pina, C. M., Fernández-Díaz, L. & Putnis, A. The effect of barium on calcite {10$\bar{1}$4} surfaces during growth. *Geochim. Cosmochim. Acta* **64**, 2965–2972 (2000).

47. Gower, L. B. & Odom, D. J. Deposition of calcium carbonate films by a polymer-induced liquid-precursor (PILP) process. *J. Cryst. Growth* **210**, 719–734 (2000).

48. Cantaert, B. *et al.* Think positive: Phase separation enables a positively charged additive to induce dramatic changes in calcium carbonate morphology. *Adv. Funct. Mater.* **22**, 907–915 (2012).

49. Gal, A., Weiner, S. & Addadi, L. The stabilizing effect of silicate on biogenic and synthetic amorphous calcium carbonate. *J. Am. Chem. Soc.* **132**, 13208–13211 (2010).

50. Cantaert, B. *et al.* Use of Amorphous Calcium Carbonate for the Design of New Materials. *ChemPlusChem* **82**, 107–120 (2017).

51. Kababya, S. *et al.* Phosphate-water interplay tunes amorphous calcium carbonate metastability: Spontaneous phase separation and crystallization vs stabilization viewed by solid state NMR. *J. Am. Chem. Soc.* **137**, 990–998 (2015).

52. Bentov, S., Weil, S., Glazer, L., Sagi, A. & Berman, A. Stabilization of amorphous calcium carbonate by phosphate rich organic matrix proteins and by single phosphoamino acids. *J. Struct. Biol.* **171**, 207–215 (2010).

53. Habraken, W. J. E. M. *et al.* Layered growth of crayfish gastrolith: About the stability of amorphous calcium carbonate and role of additives. *J. Struct. Biol.* **189**, 28–36 (2015).

54. Smeets, P. J. M., Cho, K. R., Kempen, R. G. E., Sommerdijk, N. A. J. M. & De Yoreo,

J. J. Calcium carbonate nucleation driven by ion binding in a biomimetic matrix revealed by in situ electron microscopy. *Nat. Mater.* **14**, 394–399 (2015).

55. Demmert, B. *et al.* Polymer-Functionalised Nanograins of Mg-Doped Amorphous Calcium Carbonate via a Flow-Chemistry Approach. *Materials.* **12**, 1818 (2019).

56. Schenk, A. S. *et al.* Polymer-induced liquid precursor (PILP) phases of calcium carbonate formed in the presence of synthetic acidic polypeptides - Relevance to biomineralization. *Faraday Discuss.* **159**, 327–344 (2012).

57. Kasting, J. F. *et al.* Paleoclimates, ocean depth, and the oxygen isotopic composition of seawater. *Earth Planet. Sci. Lett.* **252**, 82–93 (2006).

58. Wolf, S. E. *et al.* Phase selection of calcium carbonate through the chirality of adsorbed amino acids. *Angew. Chemie Int. Ed.* **46**, 5618–5623 (2007).

59. Devriendt, L. S., Watkins, J. M. & McGregor, H. V. Oxygen isotope fractionation in the $CaCO_3$-DIC-H_2O system. *Geochim. Cosmochim. Acta* **214**, 115–142 (2017).

60. Zeebe, R. E. An expression for the overall oxygen isotope fractionation between the sum of dissolved inorganic carbon and water. *Geochemistry, Geophys. Geosystems* **8**, (2007).

61. Addadi, L., Joester, D., Nudelman, F. & Weiner, S. Mollusk shell formation: A source of new concepts for understanding biomineralization processes. *Chem. - A Eur. J.* **12**, 980–987 (2006).

62. Tambutté, S. *et al.* Coral biomineralization: From the gene to the environment. *J. Exp. Mar. Bio. Ecol.* **408**, 58–78 (2011).

2.6 Supplementary

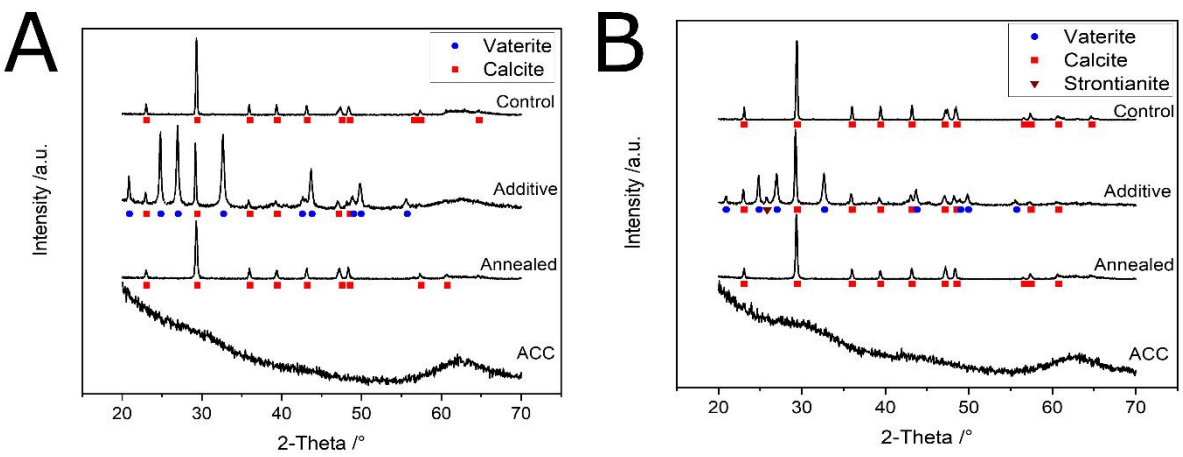

Supplementary Figure 2.1. XRD patterns of the calcium carbonate powders doped with **(A)** 6 mM and **(B)** 8 mM of strontium chloride.

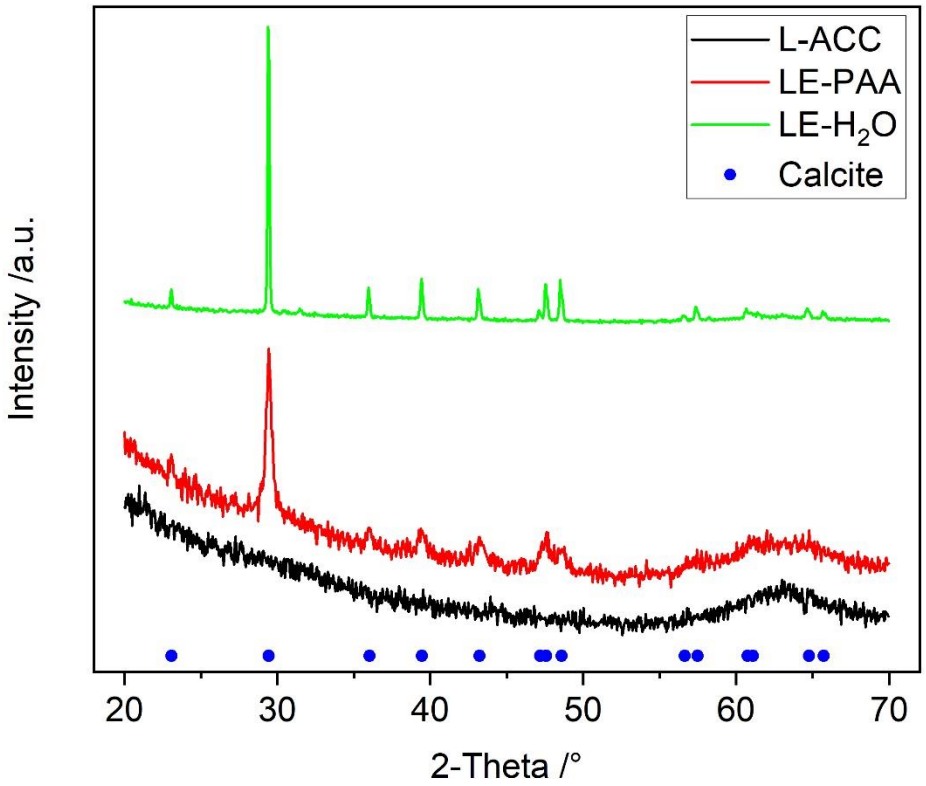

Supplementary Figure 2.2. XRD patterns of the calcium carbonate samples in which “Lab Water” was applied at position 1.

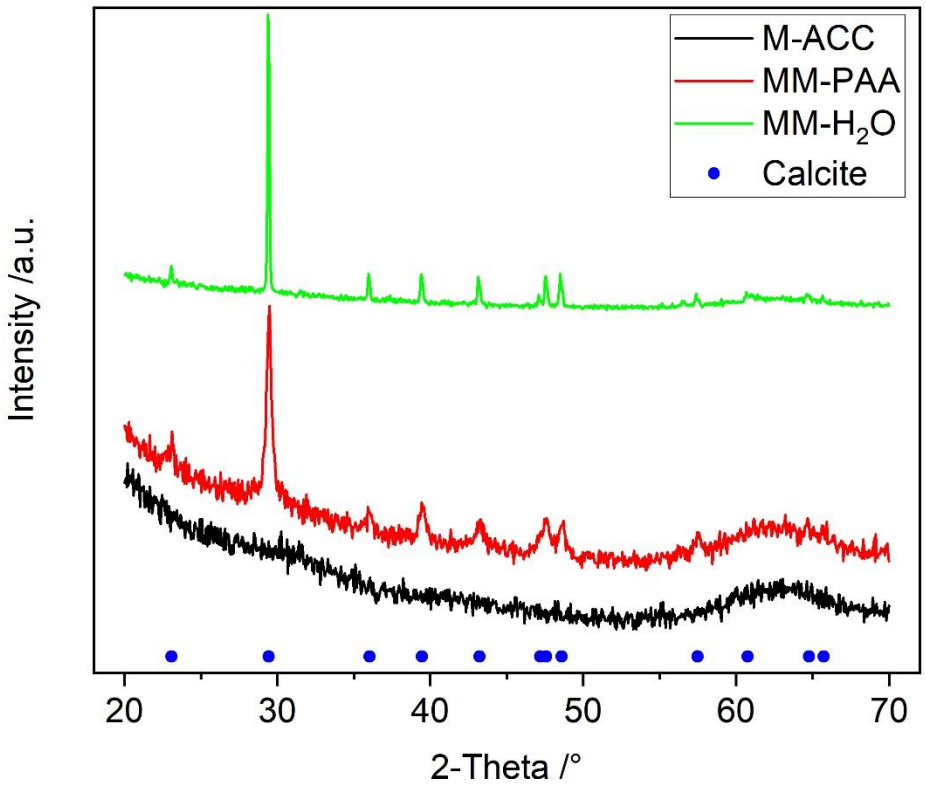

Supplementary Figure 2.3. XRD patterns of the calcium carbonate samples in which “M-water” was applied at position 1.

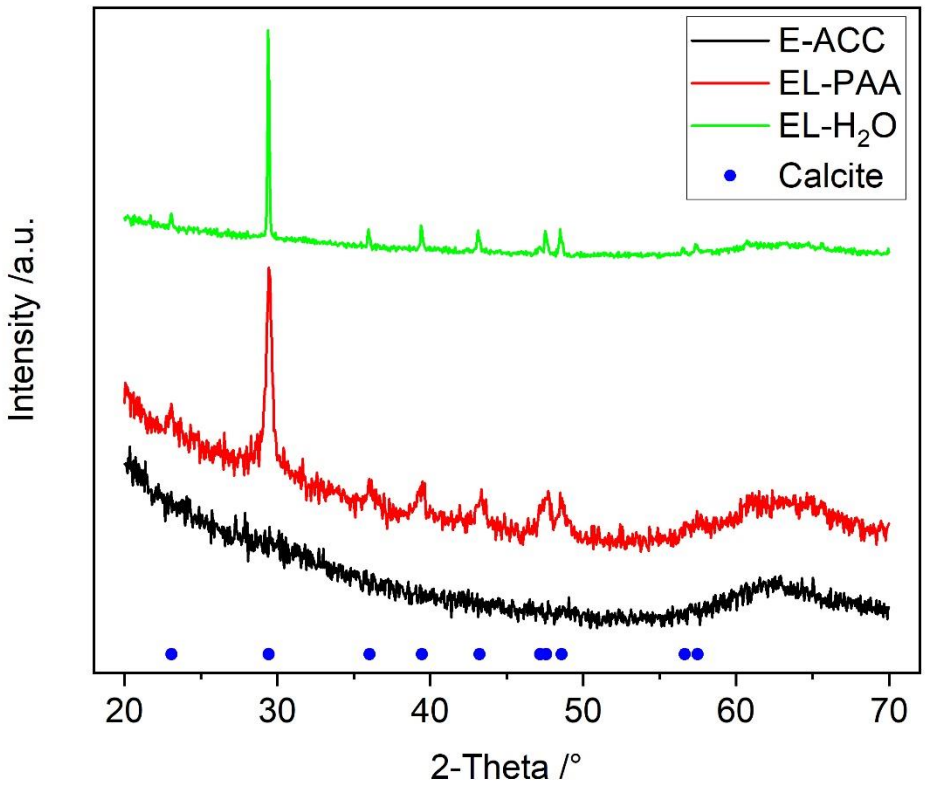

Supplementary Figure 2.4. XRD patterns of the calcium carbonate samples which were utilized by applying “Estonian Groundwater” at position 1.

3. SYNTHESIS-DEPENDENT PROPERTIES AND COMPOSITION OF UNDOPED AND DOPED ACC

Demmert, B.[1,2]; Schüßler, M.[1]; Schodder, P. I.[1]; Jacob, D. E.[2] and Wolf, S. E.[1,3]

[1]Department of Materials Science and Engineering, Institute of Glass and Ceramics (WW3), Friedrich-Alexander University Erlangen-Nürnberg, 90158 Erlangen, Germany.

[2]Department of Earth and Environmental Sciences, Macquarie University, NSW 2109, Australia.

[3]Interdisciplinary Center for Functional Particle Systems (FPS), Friedrich-Alexander University Erlangen-Nürnberg, 91058 Erlangen, Germany.

The author's contribution to the publication is as follows: BD designed the study, performed the experiments, conducted ATR-FTIR, SEM, TGA/DSC, and ICP-OES measurements. BD supported XRD measurements. BD evaluated the data and drafted the manuscript.

Abstract

Despite the recognised importance of ACC in biomineral crystallisation, there is little knowledge about whether and how synthesis conditions impact ACC mineral properties or its chemical composition. Since ACC is known to be a common precursor in the crystallisation of many biological and geological carbonates, knowledge about how synthesis conditions affect ACC may have implications for how trace elements are incorporated in the final carbonates endproducts.

This chapter employs three different synthesis approaches — a batch mixing synthesis and two different flow-through methods — to generate ACC under different conditions, but from the same starting solutions. The experiments were designed so that these three syntheses differed only in their mixing conditions/flow conditions, *i.e.*, turbulent vs. laminar, and their mixing rates. The analyses of the resulting ACC powders showed that these differed significantly in their material properties such as particle size, density, and level of hydration depending on the synthesis method. Higher particle sizes, lower densities and, at least for Ba-doped ACC, higher hydration levels, compared to all other samples were determined for ACC samples synthesised via the batch mixing. These results suggest that different synthesis methods yield different ACC variants, and suggests that the formation of ACC is a kinetically controlled process affected by pH, which regulates the solution speciation and mixing conditions. This finding sheds light on the fundamental processes of ACC formation and raises questions about the common preconception of defined ACC polyamorphs in favour of ACC as a much more complex composite phase.

3.1 Introduction

Amorphous calcium carbonate (ACC), a metastable precursor to crystalline calcium carbonate, is of significant scientific interest as it plays a vital role in biomineralisation as a precursor phase of crystalline calcium carbonate[1–7]. The presence of trace elements in fossilised biominerals are often used to reconstruct past environmental conditions[8–15] which, in turn, provide us with a solid data basis validating our climate models[8,11,16]. However, the role of ACC as a precursor to these biominerals, could affect the incorporation rates of chemical elements and isotopes, in the final biominerals. The impact of an ACC precursor on the accuracy of quantitative paleo-environmental reconstructions is still being investigated and may also unravel the enigmatic deviation of distribution coefficients and isotope fractionation factors from the predicted thermodynamic equilibrium behaviour in biogenic minerals[17,18].

ACC has attracted recent interest for its use in waste extraction since it offers a cheap way for remediation of $^{90}Sr^{2+}$ ions contaminated waters by incorporating the strontium ions into calcium carbonate[19–21]. A better understanding of the dependence of incorporation rates from process

parameters, *e.g.*, synthesis conditions, would enhance the exploitation of ACC as a “functional” material[19,22].

Recently, the presence of ACC with distinct short-range order was reported and was convincingly linked to the pH value during synthesis[23,24]. Thus, ACC is seen to be polyamorph, *i.e.*, it is assumed to occur in several distinct amorphous structures[4]. So far, only the impact of pH on the polyamorphism of ACC has been demonstrated, although there exists a variety of ACC synthesis protocols currently used interchangeably, *i.e.*, it is assumed that the material properties and chemical compositions of the synthesised ACC samples are comparable[25–36]. The question that still remains unsolved is: What are the hidden factors that influence both material and chemical properties of ACC during synthesis[37,38]?

To address this yet poorly investigated aspect, three different synthesis procedures were applied to precipitate undoped and doped ACC, which differed in their mixing conditions/flow conditions (Supplementary Table 3.1). In one approach, a batch mixing (“BM”) synthesis was used, which is common in the current literature[39,40], and involves mixing two solutions in a beaker through vigorous stirring (Figure 3.1A). In a second approach, ACC was synthesised via flow chemistry[26,41–43].Two different flow reactors were used, namely a Ball-Berger mixer (“BBM”) and a microfluidic chip with three converging channels (“MFC”). For the latter, syntheses at low pH (pH 7.5) and high pH (pH 11) were performed.

The Ball-Berger mixer, a four-jet ball mixer, provides an efficient and turbulent mixing across a spherical surface with flow velocities up to 25 m/s. This design ensures homogenous mixing on very fast time scales. To achieve controlled mixing, the solutions are injected through four inlets which are separated by a 45° angle (Figure 3.1B)[44].

For the microfluidic approach, a commercially available setup was used, *i.e.*, a µ-Slide III^{3in1} microfluidic chip (Figure 3.1C). This flow setup up provides slow initial laminar flow mixing, followed by turbulent mixing due to an orifice that combines all three of the channels[26].

3.2 Materials and methods

Ultrapure water was used for all experiments (Milli-Q Direct 8 with UV photooxidation, Merck Millipore, Burlington, MA, USA, 18.2 MΩ cm^{-1}). Synthesising ACC was achieved by mixing a 40 mM calcium chloride solution with a 40 mM sodium carbonate solution; for the low pH experiments a 40 mM sodium bicarbonate solution was used (below).

For the doped ACC samples, the calcium chloride powder was mixed with the respective additive powders, namely strontium chloride and barium chloride to achieve the following dopant concentration in the 40 mM calcium chloride solutions: Strontium chloride (2 mM) and barium chloride (2 mM). Subsequently, 25 mL of the 40 mM calcium chloride/additive solutions were mixed with 25 mL of a 40 mM sodium carbonate solution to precipitate ACC. The

syntheses were conducted at ambient temperatures. The chemical reagents were supplied by Sigma-Aldrich (St. Louis, MO, USA) and used without further purification (purity >99%).

For the batch mixing method (“BM”), 25 mL of a sodium carbonate solution was manually dosed into 25 mL of calcium chloride solution in a 200 mL beaker. The mixing of both solutions occurred under vigorous stirring (Figure 3.1A).

During the synthesis via the Ball-Berger mixer (“BBM", Figure 3.1B)[44] and a µ-Slide III^{3in1} microfluidic chip (“MFC”, ibidi GmbH, Gräfelfing, Germany, Figure 3.1C), flow rates were controlled by a peristaltic pump (MA1 70-7000R, Harvard Apparatus, Holliston, MA, USA) connected with standard tubes. Tube sizes of 1.52 mm and 2.79 mm were used for “BBM” and “MFC”, respectively. “BBM” synthesis took place at a flow rate of 25 mL/min by mixing 25 mL of calcium chloride solution with 25 mL of sodium carbonate solution.

For “MFC” experiments, mixing was achieved with a y-piece placed in front of the microfluidic chip (Figure 3.1C). In the microfluidic chip 50 mL of ethanol was added to stabilise ACC. As adding EtOH not only stabilises ACC but also decreases the solubility of calcium carbonate[45], it was possible to synthesise ACC at a neutral pH. MFC synthesis was carried out at two different pH values, namely pH 11 (“MFC-H”) and pH 7.5 (“MFC-L”). While the high pH experiments (“MFC-H”) were conducted at 30 mL/min to prevent ACC crystallisation, the low pH experiments (“MFC-L”) were conducted at 10 mL/min followed by five minutes of stirring in a beaker to enable the ACC formation which takes longer at low pH. For the low pH experiments, a 40 mM sodium bicarbonate solution instead of a sodium carbonate solution was used. Prior to the synthesis, the pH of the sodium bicarbonate solution (initial pH = 8.5) was decreased to pH 7 with a 1 M HCL solution. The calcium chloride solution (pH = 5.7) as well as the strontium or barium doped calcium chloride solutions (pH = 5.8 for both solutions) were used without any pH modification. After mixing calcium chloride and sodium carbonate, pH values of 7.3 and 7.5 were measured after the y-piece and the microfluidic chip, respectively (Supplementary Table 3.2). For the “BM” and “BBM” samples, the pH was measured after mixing calcium chloride and sodium carbonate.

With the exception of the “MFC-L” samples, the mixtures were immediately filtered (nitrocellulose membranes; GVS North America), the residues were washed with ethanol and dried in a desiccator filled with silica-gel.

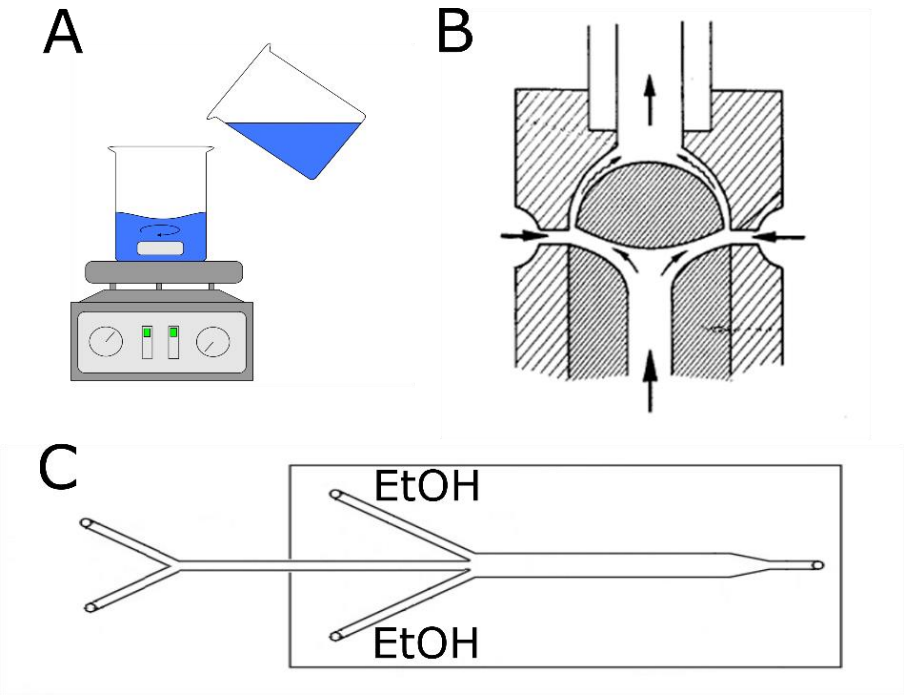

Figure 3.1. Schematic of the mixing processes for the different syntheses. **(A)** For "BM" mixing occurred in a beaker under vigorous stirring. **(B)** The Ball-Berger mixer enabled an efficient and homogenous turbulent mixing[44]. **(C)** For microfluidic chip synthesis, mixing of calcium chloride and sodium carbonate or sodium bicarbonate solutions took place in the y-piece in front of the microfluidic chip. In the microfluidic chip ethanol was always added to stabilise ACC.

Phase analysis was carried out via X-ray diffraction (D8 Advance Eco, Bruker, Karlsruhe, Germany; Cu Kα radiation with λ= 1.5406 Å). The following parameters were used during the measurements: 2θ range between 20° and 70°, step size of 0.05° and a dwell time of 0.3 s. Additionally, attenuated total reflection Fourier transform infrared (ATR-FTIR, Nicolet IS10, Thermo Scientific, Waltham, MA, USA; accumulation of 64 scans) measurements were conducted to identify the precipitated phase.

Particle morphologies were analysed by scanning electron microscopy (SEM, GeminiSEM 500, Carl Zeiss, Oberkochen, Germany). For this purpose, samples were mounted on a SEM stub and sputtered with gold, an accelerating voltage 1.0 kV was applied and the working distance was 6.5 mm. The average particle sizes were estimated using SEM images to graphically measure the diameter of hundred spherical particles each with the freely available software Fiji[46].

Simultaneous thermogravimetric analysis (TGA) and differential scanning calorimetry (DSC) measurements were conducted by a STA449F3 instrument (Netzsch, Selb, Germany) to determine the crystallisation temperature and hydration. The measurements took place in a nitrogen atmosphere, a heating rate of 5 °C/min was applied to bring the system to a max of 800 °C.

Density measurements were conducted with a Helium (He) pycnometer (ACCuPyc II 1340 pycnometer, Micromeritics, Norcross, GA, USA) within a 1 cm^3 cell. To achieve reliable measurements, at least 100 mg of powder was used. Prior to the density measurements, the cell was flushed with Helium 90 times. Subsequently, 10 density measurements were conducted.

Element concentrations in the powders were measured with inductively coupled plasma optical emission spectroscopy (ICP-OES, Genesis FES, Spectro Analytical Instruments, Kleve, Germany) using external reference materials (Merck, Darmstadt, Germany). Each sample was measured in triplicate, each time using 30 mg of powder dissolved in nitric acid (1 M). Partition coefficients were calculated following the definition in Chapter 1.7, namely by dividing the element concentration by the calcium concentration in the solid by the same ratio in the liquid.

3.3 Results and discussion

3.3.1 Phase analysis of the precipitated calcium carbonate powders

The absence of diffraction peaks revealed by XRD measurements showed that amorphous calcium carbonate was precipitated independently of the applied synthesis conditions (Figure 3.2 and Supplementary Figure 3.1). This was confirmed by ATR-FTIR measurements as the expected vibration bands of ACC were present, the v_1 mode (symmetric stretching band) at 1075 cm^{-1}, the v_2 mode (carbonate out-of-plane bending) at 863 cm^{-1}, and the v_3 mode (asymmetric stretch) at 1400 cm^{-1} (Figure 3.3 and Supplementary Figure 3.2)[47–50].

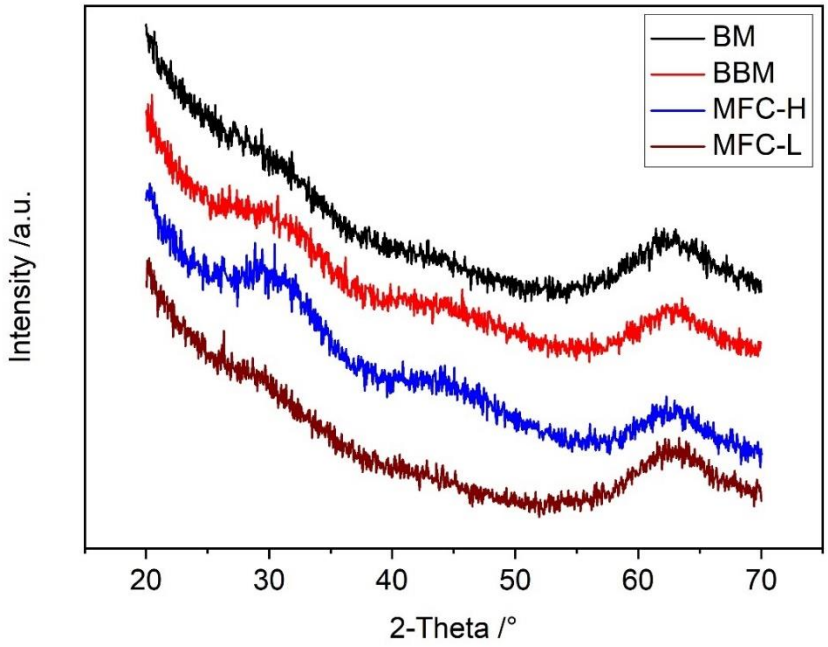

Figure 3.2. Diffraction pattern of undoped calcium carbonate samples precipitated by using different synthetic setups (BM = Batch mixing, BBM = Ball-Berger mixing, MFC-H = Microfluidic chip pH 11, MFC-L = Microfluidic chip pH 7.5).

Remarkably, the ATR-FTIR spectra already suggests that the synthesis procedure affects the hydration level of ACC, as the v_1 mode for the "BBM" samples shows a shoulder at 1050 cm^{-1} (grey arrow in the inset in Figure 3.3), which is indicative of a high level of ACC hydration[48]. A comparison of the v_1 bands for the "BBM" powders (Supplementary Figure 3.3) suggested that the undoped ACC powder had the highest level of hydration. This was corroborated by TGA measurements which revealed hydration of 18.4 % for the undoped ACC sample compared to 14.1 % for Sr-doped ACC and 12.2 % for Ba-doped ACC (Table 3.2). Notably, this specific band was only visible for "BBM" samples, despite their lower level of hydration (14.9 ± 3.2 %) compared to the "MFC-L" samples (17.3 ± 1.6 %), "MFC-H" samples (17.5 ± 2.1 %), and "BM" samples (17.7 ± 0.6 %). Since ATR-FTIR is very susceptible to the chemical environment or binding modes, this suggests a change in the chemical environment, suppressing the expected v_1 mode. The OH stretching vibrations band at 3400 cm^{-1} also indicated a change in hydration (black arrow in Figure 3.3)[51]. However, as the ATR-FTIR spectra provided only a local hydration indicator, thermogravimetric measurements were conducted to achieve quantitative results for bulk samples (Table 3.2).

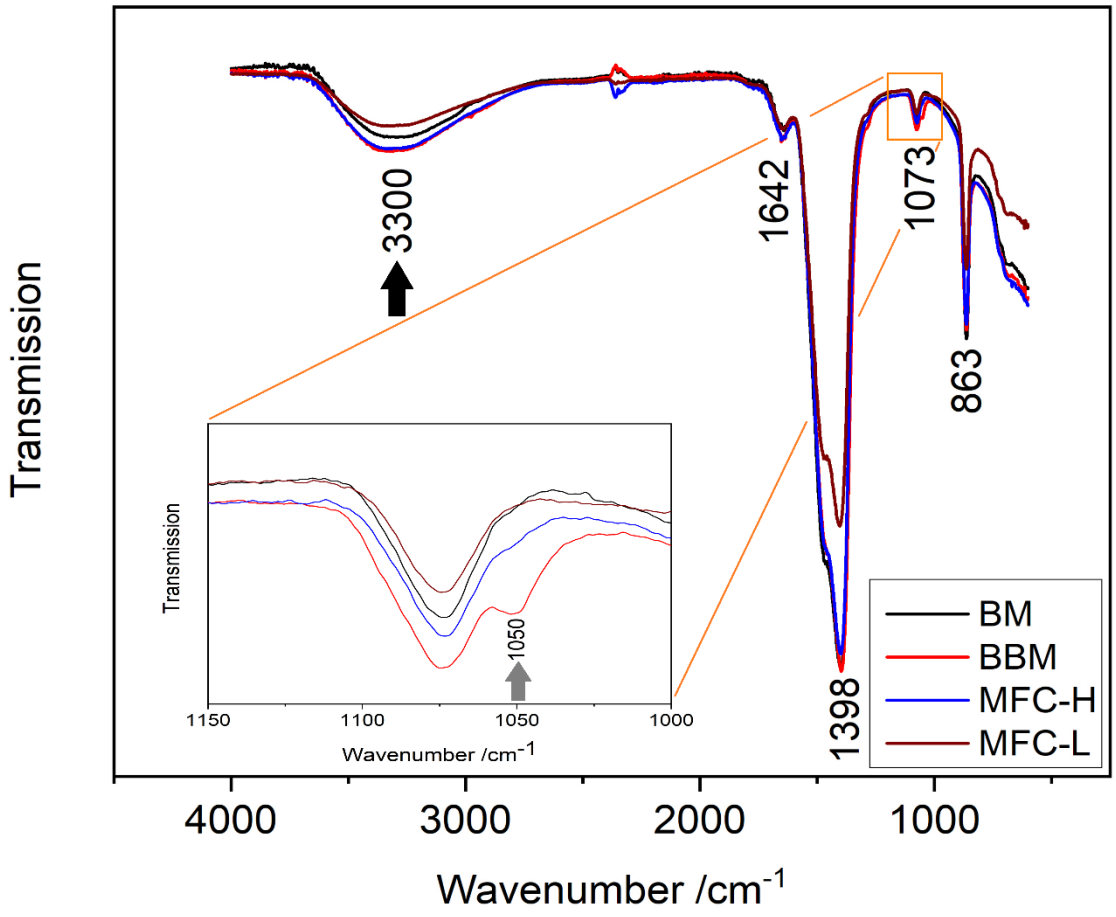

Figure 3.3. Independent of the applied synthesis the typical ACC bands were present[47–50]. The undoped "BBM" sample possessed a shoulder at 1050 cm^{-1} (grey arrow in enlargement) which was described as an indicator for a high ACC hydration[26,48].

3.3.2 SEM analysis of the precipitated ACC particles

Scanning electron micrographs showed that all samples had the same characteristic spherical morphology, which is typical of ACC (Figure 3.4 and Supplementary Figure 3.4-3.7)[52]. Particle sizes between 32 ± 7 nm (Sr-doped "BBM" sample) to 67 ± 20 nm (Ba-doped "BM" sample) were measured. While applying strontium or barium as dopants had little effect on the particle size, the specific synthesis method exhibited a marked influence on the particle size (Table 3.1) with smaller particle sizes for the flow-through system ("BBM", "MFC-H", "MFC-L") than for the "BM" samples.

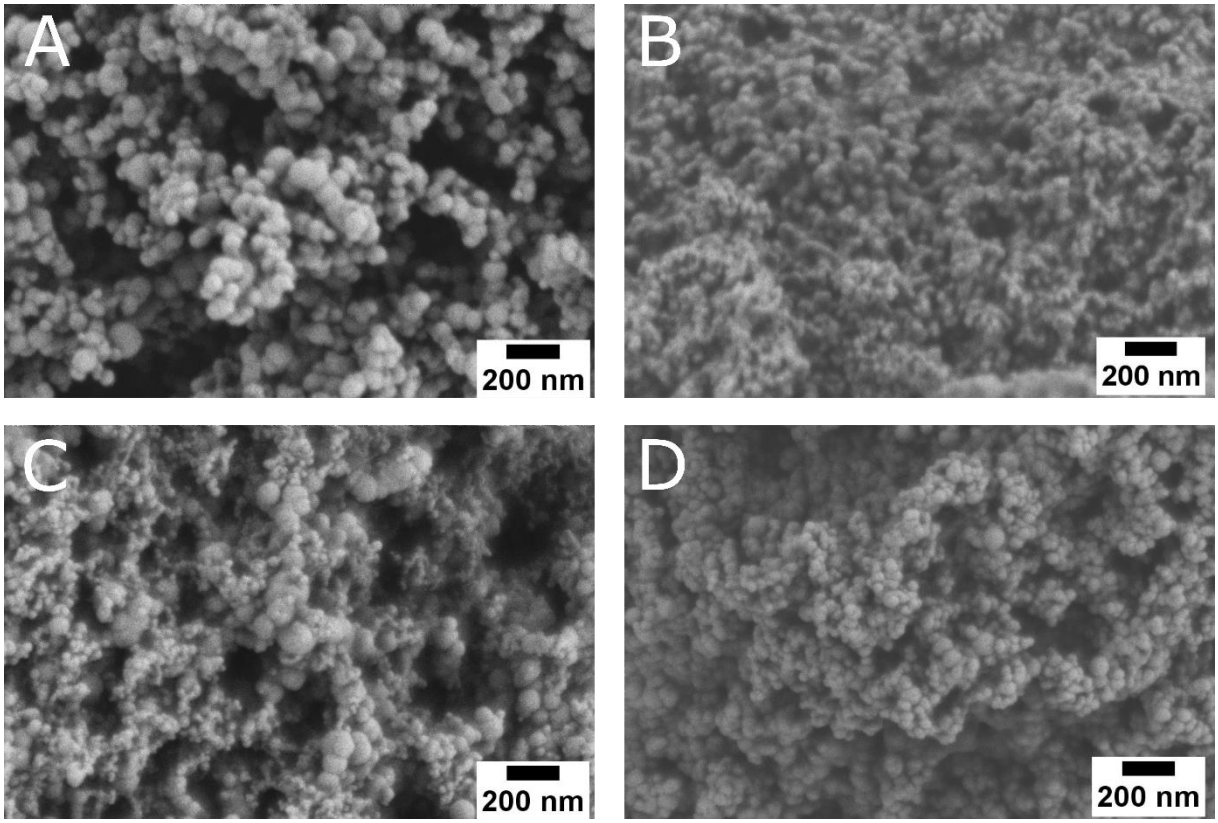

Figure 3.4. SEM micrographs of the undoped **(A)** "BM", **(B)** "BBM", **(C)** "MFC-H" and **(D) "**MFC-L" samples. Equivalent images for doped samples can be found in Supplementary Figure 3.4-3.7.

Applying the microfluidic chip resulted in particle sizes of around 40 nm for the "MFC-H" and "MFC-L" samples. However, a slight influence of the pH on the particle size was observed, as the "MFC-H" samples were larger than the "MFC-L" samples. Furthermore, the "MFC-H" particle sizes were less uniform than the "MFC-L" samples (Table 3.1), as shown by the higher standard deviation for the "MFC-H" samples. The higher polydispersity of the "MFC-H" samples can be explained by considering the higher rate of ACC formation at higher pH in combination with the layout of the microfluidic chip. Light microscopy showed that particles were already present before ethanol was added (black arrows indicate ethanol addition in Figure 3.5B). With the addition of ethanol, which acts as antisolvent, the ACC solubility decreased, forcing the formation of additional ACC particles[45,53]. The larger standard deviation is thus a result of a second, ethanol-induced ACC precipitation, forming two independent ACC precipitation steps.

For the "MFC-L" samples, no precipitated particles were detected before ethanol was added (Figure 3.5C). However, after quenching of the reaction mixture with ethanol, a small number of particles were visible (red arrow in Figure 3.5C). Thus, it is assumed that ethanol-induced precipitation allowed for the observed ACC precipitation at low pH of 7.5 in this specific setup.

Table 3.1. Comparison of measured particle sizes for each experimental setup including standard deviations (n=100).

Particle size (nm)	ACC	ACC + Sr	ACC + Ba
BM	65 ± 19	61 ± 19	67 ± 20
BBM	38 ± 7	32 ± 7	33 ± 5
MFC-H	47 ± 24	45 ± 23	48 ± 21
MFC-L	38 ± 11	40 ± 12	40 ± 17

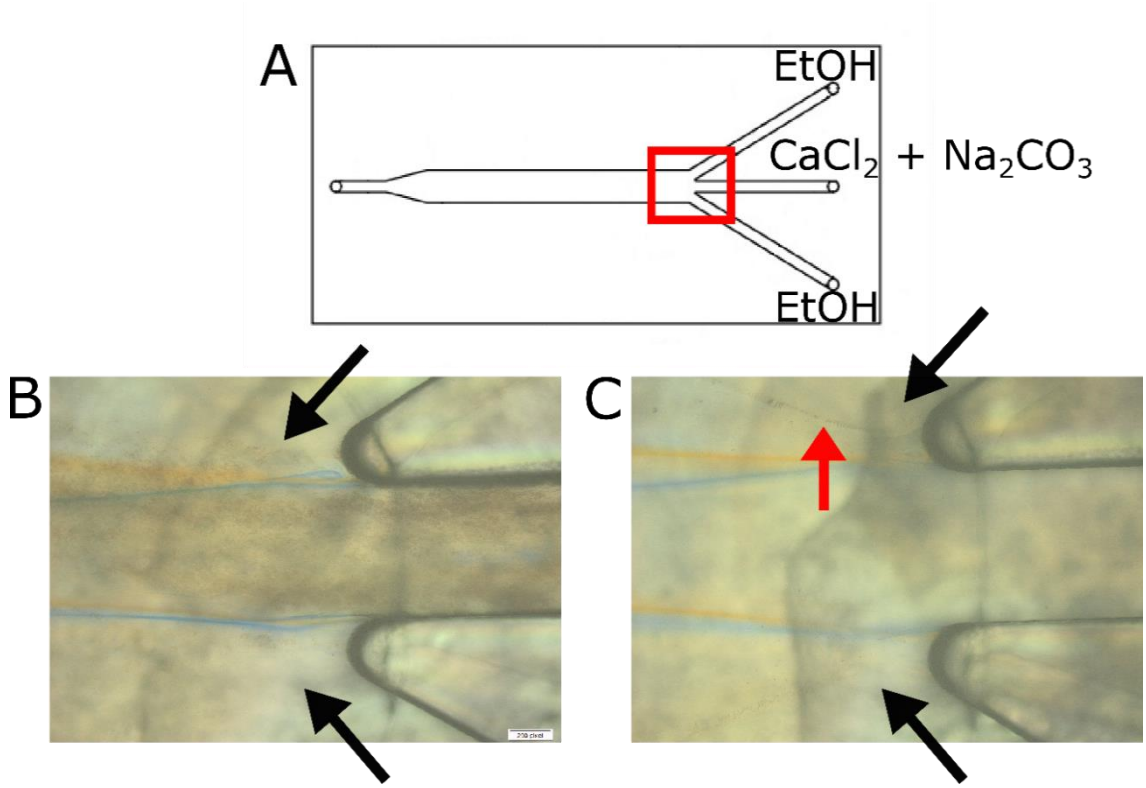

Figure 3.5. Investigating pH influence on ACC precipitation. **(A)** Schematic of the microfluidic chip with the red box depicting the detail shown in **(B)** for "MFC-H" and **(C)** for "MFC-L" experiments. **(B)** Particles were already precipitated before ethanol was added (black arrows indicate ethanol addition). **(C)** No particles were visible before ethanol was added (black arrows indicate ethanol addition). After the ethanol addition, particles were only visible at the point where the calcium chloride – sodium carbonate solution and ethanol merged (red arrow).

To test if a microfluidic chip is critical for precipitating ACC at a pH of 7.5, a batch mixing synthesis was conducted at a similarly low pH. After mixing the calcium chloride and sodium bicarbonate solutions, ethanol was immediately added and after 5 minutes of stirring, the solution was filtered similarly to the "MFC-L" samples. Although ACC was precipitated, the amount was less than 10 % of what was observed for the "MFC-L" samples. Hence, the MFC setup is thus highly beneficial for ACC precipitation at such a low pH. It is reasonable to assume

that it is the controlled pre-diffusion of ethanol in the laminar flow section of the microfluidic chip which already enhances ACC precipitation.

3.3.3 Analysing the level of hydration and crystallisation behaviour

As dehydration of ACC triggers crystallisation, water takes a fundamental role in stabilising ACC[54–56]. Thus, the hydration of the powders was analysed via coupled TGA/DSC measurements (Figure 3.6 and Supplementary Figure 3.8). All TGA measurements exhibited similar behaviour, namely a release of water at low temperatures (black arrow), followed by a release of carbon dioxide above 600 °C (grey arrow), accompanied by the formation of calcium oxide[57–59]. However, closer inspection revealed small but significant differences in the hydration state of the different ACC synthesis variants.

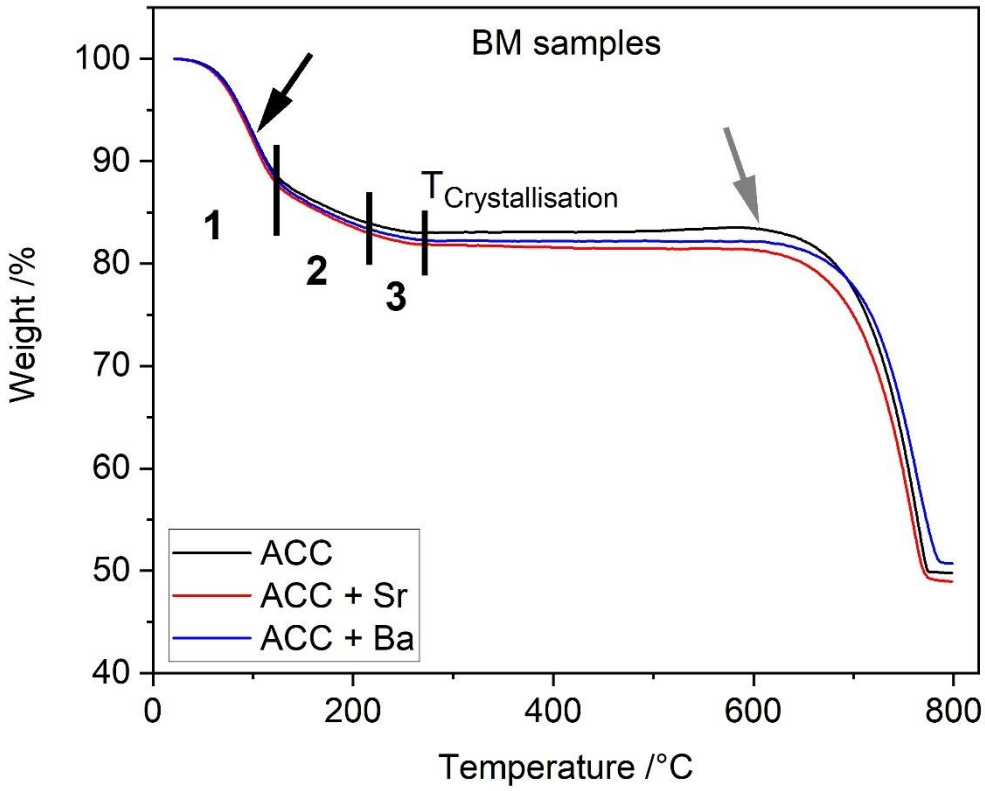

Figure 3.6. Thermal gravimetric analysis (TGA) measurements for the “BM” samples.

To assess this quantitatively, the approach by Schmidt *et al.*[58] was followed who used ^{1}H-NMR to show that four hydrous components – *(a)* rigid structural water, *(b)* water molecules with limited mobility, *(c)* mobile water, and *(d)* hydroxyl moieties – are present in ACC. During dehydration, the mobile and rigid water were expelled while hydroxyl groups remained incorporated until crystallisation. Therefore, Schmidt *et al.* divided the different dehydration stages into three mass loss regimes defined by the intersections of their weight loss slopes. The black bars in Figure 3.6 indicate the boundaries of the different mass-loss regimes, whose

exact temperatures are provided in Supplementary Table 3.3. The upper limit of the third mass loss regimes was set by the crystallisation temperatures ($T_{crystallisation}$ in Figure 3.6) which were determined by DSC measurements (below). Subsequently, the hydration level of each regime was determined (Figure 3.7).

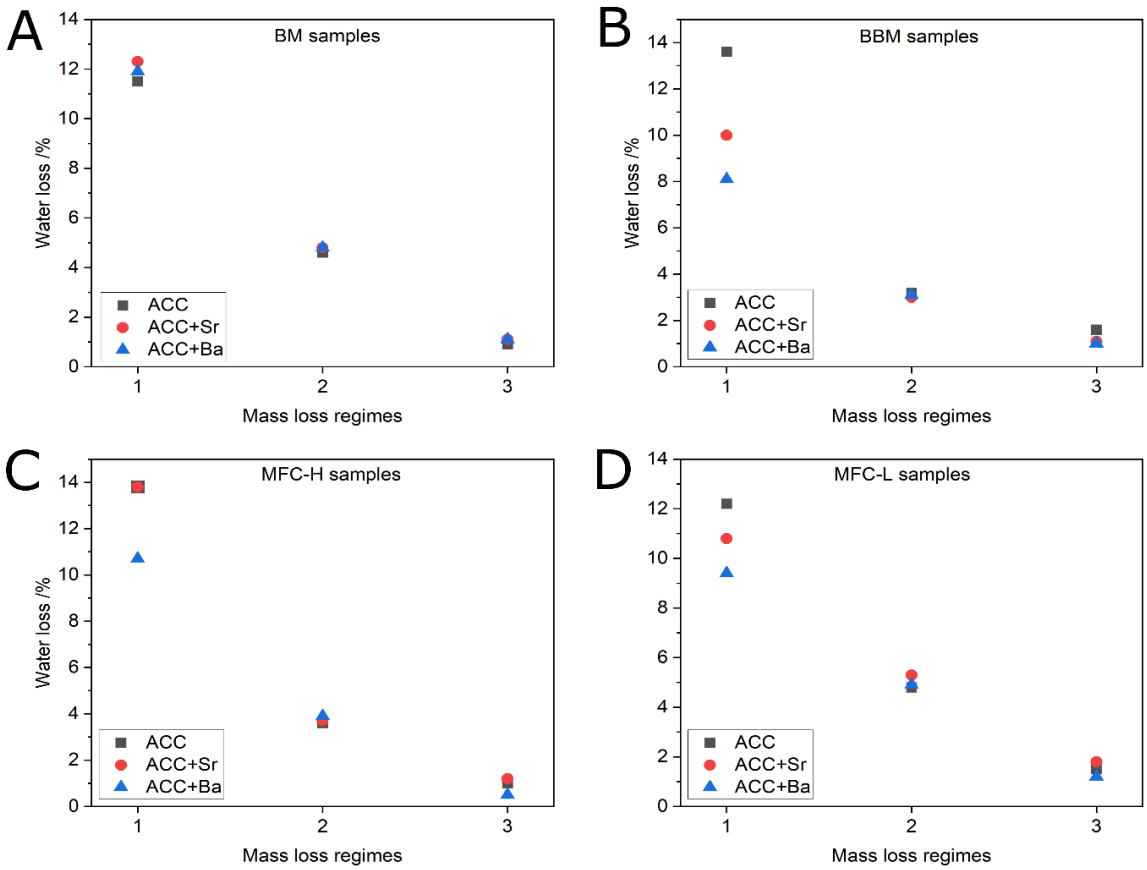

Figure 3.7. Water loss of the **(A)** "BM", **(B)** "BBM", **(C)** "MFC-H", and **(D)** "MFC-L" samples at the three different hydration regimes.

Table 3.2. TGA analysis of water loss for each sample and classification into the three temperature regimes as defined by Schmidt *et al.*[58] (n=1). Standard deviation is given for the averages.

Water loss (%)	Dopant	Regime 1	Regime 2	Regime 3	Total
BM	---	11.5	4.6	0.9	17
BM	Sr	12.3	4.8	1.1	18.2
BM	Ba	11.9	4.8	1.1	17.8
BBM	---	13.6	3.2	1.6	18.4
BBM	Sr	10	3	1.1	14.1
BBM	Ba	8.1	3.1	1	12.2
MFC-H	---	13.8	3.6	1	18.6
MFC-H	Sr	13.8	3.7	1.2	18.7
MFC-H	Ba	10.7	3.9	0.5	15.1
MFC-L	---	12.2	4.8	1.5	18.5
MFC-L	Sr	10.8	5.3	1.8	17.9
MFC-L	Ba	9.4	4.9	1.2	15.5
Average water loss	---	11.5 ± 1.8	4.1 ± 0.8	1.2 ± 0.3	16.8 ± 2.1

The average loss of water in the first regime exhibits a significantly larger standard deviation compared to all other regimes (Table 3.2). According to the literature, loss of water at temperatures of up to 140 °C indicates release of mobile water from internal pores[57,58].

In all synthesis variants except for batch mixing, Ba-doped ACC features a significantly lower level of total hydration; at least 13 % lower than Sr-doped ACC and 16 % lower than pure ACC (Table 3.2). The lower levels of hydration were primarily caused by a lower presence of mobile water, according to the loss in the first regime. This correlates with the lower hydration energy of barium compared to strontium and calcium[60,61].

Remarkably, Ba-doped samples generated by batch mixing did not exhibit a comparable decrease in hydration (Table 3.2). A possible explanation is that under batch mixing conditions, *i.e.*, by vigorously stirring, the aggregation of small particles is enforced and presumably led to a higher porosity. This rationalisation finds corroboration in the literature since a comparable synthesis was used to achieve porous ACC based on the aggregation of spherical particles[62]. Thus, batch mixing leads either to a higher porosity of the Ba-doped samples, entrapping fluid-

like water or, when assuming a constant composition, the chemically bound fraction of incorporated water is lower due to the significantly lower hydration enthalpy of barium. In order to differentiate between these two alternative explanations, density measurements were conducted which revealed a significantly lower density of the batch samples compared to all samples produced by flow mixing. Hence, flow mixing yields ACC particles with a lower porosity and, thus, with a lower amount of mobile water (Figure 3.9).

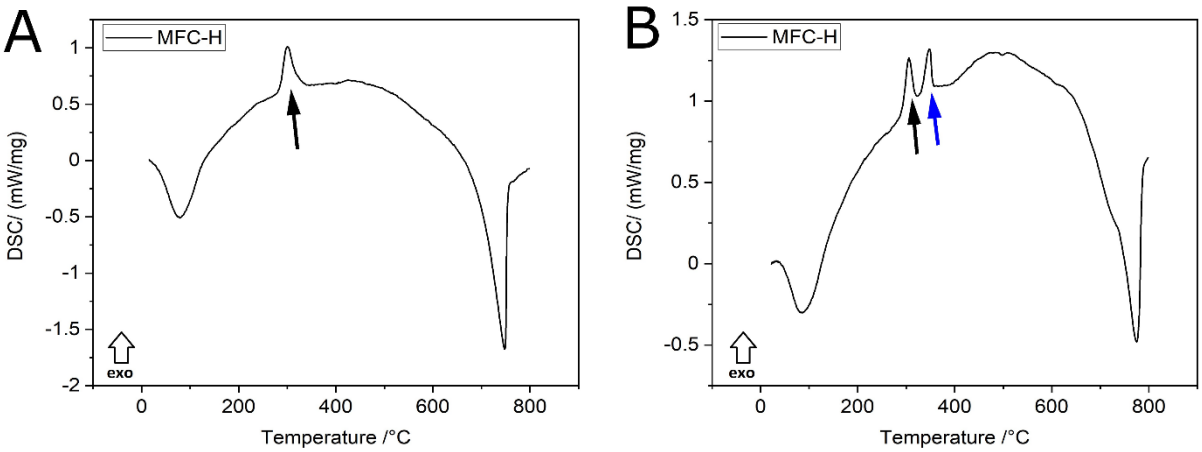

Figure 3.8. DSC measurements of undoped and Ba-doped "MFC-H" samples. **(A)** For the undoped sample a crystallisation temperature of 300 °C was measured (black arrow), while **(B)** for the Ba-doped powder two crystallisation peaks at 306 °C (black arrow) and 349 °C (blue arrow) were determined. The "exo" arrows indicates the peak direction of an exothermic reaction.

The crystallisation temperatures of the doped and undoped ACC variants were determined (Figure 3.8 and Supplementary Figure 3.9-3.12). They ranged between 264 °C and 349 °C (Table 3.3) and agree with previously reported crystallisation temperatures of ACC in the literature (150 °C to 350 °C)[54,58,63–65].

The synthesis via batch mixing and via microfluidic chip at a low pH showed crystallisation temperatures below 300 °C. For both syntheses, barium incorporation resulted in an increase of the crystallisation temperature (Table 3.3). However, this effect was more pronounced for the "MFC-L" sample, presumably due to the high barium incorporation at a low pH (Figure 3.10), as dopants such as barium affect the ACC structure and have a hampering effect on crystal lattice formation[30,63,66,67].

Samples generated by Ball-Berger mixing and by microfluidic chip at pH 11 exhibited crystallisation temperatures mostly above 300 °C (Table 3.3). Despite their low levels of hydration (Table 3.2), even the Sr- and Ba-doped ACC variants showed crystallisation temperatures well above 300 °C (321 °C and 334 °C). This is an unexpected observation, since barely hydrated ACC is less stable than hydrated ACC, because water has to be expelled before the crystallisation of an anhydrous polymorph can take place[25,68]. The observed stabilisation might therefore arise from the incorporation of the foreign ions into the ACC

structure, as such additives often stabilise ACC[66,67]. However, the partition coefficients of Sr- and Ba-doped “BBM” samples differed only slightly from most of the other doped ACC samples (Figure 3.10 and Table 3.5). This suggests that the elevated crystallisation temperatures of Sr- and Ba-doped “BBM” samples were not a result of a higher dopant concentration. In the light of the observed level of hydration, it is unclear which effect stabilised Sr- and Ba-doped “BBM” samples.

Table 3.3. Crystallisation temperatures for samples from different synthesis methods and different dopants (n=1).

Temperature (°C)	ACC	ACC + Sr	ACC + Ba
BM	265	268	284
BBM	314	321	334
MFC-H	300	292	306 / 349
MFC-L	264	266	297

Analysis of the dopant influence on the crystallisation temperatures revealed that the strontium incorporation affected crystallisation temperatures by less than 10 °C (Table 3.3). For the Sr-doped “MFC-H” sample, an even lower crystallisation, temperature was measured than for undoped ACC. Littlewood *et al.*[19] indicated in their work that strontium ions were substituting calcium ions in ACC, as Sr K-edge X-ray absorption near edge structure (XANES) and extended X-ray absorption fine structure (EXAFS) spectra were comparable to Ca K-edge XANES and EXAFS spectra. This substitution of calcium by strontium provides a potential explanation for the low influence of strontium on the crystallisation temperatures presented in this chapter. In contrast to strontium, barium incorporation increased the crystallisation temperature independent of the applied synthesis, which is in accordance with the literature (Table 3.3)[69].

Notably, the Ba-doped “MFC-H“ sample had two exothermic peaks at 306 °C and 349 °C (arrows in Figure 3.8B; Table 3.3). Apart from the Ba-doped “MFC-H” sample, no other “MFC” samples exhibited this peak. A possible explanation for the occurrence of these distinct peaks is that the samples could consist of a bimodal mixture of differently sized ACC particles. This non-uniformity of the particle size might generate different transformation behaviours as larger ACC particles crystallise earlier than smaller ones[54,64]. This observation substantiates the previous explanation of the broad particle size distributions for “MFC-H” samples, indicated by the highest standard deviation compared to the other samples (20 % higher; Table 3.1). Larger ACC particles crystallise when water is released from internal pores while smaller ACC particles formed by the antisolvent precipitation, *i.e.*, the addition of ethanol, crystallise after

water evaporation is completed. For pure ACC, an increase of the crystallisation temperature from ~130 °C (200 nm) to ~205 °C (66 nm) was determined in literature[64]. This rationalises the observation of two distinct crystallisation temperatures.

3.3.4 Density of ACC powders

The ACC densities can be grouped into two sets, which clearly correlate with the synthesis method (Figure 3.9 and Table 3.4). Batch samples exhibited an average density of 1.69 ± 0.06 g·cm^{-3} which is in line with the literature, which reports densities from 1.62 g·cm^{-3} to 2.18 g·cm^{-3} (Table 3.4)[24,43,57].

Flow mixed samples, be it by Ball-Berger mixing or in the microfluidic chip at high and low pH values, exhibited average densities of 2.42 ± 0.13 g·cm^{-3}, 2.63 ± 0.2 g·cm^{-3}, and 2.63 ± 0.27 g·cm^{-3}, respectively (Table 3.4). Saharay *et al.*[56] used molecular dynamics simulations to predict an increased ACC density (2.59 g·cm^{-3} to 2.71 g·cm^{-3}) with decreasing hydration. However, only the Sr-doped "BBM" sample and the Ba-doped samples exhibited low hydration (Table 3.2), suggesting the contribution of another, yet unknown, effect.

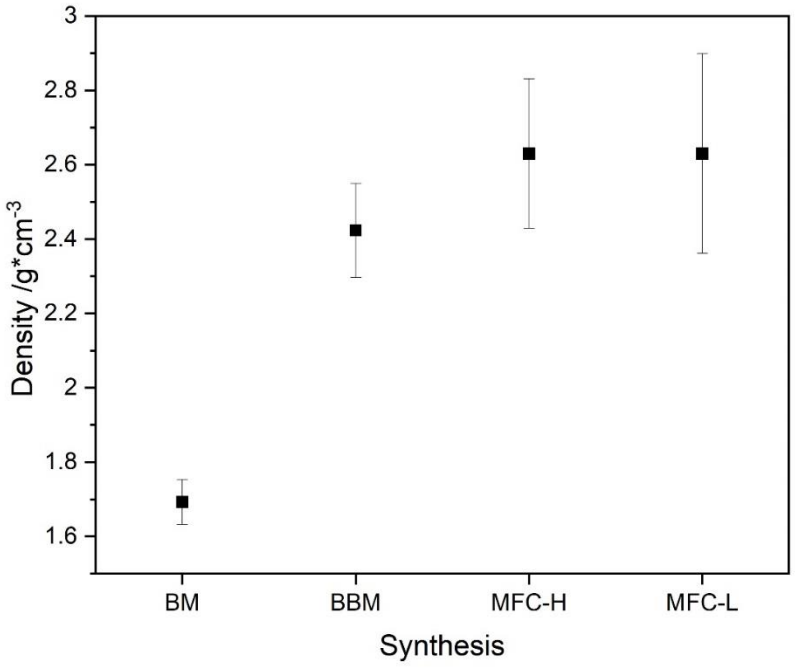

Figure 3.9. Densities of ACC for different synthesis procedures.

Gebauer *et al.*[23] showed the existence of two ACC types with distinct short-range order, *i.e.*, proto-calcite ACC and proto-vaterite ACC, at different pH values of 8.75 and 9.8, respectively. While Gebauer *et al.* achieved the formation of distinct ACC near-range orders by changing the solution's pH, the data presented herein suggests that altering the reaction conditions, *i.e.,* mixing profiles, also resulted in the formation of distinct ACC structures, either on the molecular

or microstructural level. Two different ACC types are assumed to be distinguishable by their densities. The “BM” (batch mixing) samples represented a low-density ACC structure, while the “BBM”, “MFC-H”, and “MFC-L” samples, which were synthesised by applying flow-through syntheses, reflected a high-density ACC structure. EXAFS analysis could be conducted in the future in order to confirm the presence of distinct ACC structures at the molecular level.

Except for the batch samples, Sr-doped ACC had lower densities compared to undoped ACC. In the case of barium-doped ACC, a higher density was determined for all samples except the batch samples. Therefore, it is reasonable to assume that the high-density ACC is more affected by dopant incorporation than the low-density ACC type, which suggests that the density effects originate at the microstructural level. In accordance with these results, a Monte Carlo simulation constrained by scattering data revealed that ACC consists of a calcium-rich framework with interconnected channels which contain water and carbonate molecules[70].

Table 3.4. Influence of the synthesis and dopant incorporation on the ACC density (n=1). The “Average” column reflects the average density for each synthesis method, standard deviation is given for this column.

Density (g*cm^{-3})	ACC	ACC + Sr	ACC + Ba	Average Synthesis
BM	1.63	1.7	1.75	1.69 ± 0.06
BBM	2.56	2.31	2.4	2.42 ± 0.13
MFC-H	2.61	2.44	2.84	2.63 ± 0.2
MFC-L	2.58	2.39	2.92	2.63 ± 0.27

3.3.5 Partition coefficients of strontium and barium doped ACC

ICP-OES measurements were conducted to investigate if the synthesis affected the calculated partition coefficients of doped ACC. For Sr-doped ACC, strontium partition coefficients ranged between 0.89 ± 0.03 (“MFC-L”) and 0.97 ± 0.03 (“MFC-H”, Figure 3.10 and Table 3.5). These values are in accordance with the literature and Chapter 2 (Figure 2.7), in which Sr partition coefficients from 0.7 to 1 were reported[19,71]. For Ba-doped ACC, calculated partition coefficients from 1.03 ± 0.01 to 1.13 ± 0.01 were determined in case of “BM”, “BBM”, and “MFC-H” (Figure 3.10 and Table 3.5). In the literature, Ba partition coefficients between 1.2 and 1.4 were determined[71]. Only the values of the Ba-doped “MFC-L” sample were significantly outside the reported range in the literature.

Regardless of the applied dopant, the “MFC-H” partition coefficients differed from those of the other samples. While the calculated partition coefficients for “MFC-H” are higher for Sr, they are lower for Ba compared to all other samples. As ethanol decreases the solubility of calcium carbonate[45,53], an accelerated ACC formation is assumed to enforce the trace element to

calcium ratio, which was present in solution through co-precipitation. Thus, the calculated partition coefficients of both dopants were approximately one.

Table 3.5. Partition coefficients of strontium and barium doped ACC produced via different synthesis including standard deviations (n=3).

K_D	ACC + Sr	ACC + Ba
BM	$0.89 \pm 4.8 \cdot 10^{-3}$	1.13 ± 0.01
BBM	0.91 ± 0.04	1.11 ± 0.01
MFC-H	0.97 ± 0.03	1.03 ± 0.01
MFC-L	0.89 ± 0.03	2.47 ± 0.03

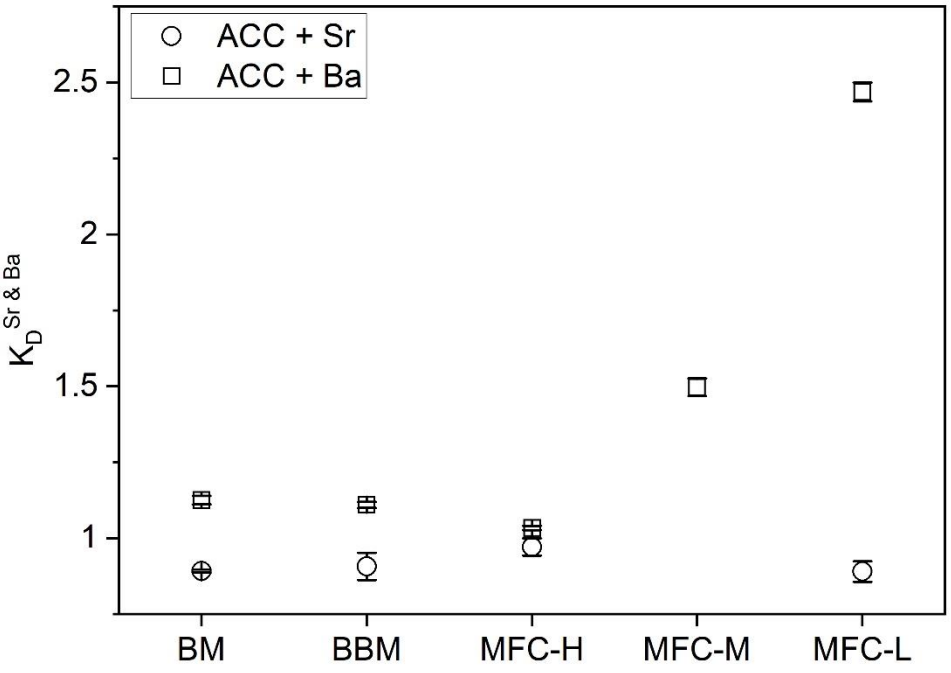

Figure 3.10. Calculated partition coefficients of strontium and barium doped ACC synthesised via different routes. To confirm the strong influence of the pH on the calculated Ba partition coefficients, the partition coefficient Ba-doped ACC synthesised at a pH 10 ("MFC-M") was measured.

An unexpected finding was that the calculated Ba-doped "MFC-L" partition coefficients increased by a factor of about two, compared to "MFC-H" samples. This suggests that the pH has a strong influence on Ba partitioning. To test this hypothesis, ACC was precipitated at a pH of 10 ("MFC-M" samples) resulting in a calculated partition coefficient of 1.5 ± 0.03

(Figure 3.10 and Table 3.6) which is intermediate between those determined at lower and at higher pH and clearly shows that pH impacts on the Ba-incorporation rates in the MFC setup.

Table 3.6. Synthesis of Ba-doped ACC at varying pH including standard deviations (n=3).

K_D	pH 11	pH 10	pH 7.5
ACC + Ba	1.03 ± 0.01	1.5 ± 0.03	2.47 ± 0.03

3.4 Conclusion

This chapter reveals for the first time that the synthesis method has a significant impact on various characteristics of undoped, Sr- and Ba-doped ACC. The mixing conditions, namely stirring or flow-based, strongly affect the particle size as sizes between 32 ± 7 nm (Sr-doped "BBM" samples) and 67 ± 20 nm (Ba-doped "BM" powders) were measured depending on the mixing method. Density measurements revealed the existence of low-density ACC ("BM" samples) and high-density ACC ("BBM", "MFC-H", and "MFC-L" powders) as a result of the different mixing conditions.

Analysing the hydration of all ACC variants following the approach of Schmidt *et al.*[58] revealed that the Ba-doped "BBM", "MFC-H", and "MFC-L" samples exhibited a decreased hydration as less fluid-like water was present in the first regime. DSC measurements demonstrated crystallisation temperatures below 300 °C for the "BM" and "MFC-L" samples and above 300 °C for the "BBM" and "MFC-H" samples. While the incorporation of strontium barely affected the crystallisation temperatures, Ba-doped ACC exhibited increased crystallisation temperatures. Also here, a difference as a result to changing mixing conditions was observed.

The calculated strontium and barium partition coefficients determined in this chapter were comparable to those reported in the literature, except for that of Ba-doped "MFC-L"[19,71]. Independent of the applied dopants, the calculated "MFC-H" partition coefficients differed from those of the other samples. "MFC-H" had higher amounts of Sr but lower amounts of Ba incorporated compared to the other samples. It is assumed that the decreased calcium carbonate solubility[45,53] caused an accelerated ACC precipitation, resulting in kinetically mediated unpartitioned uptake of Sr and Ba into ACC. Furthermore, it was revealed that the chemical composition of the Ba-doped "MFC-H" was strongly affected by the pH.

Larger particle sizes, lower densities and, at least for Ba-doped ACC, higher hydration levels measured for the batch samples indicate that distinct ACC structures were formed. Thus, the precipitation of distinct ACC structures is not only possible by varying the pH[4,23], but also by changing the conditions of mixing. It is a key finding of this chapter that more attention must be paid to how ACC was synthesised when studying the structure and composition of ACC. In the literature, an unmanageable plurality of different ACC syntheses was described and are

still commonly used. In many publications, ACC was precipitated by simply mixing solutions containing Ca^{2+} and CO_3^{2-} ions[25,26,29–31]. Formation of ACC was also achieved by uptake of carbon dioxide by a calcium bearing solution, be it by incubating it over decomposing ammonium carbonate[34–36] or by direct exposure to carbon dioxide[27,28]. Furthermore, a variety of more “exotic” syntheses are described in the literature[72,73]. Corresponding to this multitude of syntheses, how these syntheses influenced the structure, the material properties, and chemical composition of ACC must be analysed. So far, syntheses are seen as interchangeable, assuming that only pH affects the properties of the ACC, but this chapter debunks this major misconception.

The results in this thesis show that changes in microfluidic conditions impact on various ACC properties. This finding indisputably deserves further elucidation, *e.g.*, by evaluating Reynolds numbers and characteristic mixing times. However, these questions are beyond the scope of this study which focusses on synthesis-dependent changes of ACC composition.

3.5 References

1. Addadi, L., Raz, S. & Weiner, S. Taking advantage of disorder: Amorphous calcium carbonate and its roles in biomineralization. *Adv. Mater.* **15**, 959–970 (2003).

2. Weiner, S., Mahamid, J., Politi, Y., Ma, Y. & Addadi, L. Overview of the amorphous precursor phase strategy in biomineralization. *Front. Mater. Sci. China* **3**, 104–108 (2009).

3. Politi, Y. *et al.* Transformation mechanism of amorphous calcium carbonate into calcite in the sea urchin larval spicule. *Proc. Natl. Acad. Sci. U. S. A.* **105**, 17362–17366 (2008).

4. Cartwright, J. H. E., Checa, A. G., Gale, J. D., Gebauer, D. & Sainz-Diaz, C. I. Calcium Carbonate Polyamorphism and Its Role in Biomineralization: How Many Amorphous Calcium Carbonates Are There? *Angew. Chem. Int. Ed* **51**, 11960–11970 (2012).

5. Gebauer, D., Jansson, K., Oliveberg, M. & Hedin, N. Indications that Amorphous Calcium Carbonates Occur in Pathological Mineralisation—A Urinary Stone from a Guinea Pig. *Minerals* **8**, 84 (2018).

6. Mass, T. *et al.* Amorphous calcium carbonate particles form coral skeletons. *Proc. Natl. Acad. Sci. U. S. A.* **114**, E7670–E7678 (2017).

7. Jacob, D. E., Wirth, R., Soldati, A. L., Wehrmeister, U. & Schreiber, A. Amorphous calcium carbonate in the shells of adult *Unionoida*. *J. Struct. Biol.* **173**, 241–249 (2011).

8. Henderson, G. M. New oceanic proxies for paleoclimate. *Earth Planet. Sci. Lett.* **203**, 1–13 (2002).

9. Gabitov, R. I. & Watson, E. B. Partitioning of strontium between calcite and fluid. *Geochemistry, Geophys. Geosystems* **7**, (2006).

10. Katz, A. The interaction of magnesium with calcite during crystal growth at 25-90°C and one atmosphere. *Geochim. Cosmochim. Acta* **37**, 1563–1586 (1973).

11. Gascoyne, M. Trace-element partition coefficients in the calcite-water system and their paleoclimatic significance in cave studies. *J. Hydrol.* **61**, 213–222 (1983).

12. Gaetani, G. A. & Cohen, A. L. Element partitioning during precipitation of aragonite from seawater: A framework for understanding paleoproxies. *Geochim. Cosmochim. Acta* **70**, 4617–4634 (2006).

13. Wassenburg, J. A. *et al.* Determination of aragonite trace element distribution coefficients from speleothem calcite–aragonite transitions. *Geochim. Cosmochim. Acta* **190**, 347–367 (2016).

14. Lorens, R. B. Sr, Cd, Mn and Co distribution coefficients in calcite as a function of calcite

precipitation rate. *Geochim. Cosmochim. Acta* **45**, 553–561 (1981).

15. Tesoriero, A. J. & Pankow, J. F. Solid solution partitioning of Sr^{2+}, Ba^{2+}, and Cd^{2+} to calcite. *Geochim. Cosmochim. Acta* **60**, 1053–1063 (1996).

16. Soldati, A. L., Jacob, D. E., Glatzel, P., Swarbrick, J. C. & Geck, J. Element substitution by living organisms: The case of manganese in mollusc shell aragonite. *Sci. Rep.* **6**, (2016).

17. Demény, A. *et al.* Formation of amorphous calcium carbonate in caves and its implications for speleothem research. *Sci. Rep.* **6**, 39602 (2016).

18. Martignier, A. *et al.* Marine and freshwater micropearls: Biomineralization producing strontium-rich amorphous calcium carbonate inclusions is widespread in the genus *Tetraselmis* (Chlorophyta). *Biogeosciences* **15**, 6591–6605 (2018).

19. Littlewood, J. L. *et al.* Mechanism of enhanced strontium uptake into calcite via an amorphous calcium carbonate (ACC) crystallisation pathway. *Cryst. Growth Des.* **17**, 1214–1223 (2017).

20. Hoppe, A., Güldal, N. S. & Boccaccini, A. R. A review of the biological response to ionic dissolution products from bioactive glasses and glass-ceramics. *Biomaterials* **32**, 2757–2774 (2011).

21. Hodkin, D. J., Stewart, D. I., Graham, J. T. & Burke, I. T. Coprecipitation of ^{14}C and Sr with carbonate precipitates: The importance of reaction kinetics and recrystallization pathways. *Sci. Total Environ.* **562**, 335–343 (2016).

22. Matsunuma, S., Kagi, H., Komatsu, K., Maruyama, K. & Yoshino, T. Doping incompatible elements into calcite through amorphous calcium carbonate. *Cryst. Growth Des.* **14**, 5344–5348 (2014).

23. Gebauer, D. *et al.* Proto-calcite and proto-vaterite in amorphous calcium carbonates. *Angew. Chemie - Int. Ed.* **122**, 9073–9075 (2010).

24. Fernandez-Martinez, A., Kalkan, B., Clark, S. M. & Waychunas, G. A. Pressure-induced polyamorphism and formation of ‘aragonitic’ amorphous calcium carbonate. *Angew. Chemie - Int. Ed.* **125**, 8512–8515 (2013).

25. Bots, P., Benning, L. G., Rodriguez-Blanco, J. D., Roncal-Herrero, T. & Shaw, S. Mechanistic insights into the crystallization of amorphous calcium carbonate (ACC). *Cryst. Growth Des.* **12**, 3806–3814 (2012).

26. Demmert, B. *et al.* Polymer-Functionalised Nanograins of Mg-Doped Amorphous Calcium Carbonate via a Flow-Chemistry Approach. *Materials.* **12**, 1818 (2019).

27. Du, H. *et al.* Amorphous $CaCO_3$: Influence of the Formation Time on Its Degree of Hydration and Stability. *J. Am. Chem. Soc.* **140**, 14289−14299 Article (2018).

28. Rodriguez-Navarro, C., Kudłacz, K., Cizer, Ö. & Ruiz-Agudo, E. Formation of amorphous calcium carbonate and its transformation into mesostructured calcite. *CrystEngComm* **17**, 58–72 (2015).

29. Myszka, B. *et al.* Phase-specific bioactivity and altered Ostwald ripening pathways of calcium carbonate polymorphs in simulated body fluid. *RSC Adv.* **9**, 18232–18244 (2019).

30. Ihli, J., Kim, Y.-Y., Noel, E. H. & Meldrum, F. C. The effect of additives on amorphous calcium carbonate (ACC): Janus behavior in solution and the solid state. *Adv. Funct. Mater.* **23**, 1575–1585 (2013).

31. Wang, H.-W. *et al.* Synthesis and structure of synthetically pure and deuterated amorphous (basic) calcium carbonates. *Chem. Commun.* **53**, 2942–2945 (2017).

32. Loste, E., Park, R. J., Warren, J. & Meldrum, F. C. Precipitation of calcium carbonate in confinement. *Adv. Funct. Mater.* **14**, 1211–1220 (2004).

33. Tester, C. C. *et al.* In vitro synthesis and stabilization of amorphous calcium carbonate (ACC) nanoparticles within liposomes. *CrystEngComm* **13**, 3975–3978 (2011).

34. Harris, J., Mey, I., Hajir, M., Mondeshki, M. & Wolf, S. E. Pseudomorphic transformation of amorphous calcium carbonate films follows spherulitic growth mechanisms and can give rise to crystal lattice tilting. *CrystEngComm* **17**, 6831–6837 (2015).

35. Gower, L. B. & Odom, D. J. Deposition of calcium carbonate films by a polymer-induced liquid-precursor (PILP) process. *J. Cryst. Growth* **210**, 719–734 (2000).

36. Smeets, P. J. M., Cho, K. R., Kempen, R. G. E., Sommerdijk, N. A. J. M. & De Yoreo, J. J. Calcium carbonate nucleation driven by ion binding in a biomimetic matrix revealed by in situ electron microscopy. *Nat. Mater.* **14**, 394–399 (2015).

37. Lam, R. S. K., Charnock, J. M., Lennie, A. & Meldrum, F. C. Synthesis-dependant structural variations in amorphous calcium carbonate. *CrystEngComm* **9**, 1226–1236 (2007).

38. Boyjoo, Y., Pareek, V. K. & Liu, J. Synthesis of micro and nano-sized calcium carbonate particles and their applications. *J. Mater. Chem. A* **2**, 14270–14288 (2014).

39. Shen, Q. *et al.* Properties of amorphous calcium carbonate and the template action of vaterite spheres. *J. Phys. Chem. B* **110**, 2994–3000 (2006).

40. Jiang, J. *et al.* Confined crystallization of polycrystalline high-magnesium calcite from

compact Mg-ACC precursor tablets and its biological implications. *CrystEngComm* **13**, 952–956 (2011).

41. Blue, C. R., Rimstidt, J. D. & Dove, P. M. A mixed flow reactor method to synthesize amorphous calcium carbonate under controlled chemical conditions. *Methods in Enzymology* **532**, (2013).

42. Nudelman, F., Sonmezler, E., Bomans, P. H. H., De With, G. & Sommerdijk, N. A. J. M. Stabilization of amorphous calcium carbonate by controlling its particle size. *Nanoscale* **2**, 2436–2439 (2010).

43. Liu, J. *et al.* Evaluation of the particle growth of amorphous calcium carbonate in water by means of the Porod invariant from SAXS. *Langmuir* **26**, 17405–17412 (2010).

44. Berger, R. L., Balko, B. & Chapman, H. F. High resolution mixer for the study of the kinetics of rapid reactions in solution. *Rev. Sci. Instrum.* **39**, 493–498 (1968).

45. Gomaa, E. A. Solubility and Solvation Parameters of Calcium Carbonate in Mixed Ethanol-water Mixtures at 301.15 K. *Sci. Technol.* **2**, 51–52 (2012).

46. Schindelin, J. *et al.* Fiji: An open-source platform for biological-image analysis. *Nat. Methods* **9**, 676–682 (2012).

47. Han, M. *et al.* A comparison of amorphous calcium carbonate crystallization in aqueous solutions of $MgCl_2$ and $MgSO_4$: implications for paleo-ocean chemistry. *Mineral. Petrol.* **112**, 229–244 (2018).

48. Jensen, A. C. S. *et al.* Hydrogen Bonding in Amorphous Calcium Carbonate and Molecular Reorientation Induced by Dehydration. *J. Phys. Chem. C* **122**, 3591–3598 (2018).

49. Rodriguez-Blanco, J. D., Shaw, S. & Benning, L. G. The kinetics and mechanisms of amorphous calcium carbonate (ACC) crystallization to calcite, via vaterite. *Nanoscale* **3**, 265–271 (2011).

50. Andersen, F. A. & Brečević, L. Infrared spectra of amorphous and crystalline calcium carbonate. *Acta Chemica Scandinavica* **45**, 1018–1024 (1991).

51. Brubach, J. B., Mermet, A., Filabozzi, A., Gerschel, A. & Roy, P. Signatures of the hydrogen bonding in the infrared bands of water. *J. Chem. Phys.* **122**, 184509 (2005).

52. Pai, R. K. & Pillai, S. Nanoparticles of amorphous calcium carbonate by miniemulsion: Synthesis and mechanism. *CrystEngComm* **10**, 865–872 (2008).

53. Sand, K. K., Rodriguez-Blanco, J. D., Makovicky, E., Benning, L. G. & Stipp, S. L. S. Crystallization of $CaCO_3$ in Water − Alcohol Mixtures: Spherulitic Growth, Polymorph

Stabilization, and Morphology Change. *Cryst. Growth Des.* **12**, 842–853 (2012).

54. Albéric, M. *et al.* The Crystallization of Amorphous Calcium Carbonate is Kinetically Governed by Ion Impurities and Water. *Adv. Sci.* **5**, (2018).

55. Raiteri, P. & Gale, J. D. Water is the key to nonclassical nucleation of amorphous calcium carbonate. *J. Am. Chem. Soc.* **132**, 17623–17634 (2010).

56. Saharay, M. & Kirkpatrick, R. J. Water dynamics in hydrated amorphous materials: a molecular dynamics study of the effects of dehydration in amorphous calcium carbonate. *Phys. Chem. Chem. Phys.* **19**, 29594–29600 (2017).

57. Ihli, J. *et al.* Dehydration and crystallization of amorphous calcium carbonate in solution and in air. *CrystEngComm* **5**, 3169 (2014).

58. Schmidt, M. P., Ilott, A. J., Phillips, B. L. & Reeder, R. J. Structural Changes upon Dehydration of Amorphous Calcium Carbonate. *Cryst. Growth Des.* **14**, 938–951 (2014).

59. Faatz, M., Gröhn, F. & Wegner, G. Amorphous calcium carbonate: Synthesis and potential intermediate in biomineralization. *Adv. Mater.* **16**, 996–1000 (2004).

60. Rodriguez-Cruz, S. E., Jockusch, R. A. & Williams, E. R. Hydration Energies and Structures of Alkaline Earth Metal Ions, $M^{2+}(H_2O)_n$, n = 5–7, M = Mg, Ca, Sr, and Ba. *J. Am. Chem. Soc.* **121**, 8898–8906 (1999).

61. Marcus, Y. A simple empirical model describing the thermodynamics of hydration of ions of widely varying charges, sizes, and shapes. *Biophys. Chem.* **51**, 111–127 (1994).

62. Sun, R. *et al.* Amorphous Calcium Carbonate Constructed from Nanoparticle Aggregates with Unprecedented Surface Area and Mesoporosity. *ACS Appl. Mater. Interfaces* **10**, 21556–21564 (2018).

63. Zou, Z. *et al.* Additives Control the Stability of Amorphous Calcium Carbonate via Two Different Mechanisms: Surface Adsorption versus Bulk Incorporation. *Adv. Funct. Mater.* **30**, (2020).

64. Zou, Z. *et al.* Opposite Particle Size Effect on Amorphous Calcium Carbonate Crystallization in Water and during Heating in Air. *Chem. Mater.* **27**, 4237–4246 (2015).

65. Radha, A. V., Forbes, T. Z., Killian, C. E., Gilbert, P. U. P. A. & Navrotsky, A. Transformation and crystallization energetics of synthetic and biogenic amorphous calcium carbonate. *Proc. Natl. Acad. Sci. U. S. A.* **107**, 16438–16443 (2010).

66. Gal, A., Weiner, S. & Addadi, L. The stabilizing effect of silicate on biogenic and synthetic amorphous calcium carbonate. *J. Am. Chem. Soc.* **132**, 13208–13211 (2010).

67. Politi, Y. *et al.* Role of magnesium ion in the stabilization of biogenic amorphous calcium carbonate: A structure-function investigation. *Chem. Mater.* **22**, 161–166 (2010).

68. Xiao, J. & Yang, S. Biomimetic synthesis, hierarchical assembly and mechanical properties of calcite/chitosan composites in a three-dimensional chitosan scaffold. *Adv. Eng. Mater.* **13**, 32–40 (2011).

69. Whittaker, M. L. *et al.* Structural Basis for Metastability in Amorphous Calcium Barium Carbonate (ACBC). *Adv. Funct. Mater.* **28**, 1704202 (2017).

70. Goodwin, A. L. *et al.* Nanoporous structure and medium-range order in synthetic amorphous calcium carbonate. *Chem. Mater.* **22**, 3197–3205 (2010).

71. Cam, N., Georgelin, T., Jaber, M., Lambert, J. F. & Benzerara, K. In vitro synthesis of amorphous Mg-, Ca-, Sr- and Ba-carbonates: What do we learn about intracellular calcification by cyanobacteria? *Geochim. Cosmochim. Acta* **161**, 36–49 (2015).

72. Ihli, J., Kulak, A. N. & Meldrum, F. C. Freeze-drying yields stable and pure amorphous calcium carbonate (ACC). *Chem. Commun.* **49**, 3134–3136 (2013).

73. Wolf, S. E., Leiterer, J., Kappl, M., Emmerling, F. & Tremel, W. Early Homogenous Amorphous Precursor Stages of Calcium Carbonate and Subsequent Crystal Growth in Levitated Droplets. *J. Am. Chem. Soc.* **130**, 12342–12347 (2008).

74. Xia, C. & Shi, S. Q. Self-activation for activated carbon from biomass: Theory and parameters. *Green Chem.* **18**, 2063–2071 (2016).

3.6 Supplementary

Supplementary Table 3.1. Overview of the applied flow rates and filtration procedures.

pH	Flow rate	Filtration
BM	---	Immediately
BBM	25 mL/min	Immediately
MFC-H	30 mL/min	Immediately
MFC-L	10 mL/min	After 5 minutes of stirring

Supplementary Table 3.2. Measured pH values after ACC precipitation. For the MFC samples the pH was measured in two locations, namely after the y-piece and after the microfluidic chip.

pH	ACC	ACC + Sr	ACC + Ba
BM	10.8	10.7	10.7
BBM	10.7	10.6	10.7
MFC-H	10.9 / 11.4	10.9 / 11.7	10.9 / 11.7
MFC-L	7.3 / 7.5	7.3 / 7.5	7.3 / 7.5

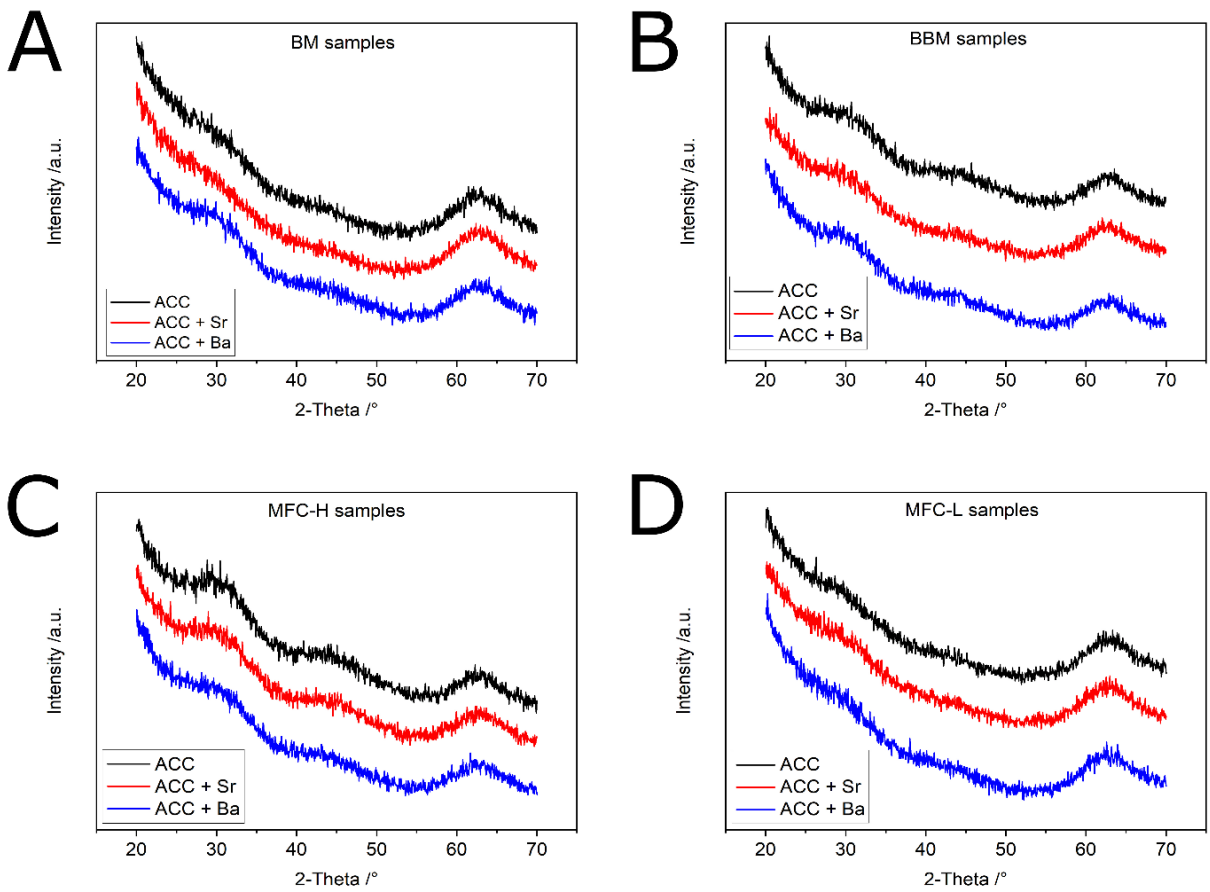

Supplementary Figure 3.1. XRD patterns of the **(A)** “BM”, **(B)** “BBM”, **(C)** “MFC-H”, and **(D)** “MFC-L” samples.

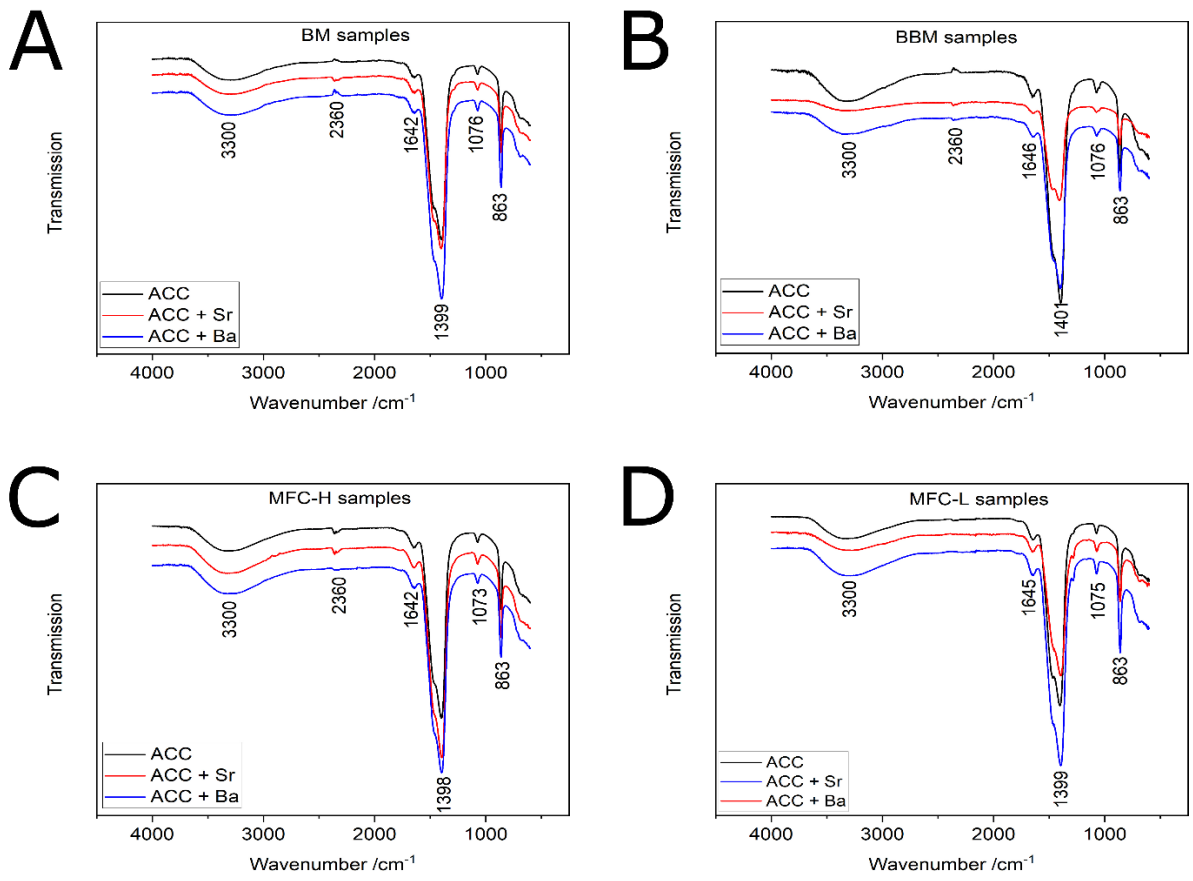

Supplementary Figure 3.2. FTIR spectra of the **(A)** "BM", **(B)** "BBM", **(C)** "MFC-H", and **(D)** "MFC-L" samples. The bands at around 2360 cm^{-1} were related to carbon dioxide in air[74].

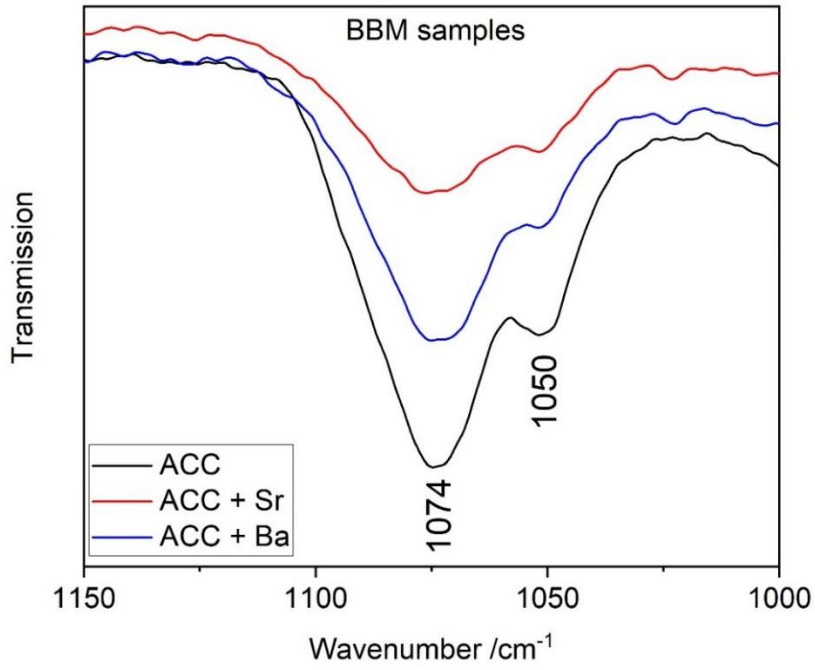

Supplementary Figure 3.3. Enlarged FTIR spectra for the 1000 – 1150 cm^{-1} region for the “BBM” samples.

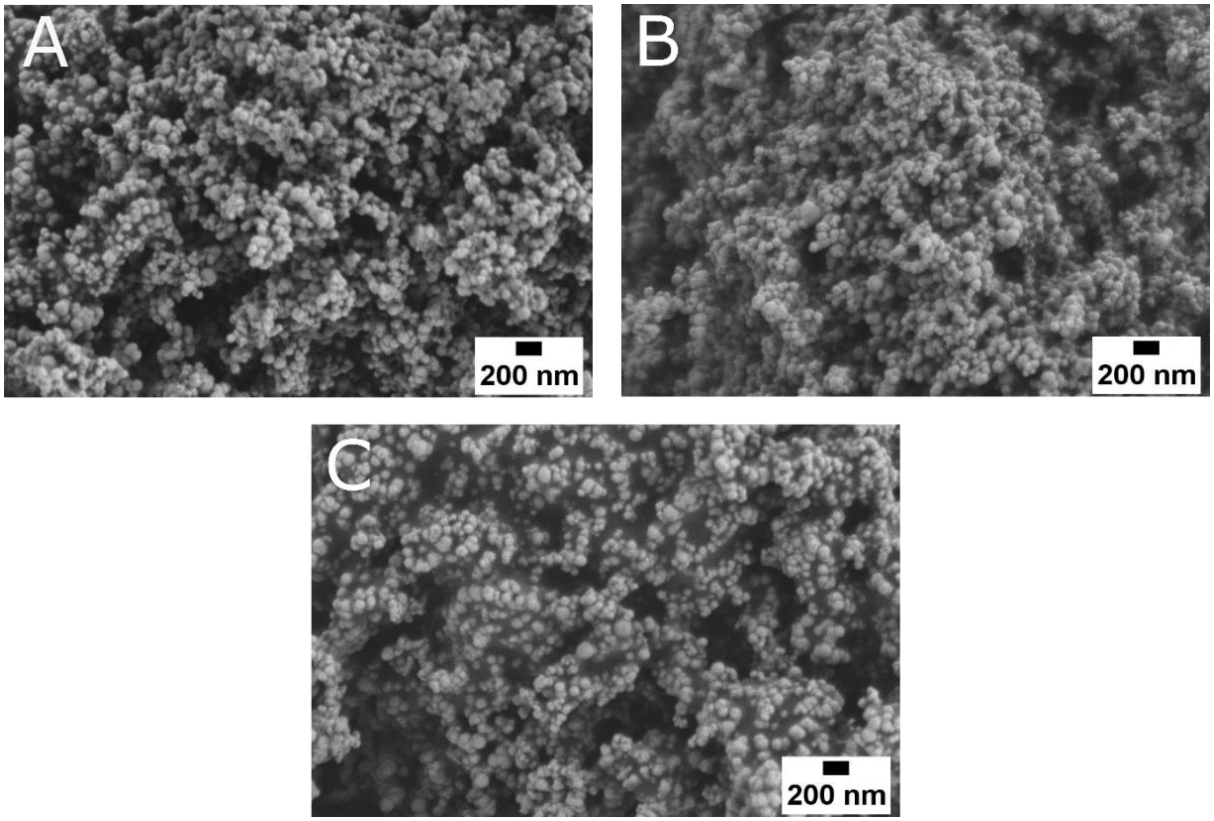

Supplementary Figure 3.4. Scanning electron micrographs for the **(A)** undoped, **(B)** Sr-doped, **(C)** and Ba-doped “BM” samples.

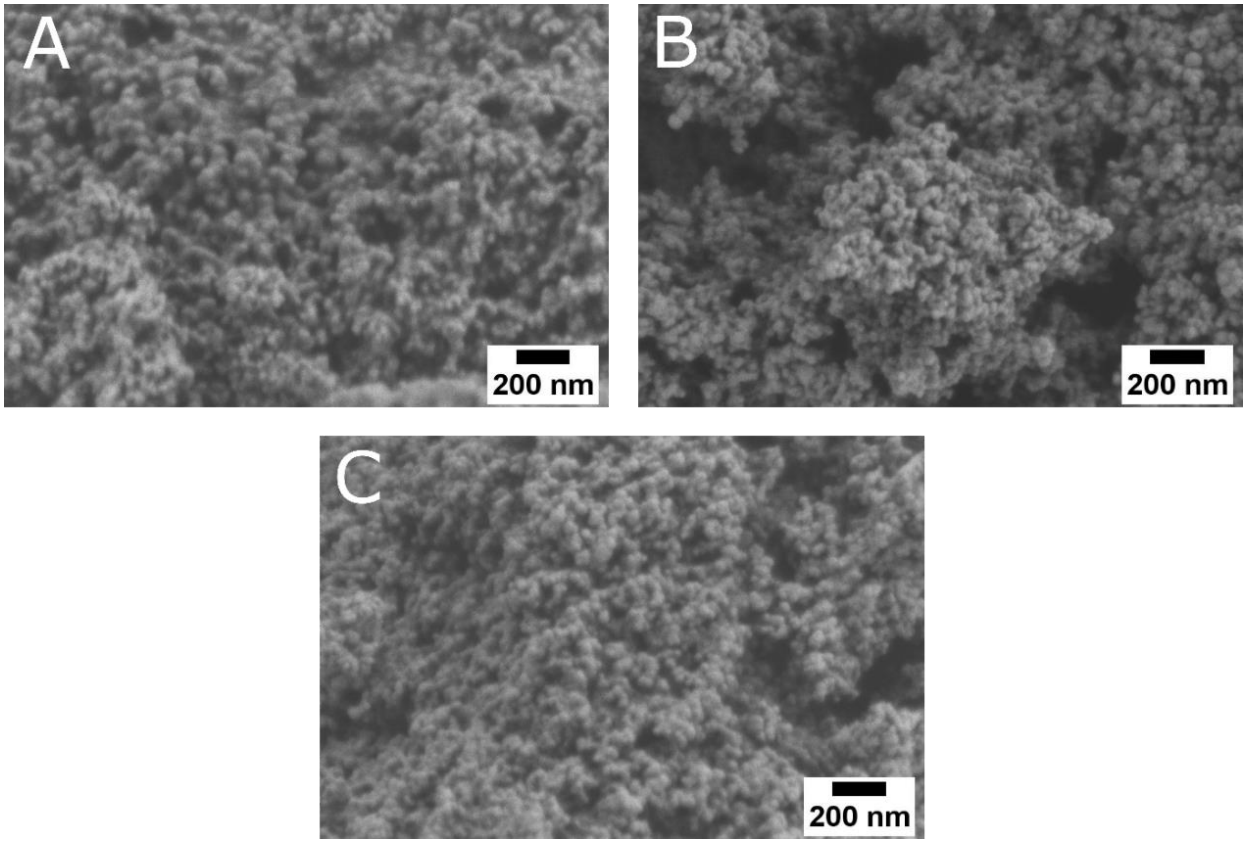

Supplementary Figure 3.5. Scanning electron micrographs for the **(A)** undoped, **(B)** Sr-doped, **(C)** and Ba-doped “BBM” samples.

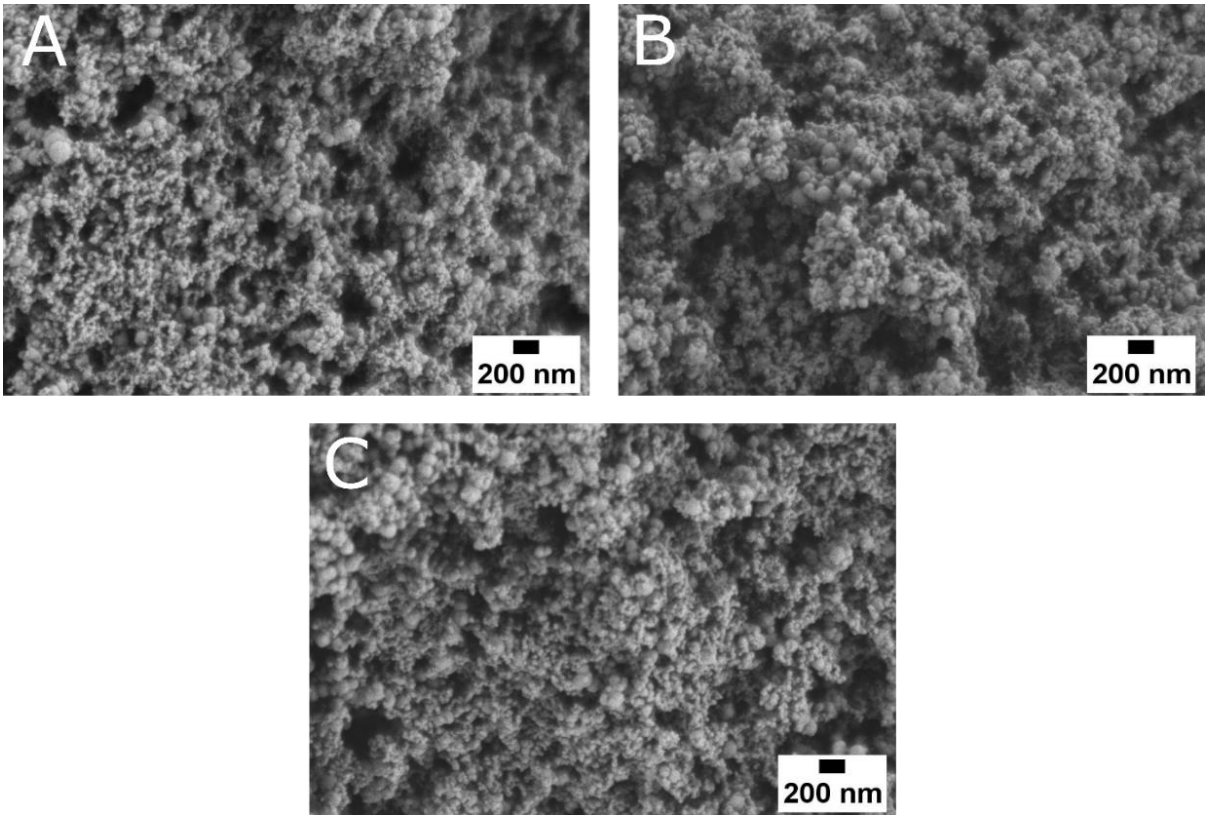

Supplementary Figure 3.6. Scanning electron micrographs for the **(A)** undoped, **(B)** Sr-doped, **(C)** and Ba-doped “MFC-L” samples.

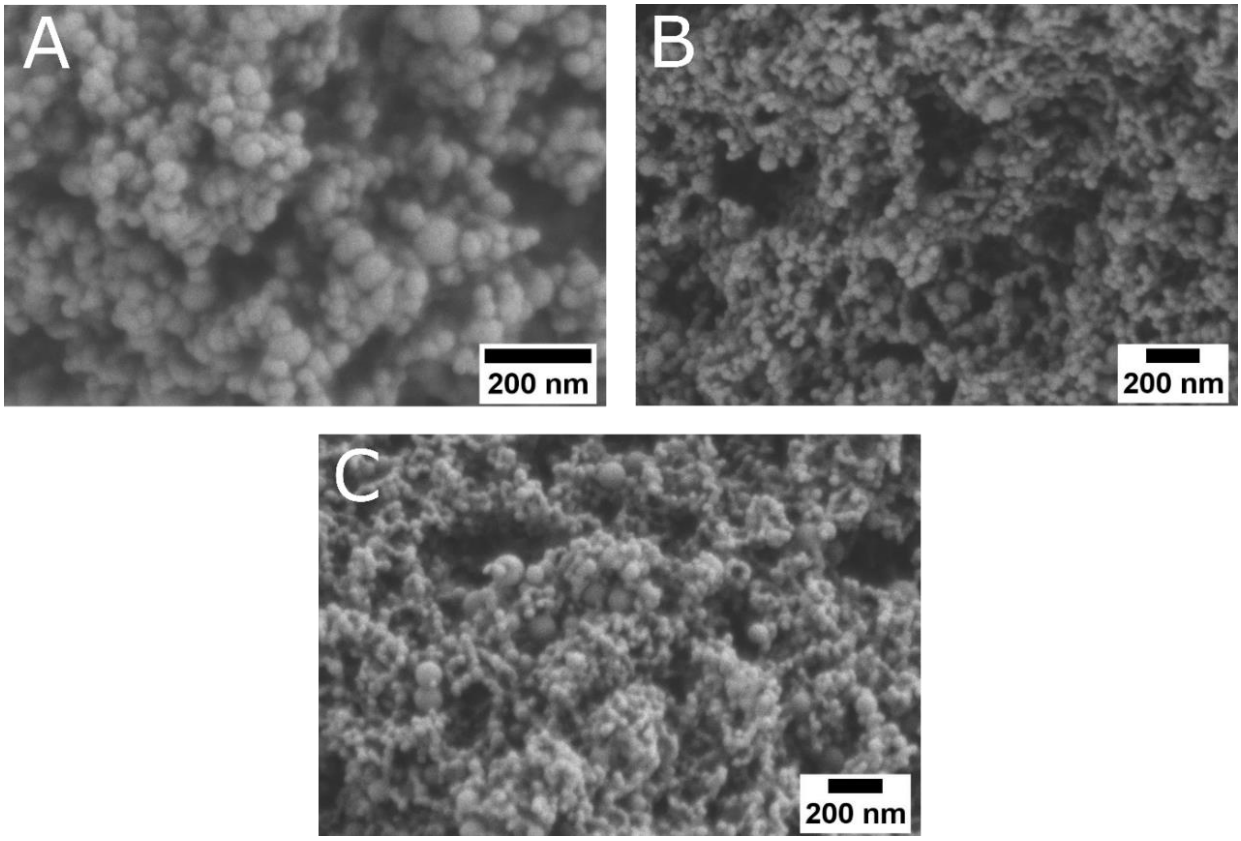

Supplementary Figure 3.7. Scanning electron micrographs for the **(A)** undoped, **(B)** Sr-doped, **(C)** and Ba-doped “MFC-L” samples.

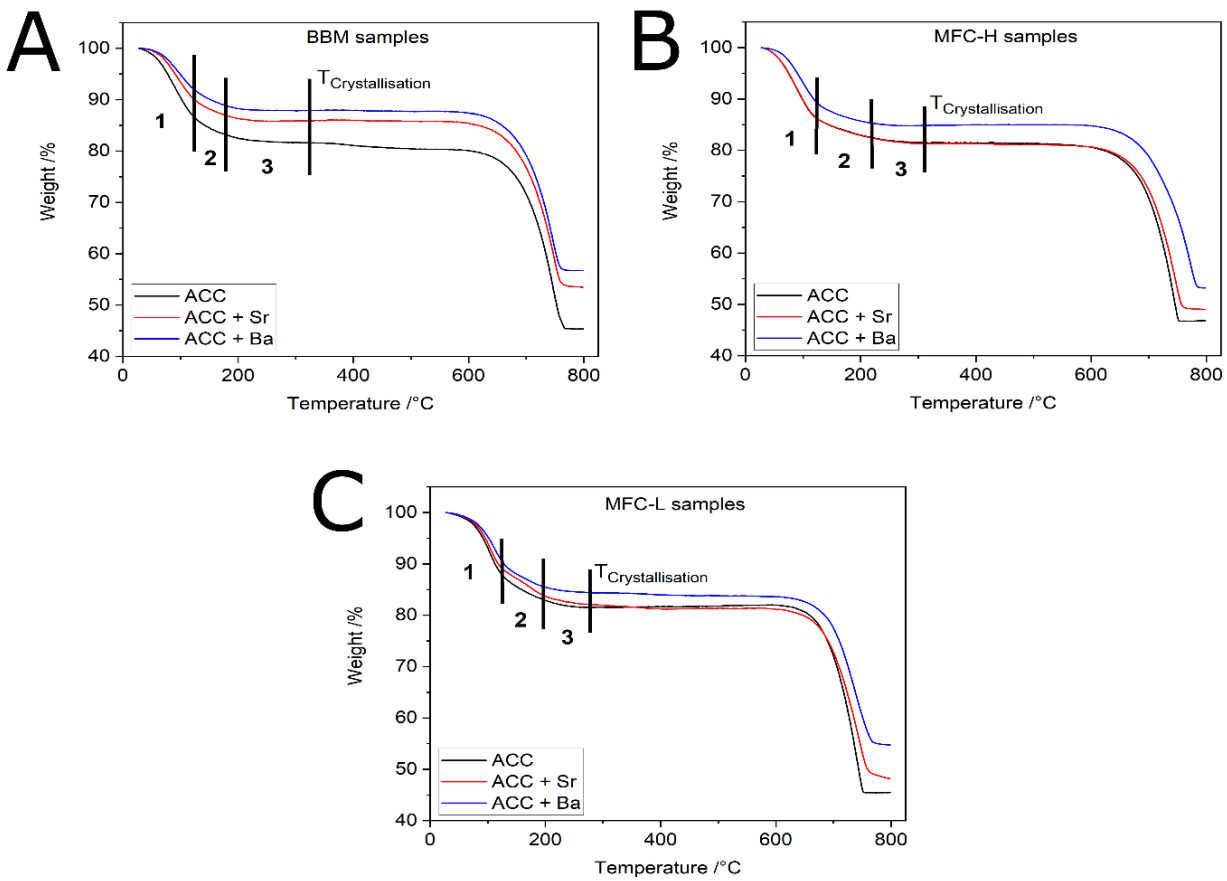

Supplementary Figure 3.8. TGA measurements for the **(A)** "BBM", **(B)** "MFC-H", and **(C)** "MFC-L" samples. Hydration was determined by dividing the water loss into three regimes similar to the "BM" samples (Figure 3.6).

Supplementary Table 3.3. Temperature boundaries of the three distinct mass loss regimes as defined by Schmidt *et al.*[58].

Temperature boundaries (°C)	Regime 1	Regime 2	Regime 3
BM	124	216	272
BBM	124	177	323
MFC-H	124	216	312
MFC-L	124	195	277

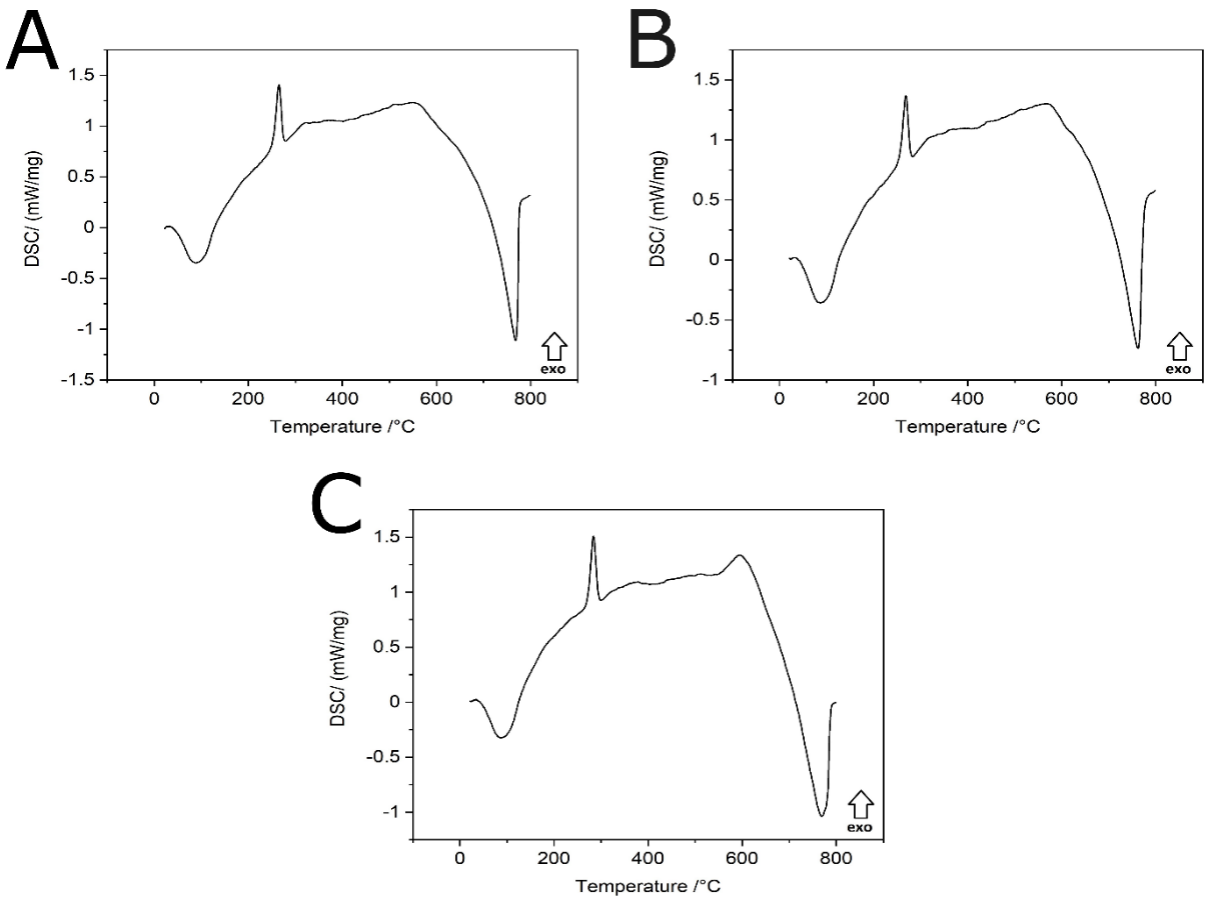

Supplementary Figure 3.9. DSC measurements for the “BM” samples. The “exo” arrows demonstrate the peak direction of an exothermic reaction.

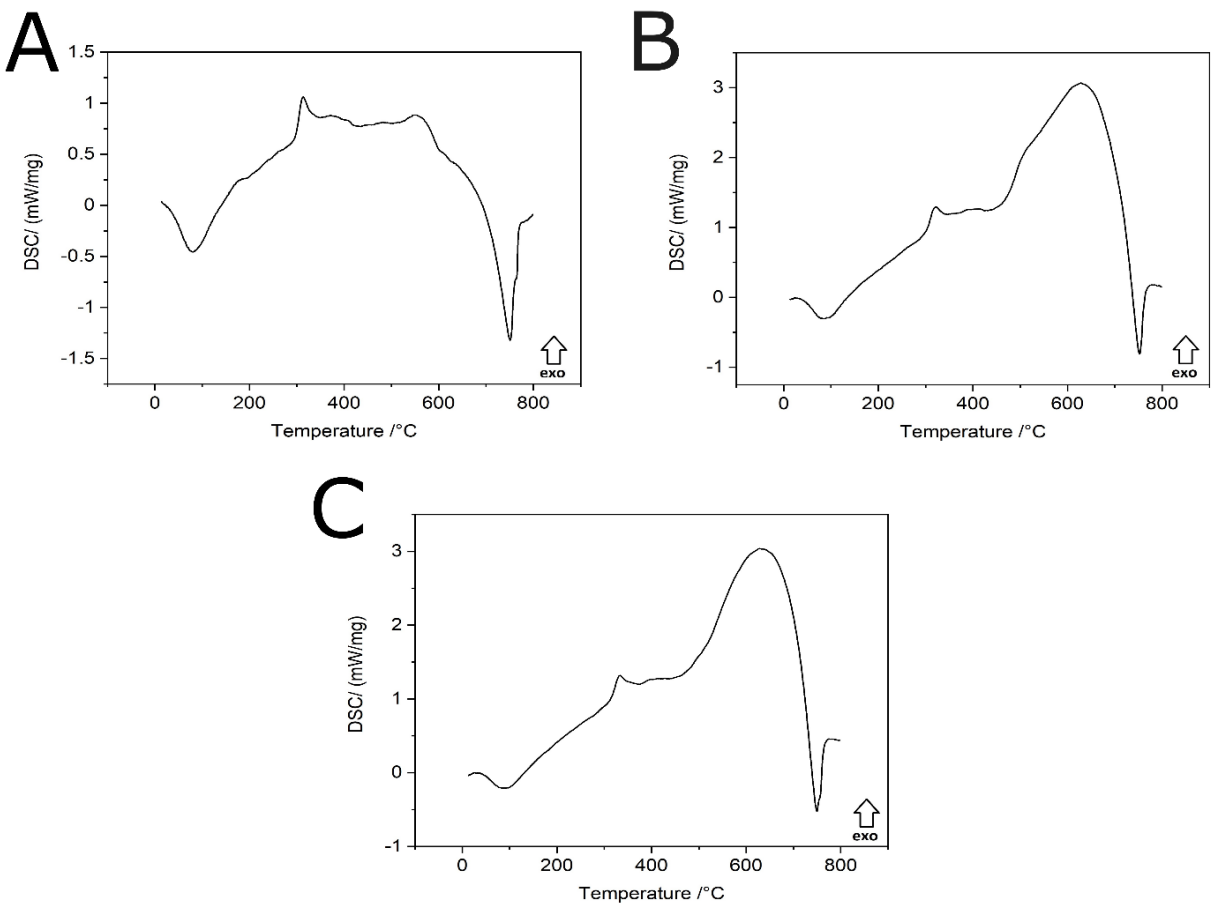

Supplementary Figure 3.10. DSC measurements for the “BBM” samples. The “exo” arrows demonstrate the peak direction of an exothermic reaction.

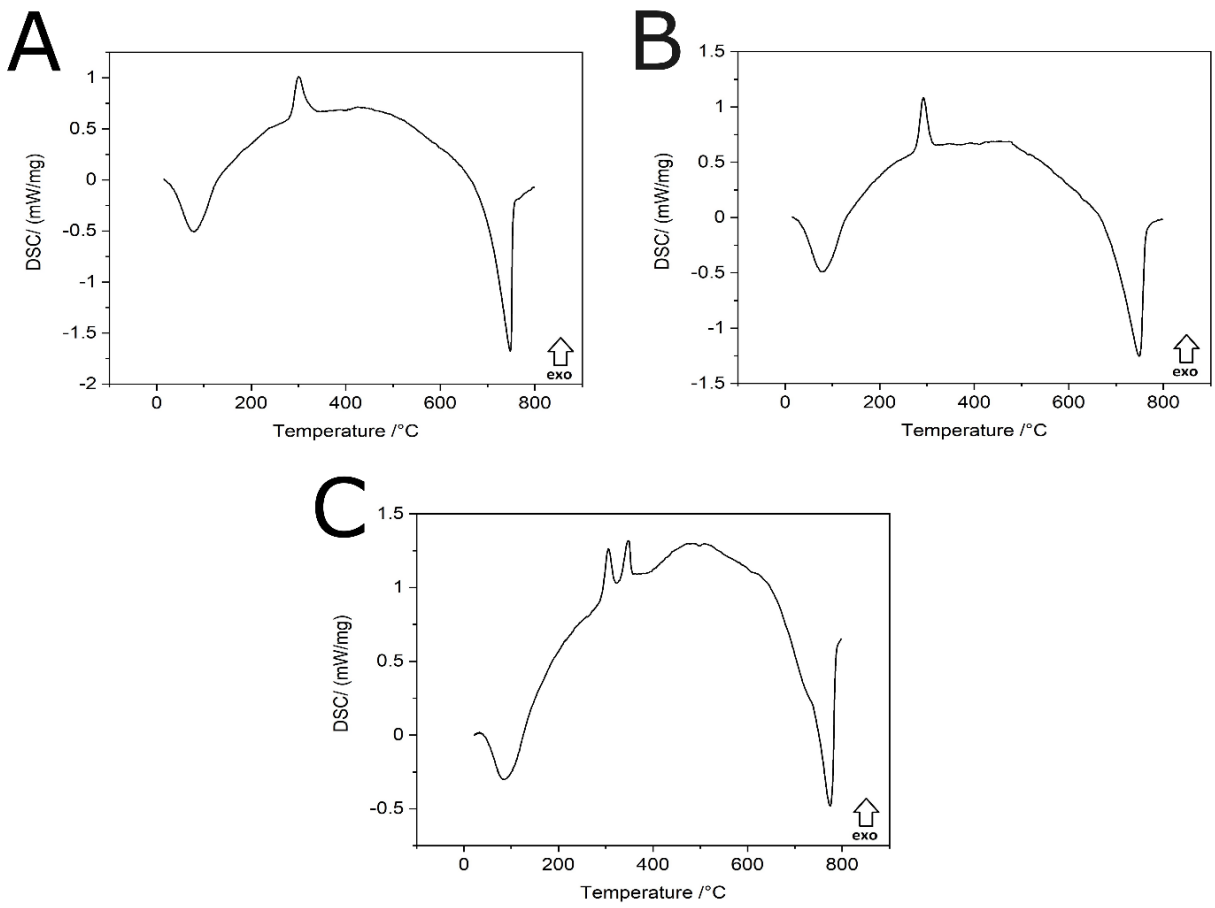

Supplementary Figure 3.11. DSC measurements for the “MFC-H” samples. The “exo” arrows demonstrate the peak direction of an exothermic reaction.

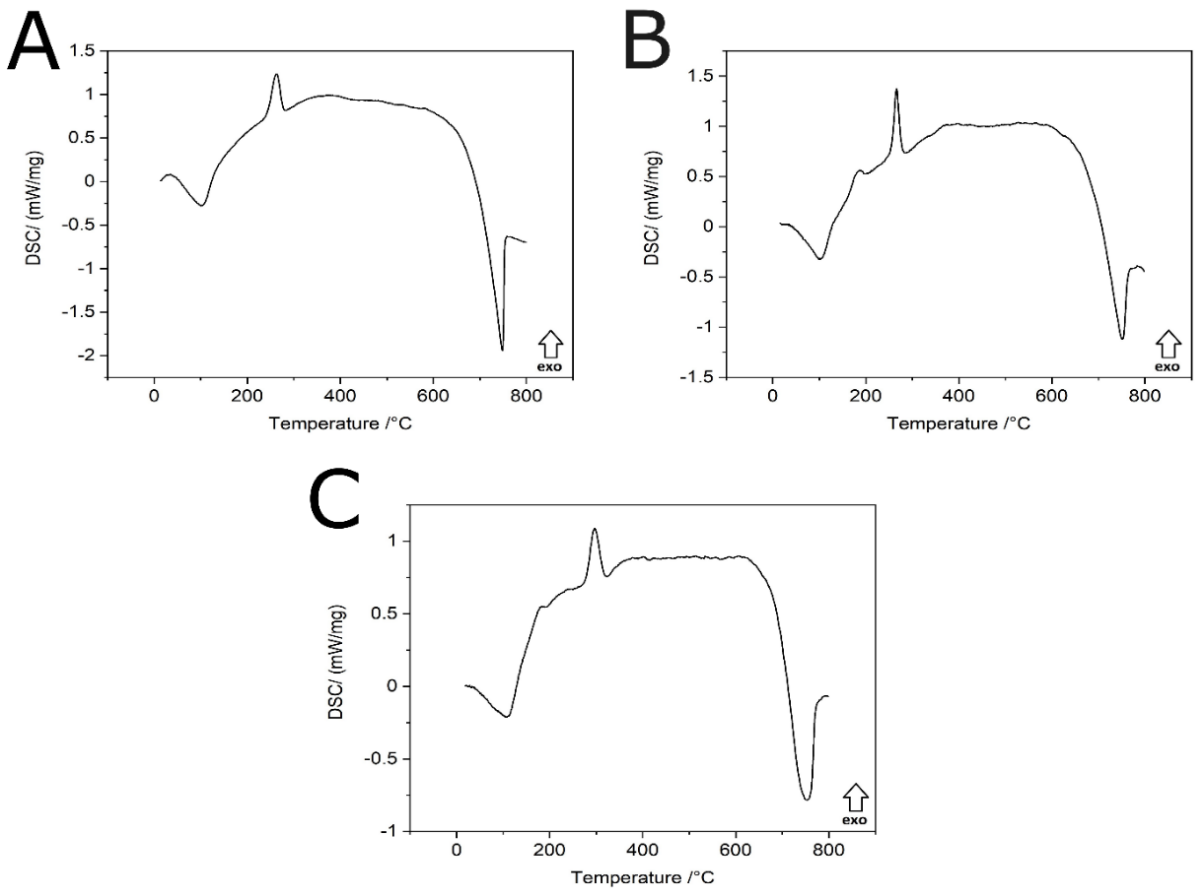

Supplementary Figure 3.12. DSC measurements for the “MFC-L” samples. The white “exo” arrows indicate the direction of an exothermic reaction.

4. Foreign element partitioning rates change in ACC at varying mixing conditions

Demmert, B.[1,2]; Schüßler, M.[1]; Schodder, P. I.[1]; Jacob, D. E.[2] and Wolf, S. E.[1,3]

[1]Department of Materials Science and Engineering, Institute of Glass and Ceramics (WW3), Friedrich-Alexander University Erlangen-Nürnberg, 90158 Erlangen, Germany.

[2]Department of Earth and Environmental Sciences, Macquarie University, NSW 2109, Australia.

[3]Interdisciplinary Center for Functional Particle Systems (FPS), Friedrich-Alexander University Erlangen-Nürnberg, 91058 Erlangen, Germany.

The author's contribution to the publication is as follows: BD designed the study, performed the experiments, conducted SEM, and ICP-OES measurements. BD supported XRD measurements. BD evaluated the data and drafted the manuscript.

Abstract

Despite knowledge that kinetics affect ACC formation, little research has been conducted so far on the kinetic influence on element partitioning into ACC. This is especially notable, as large research efforts are currently taken to investigate the mode and amount of tracer incorporation into ACC, *i.e.*, to determine trace element partitioning coefficients of ACC. In light of the results presented in the previous chapter, in which structural variants of ACC were generated only as a function of changing syntheses, this chapter aims to estimate whether partition coefficients are also affected by changes at fixed solution composition due to changes in kinetics, *i.e.*, mixing conditions. For this, different flow rates were applied to generate magnesium, strontium, and barium-doped ACC and their partition coefficients were determined and compared. These results show that for magnesium doped ACC, decreasing magnesium incorporation was determined by increasing flow rates. In contrast, Sr-doped ACC showed an increase of strontium incorporation by increasing flow rates. Most remarkably, the incorporation rate of Ba exhibited no sensitivity toward flow rate. With that, this chapter evidences for the first time that element partitioning is highly sensitive to changes of mixing conditions. Moreover, this sensitivity is element-specific, pointing at a complex processed under molecular control, implying the involvement of preformed solute species such as prenucleation clusters (PNC) in ACC formation.

4.1 Introduction

An influence of kinetic parameters such as precipitation rate and crystal growth on partition coefficients for calcite and aragonite is known from the literature[1–4]. To determine kinetic effects on element partitioning and isotope fractionation, different models were developed. While Watson *et al.*[5] established a growth entrapment model, DePaolo[6] put up a surface kinetic model. Despite the intensive research done on trace element doped ACC[7–12] and initial indications that element partitioning in ACC is affected by kinetic parameters[12–14], the influence of kinetics on ACC element partitioning was hitherto not analysed in detail, despite their likely implications for both geochemistry and biomineralisation.

In this chapter, the influence of mixing kinetics on particle size and partitioning of magnesium, strontium, and barium doped ACC was investigated. To explore this, different flow rates were applied during synthesis while keeping solution compositions constant. A Ball-Berger mixer system[15], which ensures rapid and near-instantaneous mixing, and a stopped-flow device with a laminar premixing phase, were used to cover flow rates of 5, 10, 15, 20, 25, and 200 mL/min.

4.2 Materials and methods

All solutions were prepared with ultrapure water (Milli-Q Direct 8 with UV photooxidation, Merck Millipore, Burlington, MA, USA, 18.2 MΩ cm^{-1}). The calcium carbonate syntheses were

conducted at ambient temperature. In order to enable six flow rates (5, 10, 15, 20, 25, and 200 mL/min), two different mixing devices were used. Flow rates from 5 to 25 mL/min were achieved by connecting a Ball-Berger mixer with standard tubes (tube size = 1.52 mm) to a peristaltic pump (MA1 70-7000R, Harvard Apparatus, Holliston, MA, USA)[15]. A flow rate of 200 mL/min was achieved using a stopped-flow device (SFM 3000, Bio-Logic Science Instruments, Seyssinet-Pariset, France) in which another Ball-Berger mixer was installed.

All chemical reagents were supplied by Sigma-Aldrich (St. Louis, MO, USA) and used without further purification (purity >99%).

Synthesis of doped ACC was achieved by mixing the calcium chloride powder with the additive powders, namely either strontium chloride, barium chloride, or magnesium chloride, to achieve the following dopant concentrations in the 40 mM calcium chloride solutions: 4 mM of strontium chloride, 4 mM of barium chloride, and 120 mM of magnesium chloride. Subsequently, the doped calcium chloride solution was mixed with a 40 mM sodium carbonate solution. While 20 mL of each solution were used for the Ball-Berger experiments, 6 mL were used when the stopped-flow device was used.

Independent of whether the peristaltic pump or the stopped flow device was used, all solutions were immediately filtered (nitrocellulose membranes, GVS North America), the residues were washed with ethanol and dried in a desiccator filled with silica-gel.

Phase analysis was done via X-ray diffraction (D8 Advance Eco, Bruker, Karlsruhe, Germany; Cu Kα radiation with λ= 1.5406 Å) by applying the following parameters: 2θ range between 20° - 70°, step size of 0.05° and dwell time of 0.2 seconds.

Particle morphologies were analysed by scanning electron microscopy (SEM, GeminiSEM 500, Carl Zeiss, Oberkochen, Germany) after sputtering the samples with gold. An accelerating voltage 1.0 kV was applied, the working distance was set to 6.5 mm. The average particle sizes were determined by using SEM images to graphically measure the diameter of hundred spherical particles each with the freely available software Fiji[16].

Element concentrations in the solids were measured by inductively coupled plasma optical emission spectroscopy (ICP-OES, Genesis FES, Spectro Analytical Instruments, Kleve, Germany) using external reference materials (Merck, Darmstadt, Germany). Each sample was measured in triplicate, each time using 30 mg of powder dissolved in nitric acid (1 M). Following the definition in Chapter 1.7, partition coefficients were calculated by dividing the trace element concentration to calcium concentration in the solid by the same ratio in the liquid.

4.3 Results and Discussion

4.3.1 Influence of the flow rate on particle size

X-ray diffraction showed in all syntheses the characteristic patterns of ACC (Supplementary Figure 4.1). Moreover, all samples exhibited a spherical morphology which is typical for ACC (Figure 4.1 and Supplementary Figure 4.2-4.4)[17]. Except for the samples synthesised at 5 mL/min, all samples analysed in this chapter had a particle size of around 30 nm (Table 4.1), neither the presence of a dopant nor the flow rate affected particle size. The average particle size of Sr-doped ACC (35 ± 9 nm) and Ba-doped ACC (37 ± 11 nm) are in accordance with those for the "BBM" samples observed in Chapter 3 (32 ± 7 nm and 33 ± 5 nm, respectively).

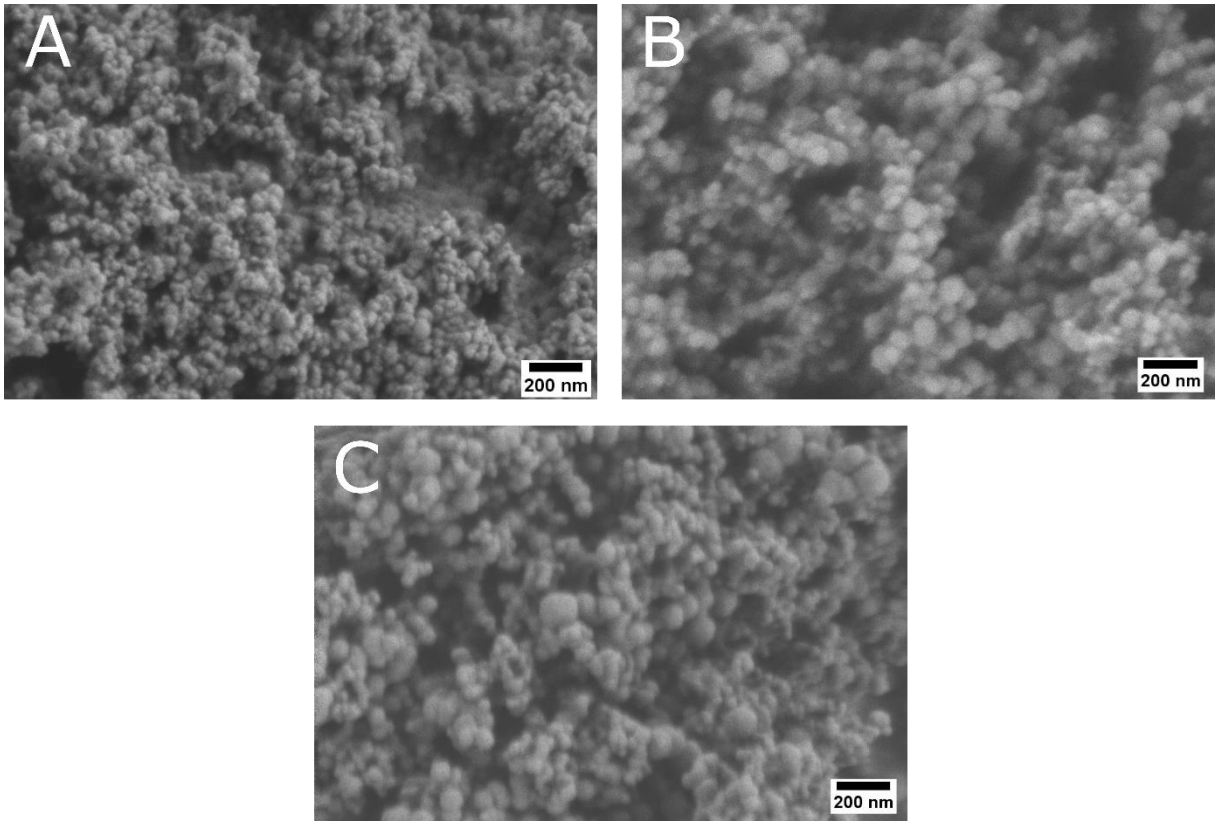

Figure 4.1. Scanning electron microscopy (SEM) micrographs of **(A)** magnesium, **(B)** strontium, and **(C)** barium doped ACC synthesised at 5 mL/min.

In experiments at a flow rate of 5 mL/min, Sr-doped ACC and Ba-doped ACC with particle sizes of 61 ± 13 nm and 60 ± 18 nm were formed (Table 4.1); thus longer reaction times before quenching yielded larger particles. This can be rationalised by a time-dependent growth of particles which ceases quickly by the addition of ethanol, an explanation which is in accordance with previous reports. For instance, Nudelman *et al*.[18] applied a flow-through system with a T-junction mixer to synthesise ACC. By controlling the length of the T-junction's exit tube, precise control of the reaction time was possible. In these experiments, a longer reaction time resulted in the development of larger ACC particles, similar to the results of the experiments that have been conducted here.

Only in the case of Mg-doped ACC, a different behaviour was observed at lower flow rates. Here, a particle size of 31 ± 6 nm was measured at 5 mL/min (Table 4.1). Thus a constant size irrespective of the synthesis procedure and flow rates was determined. It is debated that prenucleation clusters (PNCs) might play a role in calcium carbonate formation[19–22], potentially forming ACC via coalescence or aggregation[23]. Zhang *et al.*[24] stated that Mg ions might stabilise PNCs and thus may enforce ACC formation via alternative pathways. In the presence of Mg, they assumed that ACC formed via nucleation of PNCs. In the absence of Mg ions, Zhang *et al.* suggested that ACC was directly formed by calcium and carbonate ions as no PNCs were present. This speculative model might provide a coherent explanation for the observed element-specific change in particle sizes, however, direct experimental evidence for this model is hard to provide and beyond the scope of this study. Based on the fact that the presence of Mg in these simple precipitation setups triggered a marked change in particle sizes, it is reasonable to assume that this slight change in the molecular composition of the reaction solutions already alters the system markedly. This implies a complex formation behaviour under molecular control, pointing at prenucleation clusters as potential agents of ACC formation.

Table 4.1. Influence of the flow rate on the average particle sizes including standard deviations (n=100).

Particle size (nm)	ACC + Mg	ACC + Sr	ACC + Ba
5 mL/min	31 ± 6	61 ± 13	60 ± 18
10 mL/min	27 ± 5	38 ± 7	35 ± 9
15 mL/min	25 ± 4	31 ± 6	34 ± 6
20 mL/min	23 ± 5	24 ± 3	28 ± 5
25 mL/min	25 ± 4	25 ± 4	36 ± 6
200 mL/min	33 ± 5	30 ± 5	27 ± 4

4.3.2 Impact of the flow rate on partition coefficients

ICP-OES measurements of the elemental composition of the formed ACC were conducted to study the influence of the flow rate on element partitioning (Figure 4.2 and Table 4.2). In agreement with the literature, which reported partition coefficients between 0.05 and 0.18[12], a mean magnesium partition coefficient of 0.09 ± 0.01 was determined here. For Sr-doped ACC, an average partition coefficient of 0.87 ± 0.04 was determined, whereas Ba-doped ACC showed a value of 1.1 ± 0.04. Comparable partition coefficients for strontium and barium were reported in the literature (0.6 to 1 and 1.2 to 1.4, respectively)[10,25]. It is noteworthy that partition coefficients for strontium (Sr-doped "BBM" samples: 0.91 ± 0.04) and barium (Ba-doped "BBM" samples: 1.11 ± 0.01) determined in Chapter 3 and this chapter are well comparable. This evidences that partition coefficients of strontium and barium are not affected by minor changes in the dopant concentration in the parent fluid.

A decrease of the Mg partition coefficients was detected with increasing flow rates. It dropped from 0.1 ± 0.002 at 5 mL/min to 0.074 ± 0.001 at 200 mL/min. Compared to the 20 mL/min samples, the 25 mL/min samples exhibited an increased Mg incorporation (0.102 ± 0.006), however, the enhanced standard deviation indicated experimental scattering. The decrease of partition coefficients with increasing flow rates points at a complex molecular "reorganization" step as a function of reaction time. A possible explanation might be that PNC formation is a fast process but that the incorporation of Mg in these dynamic clusters is a slow process which is not completed before the system is quenched in the case of extremely high flow rates. Future work addressing this phenomenon will have to employ ultra-high time resolution experiments in combination with suitable molecular simulation, a project which is envisaged but clearly beyond the scope of this thesis.

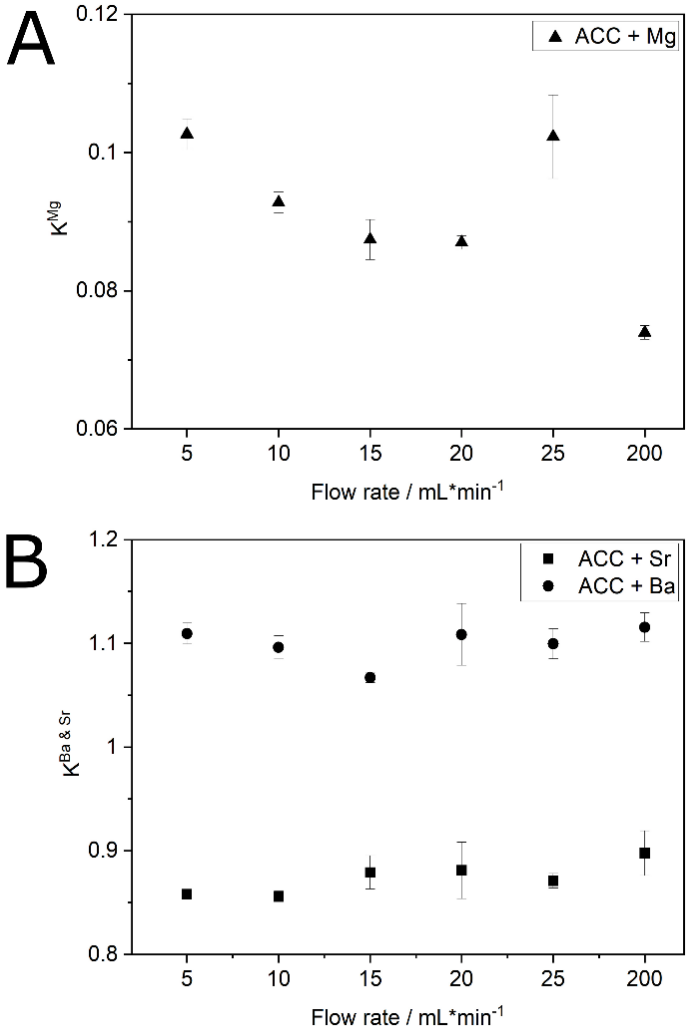

Figure 4.2. Influence of the flow rate on the partition coefficients of **(A)** magnesium, and **(B)** strontium and barium doped ACC synthesised at ambient temperatures.

Despite the common application of magnesium as an ACC additive[7–9,11,26], little is known about why magnesium is incorporated so sparsely in ACC. Zhang *et al.*[24] assumed that Mg-doped PNCs, whose existence was suggested in the literature[24,27], were stabilised due to the high hydration of magnesium, therefore preventing PNC agglomeration, *i.e.,* ACC formation. They further hypothesized that ACC could form via two pathways: either by dehydration and incorporation of the Mg ions, which takes longer due to the slow dehydration kinetics[28–30], or by expelling the Mg ions during ACC formation, yielding low Mg incorporation. In principle, this scenario would agree with the rationale that a relatively slow reorganisation process on the molecular level takes place, as indicated by the flow rate dependency of the Mg-incorporation. The results in this chapter suggest that lower flow rates allow for magnesium uptake in PNCs. At higher flow rates, this "incorporation pathway" was kinetically suppressed as it is a slow process. This favours an "expulsion pathway", in which Mg is not incorporated into ACC but remains in the parental solution. Accordingly, the results presented here suggest an

involvement of molecular processes in which complex species such as PNCs play an important role governing dopant incorporation into ACC.

In an extensive review, Du and Amstad[30] suggested that the slow dehydration kinetics of magnesium prevented the incorporation into PNCs and subsequently into ACC. In accordance with the literature[31] and the results here, they assumed increasing incorporation rates from magnesium to strontium to barium due to the incorporation kinetics. As an influence of the hydration on the Mg incorporation into PNCs was already assumed by Zhang *et al.*[24], and an increasing dopant incorporation with decreasing hydration energies (Mg>Sr>Ba)[32] was shown in the literature[31] and here, it seems that hydration energies play an important role and affect dopant incorporation into PNCs and/or ACC.

Table 4.2. Influence of the flow rate on the partition coefficients of doped ACC including standard deviations (n=3).

Partition coefficients	ACC + Mg	ACC + Sr	ACC + Ba
5 mL/min	0.1 ± 0.002	0.86 ± 0.003	1.11 ± 0.01
10 mL/min	0.093 ± 0.001	0.86 ± 0.005	1.1 ± 0.011
15 mL/min	0.087 ± 0.001	0.88 ± 0.016	1.07 ± 0.005
20 mL/min	0.087 ± 0.001	0.88 ± 0.027	1.11 ± 0.03
25 mL/min	0.102 ± 0.006	0.87 ± 0.007	1.1 ± 0.014
200 mL/min	0.074 ± 0.001	0.9 ± 0.021	1.13 ± 0.014

Strontium was better incorporated at increasing flow rates (0.86 ± 0.003 to 0.9 ± 0.021), which is indicative of an inverse selection process as in case of Mg. Strontium has a comparable hydration energy to calcium[32,33], one may assume that strontium is initially part of PNCs. Experiments at fast flow rates would intercept this initial stage and thus yield higher incorporation rates compared to magnesium. The question which now arises why strontium is less incorporated at lower flow rates. The major difference of strontium to calcium is its atomic radius, which also dictates its coordination chemistry. A recent molecular dynamics simulation by Zahn and Löffler[34] showed that carbonate binds to strontium ions mainly in a bidentate fashion, thus two oxygens of the carbonate ion are bound to the metal atom. Thus, κ2-carbonato strontium complexes form. Given that carbonate is bidentate at maximum, $[SrCO_3]^0$ elements would act as a “network modifier” in DOLLOP networks and thus always be located at the end of a chain. At longer reaction times, it might be reasonable to assume that such exposed positions in a DOLLOP undergo exchange reactions, especially when they hinder further growth of the PNC.

Contrary to magnesium and strontium, no flow rate influence was detected for the barium incorporation into ACC. Barium is an even larger alkaline earth metal, which may allow for a higher coordination number, as often observed in coordination chemistry, and thus barium experiences no expulsion like strontium.

4.4 Conclusion

With the exception of Mg-doped ACC, an influence of the flow rate on particle sizes of doped ACC was revealed in this chapter. In the literature, it was generally demonstrated that increasing the reaction time yielded larger ACC particles which is in accordance with the results[18].

Contrary to Ba-doped ACC, the chemical compositions of Mg- and Sr-doped ACC were affected by flow rate variations. With increasing flow rates, less magnesium was incorporated into ACC. An inverse case was observed for strontium. This deviating behaviour can be rationalised when taking the coordination chemistry and preferred coordination ligands of the respective elements into account. Mg features a high hydration energy, favouring water as a binding partner, whereas strontium and barium likely prefer carbonates. Strontium, being larger than calcium, forces the carbonate ion into a bidentate binding mode which renders strontium into a DOLLOP network modifier, which may account for the observation that only at higher flow rates, higher strontium incorporation rates are determined. Barium, an even larger ion, may act as a better cross-linker in DOLLOPs, so that it suffers no expulsion from DOLLOPs. Some of these arguments found their initial support by molecular dynamics simulations but further and time-consuming simulations and experiments are being undertaken. Notwithstanding, this chapter provides evidence that PNC are “gate-keepers” in ACC formation and control the dopant incorporation into ACC.

The central finding that the incorporation rates of foreign elements in ACC are also highly dependent on flow rates and, thus, on mixing conditions is an important finding as it highlights that ACC formation is a kinetically controlled process, in which unforeseen partitioning processes at different time scales take place. It shows that the vast literature on this topic has to be considered carefully when exploring the structure and composition of ACC[35–41].

4.5 References

1. Lorens, R. B. Sr, Cd, Mn and Co distribution coefficients in calcite as a function of calcite precipitation rate. *Geochim. Cosmochim. Acta* **45**, 553–561 (1981).

2. Tesoriero, A. J. & Pankow, J. F. Solid solution partitioning of Sr^{2+}, Ba^{2+}, and Cd^{2+} to calcite. *Geochim. Cosmochim. Acta* **60**, 1053–1063 (1996).

3. Gabitov, R. I. & Watson, E. B. Partitioning of strontium between calcite and fluid. *Geochemistry, Geophys. Geosystems* **7**, (2006).

4. Gabitov, R. I., Gaetani, G. A., Watson, E. B., Cohen, A. L. & Ehrlich, H. L. Experimental determination of growth rate effect on U^{6+} and Mg^{2+} partitioning between aragonite and fluid at elevated U^{6+} concentration. *Geochim. Cosmochim. Acta* **72**, 4058–4068 (2008).

5. Watson, E. B. A conceptual model for near-surface kinetic controls on the trace-element and stable isotope composition of abiogenic calcite crystals. *Geochim. Cosmochim. Acta* **68**, 1473–1488 (2004).

6. DePaolo, D. J. Surface kinetic model for isotopic and trace element fractionation during precipitation of calcite from aqueous solutions. *Geochim. Cosmochim. Acta* **75**, 1039–1056 (2011).

7. Myszka, B. *et al.* Phase-specific bioactivity and altered Ostwald ripening pathways of calcium carbonate polymorphs in simulated body fluid. *RSC Adv.* **9**, 18232–18244 (2019).

8. Demmert, B. *et al.* Polymer-Functionalised Nanograins of Mg-Doped Amorphous Calcium Carbonate via a Flow-Chemistry Approach. *Materials.* **12**, 1818 (2019).

9. Purgstaller, B., Mavromatis, V., Immenhauser, A. & Dietzel, M. Transformation of Mg-bearing amorphous calcium carbonate to Mg-calcite - In situ monitoring. *Geochim. Cosmochim. Acta* **174**, 180–195 (2016).

10. Littlewood, J. L. *et al.* Mechanism of enhanced strontium uptake into calcite via an amorphous calcium carbonate (ACC) crystallisation pathway. *Cryst. Growth Des.* **17**, 1214–1223 (2017).

11. Loste, E., Wilson, R. M., Seshadri, R. & Meldrum, F. C. The role of magnesium in stabilising amorphous calcium carbonate and controlling calcite morphologies. *J. Cryst. Growth* **254**, 206–218 (2003).

12. Blue, C. R. & Dove, P. M. Chemical controls on the magnesium content of amorphous calcium carbonate. *Geochim. Cosmochim. Acta* **148**, 23–33 (2015).

13. Blue, C. R., Rimstidt, J. D. & Dove, P. M. A mixed flow reactor method to synthesize

amorphous calcium carbonate under controlled chemical conditions. *Methods in Enzymology* **532**, (2013).

14. Jensen, A. C. S., Birkedal, H. & Bertinetti, L. Co-incorporation of alkali metal ions during amorphous calcium carbonate precipitation and their stabilizing effect. *Phys. Chem. Chem. Phys.* **21**, 13230–13233 (2019).

15. Berger, R. L., Balko, B. & Chapman, H. F. High resolution mixer for the study of the kinetics of rapid reactions in solution. *Rev. Sci. Instrum.* **39**, 493–498 (1968).

16. Schindelin, J. *et al.* Fiji: An open-source platform for biological-image analysis. *Nat. Methods* **9**, 676–682 (2012).

17. Pai, R. K. & Pillai, S. Nanoparticles of amorphous calcium carbonate by miniemulsion: Synthesis and mechanism. *CrystEngComm* **10**, 865–872 (2008).

18. Nudelman, F., Sonmezler, E., Bomans, P. H. H., De With, G. & Sommerdijk, N. A. J. M. Stabilization of amorphous calcium carbonate by controlling its particle size. *Nanoscale* **2**, 2436–2439 (2010).

19. Demichelis, R., Raiteri, P., Gale, J. D., Quigley, D. & Gebauer, D. Stable prenucleation mineral clusters are liquid-like ionic polymers. *Nat. Commun.* **2**, (2011).

20. Gebauer, D., Kellermeier, M., Gale, J. D., Bergström, L. & Cölfen, H. Pre-nucleation clusters as solute precursors in crystallisation. *Chem. Soc. Rev.* **43**, 2348–2371 (2014).

21. Pouget, E. M. *et al.* The Initial Stages of Template-Controlled $CaCO_3$ Formation Revealed by Cryo-TEM. *Science.* **323**, 1455–1458 (2009).

22. Gebauer, D., Völkel, A. & Cölfen, H. Stable Prenucleation Calcium Carbonate Clusters. *Science.* **322**, 1819–1822 (2008).

23. Gebauer, D. & Wolf, S. E. Designing Solid Materials from Their Solute State: A Shift in Paradigms towards a Holistic Approach in Functional Materials Chemistry. *J. Am. Chem. Soc.* **141**, 4490−4504 (2019).

24. Zhang, J., Zhou, X., Dong, C., Sun, Y. & Yu, J. Investigation of Amorphous Calcium Carbonate's Formation under High Concentration of Magnesium: the prenucleation cluster pathway. *J. Cryst. Growth* **494**, 8–16 (2018).

25. Cam, N., Georgelin, T., Jaber, M., Lambert, J. F. & Benzerara, K. In vitro synthesis of amorphous Mg-, Ca-, Sr- and Ba-carbonates: What do we learn about intracellular calcification by cyanobacteria? *Geochim. Cosmochim. Acta* **161**, 36–49 (2015).

26. Rodriguez-Blanco, J. D., Shaw, S., Bots, P., Roncal-Herrero, T. & Benning, L. G. The role of pH and Mg on the stability and crystallization of amorphous calcium carbonate.

J. Alloys Compd. **536S**, S477– S479 (2012).

27. Verch, A., Antonietti, M. & Cölfen, H. Mixed calcium-magnesium pre-nucleation clusters enrich calcium. *Zeitschrift fur Krist.* **227**, 718–722 (2012).

28. Radha, A. V. *et al.* Energetic and structural studies of amorphous $Ca_{1-x}Mg_xCO_3 \cdot nH_2O$ ($0 \leqslant x \leqslant 1$). *Geochim. Cosmochim. Acta* **90**, 83–95 (2012).

29. Tommaso, D. Di & De Leeuw, N. H. Structure and dynamics of the hydrated magnesium ion and of the solvated magnesium carbonates: Insights from first principles simulations. *Phys. Chem. Chem. Phys.* **12**, 894–901 (2010).

30. Du, H. & Amstad, E. Water: How Does It Influence the $CaCO_3$ Formation? *Angew. Chemie - Int. Ed.* **59**, 1798–1816 (2020).

31. Zou, Z. *et al.* Additives influence the phase behavior of calcium carbonate solution by a cooperative ion-association process. *J. Mater. Chem. B* **6**, 449–457 (2018).

32. Rodriguez-Cruz, S. E., Jockusch, R. A. & Williams, E. R. Hydration Energies and Structures of Alkaline Earth Metal Ions, $M^{2+}(H_2O)_n$, n = 5–7, M = Mg, Ca, Sr, and Ba. *J. Am. Chem. Soc.* **121**, 8898–8906 (1999).

33. Marcus, Y. A simple empirical model describing the thermodynamics of hydration of ions of widely varying charges, sizes, and shapes. *Biophys. Chem.* **51**, 111–127 (1994).

34. Zahn, D. & Löffler, F. Personal communication.

35. Addadi, L., Raz, S. & Weiner, S. Taking advantage of disorder: Amorphous calcium carbonate and its roles in biomineralization. *Adv. Mater.* **15**, 959–970 (2003).

36. Weiner, S., Mahamid, J., Politi, Y., Ma, Y. & Addadi, L. Overview of the amorphous precursor phase strategy in biomineralization. *Front. Mater. Sci. China* **3**, 104–108 (2009).

37. Politi, Y. *et al.* Transformation mechanism of amorphous calcium carbonate into calcite in the sea urchin larval spicule. *Proc. Natl. Acad. Sci. U. S. A.* **105**, 17362–17366 (2008).

38. Cartwright, J. H. E., Checa, A. G., Gale, J. D., Gebauer, D. & Sainz-Diaz, C. I. Calcium Carbonate Polyamorphism and Its Role in Biomineralization: How Many Amorphous Calcium Carbonates Are There? *Angew. Chem. Int. Ed* **51**, 11960–11970 (2012).

39. Gebauer, D., Jansson, K., Oliveberg, M. & Hedin, N. Indications that Amorphous Calcium Carbonates Occur in Pathological Mineralisation—A Urinary Stone from a Guinea Pig. *Minerals* **8**, 84 (2018).

40. Mass, T. *et al.* Amorphous calcium carbonate particles form coral skeletons. *Proc. Natl. Acad. Sci. U. S. A.* **114**, E7670–E7678 (2017).

41. Jacob, D. E., Wirth, R., Soldati, A. L., Wehrmeister, U. & Schreiber, A. Amorphous calcium carbonate in the shells of adult *Unionoida*. *J. Struct. Biol.* **173**, 241–249 (2011).

4.6 Supplementary

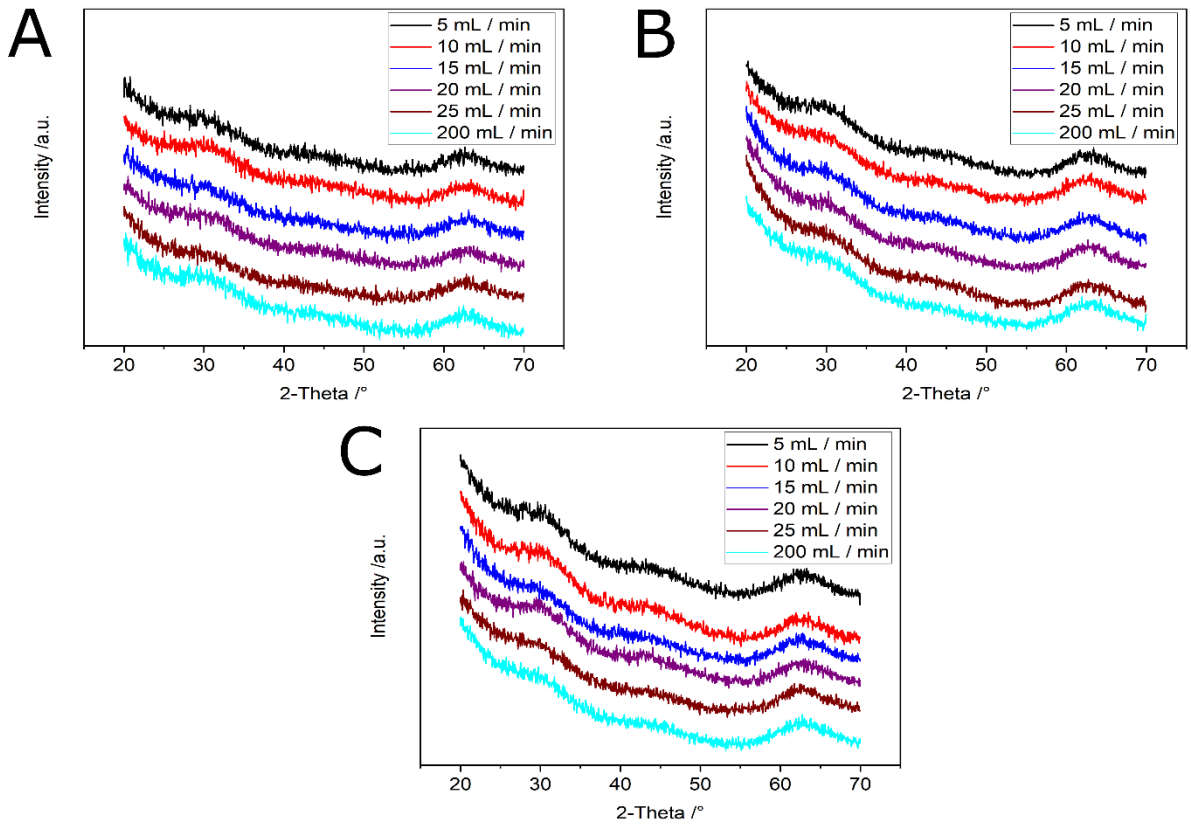

Supplementary Figure 4.1. XRD patterns for the **(A)** Mg-doped, **(B)** Sr-doped, and **(C)** Ba-doped calcium carbonate samples.

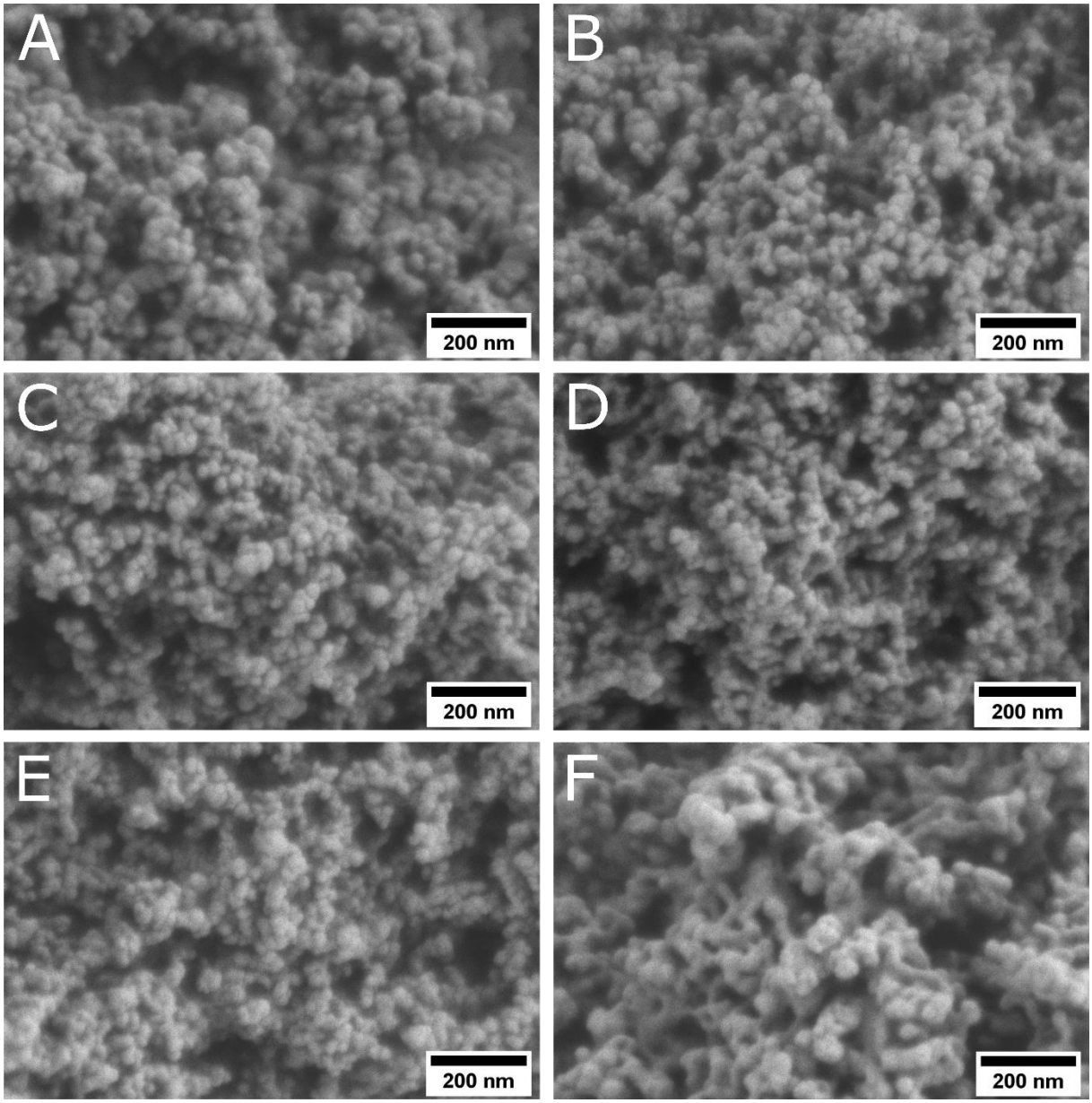

Supplementary Figure 4.2. Scanning electron micrographs of the Mg-doped ACC samples synthesised at various flow rates, namely **(A)** 5 mL/min, **(B)** 10 mL/min, **(C)** 15 mL/min, **(D)** 20 mL/min, **(E)** 25 mL/min, and **(F)** 200 mL/min.

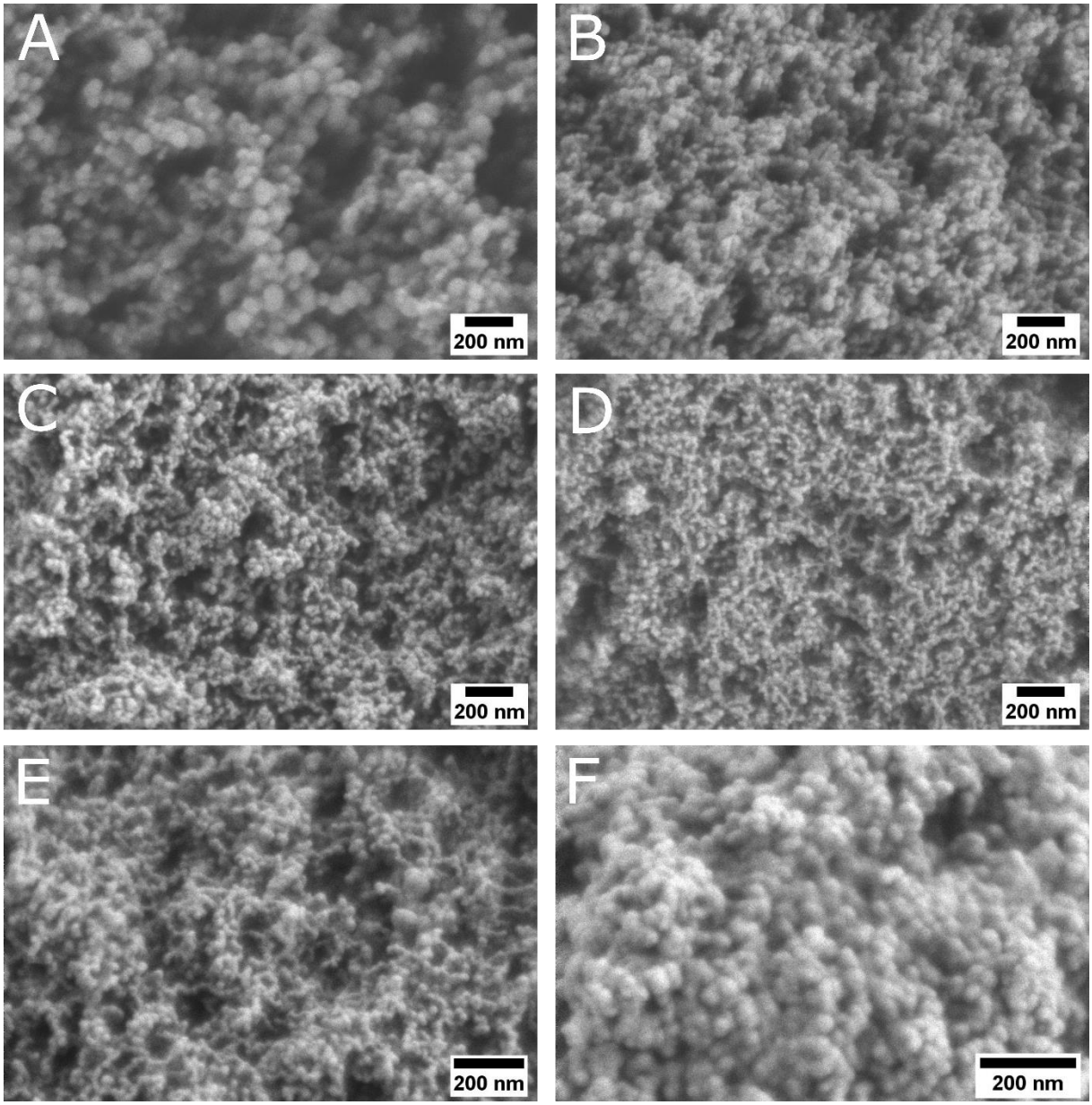

Supplementary Figure 4.3. Scanning electron micrographs of the Sr-doped ACC samples synthesised at various flow rates, namely **(A)** 5 mL/min, **(B)** 10 mL/min, **(C)** 15 mL/min, **(D)** 20 mL/min, **(E)** 25 mL/min, and **(F)** 200 mL/min.

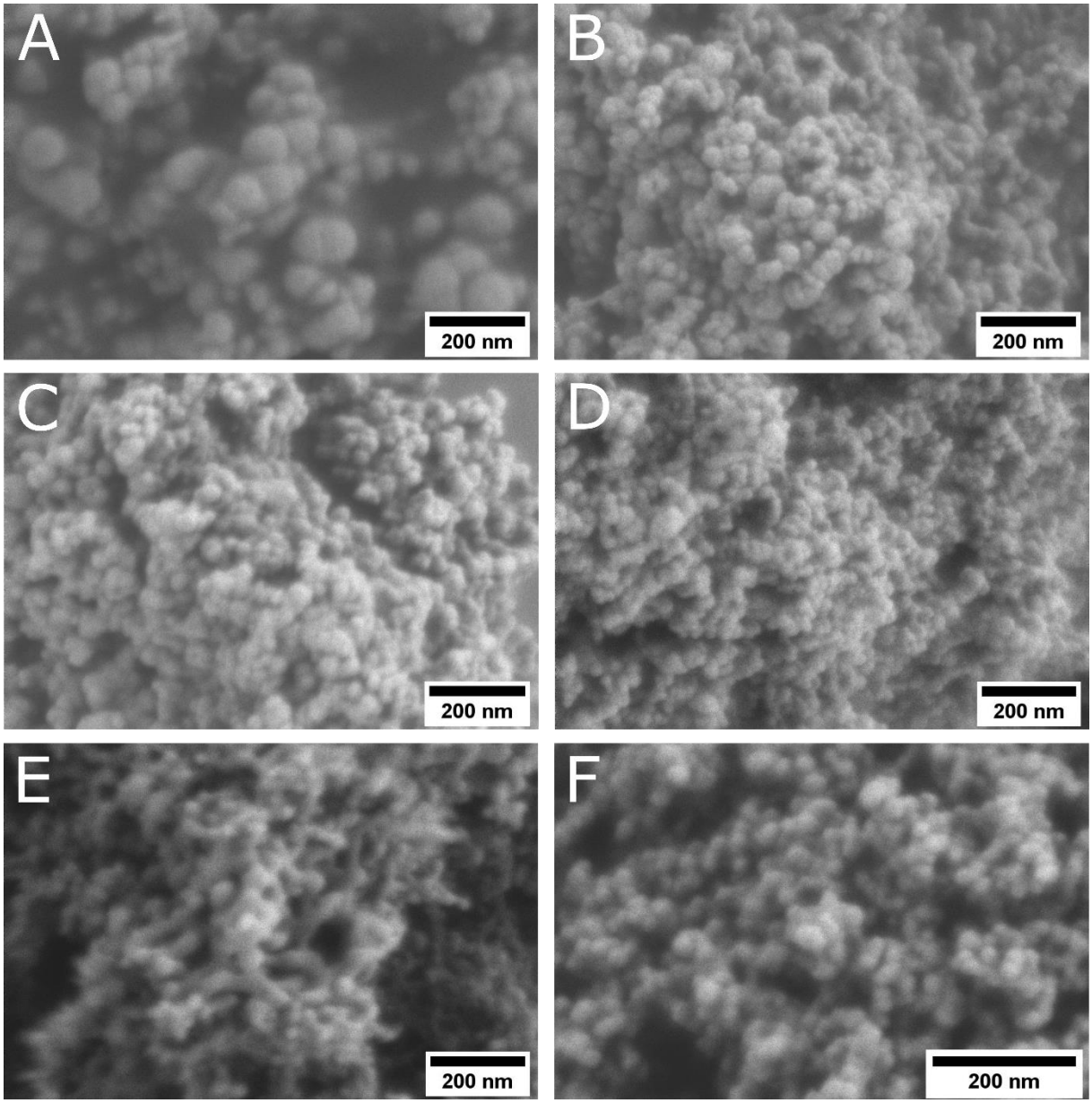

Supplementary Figure 4.4. Scanning electron micrographs of the Ba-doped ACC samples synthesised at various flow rates, namely **(A)** 5 mL/min, **(B)** 10 mL/min, **(C)** 15 mL/min, **(D)** 20 mL/min, **(E)** 25 mL/min, and **(F)** 200 mL/min.

5. MULTIPLE DOPING OF ACC IN ARTIFICIAL SEAWATER UNDER VARYING SYNTHESIS CONDITIONS

Demmert, B.[1,2]; Schodder, P. I.[1]; Schüßler, M.[1]; Jacob, D. E.[2] and Wolf, S. E.[1,3]

[1]Department of Materials Science and Engineering, Institute of Glass and Ceramics (WW3), Friedrich-Alexander University Erlangen-Nürnberg, 90158 Erlangen, Germany.

[2]Department of Earth and Environmental Sciences, Macquarie University, NSW 2109, Australia.

[3]Interdisciplinary Center for Functional Particle Systems (FPS), Friedrich-Alexander University Erlangen-Nürnberg, 91058 Erlangen, Germany.

The author's contribution to the publication is as follows: BD designed the study, performed the experiments, conducted ATR-FTIR, SEM, TGA/DSC, and ICP-OES measurements. BD supported XRD measurements. BD evaluated the data and drafted the manuscript.

Abstract

The crystallochemical properties of calcitic and aragonitic biominerals are commonly utilised to extract past seawater composition and temperature data resulting in a better understanding of the paleoclimatic and paleo-environmental conditions. However, the presence of an amorphous precursors phase, which is widely found in biominerals and in speleothems, affect these crystallochemical properties and therefore impact the accuracy of our reconstructions. To study this influence, natural biominerals as well as synthetic ACC are investigated. However, in most studies in which synthetic ACC is analysed the uptake of only a few ions of interest is studied which results in conditions that are not easily comparable to the natural ACC formation in a seawater. In this chapter, ACC is synthesised in artificial seawater, and synthesis conditions such as flow rate, temperature, and pH are systematically varied.

ACC precipitation in artificial seawater led to simultaneous doping with a large number of trace elements. It was observed that not only material properties, such as the particle size, were affected by the choice of synthesis conditions, but also the chemical composition of the resulting ACC. Changing the flow rate and temperature affected particularly the magnesium and sulphur concentration in the precipitated ACC. While increasing flow rates resulted in a decrease in magnesium incorporation, an increased sulphur incorporation was detected. Enhancing the temperatures yielded in better incorporation of both trace elements. Furthermore, the concentrations of all trace elements in ACC increased with increasing pH.

5.1 Introduction

Calcium carbonate is abundant as it forms the hard tissues of calcifying marine organisms. Some skeletal hard parts, such as corals, grow incrementally over hundreds of years and incorporate information on environmental conditions, such as sea surface temperature, salinity or pH as they grow. The information archived in their chemical composition is quantified based on the known equilibrium partitioning behaviour of specific chemical trace elements, termed proxies[1–7]. However, the situation is complicated by the recent findings that many bio-carbonates form via nonclassical crystallisation[8–10], *i.e.*, by a particle-mediated growth and deposition of ACC and its stepwise transformation to crystalline calcium carbonate[11–14]. Instead, quantitative environmental reconstructions up to now assume direct precipitation of calcite or aragonite from seawater, which is no longer appropriate. In addition, partitioning data for ACC that is required to develop new theoretical models for the accurate quantitative reconstructions of environmental conditions is still scare. Hence, understanding the uptake and partitioning for elements throughout this stepwise crystallisation pathway advances our understanding on how crystallisation pathways influence the incorporation of chemical proxies that are used to reconstruct the paleoclimate.

Therefore, two different approaches are usually applied in the literature: Firstly, the effect of ACC as a metastable precursor on trace element incorporation and isotope fractionation is investigated by analysis of biominerals and speleothems[15–18]. Secondly, synthetic ACC is examined directly, as this approach allows a systemic analysis of how environmental conditions, *e.g.,* initial solution composition, temperature, and pH, affect the ion incorporation and isotope fractionation in ACC[19–21].

Regarding the latter approach, it is noteworthy that these studies are mostly carried out with the essential ions dissolved in purified water[19,22–24], thus under conditions that are not easily comparable with natural ACC formation in a seawater environment[25]. To address this issue, ACC was synthesised in artificial seawater under varying conditions in this chapter. As the thesis deals exclusively with the synthetic perspective, the major part of the relevant literature is situated in this space[26].

5.2 Materials and methods

All chemicals used here were supplied by Sigma-Aldrich (St. Louis, MO, USA) and used without further purification. Ultrapure water (Milli-Q Direct 8 with UV photooxidation, Merck Millipore, Burlington, MA, USA, 18.2 MΩ cm^{-1}) was used in all experiments, and artificial seawater was prepared following a modified protocol by Millero *et al.* (Table 5.1)[27].

ACC precipitation was controlled by dividing the artificial seawater in two batches (Table 5.1). While NaCl, Na_2SO_4, KCl, KBr, $B(OH)_3$, and NaF were present in both batches, Na_2CO_3 and $NaHCO_3$ were only present in batch 1 and $CaCl_2$, $MgCl_2$, $SrCl_2$, and $BaCl_2$ were only present in batch 2. In contrast to the protocol of Millero *et al.*[27], 40 mM of sodium carbonate were added to batch 1, while 40 mM of calcium chloride were added to batch 2. To achieve the composition of Millero *et al.* after mixing, all chemicals that were only present in one batch were doubled, which resulted in a final calcium concentration of 60.6 mM for batch 2.

Table 5.1. Modified artificial seawater composition following Millero *et al.*[27] with modifications.

Batch	Chemical	Final concentrations in mixtures	Modification
1 & 2	NaCl	$4.1 \cdot 10^{-1}$	
1 & 2	Na_2SO_4	$2.82 \cdot 10^{-2}$	
1 & 2	KCl	$9.37 \cdot 10^{-3}$	
1 & 2	KBr	$8.4 \cdot 10^{-4}$	
1 & 2	$B(OH)_3$	$4.11 \cdot 10^{-4}$	
1 & 2	NaF	$6.91 \cdot 10^{-5}$	
1	Na_2CO_3	$4 \cdot 10^{-2}$	Addition of chemical (40 mM)
1	$NaHCO_3$	$4.26 \cdot 10^{-3}$	Concentration doubled
2	$CaCl_2$	$6.06 \cdot 10^{-2}$	Doubling of initial concentration & further addition of 40 mM
2	$MgCl_2$	$1.06 \cdot 10^{-1}$	Concentration doubled
2	$SrCl_2$	$1.8 \cdot 10^{-4}$	Concentration doubled
2	$BaCl_2$	$8.00 \cdot 10^{-8}$	Concentration doubled

In analogy to the experimental setup described in Chapter 3 and Chapter 4, a Ball-Berger mixer connected with standard tubes (tube size = 1.52 mm) to a peristaltic pump (MA1 70-7000R, Harvard Apparatus, Holliston, MA, USA) was used to mix the solutions[28]. The influence of the flow rate on the ACC material properties and chemical composition were investigated by applying five different flow rates, namely 5, 10, 15, 20 and 25 mL/min. To determine the temperature influence on the precipitation, a titration vessel with a thermostat jacket (Metrohm, Herisau, Switzerland) combined with a thermostat (Corio CD-200F, Julabo, Seelbach, Germany; temperature stability: ± 0.03 °C) was used to achieve 20 °C, 30 °C, 40 °C, and 50 °C. To measure the effect of pH, the pH of batch 1 was adjusted by either hydrochloric acid (1 M) or sodium hydroxide (0.1 M) to pH 10, 11 or 12 while the pH of batch 2 remained unchanged at 5.6. After mixing both solutions, pH values of 9, 9.74 and 10.5, respectively, were measured. Except for the mixture with pH 9, the mixed solutions were immediately filtered (nitrocellulose membranes, GVS North America). Subsequently, the residues were washed

with ethanol and dried. The pH 9 samples were stirred for one minute prior to the filtration to allow precipitation to take place as a lower pH leads to slower reaction kinetics.

Phase analysis was conducted by X-ray diffraction (XRD, D8 Advance Eco, Bruker, Karlsruhe, Germany; Cu Kα radiation with λ= 1.5406 Å) and attenuated total reflection Fourier transform infrared (ATR-FTIR, Nicolet IS10, Thermo Scientific, Waltham, MA, USA; accumulation of 64 scans) measurements. The parameters applied for the XRD measurements are: 2θ range of 20° to 70°, step size of 0.05° and dwell time of 0.2 seconds.

Morphologies of the powders were analysed by scanning electron microscopy (SEM, GeminiSEM 500, Carl Zeiss, Oberkochen, Germany) after sputtering it with gold (thickness ca. 5 – 10 nm). An accelerating voltage of 1 kV was applied, the working distance was 6.5 mm. The average particle size was estimated by graphically measuring the diameter of hundred spherical particles each with the freely available software Fiji[29].

Simultaneous thermogravimetric analysis (TGA) and differential scanning calorimetry (DSC) measurements were conducted by a STA449F3 instrument (Netzsch, Selb, Germany) to determine the crystallisation temperature and the level of hydration. All measurements were done in a nitrogen atmosphere, a heating rate of 5 °C/min was applied to bring the system to a max of 800 °C.

Element concentrations in the solids were measured by inductively coupled plasma optical emission spectroscopy (ICP-OES, Genesis FES, Spectro Analytical Instruments, Kleve, Germany) using external reference materials (Merck, Darmstadt, Germany). Each sample was measured in triplicate, each time using 30 mg of powder dissolved in nitric acid (1 M). Following the definition in Chapter 1.7, partition coefficients were calculated by dividing the trace element to calcium ratio given in the solid by the same ratio in the liquid.

5.3 Results and discussion

5.3.1 Morphology of ACC as a function of flow rate, temperature, and pH

XRD measurements (Supplementary Figure 5.1) and ATR-FTIR spectra (Supplementary Figure 5.2) showed that all samples consisted of ACC irrespective of the synthesis conditions. Similar to the ATR-FTIR spectra of the “BBM” samples presented in Chapter 3, the ATR-FTIR spectra for the samples synthesised here exhibited a shoulder at 1050 cm^{-1} (black arrow in Supplementary Figure 5.3), which is indicative for a high level of hydration[30]. Scanning electron microscope imaging showed spherical morphology for all samples, which is characteristic for amorphous precipitates of calcium carbonate (Supplementary Figure 5.4-5.6)[31]. While the synthesis temperature did not affect the particle size of ACC (Table 5.2)[32], increasing the flow rate reduced the reaction time which resulted in smaller particle sizes (Table 5.2)[33]. A similar observation was made for Sr- and Ba-doped ACC in Chapter 4, and points at an Ostwald-

Lussac ripening or particle growth process which gives larger particle sizes for longer residence times. Standard deviations decrease with increasing flow rate (Table 5.2), indicating that the particles are more uniform in size at higher flow rates which further indicates Ostwald-Lussac ripening processes (Table 5.2). The most pronounced effect on particle sizes resulted from changing the pH. Increasing the pH from 9 to 10.5 yielded a decrease of particle sizes from 148 ± 28 nm to 22 ± 3 nm due to the increasing supersaturation which facilitates ACC formation (Table 5.2), as also shown in the literature[34].

Table 5.2. Average particle sizes with standard deviations for all samples measured in SEM images (n=100).

Flow rate (mL/min)	**5**	**10**	**15**	**20**	**25**
Particle size (nm)	61 ± 17	43 ± 10	37 ± 6	37 ± 7	30 ± 6
Temperature (°C)	**20**	**30**	**40**	**50**	
Particle size (nm)	30 ± 6	29 ± 6	27 ± 5	29 ± 6	
pH	**9**	**9.74**	**10.5**		
Particle size (nm)	148 ± 28	30 ± 6	22 ± 3		

5.3.2 Investigation of the level of hydration and crystallisation behaviour

Water has been shown to be a key factor in stabilising ACC[35–37], while dehydration was reported to trigger crystallisation[38,39]. To estimate the level of hydration and the crystallisation temperatures of the samples, coupled TGA and DSC measurements were conducted. The level of hydration was determined by defining three mass loss regimes (black bars in Figure 5.1) as introduced previously (Chapter 3) and by Schmidt *et al.*[40]. The three regimes were defined by to the loss of rigid structural H_2O (Regime 1), a restricted mobile H_2O environment, mobile H_2O (Regime 2), and chemically-bound hydroxyl ions (Regime 3). The authors stated that during ACC dehydration mobile and rigid water components are simultaneously lost, while hydroxyl ions remains incorporated until final crystallisation.

In general, similar observations were made for all TGA measurements (Figure 5.1 and Supplementary Figure 5.7). An initial release of water was observed at temperatures below 150 °C (black arrow) and the measurement concluded with the formation of calcium oxide under release of CO_2 at temperatures of above 600 °C (grey arrow)[11,40,41]. Contrary to Chapter 3, in which no kinks were present between 350 °C and 450 °C, the TGA measurements here exhibited a kink at around 400 °C (brown arrow), which is attributed to the decomposition of $MgCO_3$ present in the synthesised powders[24,42,43].

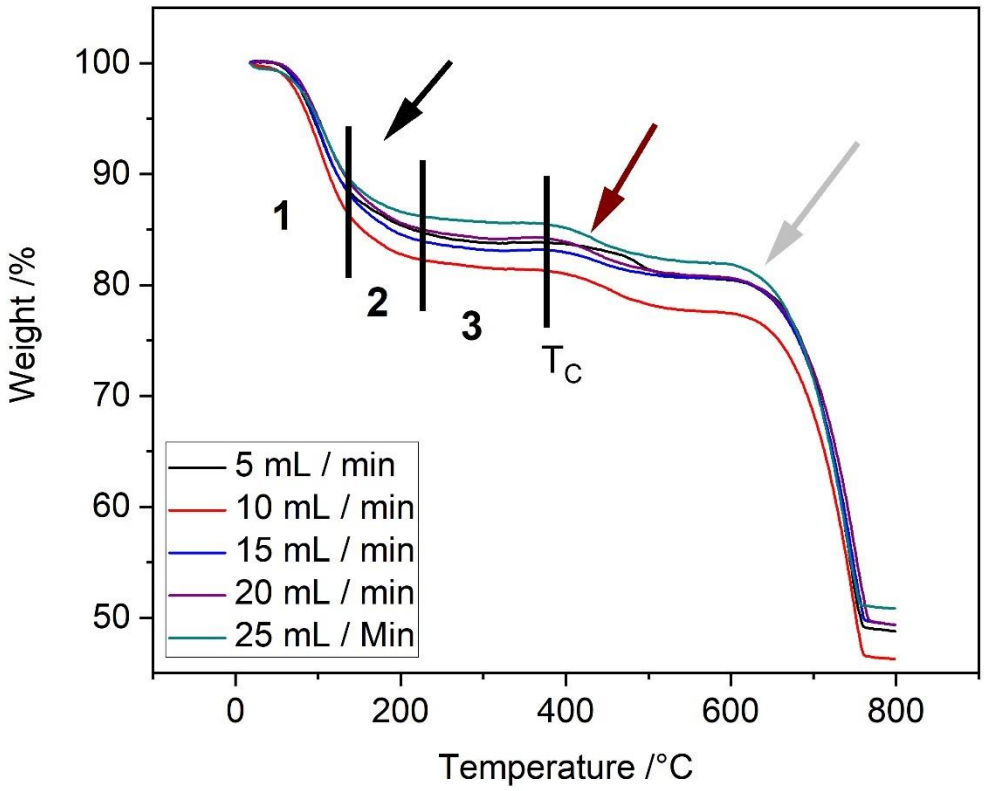

Figure 5.1. TGA measurements of ACC precipitated at different flow rates.

Hydration levels of 14.1 % to 18.7 % were determined (Table 5.3) which are similar to the hydration levels found in Chapter 3 (12.2 % to 18.7 %), in which ACC was precipitated by using different synthesis methods. Apart from the 5 mL/min sample, a decrease of the hydration level with increasing flow rates was observed (Table 5.3). Despite an enhanced magnesium incorporation ($0.07 \pm 2 \cdot 10^{-3}$ to $0.114 \pm 7 \cdot 10^{-4}$; Figure 5.3), no significantly increased level of hydration (14.8 to 15.5; Table 5.3) was determined with increasing temperatures (below). Therefore, it is assumed that magnesium did not affect the water content in the experiments, but a different effect has to be responsible for the decreasing water content with increasing flow rates. In the literature, increased particle sizes and higher incorporation of mobile water were described as a result of longer time periods before quenching[44], which is in line with the observation of decreasing particle sizes as reported in Chapter 4. Also, the above results here support this rationalisation, as lower flow rates, *i.e.*, longer reaction times, yield higher particle sizes (Table 5.2) and levels of hydration (except for the 5 mL/min sample; Table 5.3).

Table 5.3. Water loss for the three regimes defined by Schmidt *et al.*[40] (n=1). Average is given with standard deviations.

Water loss (%)	Regime 1	Regime 2	Regime 3	Total
5 mL/min	11.6	3.6	1	16.2
10 mL/min	13.7	4	1	18.7
15 mL/min	11.8	4.2	0.8	16.8
20 mL/min	10.7	4.2	0.8	15.7
25 mL/min	10.4	3.4	0.8	14.6
20 °C	11.1	3	0.7	14.8
30 °C	13.4	3.7	1.2	18.3
40 °C	9.5	3.5	1.1	14.1
50 °C	10.2	4	1.3	15.5
pH 9	11.5	3.4	0.4	15.3
pH 9.74	10.8	3.3	0.6	14.7
pH 10.5	11.9	5.1	2.7	19.7
Average water loss	11.4 ± 1.2	3.8 ± 0.6	1 ± 0.6	16.2 ± 1.8

While no temperature influence on hydration level was detectable, a change in pH had a noticeable effect. The increasing pH value correlated with higher incorporation rates of water, especially in the second and third regimes (Table 5.3). Tobler *et al.*[45]. stated that the hydroxide mole fraction started to increase at pH 10.6, which agrees with the results here. Therefore, it is assumed that the higher water content is, *i.a.,* caused by enhanced hydroxide incorporation.

Crystallisation of the samples occurred between 347 °C and 379 °C depending on the synthesis conditions (Supplementary Figure 5.8 and Table 5.4). This is at the high end of crystallisation temperatures (150 °C to 350 °C) reported in the literature[34,35,40,46,47]. Furthermore, the crystallisation temperatures are higher than those observed in Chapter 3 (264 °C to 349 °C), in which ACC was synthesised via different methods.

While hydration levels for ACC synthesised in artificial seawater (this chapter) and in ultrapure water (Chapter 3) were similar, the crystallisation temperatures differed. The main difference between the research in the different chapters was that the number of ions incorporated during ACC precipitation differed as ACC synthesis in artificial seawater resulted in multiple-doped

ACC, as shown below. In fact, the effect of dopants on increasing the crystallisation temperatures has been described in the literature[43,46,48], although, the simultaneous incorporation of multiple ions has not been systematically investigated so far. It is nevertheless, to be expected that the incorporation of multiple dopants also resulted in higher crystallisation temperatures.

Table 5.4. ACC crystallisation temperatures (T_C) for varying experimental conditions (n=1).

Flow rate (mL/min)	**5**	**10**	**15**	**20**	**25**
T_C (°C)	373	374	375	377	374
Temperature (°C)	**20**	**30**	**40**	**50**	
T_C (°C)	374	373	347 & 379	348 & 378	
pH	**9**	**9.74**	**10.5**		
T_C (°C)	346	374	360		

While crystallisation temperatures were not affected by the flow rate (Table 5.4), they were affected by temperature. For the samples synthesised at 40 °C and 50 °C an additional exothermic peak at around 350 °C was measured (Supplementary Figure 5.8C and Table 5.4). The occurrence of two crystallisation peaks was previously attributed to a large particle size distribution, as larger ACC particles tend to crystallise earlier than smaller ones[34,35]. However, the particle sizes of the 40 °C and 50 °C samples had only small standard deviations (Table 5.2), pointing to a uniform size distribution. As more magnesium was incorporated at higher temperatures (Figure 5.3), it is assumed that Mg ions were heterogeneously distributed in ACC[49], resulting in a higher crystallisation temperature of Mg-rich ACC particles compared to Mg-poor ones[35,50].

Crystallisation temperatures between 346 °C and 374 °C were measured depending on the pH (Table 5.4). Increasing the pH from 9 to 9.74 shifts the crystallisation from 346 °C to 374 °C, and further increasing the pH resulted in an intermediate crystallisation temperature (360 °C; Table 5.4). Koga *et al.*[51] observed increasing crystallisation temperatures up to pH 13 in the stock solution, while further increasing the pH of the stock solution resulted in a decrease of the crystallisation temperatures. Koga *et al.* interpreted that the increasing pH resulted in lower atomic ordering of the resulting ACC, which, in turn, resulted in higher crystallisation temperatures. As batch 1, which contained sodium (bi-)carbonate (Table 5.1), was at pH 12 a similar behaviour was revealed, however, at slightly lower pH as in the work of Koga *et al.* Nevertheless, the results here support the hypothesis put forward by these authors.

5.3.3 Partition coefficients of multiple-doped ACC

Calculated partition coefficients for magnesium, strontium, sulphur, sodium, potassium, and boron between artificial seawater and ACC are presented here. All other ions, which were present in artificial seawater, were not detectable during ICP-OES measurements. The temperature dependence of the magnesium and sulphur incorporation was determined by applying the following equation:

$$K(T) = t + m * T \tag{5.1}$$

In this equation, *t* reflects the intersection with the ordinate, *T* stands for the temperature, and *m* describes the slope and, accordingly, the temperature dependence. The unit of *m* is $\frac{1}{°C}$.

5.3.3.1 Applying different flow rates

ICP-OES measurements were conducted to determine the trace elements concentrations in order to calculate the partition coefficients of multiple-doped ACC formed at varying flow rates (Figure 5.2 and Supplementary Table 5.2).

While the calculated partition coefficients for strontium ($0.63 \pm 2 \cdot 10^{-2}$, Figure 5.2B), sodium ($4 \cdot 10^{-3} \pm 6 \cdot 10^{-4}$), potassium ($3 \cdot 10^{3} \pm 7 \cdot 10^{-4}$), and boron ($3 \cdot 10^{-3} \pm 1 \cdot 10^{-3}$, all Figure 5.2C) were not affected by increasing flow rates, calculated magnesium partition coefficients decreased from $0.074 \pm 5 \cdot 10^{-4}$ (5 mL/min) to $0.07 \pm 2 \cdot 10^{-3}$ (25 mL/min, Figure 5.2A). For sulphur, an increase from $0.006 \pm 4 \cdot 10^{-4}$ (5 mL/min) to $0.009 \pm 5 \cdot 10^{-4}$ (25 mL/min; Figure 5.2C) was observed.

In agreement with the results presented in Chapter 4, in which doped ACC was synthesised under varying flow rates, the Mg partition coefficients decreased with increasing flow rates (Figure 4.2A). However, lower magnesium partition coefficients were determined in this chapter ($0.074 \pm 5 \cdot 10^{-4}$ to $0.07 \pm 2 \cdot 10^{-3}$) compared to Chapter 4 ($0.1 \pm 2 \cdot 10^{-3}$ to $0.074 \pm 1 \cdot 10^{-3}$). Between this chapter and Chapter 4, the behaviour of the strontium partition coefficients synthesised at varying flow rates differed: while no flow rate influence was detected in this chapter (Figure 5.2B and Supplementary Table 5.2), increasing Sr partition coefficients were calculated in Chapter 4 by increasing flow rates (25 mL/min: $0.86 \pm 3 \cdot 10^{-3}$, 200 mL/min: $0.9 \pm 2 \cdot 10^{-2}$). Furthermore, the partition coefficients were lower in this chapter (average Sr partition coefficient: $0.63 \pm 2 \cdot 10^{-2}$) compared to Chapter 4.

It can be concluded that the lower partition coefficients and the differences in partition coefficients depending on flow rate were either caused by the different synthesis conditions (Table 5.5) or by changes in the solution speciation, *i.e.*, the action of prenucleation clusters (PNCs): As shown in Table 5.5, a higher flow rate was used in Chapter 4 (200 mL/min instead

of 25 mL/min). Furthermore, the $CaCl_2$, $MgCl_2$, and $SrCl_2$ concentrations differed in both chapters, which may be the reason for the different partition coefficients between both chapters.

Table 5.5. Comparison of concentrations and flow rates used in Chapter 4 and here (Chapter 5).

Difference	Chapter 4	Chapter 5
$CaCl_2$	40 mM	60.6 mM
$MgCl_2$	120 mM	106 mM
$SrCl_2$	4 mM	0.18 mM
Highest flow rate	200 mL/min	25 mL/min

However, the presence of PNCs may also be the reason for the differing partition coefficients. Verch *et al.*[52] showed that the stabilities of pure $CaCO_3$ PNCs and pure $MgCO_3$ PNCs were affected by increasing Mg and Ca ion concentrations, respectively. As an influence on the dopant incorporation on the PNC stability was shown, they assumed that the presence of multiple ions in seawater, which may be incorporated into the PNCs, can also affect their stability. Accordingly, it is possible that the stability of the PNCs resulted in different Mg and Sr partition coefficients.

Littlewood *et al.*[19] determined partition coefficients of Sr-doped ACC in the presence (ca. 0.95 to ca. 1) and the absence (ca. 0.6 to ca. 0.7) of magnesium. Notably, in Chapter 3 ($0.89 \pm 3 \cdot 10^{-2}$ - $0.97 \pm 3 \cdot 10^{-2}$), in which ACC was synthesised by applying different methods, and in Chapter 4 ($0.86 \pm 5 \cdot 10^{-3}$ - $0.9 \pm 2 \cdot 10^{-2}$), in which doped ACC was synthesised by varying flow rates, similar partition coefficients were detected to the ones Littlewood *et al.* calculated in the presence of magnesium. However, magnesium wasn't present during ACC formation in either chapter. In this chapter, magnesium was present during ACC formation which yielded in an average strontium partition coefficient of $0.63 \pm 2 \cdot 10^{-2}$. This is comparable to the partition coefficients Littlewood *et al.* determined in the absence of Mg. Thus, if Sr-doped ACC was synthesised here in the absence of magnesium, the partition coefficients were similar to the ones Littlewood *et al.* determined in the presence of magnesium and *vice versa*. It seems that this contradictory behaviour is due to the fact that Littlewood *et al.*[19] used higher concentrations (1 M) compared to this work. In this chapter, a $CaCl_2$ concentration of 60.6 mM was used, while 40 mM were used in Chapter 3 and Chapter 4. Furthermore, different strontium chloride concentrations were applied throughout this thesis, namely 2 mM (Chapter 3), 4 mM (Chapter 4), and 0.18 mM (here).

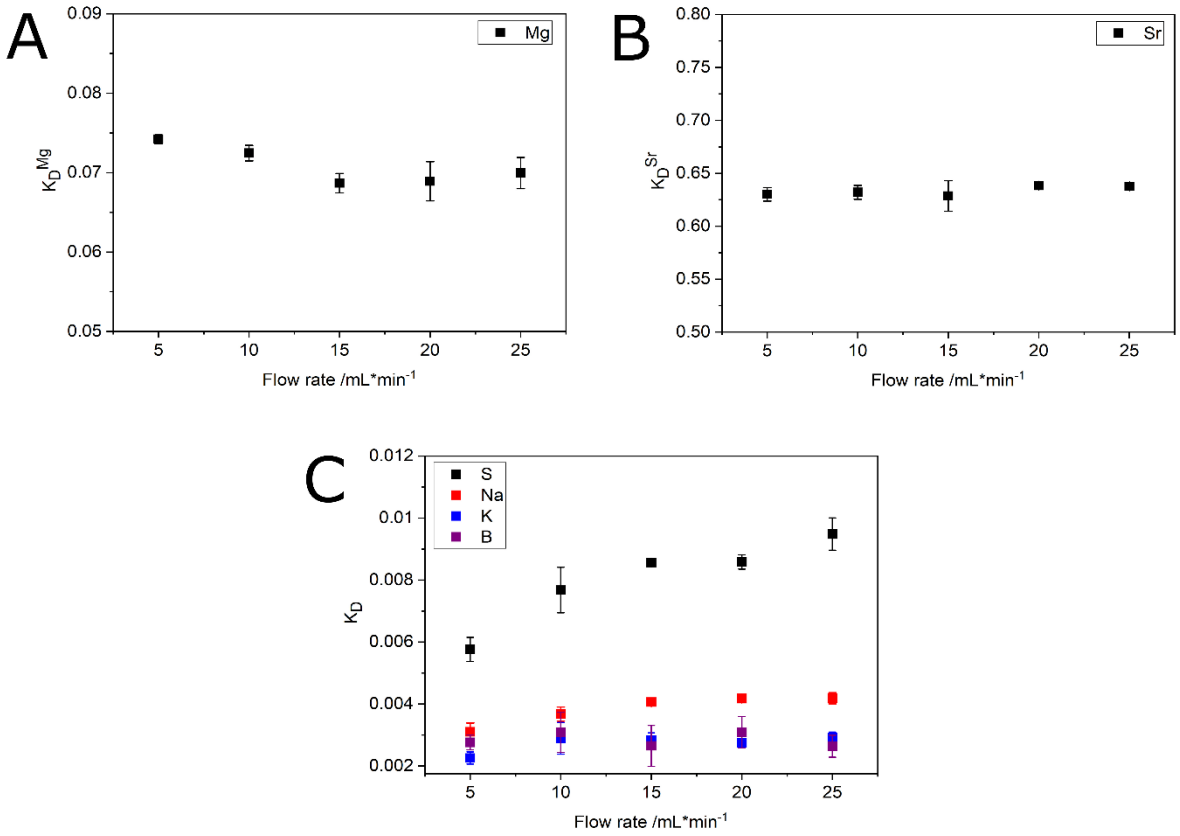

Figure 5.2. Influence of the flow rate on the **(A)** Mg, **(B)** Sr, and **(C)** S, Na, K and B partition coefficients of multiple-doped ACC. Note that some error bars are smaller than the symbols.

5.3.3.2 Change of the synthesis temperature

Four different temperatures were applied to determine the temperature dependence of the dopant incorporation into ACC. While strontium ($0.65 \pm 1{\cdot}10^{-2}$; Figure 5.3B), sodium ($0.004 \pm 6{\cdot}10^{-4}$), potassium ($0.003 \pm 3{\cdot}10^{-4}$) and boron ($0.002 \pm 7{\cdot}10^{-4}$; all Figure 5.3C) partitioning were not affected by the temperature, increased magnesium incorporation ($0.07 \pm 2{\cdot}10^{-3}$ to $0.114 \pm 7{\cdot}10^{-4}$; Figure 5.3A) as well as increased sulphur incorporation ($0.009 \pm 5{\cdot}10^{-4}$ to $0.012 \pm 8{\cdot}10^{-4}$; Figure 5.3C) were determined with increasing temperature (Supplementary Table 5.2).

By linearly fitting the calculated magnesium partition coefficients, a temperature dependency of $1.5{\cdot}10^{-3} \pm 4.8{\cdot}10^{-5} \frac{1}{°C}$ was determined (Equation 5.2).

$$K^{Mg} = (0.04 \pm 1.5 \cdot 10^{-3}) + (1.5 \cdot 10^{-3} \pm 4.8 \cdot 10^{-5}) \cdot T \quad (5.2)$$

Notably, ACC, aragonite, and calcite were affected by the synthesis temperature[4,6,53–56]. While Mg incorporation into aragonite resulted in a negative temperature dependence[6], temperature dependences between $6{\cdot}10^{-4} \frac{1}{°C}$ and $1.7{\cdot}10^{-3} \frac{1}{°C}$ were stated for magnesium incorporation in calcite[4,53,57–59].

For sulphur incorporation a temperature dependence of $8.5 \cdot 10^{-5} \pm 1.6 \cdot 10^{-5}$ was determined (Equation 5.3).

$$K^S = (7.9 \cdot 10^{-3} \pm 6.4 \cdot 10^{-4}) + (8.5 \cdot 10^{-5} \pm 1.6 \cdot 10^{-5}) \cdot T \quad (5.3)$$

Only a very limited amount of literature is available on sulphur incorporation in calcium carbonate[60,61]. Furthermore, the sulphur partition coefficients into crystalline calcium carbonate have not been determined so far.

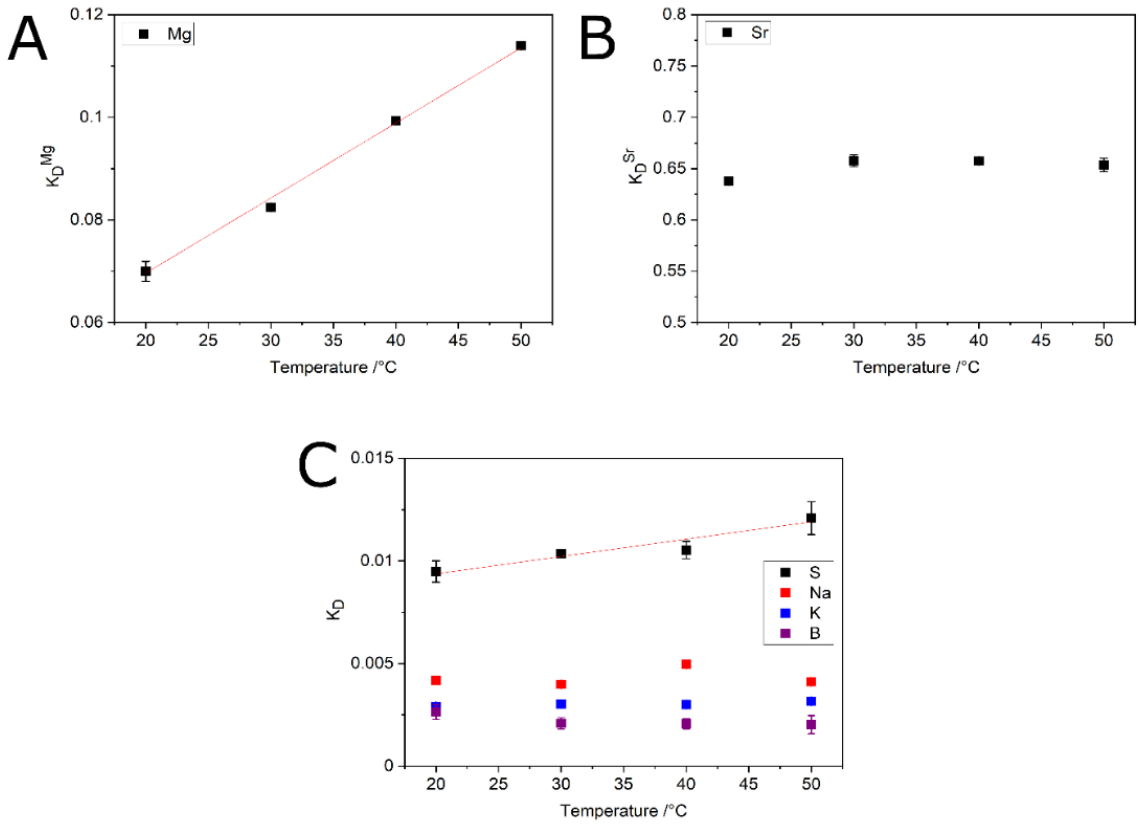

Figure 5.3. Analysing the temperature influence on the **(A)** Mg, **(B)** Sr, and **(C)** S, Na, K and B partition coefficients of multiple-doped ACC. Note that some error bars were smaller than the symbols.

A negative effect of bicarbonate on the PNCs stability was reported in the literature[62,63]. Increasing temperatures shifted the carbonate equilibrium to a higher concentration of carbonate compared to bicarbonate[64]. One may assume that the PNCs reached a larger cluster size, resulting in an enhanced magnesium and sulphur incorporation. A similar effect, namely enhanced trace element incorporation by increasing PNCs cluster size, is assumed in Chapter 5.3.3.3. However, this raises the question of why other dopants were not similarly incorporated at higher temperatures.

5.3.3.3 Applying different pH values

ICP-OES measurements revealed that all dopants were increasingly incorporated with increasing pH (Figure 5.4 and Supplementary Table 5.2). For magnesium incorporation, a more than 4.6-fold increase from $0.05 \pm 4 \cdot 10^{-4}$ (pH 9) to $0.233 \pm 3 \cdot 10^{-3}$ (pH 10.5) was

determined (Figure 5.4A). Notably, the highest magnesium partition coefficients in the whole work were measured at pH 10.5. Enhanced magnesium incorporation from $0.047 \pm 3 \cdot 10^{-3}$ (pH 8.9 – pH 9.5) to 0.178 (pH 10.3) with increasing pH was also determined in the literature[65]. Strontium partition coefficients exhibited a 10 % increase from $0.57 \pm 1 \cdot 10^{-2}$ to $0.63 \pm 1 \cdot 10^{-2}$ (Figure 5.4A). For sodium ($0.002 \pm 2 \cdot 10^{-4}$ to $0.005 \pm 4 \cdot 10^{-5}$), potassium ($0.002 \pm 2 \cdot 10^{-4}$ to $0.004 \pm 3 \cdot 10^{-4}$), and boron ($0.001 \pm 2 \cdot 10^{-4}$ to $0.003 \pm 2 \cdot 10^{-4}$) at least twofold increases were determined, likely originating from low incorporation levels (all Figure 5.4B). Besides magnesium, sulphur exhibited the second-highest increase, namely a 2.7-fold increase from $0.007 \pm 2 \cdot 10^{-4}$ to $0.019 \pm 3 \cdot 10^{-4}$ (Figure 5.4B).

Recently Evan *et al.*[66] synthesised ACC in seawater and determined in the incorporation rates of B, Na, Mg, Mn, Sr, Ba, and U into ACC. Evans *et al.* precipitated ACC under varying pH comparable to the present study, however, as they simultaneously changed the pH, the titration rate, and the “dissolved inorganic carbon” (DIC) content the comparability of the results was limited. Notwithstanding, they determined similar magnesium (0.07 to 0.16), strontium (0.61 to 0.91) and sodium ($0.7 \cdot 10^{-3}$ to $3.5 \cdot 10^{-3}$) partition coefficients (Mg: $0.05 \pm 4 \cdot 10^{-4}$ to $0.233 \pm 3 \cdot 10^{-3}$; Sr: $0.57 \pm 1 \cdot 10^{-2}$ to $0.63 \pm 1 \cdot 10^{-2}$; Na: $0.002 \pm 2 \cdot 10^{-4}$ to $0.005 \pm 4 \cdot 10^{-5}$; Supplementary Table 5.2). Notably, Evans *et al.*[66] determined boron incorporation ten times higher (0.031 to 0.068) than what found in the experiments here ($0.001 \pm 2 \cdot 10^{-4}$ to $0.003 \pm 2 \cdot 10^{-4}$; Supplementary Table 5.2), although it is unclear what caused the enhanced incorporation in their work.

As Evans *et al.*[66] varied three parameters simultaneously, the average partition coefficients of experiments, which they conducted under comparable conditions, were calculated to enable a comparison of the pH influence between both works. Therefore, two low-pH experiments and two high-pH experiments were used (Table 5.6).

Table 5.6. Calculated partition coefficients (K_D) by Evans *et al.*[66] synthesised under varying conditions.

pH	DIC content	Titration rate	K_D^{Mg}	K_D^{Sr}	K_D^{Na}	K_D^{B}
8.95	24848 µM	0.5 mL/min	0.072	0.67	$2.1 \cdot 10^{-3}$	0.031
8.95	21639 µM	0.5 mL/min	0.129	0.91	$3 \cdot 10^{-3}$	0.037
10.08	9953 µm	0.5 mL/min	0.153	0.66	$2.1 \cdot 10^{-3}$	0.068
10.11	9739 µM	0.5 mL/min	0.155	0.65	$0.7 \cdot 10^{-3}$	0.053

Table 5.7. Average low-pH and high-pH partition coefficients calculated by using the results of Evans *et al.*[66] (Table 5.6).

	Mg	Sr	Na	B
Low-pH	$0.1 \pm 4 \cdot 10^{-2}$	0.79 ± 0.17	$2.54 \cdot 10^{-3} \pm 0.6 \cdot 10^{-3}$	$0.034 \pm 4 \cdot 10^{-3}$
High-pH	$0.15 \pm 1 \cdot 10^{-3}$	0.66 ± 0.01	$1.38 \cdot 10^{-3} \pm 1 \cdot 10^{-3}$	0.06 ± 0.01

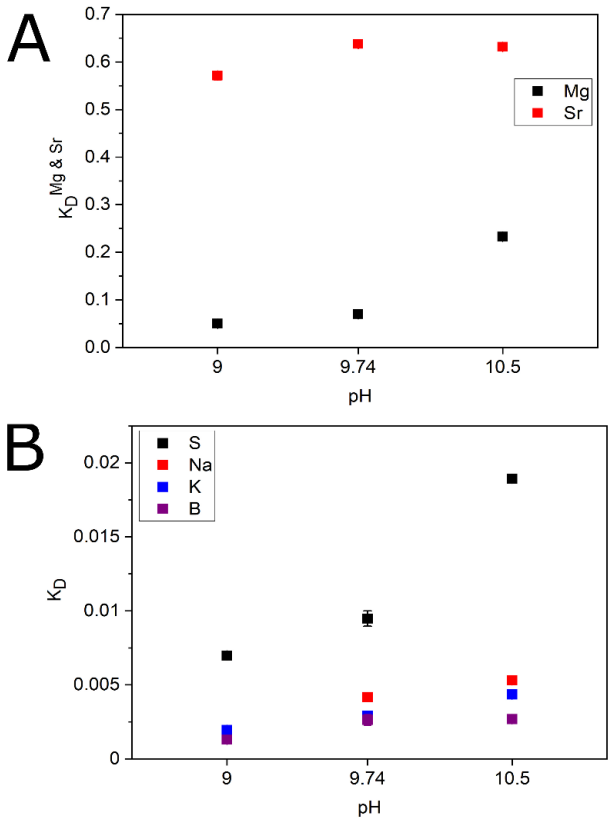

Figure 5.4. Influence of the pH on the **(A)** Mg and Sr and **(B)** S, Na, K, and B partition coefficients of multiple-doped ACC. Note that some error bars are smaller than the symbols.

The average partition coefficients for the low-pH (pH 8.95) and high-pH (pH 10.08 and pH 10.11) experiments (Table 5.7) indicate enhanced magnesium and boron incorporation

with increasing pH and decreasing incorporation of strontium and sodium. However, even when comparing experiments with similar synthesis conditions, the partition coefficients differed widely (Table 5.6). Therefore, a reliable determination of the pH influence on the partition coefficients was impossible. Notwithstanding, it can be assumed that the partition coefficients were affected by the pH comparable to the results shown in this chapter.

One may assume that pH influence is caused by the higher stability of PNCs at increased pH, which results in a larger cluster size[62,63]. Therefore, enhanced dopant incorporation can be rationalised, which is supported by the literature: Blue and Dove[65] revealed in their work three "levers" which changed the Mg incorporation into ACC, namely the Mg/Ca ratio of the initial solution, the total carbonate concentration and the pH. Notably, two of the three "levers" can be attributed to the PNC cluster size, the carbonate concentration and the pH. Accordingly, this work further indicates that PNCs control the incorporation of dopants.

5.4 Conclusion

Precipitation of ACC in an artificial seawater resulted in multiple-doped ACC. Changes to the synthesis conditions affected the material properties of ACC such as particle size, level of hydration, and crystallisation temperature.

Besides the material properties, the chemical composition was affected by the synthesis conditions. While varying the flow rate and temperature merely affected the magnesium and sulphur incorporation, all dopants exhibited an enhanced ACC incorporation with increasing pH[65]. Decreased magnesium incorporation was calculated at higher flow rates, while sulphur was increasingly incorporated at increasing flow rates. Increasing the synthesis temperatures yielded in higher incorporation for both ions.

Evans *et al.*[66] determined partition coefficients for Li, B, Na, Mg, Mn, Sr, Ba, and U doped ACC synthesised in seawater under varying synthesis conditions such as pH, similar to this work. However, the comparability between both works is limited as Evans *et al.* simultaneously changed pH, titration rate, and DIC content during their experiments. However, the Mg, Sr, and Na partition coefficients are similar in both works, indicating that pH is not co-determining the incorporation rate of these ions. Contrary to that, Evans *et al.* determined boron partitioning ten times higher than here, and it is unclear what caused the enhanced incorporation in their work.

As already stated in Chapter 4, it is a reasonable explanation that PNCs exert some control over the dopant incorporation rates. This chapter supports this assumption as the partitioning of all dopants was affected by the pH. This was, presumably, caused by the higher stability of PNCs at higher pH. As the partition coefficients of magnesium and strontium were lower and their response to flow rate alterations differed compared to Chapter 4, it can be hypothesized

that the stability of PNCs was altered by the incorporation of multiple-dopants as already expressed by Verch *et al.*[52]. Future experiments are envisaged and in progress in order to confirm this.

This chapter shows that for a better understanding of trace element incorporation into ACC, it is necessary to achieve a more detailed knowledge of the solute speciation with special regard to PNCs and their way to control the partitioning. Furthermore, future work should be done to establish which experimental conditions such as the pH affect the stability of PNCs and their ability to incorporate dopants.

5.5 References

1. Henderson, G. M. New oceanic proxies for paleoclimate. *Earth Planet. Sci. Lett.* **203**, 1–13 (2002).

2. Gabitov, R. I. & Watson, E. B. Partitioning of strontium between calcite and fluid. *Geochemistry, Geophys. Geosystems* **7**, (2006).

3. Lorens, R. B. Sr, Cd, Mn and Co distribution coefficients in calcite as a function of calcite precipitation rate. *Geochim. Cosmochim. Acta* **45**, 553–561 (1981).

4. Katz, A. The interaction of magnesium with calcite during crystal growth at 25-90°C and one atmosphere. *Geochim. Cosmochim. Acta* **37**, 1563–1586 (1973).

5. Tesoriero, A. J. & Pankow, J. F. Solid solution partitioning of Sr^{2+}, Ba^{2+}, and Cd^{2+} to calcite. *Geochim. Cosmochim. Acta* **60**, 1053–1063 (1996).

6. Gaetani, G. A. & Cohen, A. L. Element partitioning during precipitation of aragonite from seawater: A framework for understanding paleoproxies. *Geochim. Cosmochim. Acta* **70**, 4617–4634 (2006).

7. Wassenburg, J. A. *et al.* Determination of aragonite trace element distribution coefficients from speleothem calcite–aragonite transitions. *Geochim. Cosmochim. Acta* **190**, 347–367 (2016).

8. Weiss, I. M., Tuross, N., Addadi, L. & Weiner, S. Mollusc larval shell formation: Amorphous calcium carbonate is a precursor phase for aragonite. *J. Exp. Zool.* **293**, 478–491 (2002).

9. Addadi, L., Joester, D., Nudelman, F. & Weiner, S. Mollusk shell formation: A source of new concepts for understanding biomineralization processes. *Chem. - A Eur. J.* **12**, 980–987 (2006).

10. Rodríguez-Navarro, C., Ruiz-Agudo, E., Harris, J. & Wolf, S. E. Nonclassical crystallization in vivo et in vitro (II): Nanogranular features in biomimetic minerals disclose a general colloid-mediated crystal growth mechanism. *J. Struct. Biol.* **196**, 260–287 (2016).

11. Faatz, M., Gröhn, F. & Wegner, G. Amorphous calcium carbonate: Synthesis and potential intermediate in biomineralization. *Adv. Mater.* **16**, 996–1000 (2004).

12. Addadi, L., Raz, S. & Weiner, S. Taking advantage of disorder: Amorphous calcium carbonate and its roles in biomineralization. *Adv. Mater.* **15**, 959–970 (2003).

13. Gower, L. B. & Odom, D. J. Deposition of calcium carbonate films by a polymer-induced liquid-precursor (PILP) process. *J. Cryst. Growth* **210**, 719–734 (2000).

14. Wolf, S. E., Leiterer, J., Kappl, M., Emmerling, F. & Tremel, W. Early Homogenous Amorphous Precursor Stages of Calcium Carbonate and Subsequent Crystal Growth in Levitated Droplets. *J. Am. Chem. Soc.* **130**, 12342–12347 (2008).

15. Martignier, A. *et al.* Marine and freshwater micropearls: Biomineralization producing strontium-rich amorphous calcium carbonate inclusions is widespread in the genus *Tetraselmis* (Chlorophyta). *Biogeosciences* **15**, 6591–6605 (2018).

16. Demény, A. *et al.* Formation of amorphous calcium carbonate in caves and its implications for speleothem research. *Sci. Rep.* **6**, 39602 (2016).

17. Pérez-Huerta, A. *et al.* El Niño Impact on Mollusk Biomineralization-Implications for Trace Element Proxy Reconstructions and the Paleo-Archeological Record. *PLOS One* **8**, (2013).

18. Hodson, M. E. *et al.* Biomineralisation by earthworms - An investigation into the stability and distribution of amorphous calcium carbonate. *Geochem. Trans.* **16**, (2015).

19. Littlewood, J. L. *et al.* Mechanism of enhanced strontium uptake into calcite via an amorphous calcium carbonate (ACC) crystallisation pathway. *Cryst. Growth Des.* **17**, 1214–1223 (2017).

20. Dietzel, M., Purgstaller, B., Kluge, T., Leis, A. & Mavromatis, V. Oxygen and clumped isotope fractionation during the formation of Mg calcite via an amorphous precursor. *Geochim. Cosmochim. Acta* **276**, 258–273 (2020).

21. Blue, C. R., Rimstidt, J. D. & Dove, P. M. A mixed flow reactor method to synthesize amorphous calcium carbonate under controlled chemical conditions. *Methods in Enzymology* **532**, (2013).

22. Matsunuma, S., Kagi, H., Komatsu, K., Maruyama, K. & Yoshino, T. Doping incompatible elements into calcite through amorphous calcium carbonate. *Cryst. Growth Des.* **14**, 5344–5348 (2014).

23. Purgstaller, B., Mavromatis, V., Immenhauser, A. & Dietzel, M. Transformation of Mg-bearing amorphous calcium carbonate to Mg-calcite - In situ monitoring. *Geochim. Cosmochim. Acta* **174**, 180–195 (2016).

24. Demmert, B. *et al.* Polymer-Functionalised Nanograins of Mg-Doped Amorphous Calcium Carbonate via a Flow-Chemistry Approach. *Materials.* **12**, 1818 (2019).

25. Evans, D., Webb, P. B., Penkman, K., Kröger, R. & Allison, N. The Characteristics and Biological Relevance of Inorganic Amorphous Calcium Carbonate (ACC) Precipitated from Seawater. *Cryst. Growth Des.* **19**, 4300–4313 (2019).

26. Weiner, S. & Dove, P. M. An Overview of Biomineralization Processes and the Problem

of the Vital Effect. *Rev. Mineral. Geochemistry* **54**, 1–29 (2003).

27. Millero, F. J., Feistel, R., Wright, D. G. & McDougall, T. J. The composition of Standard Seawater and the definition of the Reference-Composition Salinity Scale. *Deep. Res. Part I Oceanogr. Res. Pap.* **55**, 50–72 (2008).

28. Berger, R. L., Balko, B. & Chapman, H. F. High resolution mixer for the study of the kinetics of rapid reactions in solution. *Rev. Sci. Instrum.* **39**, 493–498 (1968).

29. Schindelin, J. *et al.* Fiji: An open-source platform for biological-image analysis. *Nat. Methods* **9**, 676–682 (2012).

30. Jensen, A. C. S. *et al.* Hydrogen Bonding in Amorphous Calcium Carbonate and Molecular Reorientation Induced by Dehydration. *J. Phys. Chem. C* **122**, 3591–3598 (2018).

31. Pai, R. K. & Pillai, S. Nanoparticles of amorphous calcium carbonate by miniemulsion: Synthesis and mechanism. *CrystEngComm* **10**, 865–872 (2008).

32. Farhadi-Khouzani, M., Chevrier, D. M., Zhang, P., Hedin, N. & Gebauer, D. Water as the Key to Proto-Aragonite Amorphous $CaCO_3$. *Angew. Chem. Int. Ed.* **55**, 8117–8120 (2016).

33. Nudelman, F., Sonmezler, E., Bomans, P. H. H., De With, G. & Sommerdijk, N. A. J. M. Stabilization of amorphous calcium carbonate by controlling its particle size. *Nanoscale* **2**, 2436–2439 (2010).

34. Zou, Z. *et al.* Opposite Particle Size Effect on Amorphous Calcium Carbonate Crystallization in Water and during Heating in Air. *Chem. Mater.* **27**, 4237–4246 (2015).

35. Albéric, M. *et al.* The Crystallization of Amorphous Calcium Carbonate is Kinetically Governed by Ion Impurities and Water. *Adv. Sci.* **5**, (2018).

36. Saharay, M. & Kirkpatrick, R. J. Water dynamics in hydrated amorphous materials: a molecular dynamics study of the effects of dehydration in amorphous calcium carbonate. *Phys. Chem. Chem. Phys.* **19**, 29594–29600 (2017).

37. Raiteri, P. & Gale, J. D. Water is the key to nonclassical nucleation of amorphous calcium carbonate. *J. Am. Chem. Soc.* **132**, 17623–17634 (2010).

38. Bots, P., Benning, L. G., Rodriguez-Blanco, J. D., Roncal-Herrero, T. & Shaw, S. Mechanistic insights into the crystallization of amorphous calcium carbonate (ACC). *Cryst. Growth Des.* **12**, 3806–3814 (2012).

39. Rodriguez-Blanco, J. D., Shaw, S. & Benning, L. G. The kinetics and mechanisms of amorphous calcium carbonate (ACC) crystallization to calcite, via vaterite. *Nanoscale*

3, 265–271 (2011).

40. Schmidt, M. P., Ilott, A. J., Phillips, B. L. & Reeder, R. J. Structural Changes upon Dehydration of Amorphous Calcium Carbonate. *Cryst. Growth Des.* **14**, 938–951 (2014).

41. Ihli, J. *et al.* Dehydration and crystallization of amorphous calcium carbonate in solution and in air. *CrystEngComm* **5**, 3169 (2014).

42. Myszka, B. *et al.* Phase-specific bioactivity and altered Ostwald ripening pathways of calcium carbonate polymorphs in simulated body fluid. *RSC Adv.* **9**, 18232–18244 (2019).

43. Ihli, J., Kim, Y.-Y., Noel, E. H. & Meldrum, F. C. The effect of additives on amorphous calcium carbonate (ACC): Janus behavior in solution and the solid state. *Adv. Funct. Mater.* **23**, 1575–1585 (2013).

44. Du, H. *et al.* Amorphous $CaCO_3$: Influence of the Formation Time on Its Degree of Hydration and Stability. *J. Am. Chem. Soc.* **140**, 14289−14299 Article (2018).

45. Tobler, D. J., Rodriguez Blanco, J. D., Sørensen, H. O., Stipp, S. L. S. & Dideriksen, K. The Effect of pH on Amorphous Calcium Carbonate Structure and Transformation. *Cryst. Growth Des.* **16**, 4500–4508 (2016).

46. Zou, Z. *et al.* Additives Control the Stability of Amorphous Calcium Carbonate via Two Different Mechanisms: Surface Adsorption versus Bulk Incorporation. *Adv. Funct. Mater.* **30**, (2020).

47. Radha, A. V., Forbes, T. Z., Killian, C. E., Gilbert, P. U. P. A. & Navrotsky, A. Transformation and crystallization energetics of synthetic and biogenic amorphous calcium carbonate. *Proc. Natl. Acad. Sci. U. S. A.* **107**, 16438–16443 (2010).

48. Gal, A., Weiner, S. & Addadi, L. The stabilizing effect of silicate on biogenic and synthetic amorphous calcium carbonate. *J. Am. Chem. Soc.* **132**, 13208–13211 (2010).

49. Yang, S.-Y., Chang, H.-H., Lin, C.-J., Huang, S.-J. & Chan, J. C. C. Is Mg-stabilized amorphous calcium carbonate a homogeneous mixture of amorphous magnesium carbonate and amorphous calcium carbonate? *Chem. Commun.* **52**, 11527–11530 (2016).

50. Radha, A. V. *et al.* Energetic and structural studies of amorphous $Ca_{1-x}Mg_xCO_3 \cdot nH_2O$ ($0 \leqslant x \leqslant 1$). *Geochim. Cosmochim. Acta* **90**, 83–95 (2012).

51. Koga, N., Nakagoe, Y. & Tanaka, H. Crystallization of amorphous calcium carbonate. *Thermochim. Acta* **318**, 239–244 (1998).

52. Verch, A., Antonietti, M. & Cölfen, H. Mixed calcium-magnesium pre-nucleation clusters enrich calcium. *Zeitschrift fur Krist.* **227**, 718–722 (2012).

53. Gascoyne, M. Trace-element partition coefficients in the calcite-water system and their paleoclimatic significance in cave studies. *J. Hydrol.* **61**, 213–222 (1983).

54. Mucci, A. Manganese uptake during calcite precipitation from seawater: Conditions leading to the formation of a pseudokutnahorite. *Geochim. Cosmochim. Acta* **52**, 1859–1868 (1988).

55. Gabitov, R. I., Gaetani, G. A., Watson, E. B., Cohen, A. L. & Ehrlich, H. L. Experimental determination of growth rate effect on U^{6+} and Mg^{2+} partitioning between aragonite and fluid at elevated U^{6+} concentration. *Geochim. Cosmochim. Acta* **72**, 4058–4068 (2008).

56. Wang, Z. *et al.* Experimental calibration of Mg isotope fractionation between aragonite and seawater. *Geochim. Cosmochim. Acta* **102**, 113–123 (2013).

57. Mucci, A. Influence of temperature on the composition of magnesian calcite overgrowths precipitated from seawater. *Geochim. Cosmochim. Acta* **51**, 1977–1984 (1987).

58. Oomori, T., Kaneshima, H., Maezato, Y. & Kitano, Y. Distribution coefficient of Mg^{2+} ions between calcite and solution at 10-50°C. *Mar. Chem.* **20**, 327–336 (1987).

59. Burton, E. A. & Walter, L. M. The effects of PCO2 and temperature on magnesium incorporation in calcite in seawater and $MgCl_2$-$CaCl_2$ solutions. *Geochim. Cosmochim. Acta* **55**, 777–785 (1991).

60. van Dijk, I., de Nooijer, L. J., Boer, W. & Reichart, G.-J. Sulfur in foraminiferal calcite as a potential proxy for seawater carbonate ion concentration. *Earth Planet. Sci. Lett.* **470**, 64–72 (2017).

61. Barkan, Y., Paris, G., Webb, S. M., Adkins, J. F. & Halevy, I. Sulfur isotope fractionation between aqueous and carbonate-associated sulfate in abiotic calcite and aragonite. *Geochim. Cosmochim. Acta* **280**, 317–339 (2020).

62. Smeets, P. J. M. *et al.* A classical view on nonclassical nucleation. *Proc. Natl. Acad. Sci. U. S. A.* **114**, E7882–E7890 (2017).

63. Demichelis, R., Raiteri, P., Gale, J. D., Quigley, D. & Gebauer, D. Stable prenucleation mineral clusters are liquid-like ionic polymers. *Nat. Commun.* **2**, (2011).

64. Al-Anezi, K. & Hilal, N. Effect of Carbon Dioxide in Seawater on Desalination: A Comprehensive Review. *Sep. Purif. Rev.* **35**, 223–247 (2007).

65. Blue, C. R. & Dove, P. M. Chemical controls on the magnesium content of amorphous calcium carbonate. *Geochim. Cosmochim. Acta* **148**, 23–33 (2015).

66. Evans, D. *et al.* Trace and major element incorporation into amorphous calcium carbonate. *Geochim. Cosmochim. Acta* **290**, 293–311 (2020).

67. Xia, C. & Shi, S. Q. Self-activation for activated carbon from biomass: Theory and parameters. *Green Chem.* **18**, 2063–2071 (2016).

5.6 Supplementary

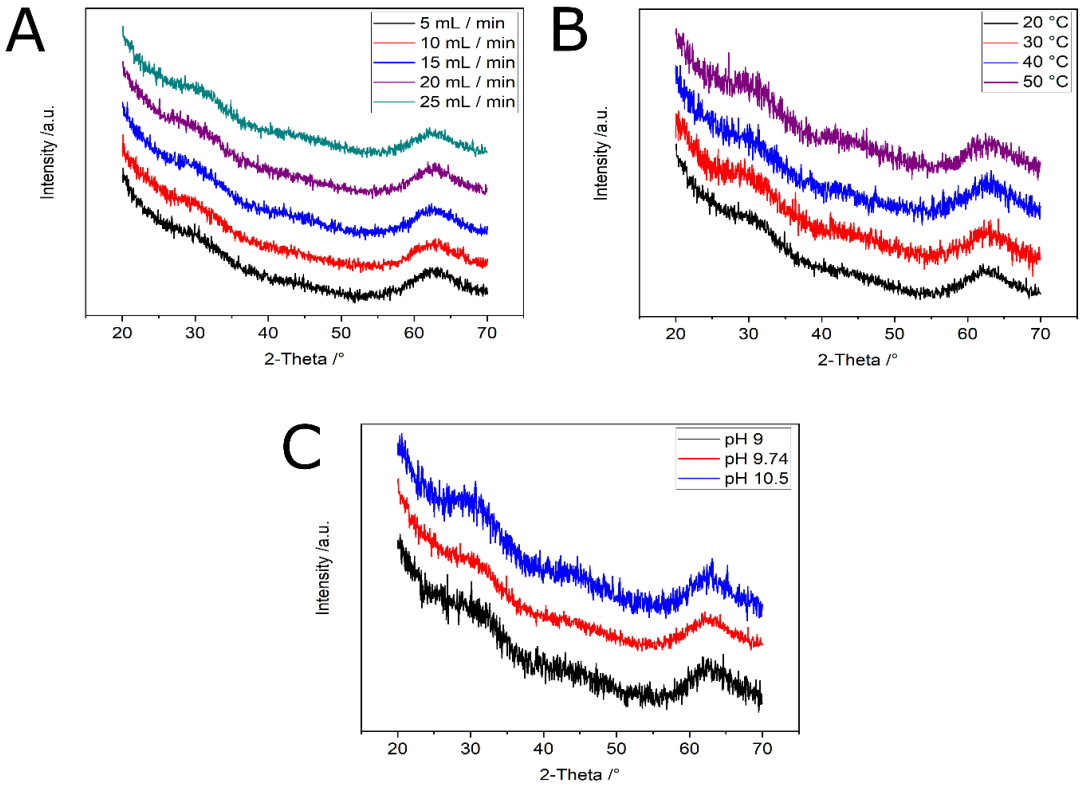

Supplementary Figure 5.1. XRD patterns of the calcium carbonate samples. Independent of varying **(A)** flow rate, **(B)** temperature, and **(C)** pH, the absence of diffraction peaks indicates that all samples were ACC.

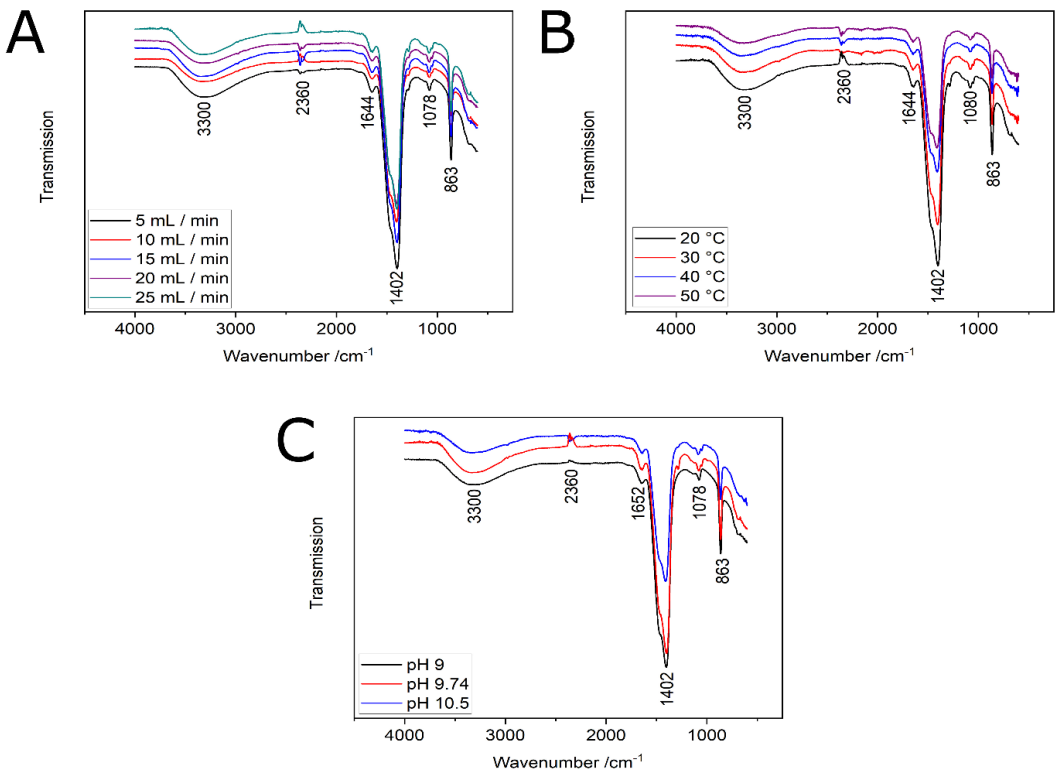

Supplementary Figure 5.2. ATR-FTIR spectra of the calcium carbonate samples synthesised with varying **(A)** flow rate, **(B)** temperature, and **(C)** pH. The bands at around 2360 cm^{-1} were related to carbon dioxide in air[67].

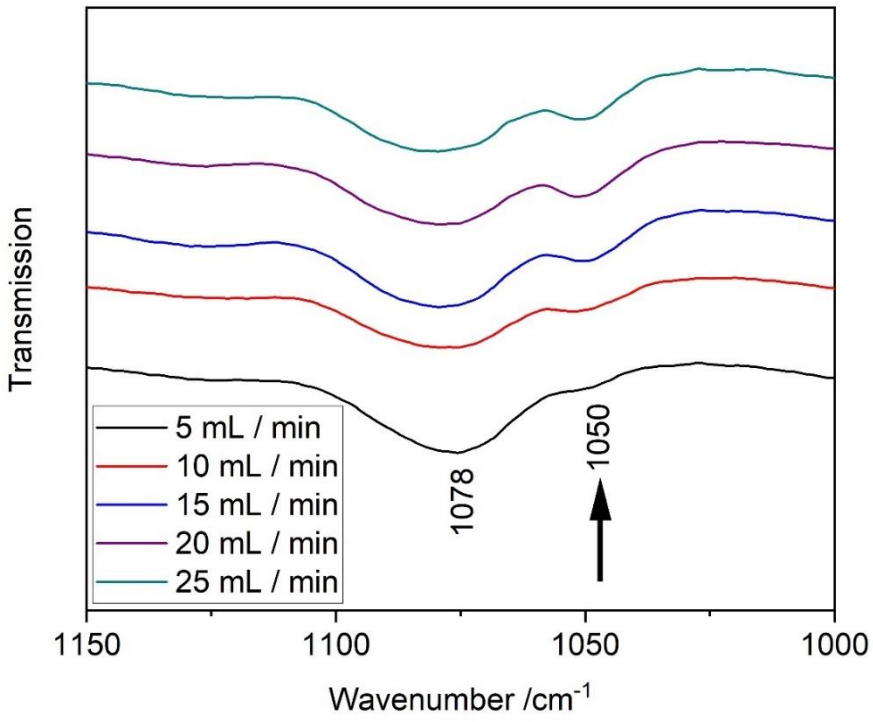

Supplementary Figure 5.3. ATR-FTIR spectra of the ACC samples synthesised at various flow rates.

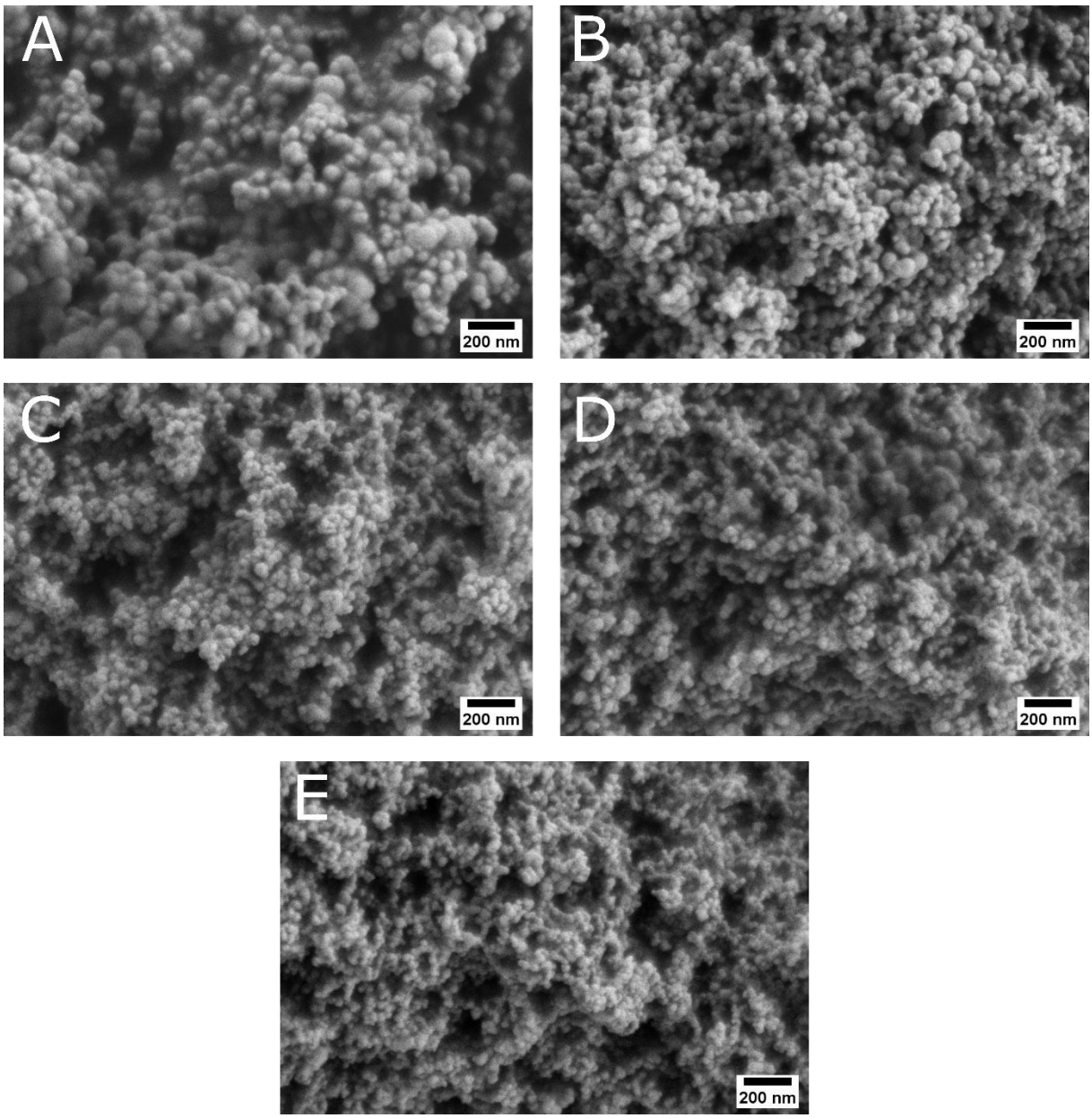

Supplementary Figure 5.4. Scanning electron micrographs of ACC samples produced using different flow rates: **(A)** 5 mL/min, **(B)** 10 mL/min, **(C)** 15 mL/min, **(D)** 20 mL/min, and **(E)** 25 mL/min.

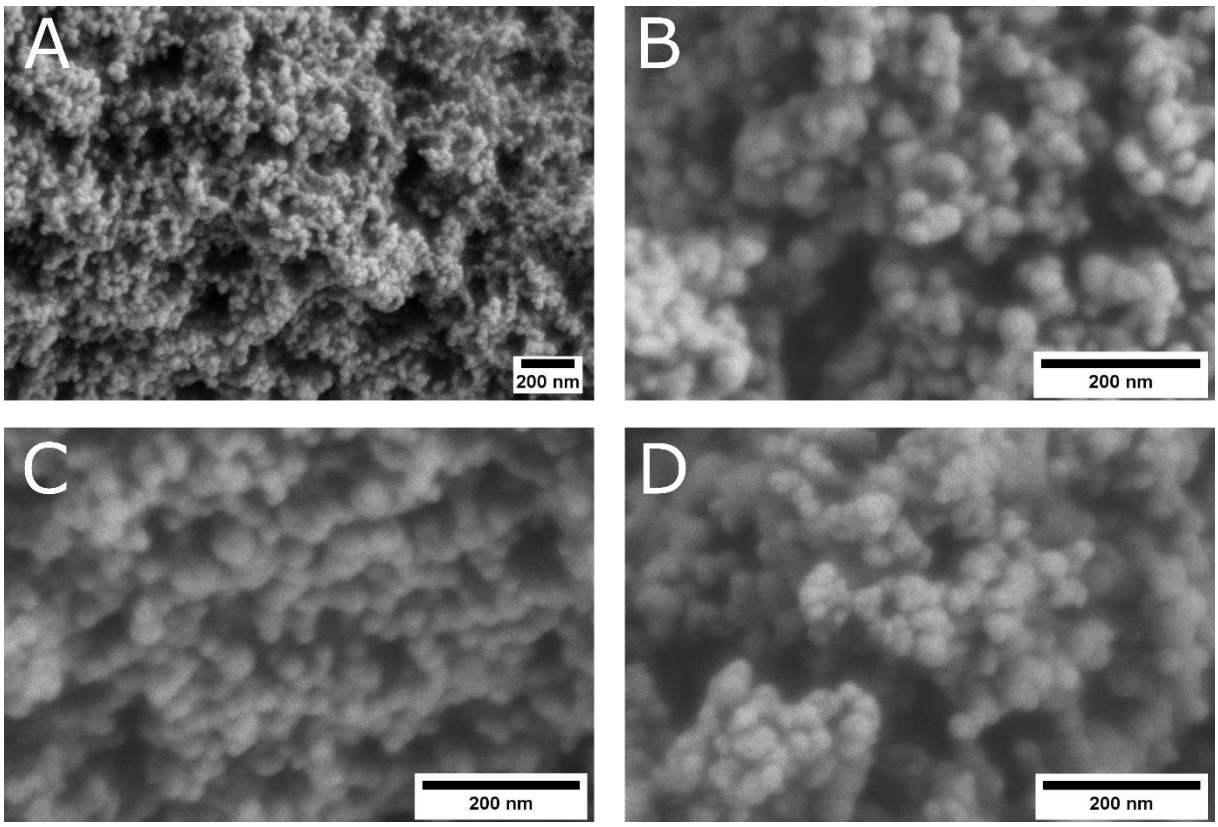

Supplementary Figure 5.5. SEM images of ACC samples produced with different temperatures: **(A)** 20 °C, **(B)** 30 °C, **(C)** 40 °C, and **(D)** 50 °C.

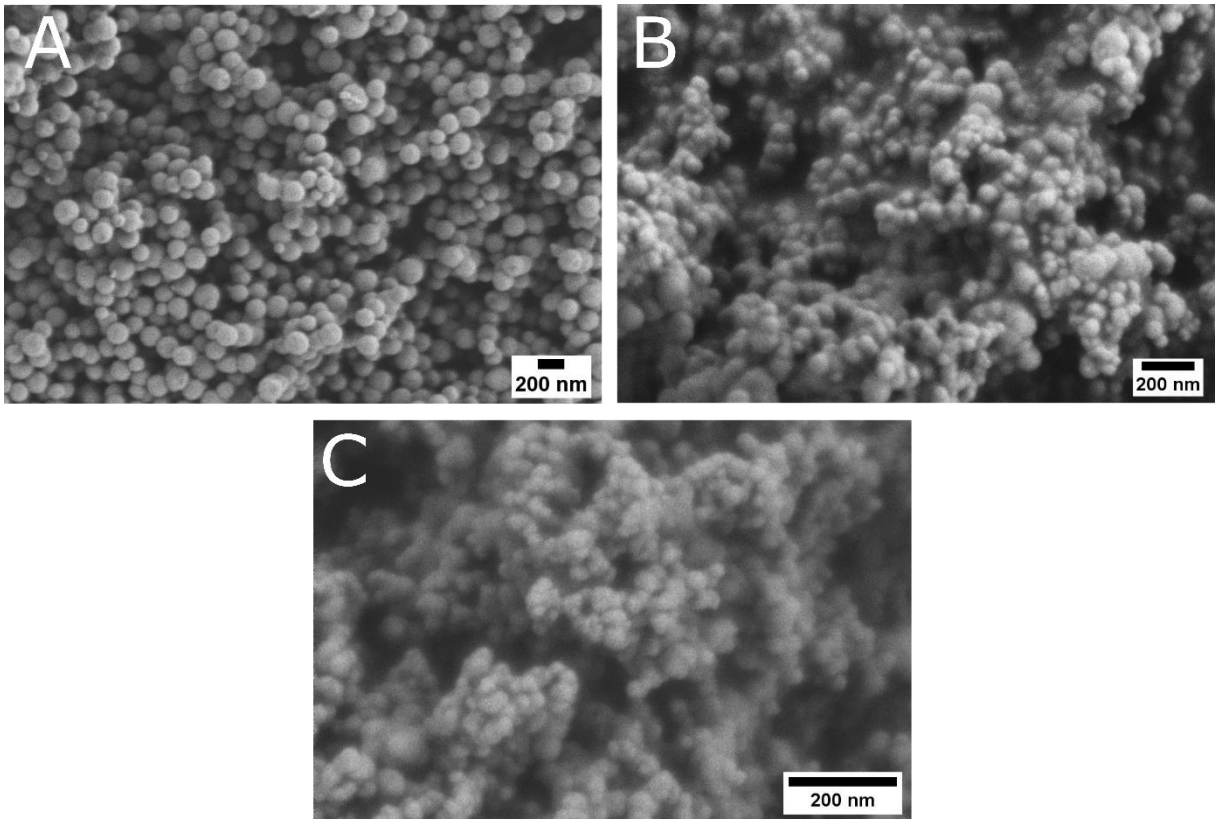

Supplementary Figure 5.6. Scanning electron micrographs of ACC samples synthesised at different pH values: **(A)** pH 9, **(B)** pH 9.74, and **(C)** pH 10.5.

Supplementary Table 5.1. Furthermore, as it is still impossible to reproduce natural conditions, the experiments were conducted under conditions which do not reflect the marine environment

Temperature boun. daries (°C)	Regime 1	Regime 2	Regime 3
Flow rate	137	222	374
Temperature	142	222	367
pH	138	225	360

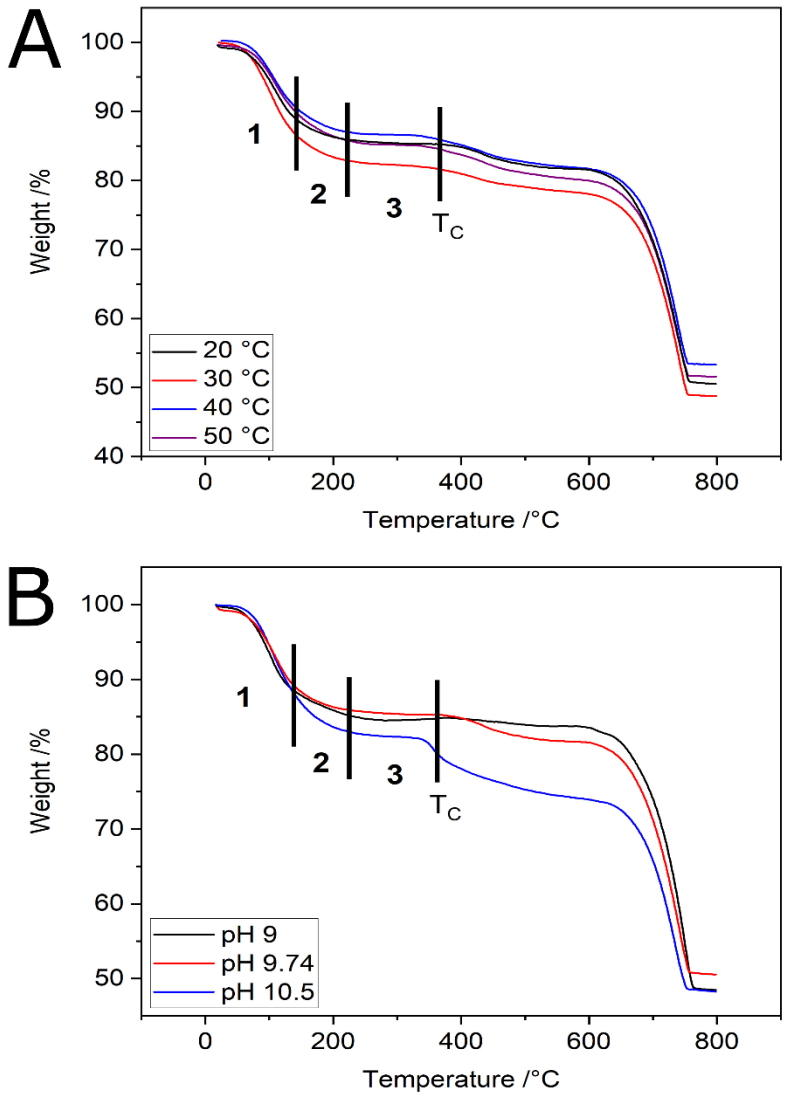

Supplementary Figure 5.7. TGA measurements for **(A)** temperature, and **(B)** pH variations. Hydration was determined by dividing the water loss into three regimes similar to flow rate variations.

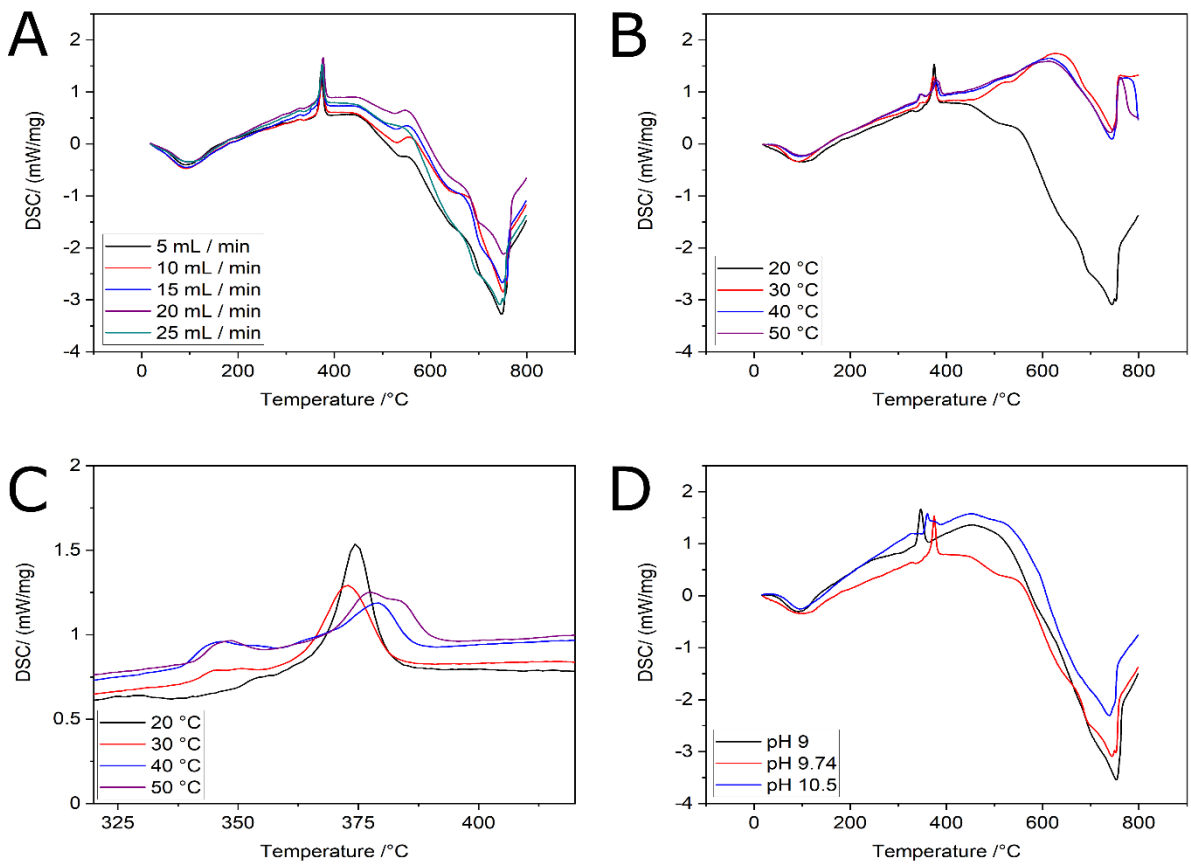

Supplementary Figure 5.8. DSC measurements to reveal the influence of the applied synthesis condition – varying **(A)** flow rate, **(B)** temperature, and **(D)** pH – on the crystallisation temperatures. **(C)** Enlargement of the crystallisation peaks presented in figure **(B)** due to the occurrence of two exothermic peaks for the 40 °C and 50 °C samples The “exo” arrows demonstrate the peak direction of an exothermic reaction.

Supplementary Table 5.2. Calculated partition coefficients (K_D) depending on the applied synthesis condition including standard deviations (n=3).

K_D	Mg	Sr	S	Na	K	B
5 mL/min	$0.074 \pm 5 \cdot 10^{-4}$	$0.63 \pm 1 \cdot 10^{-2}$	$0.006 \pm 4 \cdot 10^{-4}$	$0.003 \pm 3 \cdot 10^{-4}$	$0.002 \pm 2 \cdot 10^{-4}$	$0.003 \pm 2 \cdot 10^{-4}$
10 mL/min	$0.072 \pm 9 \cdot 10^{-4}$	$0.63 \pm 1 \cdot 10^{-2}$	$0.008 \pm 7 \cdot 10^{-4}$	$0.004 \pm 2 \cdot 10^{-4}$	$0.003 \pm 5 \cdot 10^{-4}$	$0.003 \pm 7 \cdot 10^{-4}$
15 mL/min	$0.069 \pm 1 \cdot 10^{-3}$	$0.63 \pm 1 \cdot 10^{-2}$	$0.009 \pm 1 \cdot 10^{-4}$	$0.004 \pm 1 \cdot 10^{-4}$	$0.003 \pm 2 \cdot 10^{-4}$	$0.003 \pm 7 \cdot 10^{-4}$
20 mL/min	$0.069 \pm 2 \cdot 10^{-3}$	$0.64 \pm 1 \cdot 10^{-2}$	$0.009 \pm 2 \cdot 10^{-4}$	$0.004 \pm 7 \cdot 10^{-5}$	$0.003 \pm 2 \cdot 10^{-4}$	$0.003 \pm 5 \cdot 10^{-4}$
25 mL/min	$0.07 \pm 2 \cdot 10^{-3}$	$0.64 \pm 1 \cdot 10^{-2}$	$0.009 \pm 5 \cdot 10^{-4}$	$0.004 \pm 2 \cdot 10^{-4}$	$0.003 \pm 2 \cdot 10^{-4}$	$0.003 \pm 4 \cdot 10^{-4}$
20 °C	$0.07 \pm 2 \cdot 10^{-3}$	$0.64 \pm 1 \cdot 10^{-2}$	$0.009 \pm 5 \cdot 10^{-4}$	$0.004 \pm 2 \cdot 10^{-4}$	$0.003 \pm 2 \cdot 10^{-4}$	$0.003 \pm 4 \cdot 10^{-4}$
30 °C	$0.082 \pm 6 \cdot 10^{-4}$	$0.66 \pm 1 \cdot 10^{-2}$	$0.01 \pm 2 \cdot 10^{-4}$	$0.004 \pm 9 \cdot 10^{-4}$	$0.003 \pm 2 \cdot 10^{-4}$	$0.002 \pm 3 \cdot 10^{-4}$
40 °C	$0.099 \pm 1 \cdot 10^{-4}$	$0.66 \pm 1 \cdot 10^{-2}$	$0.011 \pm 4 \cdot 10^{-4}$	$0.005 \pm 2 \cdot 10^{-4}$	$0.003 \pm 1 \cdot 10^{-4}$	$0.002 \pm 3 \cdot 10^{-4}$
50 °C	$0.114 \pm 7 \cdot 10^{-4}$	$0.65 \pm 1 \cdot 10^{-2}$	$0.012 \pm 8 \cdot 10^{-4}$	$0.004 \pm 2 \cdot 10^{-5}$	$0.003 \pm 2 \cdot 10^{-4}$	$0.002 \pm 4 \cdot 10^{-4}$
pH 9	$0.05 \pm 4 \cdot 10^{-4}$	$0.57 \pm 1 \cdot 10^{-2}$	$0.007 \pm 2 \cdot 10^{-4}$	$0.002 \pm 2 \cdot 10^{-4}$	$0.002 \pm 2 \cdot 10^{-4}$	$0.001 \pm 2 \cdot 10^{-4}$
pH 9.74	$0.07 \pm 2 \cdot 10^{-3}$	$0.64 \pm 1 \cdot 10^{-2}$	$0.009 \pm 5 \cdot 10^{-4}$	$0.004 \pm 2 \cdot 10^{-4}$	$0.003 \pm 2 \cdot 10^{-4}$	$0.003 \pm 4 \cdot 10^{-4}$
pH 10.5	$0.233 \pm 3 \cdot 10^{-3}$	$0.63 \pm 1 \cdot 10^{-2}$	$0.019 \pm 3 \cdot 10^{-4}$	$0.005 \pm 2 \cdot 10^{-5}$	$0.004 \pm 3 \cdot 10^{-4}$	$0.003 \pm 2 \cdot 10^{-4}$

6. POLYMER-FUNCTIONALISED NANOGRAINS OF MG-DOPED AMORPHOUS CALCIUM CARBONATE VIA A FLOW CHEMISTRY APPROACH

Demmert, B.[1,2]; Schinzel, F.; Schüßler, M.[1]; Mondeshki, M.[3]; Kaschta, J.[4]; Schubert, D.W.[4]; Jacob, D. E.[2] and Wolf, S. E.[1,5]

[1]Department of Materials Science and Engineering, Institute of Glass and Ceramics (WW3), Friedrich-Alexander University Erlangen-Nürnberg, 90158 Erlangen, Germany.

[2]Department of Earth and Environmental Sciences, Macquarie University, NSW 2109, Australia.

[3]Institute for Inorganic and Analytical Chemistry, Johannes Gutenberg-University, 55128 Mainz, Germany.

[4]Department of Materials Science and Engineering (WW), Institute of Polymer Materials (WW5), Friedrich-Alexander University Erlangen-Nürnberg, 91058 Erlangen, Germany.

[5]Interdisciplinary Center for Functional Particle Systems (FPS), Friedrich-Alexander University Erlangen-Nürnberg, 91058 Erlangen, Germany.

This chapter has been published as:

> **Demmert, B.**; Schinzel, F.; Schüßler, M.; Mondeshki, M.; Kaschta, J.; Schubert, D. W.; Jacob, D. E., Wolf, S. E.: *Polymer-Functionalised Nanograins of Mg-Doped Amorphous Calcium Carbonate via a Flow-Chemistry Approach.* Materials, 12(11):1818 (2019).

The author's contribution to the publication is as follows: B.D. conceived and designed the experiments in cooperation with F.S.; B.D. and F.S. performed the experiments; B.D. and conducted the measurements under contribution of F.S. (ATR-FTIR); M.S. (XRD); M.M. (NMR); J.K. (TGA) and D.W.S. (TGA); B.D. analysed the data under contribution of F.S. (ATR-FTIR, XRD); B.D. wrote the paper under contribution of D.E.J. and S.E.W. (both proof reading).

Abstract

Calcareous biominerals typically feature a hybrid nanogranular structure consisting of calcium carbonate nanograins coated with organic matrices. This nanogranular organisation has a beneficial effect on the functionality of these bioceramics. In this feasibility study, we successfully employed a flow-chemistry approach to precipitate Mg-doped amorphous calcium carbonate particles functionalized by negatively charged polyelectrolytes – either polyacrylates (PAA) or polystyrene sulfonate (PSS). It is demonstrated that the rate of Mg incorporation and, thus, the ratio of the Mg dopant to calcium in the precipitated amorphous calcium carbonate (ACC), is flow rate dependent. In the case of the PAA-functionalized Mg-doped ACC, we further observed a weak flow rate dependence concerning the hydration state of the precipitate, which is attributed to incorporated PAA acting as a water sorbent; a behaviour which is not present in experiments with PSS and without a polymer. Thus, polymer-dependent phenomena can affect flow-chemistry approaches, that is, in syntheses of functionally graded materials by layer-deposition processes.

6.1 Introduction

Calcium carbonate is of fundamental importance in various fields of research, even beyond its industrial and biological abundance[1,2]. For instance, it is of key relevance as a proxy archive in reconstructing past climates or serves as a cement additive or for exploration of biomimetic mineralisation processes[3–10]. Increasingly, calcium carbonate is suggested and introduced as an alternative to calcium phosphate-based biomaterials: Its application as a bone replacement material[11–14] and as a drug delivery system is currently explored[15–20], and it plays a central role for the bioactivity of bioglass[21]. Due to its central relevance in these various fields, the underlying mechanisms of its formation consequentially attracted broad scientific interest. As of yet, its formation mechanism is still in debate[22–25]; the binary system calcium carbonate/water is exceptionally prone to so-called nonclassical crystallization processes, namely to mineralization routes which are driven by accretion of larger entities (*e.g.,* nanoparticles)[26], instead of single ions as predicted by classical theories. Amorphous calcium carbonate (ACC) is commonly observed in such nonclassical crystallisation pathways[27–29], and it is a remarkable coincidence that biomineralizing organisms, which form their functional bioceramics from calcium carbonate, typically employ ACC as an initial building material[28,30,31]. ACC allows for the generation of non-equilibrium morphologies by pseudomorphic transformation and the incorporation of dopants and organic matrices into the final biomineral[28,32–34]. In several biominerals, remnants of amorphous calcium carbonate are found even in mature specimens[28,30,35–37].

Recently, the first direct evidence for a nonclassical and thus nanoparticle-driven mineralisation pathway in a biomineralization system was given[38]. For the prominent case of nacre*,* it was revealed by scanning transmission electron microscopy analysis that the self-

organisation of calcium carbonate colloids drives nacre growth in the model system of the Mediterranean bivalve *Pinna nobilis*. The typical size of these colloids lines up perfectly with the characteristic size of nanograins, which are the fundamental building units of biominerals of a large number of diverse species[23,35,36,39]. These nanograins are coated by an organic matrix which effectively turns the biomineral into a hybrid material. Moreover, the nanogranular organisation turns the biomineral into a nanoceramic, which has a range of beneficial effects on the biomineral's properties, of which the mechanical aspects are especially well documented[23]. According to Griffith's law, a brittle material can reach its theoretical strength by reducing the grain size below a critical threshold in the nanometre range[40–42]. Additionally, the nanogranular structure leads a crack onto a tortuous intergranular trail that distinctly increases the crack path[43,44]. Since the intergranular organic matrix enriches at the nanograin boundaries, it can efficiently increase the crack energy dissipation considerably, for example, by ligament bridging[44].

In summary, biominerals often feature a nanogranular organisation which arises from nanoparticle-driven mineralisation, and hence nonclassical pathway in which amorphous calcium carbonate colloids accrete to give a space-filling and, after pseudomorphic phase transformation, the crystalline mineral body; the colloidal origin of these functional bioceramics imprints a nanogranular structure on these materials[23,45]. At the nanograin boundaries, organic matrices are incorporated, affecting the bioceramic properties fundamentally. Ultimately, the intracrystalline and intergranular organic matrices transform the calcium carbonate body into a hybrid nanoceramic.

The mimesis of the biosynthesis of such hybrid materials often builds upon diffusion-controlled single-batch mineralisation setups in which, following the concept of LaMer[46], a high supersaturation generates a high particle number density which then self-organises into nanostructured mineral bodies and mesocrystals[30,32,47–49]. These systems often yield materials which are remarkably similar to their biogenic counterparts[49], but the chosen synthesis concept also has various major drawbacks. The one-batch synthesis approach defines only the initial reaction parameters but, in the course of the reaction, key parameters like pH or supersaturation or ionic strength may change in an unsupervised fashion. Even established systems such as the slow-diffusion process, in which a calcium-bearing solution is exposed to the vapour of decomposing ammonium carbonate, bear hidden parameters which affect reproducibility across different labs[50]. This lack of control not only impedes upscaling but also hinders an intentional change in reaction parameters during the reaction. The latter would allow designing mineralisation procedures which give access, *inter alia*, to graded functional materials. This is already excellently demonstrated by nature's functional graded biominerals, which are highly adapted to serve a given task[51,52].

In general, chemical reactions such as precipitation reactions by metathesis are governed by concentration profiles which fundamentally alter when changing the experimental design from a batch-wise to a flow-through setup. To overcome the established but limited single-batch setups in biomimetic mineralization experiments and to gain more parametric control over precipitation reactions, we explored the feasibility of a flow-chemistry approach herein. By relying on commercially available microfluidics channels, it was ensured that the approach can also be adopted when no access to lithographical technology is available. As a benchmarking model system, we chose a relatively delicate synthesis task, the generation of amorphous calcium carbonate which is subsequently surface-functionalised with representative polyelectrolytes, here either polyacrylate (PAA) or polystyrene sulfonate (PSS), without inducing phase transformation of the highly reactive amorphous phase. Thus, we aimed at generating polymer-functionalized nanograins of Mg-doped amorphous calcium carbonate particles, mimicking the fundamental building blocks of biogenic nanogranular functional ceramics to demonstrate the reliability of a flow-chemistry approach for biomimetic crystallization and bio-inspired materials synthesis.

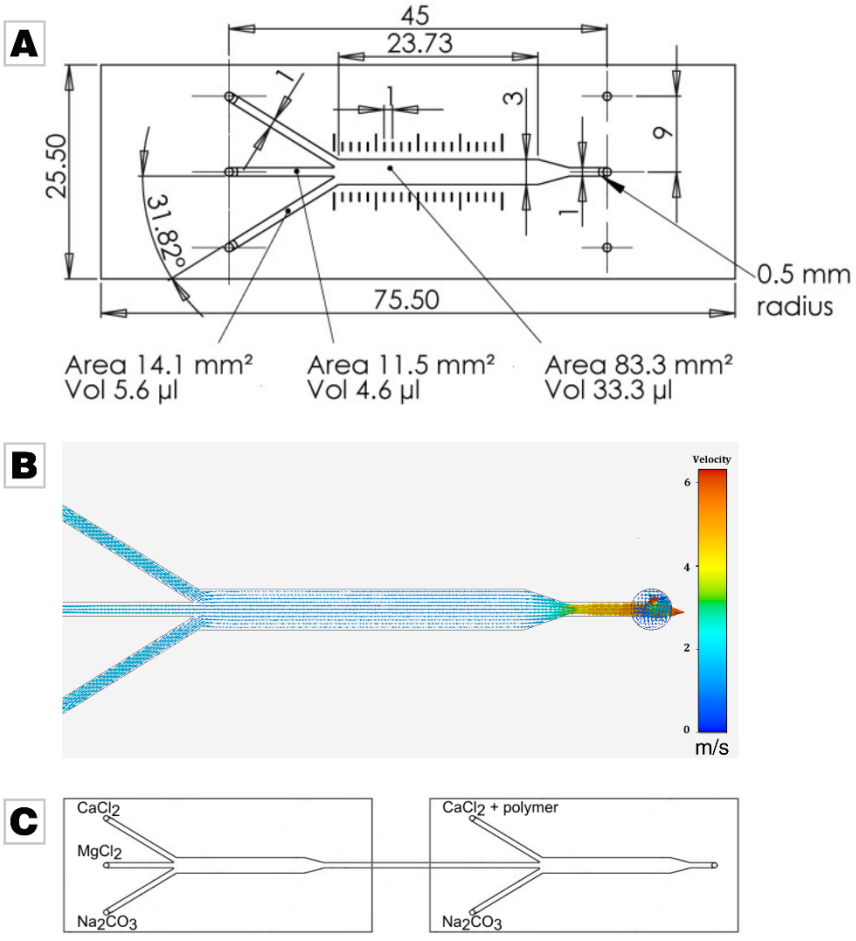

Figure 6.1. (A) Layout of the commercially available and employed microfluidic chip supplied by ibidi (Martinsried, Germany). Image used by courtesy of ibidi GmbH[53]. **(B)** Simulation of the fluid dynamics in the microfluidic chip at a feeding flow of 30 mL/min. Images used courtesy of ANSYS, Inc. (Canonsburg, PA, USA) **(C)** Scheme of the experimental setup. In control experiments, only the calcium

chloride solution was fed into the system in the second microfluidic chip, thus omitting the addition of polymer.

6.2 Materials and methods

The experimental setup consisted of two commercially microfluidic channels which merged three separately fed liquids into a single channel (ibidi GmbH, µ-Slide III3in1); the layout is given in Figure 6.1A. Simulation of fluid dynamics in the microfluidic chip at a flow rate of 30 mL/min shows that the middle part of the chip features a laminar flow profile, and the orifice induces a turbulent flow with thorough mixing (Figure 6.1B). For the simulation, the software ANSYS AIM, Release 19.0, was used[54]. The two microfluidic elements were connected in series by standard tubing, see Figure 6.1C. To control the different flow rates (5 mL/min, 15 mL/min and 30 mL/min) and the volume (20 mL), the solutions were mixed with a peristaltic pump (MA1 70-7000R, Harvard Apparatus, Holliston, MA, USA; tubing size 2.7 mm).

Ultrapure water was used in all experiments (Milli-Q Direct 8 with UV photooxidation, Merck Millipore, Burlington, MA, USA 18.2 MΩ cm^{-1}); all other reagents were used as supplied without further purification (purity >99%; Sigma-Aldrich, St. Louis, MO, USA). In the first microfluidic element, Mg-doped ACC was precipitated by mixing a 40 mM $CaCl_2$ solution simultaneously with a 0.1 M $MgCl_2$ solution and a 40 mM Na_2CO_3 solution. In the second microfluidic chip, a 40 mM Na_2CO_3 solution and a 40 mM $CaCl_2$ solution were added; the $CaCl_2$ solution contained additionally 200 µg/mL sodium polyacrylate (henceforth abbreviated as PAA, Sigma Aldrich, M_w ~ 5100, $pK_A \approx 4.5$[55]) or 82.4 µg/mL, sodium poly(4-styrenesulfonate) (henceforth abbreviated as PSS, Sigma Aldrich, M_w ~ 70000, $pK_A \approx 1.0$[56]). As a control experiment, no polymer was added in the second microfluidic chip. After mixing, the solutions were immediately filtered using nitrocellulose membranes (GVS North America), and the received precipitate was rinsed with ethanol and stored in a desiccator over freshly dried silica gel.

Phase analysis was accomplished by X-ray diffraction (D8 Advance Eco, Bruker Corporation, Billerica, MA, USA; Cu Kα source). Measurements were conducted in the 2θ range between 20° and 70° with a step size of 0.05° and a dwell time of 0.3 s. The sample morphologies were analysed by scanning electron microscopy (SEM, GeminiSEM 500, Carl Zeiss, Oberkochen, Germany). The gold sputtered samples were analysed at an accelerating voltage of 1.0 kV and a working distance of 6.5 mm; the final micrographs were evaluated with ImageJ2[57]. The incorporation of magnesium into amorphous calcium carbonate evidenced by inductively coupled plasma optical emission spectroscopy (ICP-OES, Genesis FES, Spectro Analytical Instruments, Kleve, Germany). For each ICP-OES measurement, 30 mg of powder was dissolved in nitric acid (1 mol/L). Every sample was measured at least in triplicate. The polymer incorporation was probed by attenuated total reflection Fourier transform infrared (ATR-FTIR, Nicolet IS10, Thermo Scientific, Waltham, MA, USA accumulation of 64 scans) and thermogravimetry (TGA, TGA Q5000, TA Instruments, New Castle, DE, USA, 5 K/min under

nitrogen atmosphere). Before TGA measurements were made, the samples were dried for 24 h at 60 °C to inhibit the influence of water on the measurements.

Furthermore, magic-angle-spinning cross-polarisation solid-state nuclear magnetic resonance (CP-MAS-NMR) experiments were performed (Advance DSX 400, Bruker Cooperation, Billerica, MA, USA, 10 kHz spinning, 3 s recycle delay, 2 ms CP pulse and between 24 and 26 k scans). The low amount of PAA and PSS and the 1% ^{13}C natural abundance hardly facilitated a successful recording of ^{13}C single pulse (SP) excitation spectra. SP experiments, although quantitative, are related to (sometimes extremely) long recycle delays; for crystalline carbonates containing water, they typically exceed 150 s[58]. In the case of water-free crystalline carbonates, recycle delays easily exceed 1000 s[59]. Thus, quantitative information about the content of PAA in the measured samples is not accessible. For this reason, ^{13}C cross-polarisation (CP) NMR spectra of the PAA and PSS samples were recorded at 10 kHz magic angle spinning (MAS) frequency and under heteronuclear decoupling, averaging 20 k scans. Such experiments are routinely measured at spinning speeds of 20 kHz or even higher[60,61]. However, moderate spinning speeds in the range of 8–12 kHz, at which the dipolar interaction is not significantly affected, facilitate optimum cross-polarisation and are still sufficient to average chemical shift anisotropy (CSA). This results in less or no spinning sidebands. Moreover, the ^{1}H-^{13}C CP experiments are related to the much faster ^{1}H relaxation, which extremely reduces the experimental time to provide sufficient but qualitative information about the species present in the system under investigation.

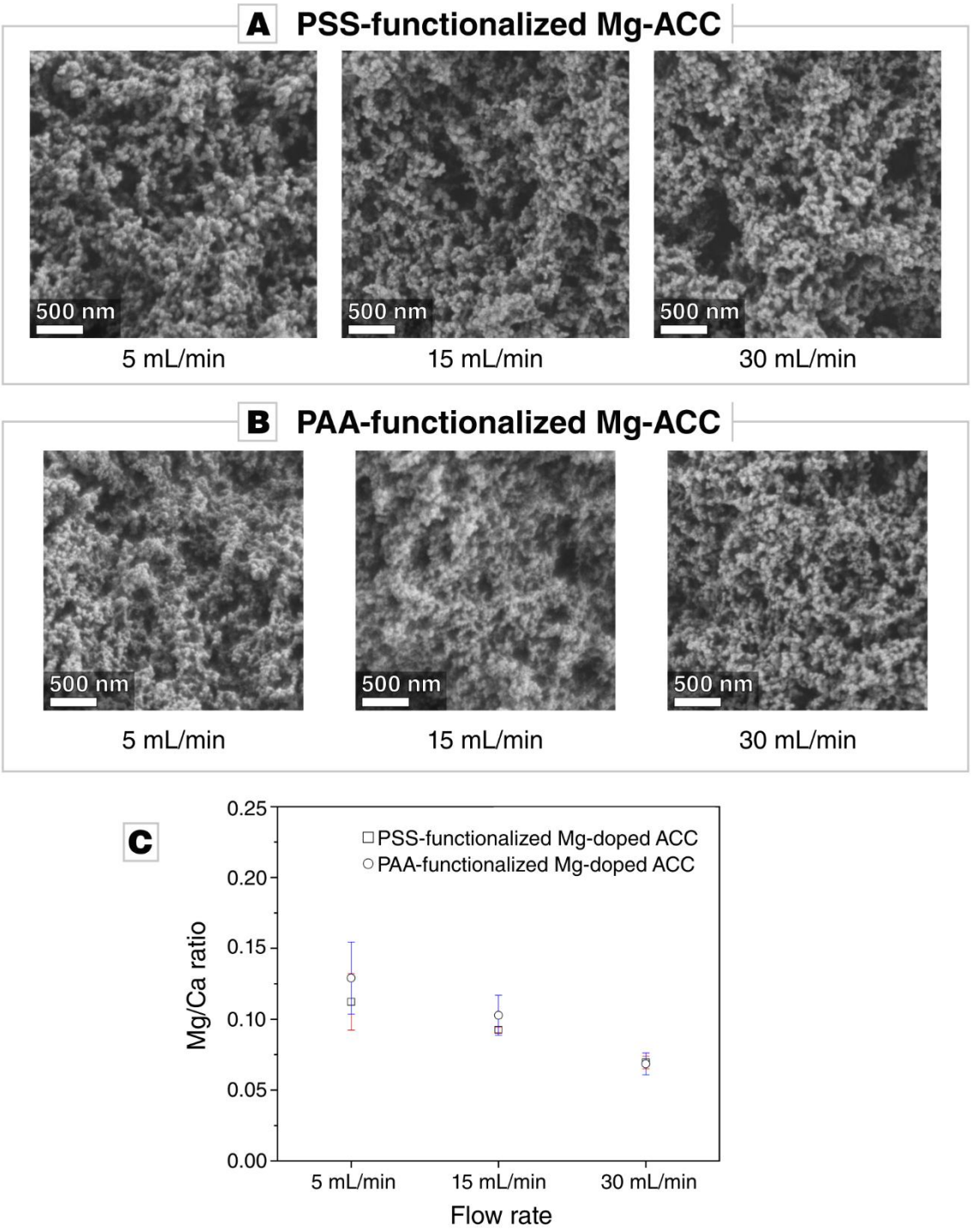

Figure 6.2. **(A,B)** Micrographs acquired by scanning electron microscopy of Mg-doped amorphous calcium carbonate (ACC) functionalized by different polymers, *i.e.*, sodium poly(4-styrenesulfonate) (PSS) or sodium polyacrylate (PAA), synthesized at different flow rates: 5 mL/min, 15 mL/min, and 30 mL/min. The morphology of the precipitate is unaffected by the flow rate and the polymer additive. **(C)** Inductively coupled plasma optical emission spectroscopy (ICP-OES) measurements of the doped ACC samples generated at different flow rates. The rate of Mg uptake is unaffected by the chemism of the polymer used for functionalization. With an increasing flow rate, the uptake of magnesium into the amorphous precipitate decreases.

6.3 Results and discussion

In this feasibility study, we aimed at generating Mg-stabilized ACC nanoparticles and subsequently coating them with a second layer of ACC containing a polyelectrolyte in order to mimic the fundamental building blocks of hybrid nanogranular biominerals. A flow-chemistry setup was chosen, which segmented the synthesis into two consecutive steps – nanoparticle synthesis and nanoparticle coating. For this, we chose commercially available microfluidic channels, which feature a laminar flow section, which ends in a smaller orifice causing thorough mixing (Figure 6.1). Each of the subsequent reaction steps was accomplished in one of the two consecutive microfluidic channels, which were connected in series. In the second step of nanoparticle coating, two representative negatively charged polyelectrolytes, that is, poly (styrene sulfonate) (PSS) and poly (acrylate) (PAA) were employed. In the following, it is demonstrated that the chosen approach gives Mg-doped ACC particles in which the polymer can be readily traced.

6.3.1 Powder Characterization and Validation of Mg Incorporation in Polymer-Functionalised Mg-Doped ACC

The precipitated Mg-doped calcium carbonate is amorphous, irrespective of the flow rate and the nature of the polymeric additive (Supplementary Figure 6.1). The particle size of the precipitated ACC is in the range of 100 to 200 nm (Figure 6.2A,B), which is the typical particle size range of ACC and congruent to the nanograin size in biominerals[23,45,62]. The morphology of the precipitate is influenced neither by the flow rate nor by the added polyelectrolyte (Figure 6.2A,B). Magnesium was incorporated in the amorphous calcium carbonate powders at a relatively low Mg/Ca ratio of around 0.1, despite the high $MgCl_2$ concentration in the mother solution (Figure 6.2C). The flow rate distinctly affects the rate of Mg incorporation: the Mg/Ca ratio decreases with increasing flow rate. The Mg/Ca remains approximately constant when replacing PAA for PSS (Figure 6.2C).

6.3.2 Validation of PSS Incorporation in Mg-Doped ACC

TGA showed a distinct weight loss of 10% is due to loss of weakly bound water (Figure 6.3A) when analysing ACC, which was precipitated in the presence of PSS. A detailed derivative analysis revealed that with an increasing flow rate, the hydration rate of the PSS samples decreases. This is consistent with the results from ICP-OES, which showed a decreasing incorporation of magnesium with higher flow rates. At 600 °C, thermal decomposition of $CaCO_3$ into CaO and CO_2 occurs, which results in a sharp weight loss. Between 200 °C and 600 °C, a gradual weight loss is visible, which was attributed to the presence of PSS in the samples. The weight loss is dependent on the flow rate, the lower the flow rate, the higher the weight loss in the given temperature window. A distinct kink is present around 400 °C, which one could attribute to the thermolysis of PSS, since PSS degradation occurs between 410 °C and

470 °C[63]. However, the kink is also present in the control reaction, in which PSS-free Mg-doped ACC was decomposed, which indicates that this weight loss does not originate from an organic component. The derivate of the weight loss shows a double peak, and the onset of the first signal is at 350 °C which coincides well with the thermal decomposition temperature of $MgCO_3$[64]; the weight loss at around 400 °C decreases with increasing flow rate, which lines up well with the decrease in Mg/Ca ratio with increasing flow rate. We, therefore, attribute the presence of this kink to the presence of Mg in the precipitate, which further corroborates the findings on the inverse dependence of Mg incorporation on the flow rate. Overall, these results demonstrate the presence of Mg in the precipitate, but the incorporation of PSS could not be established by TGA.

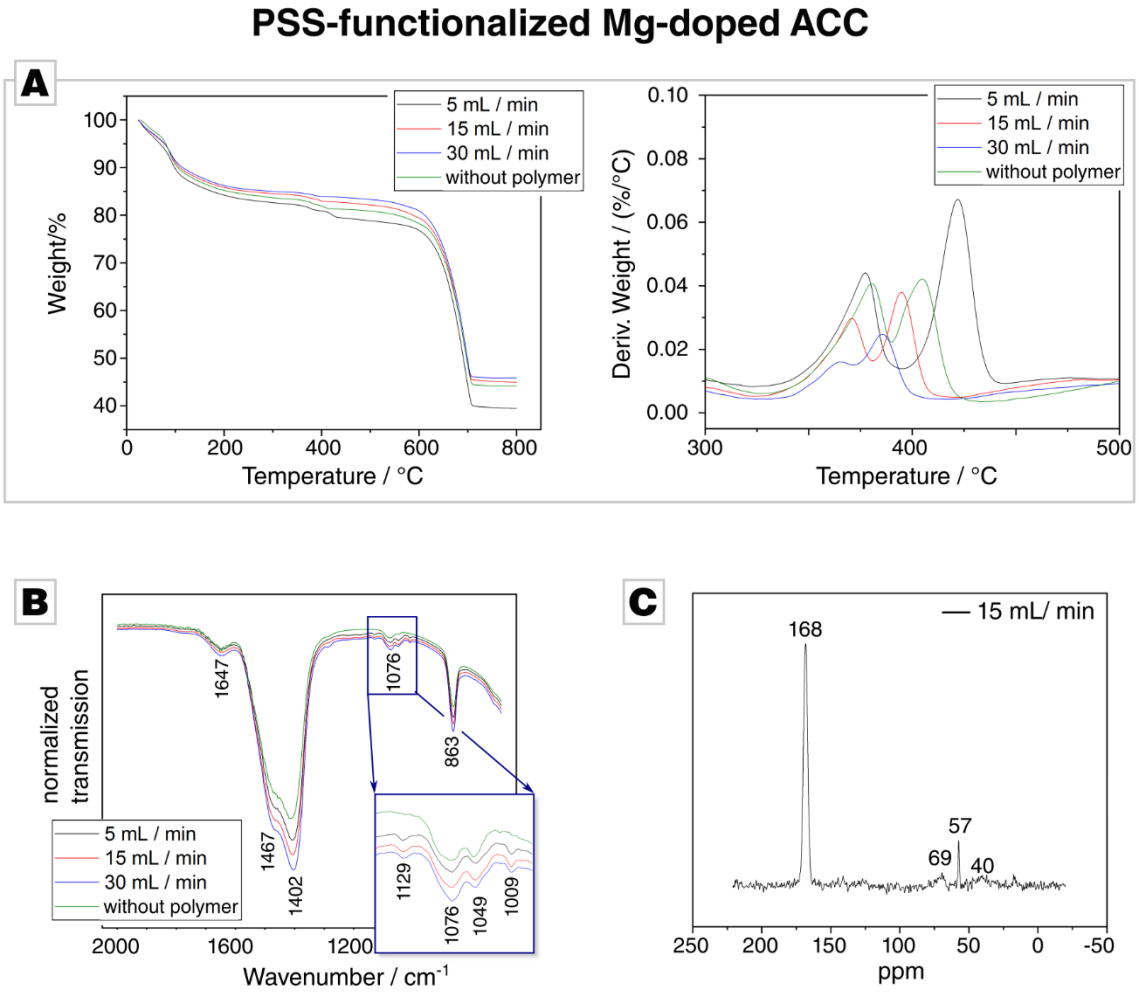

Figure 6.3. (A) Thermal gravimetric analysis (TGA) of ACC precipitated in the presence of PSS at different flow rates. **(B)** Attenuated total reflection Fourier transform infrared (ATR-FTIR) of the PSS and the Mg-doped control sample; the complete spectrum is provided in Supplementary Figure 6.3. **(C)** Cross-polarisation solid-state nuclear magnetic resonance (CP-MAS ^{13}C–SS-NMR) of PAA-functionalized Mg-doped ACC synthesized at 15 mL/min. Other signals, *e.g.,* at 57 ppm, arise from trace impurities such as residual ethanol or are insignificant to the signal/noise ratio.

ATR-FTIR measurements were able to reveal the presence of PSS in the Mg-doped ACC. The control samples and the PSS-functionalized ACC show the expected vibration band of ACC (Figure 6.3C)[62,65–67]. In the region between 1200 cm^{-1} and 900 cm^{-1}, the PSS-functionalized ACC samples show two additional bands which are absent in the control sample (inset in Figure 6.3C), at 1129 cm^{-1} and 1009 cm^{-1}. Both bands arise from the C-H bending vibration within the benzene rings[68] and are also present in ATR-FTIR spectra of the pure PSS polymer (Supplementary Figure 6.2A). This eventually gives evidence of the presence of PSS in the Mg-doped ACC.

CP-MAS ^{13}C–SS-NMR on samples precipitated at 5, and 15 mL/min was conducted in order to provide evidence for PSS incorporation (Figure 6.3C). However, the resonances of backbone CH and CH_2 groups at ca. 41 and 47 ppm and of the aromatic carbons at ca. 128 and 146 ppm were absent, probably due to the very low fraction of incorporated polymer[69]. Besides resonances arising from residual ethanol at 57 ppm[70], only one strong resonance related to carbonate is observed at 168.3 ppm; it features a constant width at half height of ca. 400 Hz across all samples[32,71,72].

6.3.3 Validation of PAA Incorporation in Mg-Doped ACC

TGA analyses of the PAA-functionalized precipitates show, below 100 °C, a distinct weight loss of about 10% occurs, which was attributed to the loss of water (Figure 6.4A). PAA degradation occurs over a wide temperature range from 250 °C to 500 °C[73]. In this regime, also the polymer-free control sample shows a distinct weight loss which we link to a loss of chemically bound water. The kink, which is caused by the decomposition of $MgCO_3$, is present in all samples. Remarkably, this decomposition occurs – like in the case of PSS – in two steps when no polymer is present but in a single step if PAA is present. Currently, this behaviour is not explainable, but it may indicate a different structural organisation of the PAA and PSS samples, that is, two different Mg-related chemical environments both present in the polymer-free and PSS-containing ACC but only one present in PAA-containing ACC. After 400 °C, the derivative weight loss is distinctly higher in the case of PAA samples than for the control samples. This might arise from decomposing PAA, whose thermolysis occurs in the temperature range of 250 °C to 500 °C[73]. Similar to the case of PSS-functionalized ACC particles, TGA evidenced the presence of Mg incorporated in the PAA-functionalized ACC, but the presence of PAA remained unsettled.

ATR-FTIR analysis was conducted, since the question whether PAA is present in these precipitates remained unanswered by TGA. All spectra showed the relevant band for ACC but gave no direct evidence for the presence of PAA in the precipitate (Figure 6.4B, the spectrum of the employed PAA is given in Supplementary Figure 6.2B). The band at 1048 cm^{-1}, which is also present in control and PSS samples, is remarkably pronounced in the presence of PAA and further increases with higher flow rates (inset in Figure 6.4B); a behaviour which was not

observed in the case of PSS. As the band is also present in the control sample, it becomes clear that this band is not connected with an incorporated polymer. Instead, this band probably arises from the hydration of the ACC; Jensen *et al.*[66] described a shoulder at 1050 cm^{-1} in ACC spectra, which decreases with dehydration. This assumption is backed by the band intensity at 3400 $cm^{-1,}$ which stems from OH stretching vibrations[74]. With an increasing flow rate, the intensity of this band increases in case of the PAA samples (Supplementary Figure 6.3B). As PAA is known to be a strong water sorbent[75], the behaviour of this band indicates that polyacrylates are indeed incorporated into the precipitate and lead to slightly more occluded water; an assumption which is backed by a slightly higher amount of water loss in the TGA measurements of PAA samples in comparison to PSS samples. In summary, the ATR-IR analysis could only give indirect evidence of PAA incorporation into the Mg-doped ACC, but shows that the hydration rate of the precipitate is affected when PAA is used as a polymeric additive.

CP-MAS ^{13}C–SS-NMR spectra showed a distinct dependence on the flow rate for the PAA-samples, indicating a sensitivity of the PAA incorporation rate on the flow rate. At a low flow rates, the NMR spectra show only one dominant, strong resonance which arises from carbonate, but no PAA signals could be detected; overall, the spectra were fully consistent with those acquired in the PSS case and thus did not indicate the incorporated polymer. At higher flow rates, new resonances appear. The ^{13}C CP spectrum of the sample synthesised at a flow rate of 30 mL/min was recorded with a recycle delay of 3 s and showed the expected signal of amorphous carbonate at ca. 168.4 ppm[76], with a full width at half height (FWHH) of about 375 Hz. This chemical shift nicely correlates with the shift of crystalline calcium carbonate at 168.2 ppm[72]. The signal is, however, significantly broadened compared to synthetic and geological crystalline calcium carbonate[32,36]. Thus, the enlarged FWHH, being a measure for the local order in a system[32,36], confirms the amorphous nature of the sample. Additionally, broad ^{13}C resonances at 187.4 ppm and 44.9 ppm for the side chain COOH group and the backbone alkyl CH and CH_2 groups were also detected in the CP spectrum[32]. Weak signals at ca. 57 and 70 ppm arose from trace contaminations: Residual ethanol was used to remove adhered water during the drying process[70].

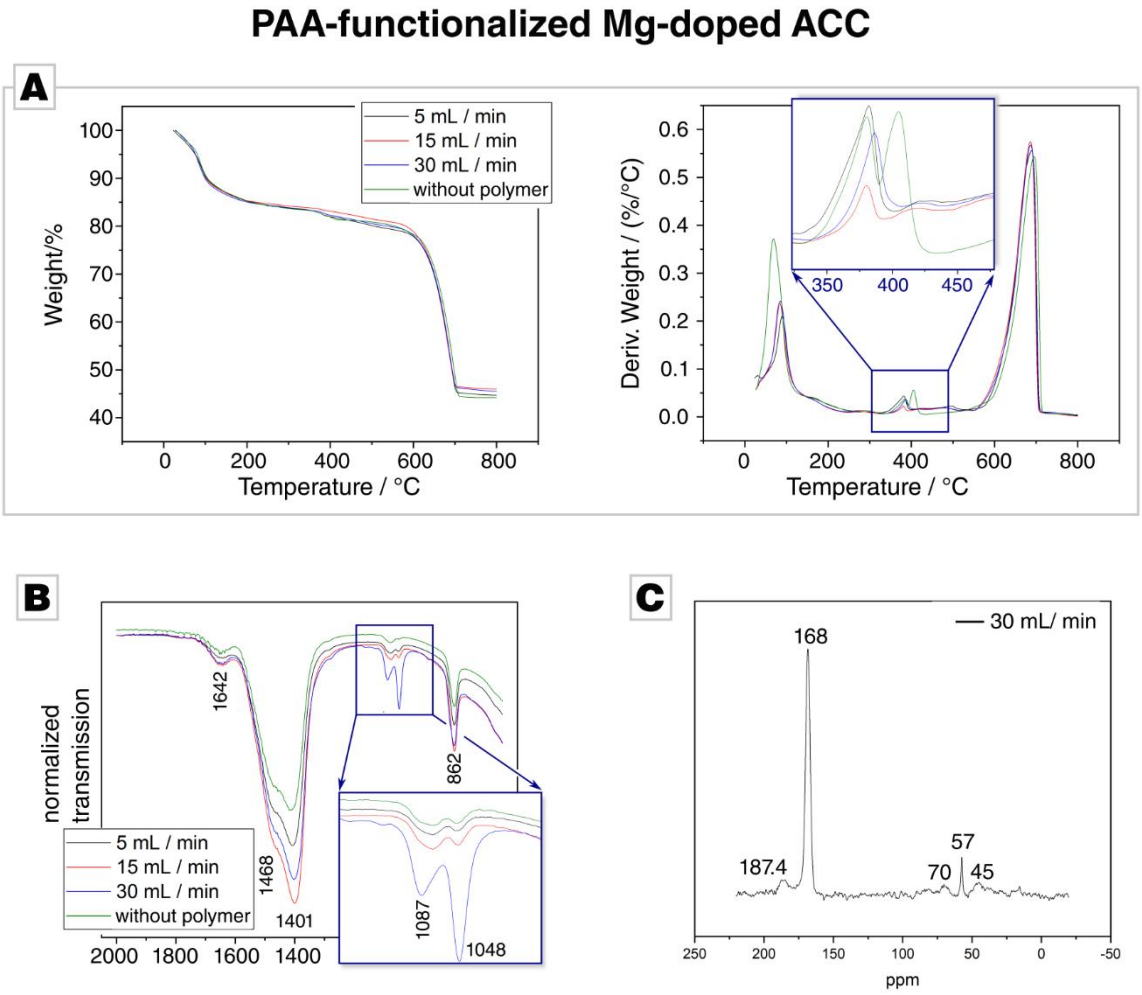

Figure 6.4. (A) Thermal gravimetric analysis of the PAA experiments and the Mg-doped ACC control sample. The different PAA-functionalized samples show no significant variation. **(B)** Fourier transform infrared spectrum of the PAA-functionalized and the control samples; the complete spectrum is provided in Supplementary Figure 6.3B. **(C)** CP-MAS ^{13}C–SS-NMR of PAA-functionalized Mg-doped ACC synthesized at 30 mL/min. The signals at 39 to 48 ppm can be attributed to overlapping signals of the CH and CH_2 moieties in the vinyl backbone of PAA; the signal at 185 ppm arises from carboxylic moieties of the PAA polymer. Other signals (*e.g.*, at 5 ppm) arise from impurities, such as residual ethanol, or are uninformative to the signal/noise ratio.

6.4 Conclusion and outlook

In this work, it was demonstrated that it is possible to reliably generate Mg-doped amorphous calcium carbonate by a simplistic flow-chemistry approach by exploiting commercially available microfluidic chips connected in series. The consecutive layout of the flow-chemistry experiments thus allows for subsequent functionalization steps of the nanoscaled precipitate: Here, with a thin polymeric corona made from PAA or PSS. It was further demonstrated that the flow rate affects the composition of the amorphous co-precipitate: Here, the Mg/Ca ratio. The polymer can also have a flow rate dependent effect on the composition, as demonstrated by the case of PAA in which the hydration rate of the ACC is slightly affected. However, this

phenomenon is polymer-dependent: PSS does not show such a flow rate dependent behaviour. In the future, we will expand on this, aiming at subsequent self-organisation steps to generate architectured and functionally or chemically graded materials. The combination of a well-controllable flow-chemistry setup with subsequent nanoparticle self-assembly may be thus a new and bio-inspired route to produce cost-effective gradient materials that may be used in a variety of different fields, such as in the generation of lightweight construction elements[77] or the development of tuneable bioactive coatings[17].

6.5 Appendix

It should be noted that, according to the ISO Technical Specification 80004, particles are not nanoparticles by definition if at least one of their external dimensions exceeds the length interval approximately from 1 nm to 100 nm. For the sake of manuscript conciseness and readability I omit this discrimination.

6.6 References

1. Wen, Y., Xiang, L. & Jin, Y. Synthesis of plate-like calcium carbonate via carbonation route. *Mater. Lett.* **57**, 2565–2571 (2003).

2. Weiner, S. & Dove, P. M. An Overview of Biomineralization Processes and the Problem of the Vital Effect. *Rev. Mineral. Geochemistry* **54**, 1–29 (2003).

3. Arp, G., Reimer, A. & Reitner, J. Photosynthesis-induced biofilm calcification and calcium concentrations in phanerozoic oceans. *Science.* **292**, 1701–1704 (2001).

4. Coggon, R. M., Teagle, D. A. H., Smith-Duque, C. E., Alt, J. C. & Cooper, M. J. Reconstructing Past Seawater Mg/Ca and Sr/Ca from Mid-Ocean Ridge Flank Calcium Carbonate Veins. *Science.* **327**, 1114–1117 (2010).

5. Pälike, H. *et al.* A Cenozoic record of the equatorial Pacific carbonate compensation depth. *Nature* **488**, 609–614 (2012).

6. Mann, S. Molecular recognition in biomineralization. *Nature* **332**, 119–124 (1988).

7. Meyers, M. A. & Chen, P.-Y. Biological Materials Science: Biological Materials, Bioinspired Materials, and Biomaterials. *Eds.; Cambridge University Press: Cambridge, UK* (Nature Publishing Group, 2014). doi:10.1038/ncomms4187

8. Matschei, T., Lothenbach, B. & Glasser, F. P. The role of calcium carbonate in cement hydration. *Cem. Concr. Res.* **37**, 551–558 (2007).

9. Lee, K. *et al.* Self-assembly of amorphous calcium carbonate microlens arrays. *Nat. Commun.* **3**, (2012).

10. Dweck, J., Buchler, P. M., Coelho, A. C. V. & Cartledge, F. K. Hydration of a Portland cement blended with calcium carbonate. *Thermochim. Acta* **346**, 105–113 (2000).

11. Fujihara, K., Kotaki, M. & Ramakrishna, S. Guided bone regeneration membrane made of polycaprolactone/calcium carbonate composite nano-fibers. *Biomaterials* **26**, 4139–4147 (2005).

12. Kasuga, T. *et al.* Preparation of poly(lactic acid) composites containing calcium carbonate (vaterite). *Biomaterials* **24**, 3247–3253 (2003).

13. Myszka, B., Hurle, K., Zheng, K., Wolf, S. E. & Boccaccini, A. R. Mechanical improvement of calcium carbonate cements by *in situ* HEMA polymerization during hardening. *J. Mater. Chem. B* **7**, 3403–3411 (2019).

14. Tolba, E. *et al.* High biocompatibility and improved osteogenic potential of amorphous calcium carbonate/vaterite. *J. Mater. Chem. B* **4**, 376–386 (2016).

15. Chen, J. F., Ding, H. M., Wang, J. X. & Shao, L. Preparation and characterization of porous hollow silica nanoparticles for drug delivery application. *Biomaterials* **25**, 723–727 (2004).

16. Ueno, Y., Futagawa, H., Takagi, Y., Ueno, A. & Mizushima, Y. Drug-incorporating calcium carbonate nanoparticles for a new delivery system. *J. Control. Release* **103**, 93–98 (2005).

17. Avaro, J. T., Ruiz-Agudo, C., Landwehr, E., Hauser, K. & Gebauer, D. Impurity-free amorphous calcium carbonate, a preferential material for pharmaceutic and medical applications. *Eur. J. Mineral.* **31**, 231–236 (2019).

18. Ramalapa, B. *et al.* Protein-polysaccharide complexes for enhanced protein delivery in hyaluronic acid templated calcium carbonate microparticles. *J. Mater. Chem. B* **5**, 7360–7368 (2017).

19. Wu, Y., Gu, W., Tang, J. & Xu, Z. P. Devising new lipid-coated calcium phosphate/carbonate hybrid nanoparticles for controlled release in endosomes for efficient gene delivery. *J. Mater. Chem. B* **5**, 7194–7203 (2017).

20. Wang, C., Chen, S., Yu, Q., Hu, F. & Yuan, H. Taking advantage of the disadvantage: employing the high aqueous instability of amorphous calcium carbonate to realize burst drug release within cancer cells. *J. Mater. Chem. B* **5**, 2068–2073 (2017).

21. Mozafari, M., Banijamali, S., Baino, F., Kargozar, S. & Hill, R. G. Calcium carbonate: Adored and ignored in bioactivity assessment. *Acta Biomater.* **91**, 35–47 (2019).

22. De Yoreo, J. J. *et al.* Crystallization by particle attachment in synthetic, biogenic, and geologic environments. *Science.* **349**, (2015).

23. Wolf, S. E. *et al.* Nonclassical crystallization in vivo et in vitro (I): Process-structure-property relationships of nanogranular biominerals. *J. Struct. Biol.* **196**, 244–259 (2016).

24. Wallace, A. F. *et al.* Microscopic evidence for liquid-liquid separation in supersaturated $CaCO_3$ solutions. *Science.* **341**, 885–889 (2013).

25. Henzler, K. *et al.* Supersaturated calcium carbonate solutions are classical. *Sci. Adv.* **4**, (2018).

26. Gebauer, D. & Wolf, S. E. Designing Solid Materials from Their Solute State: A Shift in Paradigms towards a Holistic Approach in Functional Materials Chemistry. *J. Am. Chem. Soc.* **141**, 4490−4504 (2019).

27. Politi, Y. *et al.* Transformation mechanism of amorphous calcium carbonate into calcite in the sea urchin larval spicule. *Proc. Natl. Acad. Sci. U. S. A.* **105**, 17362–17366 (2008).

28. Addadi, L., Raz, S. & Weiner, S. Taking advantage of disorder: Amorphous calcium carbonate and its roles in biomineralization. *Adv. Mater.* **15**, 959–970 (2003).

29. Politi, Y., Arad, T., Klein, E., Weiner, S. & Addadi, L. Sea Urchin Spine Calcite Forms via a Transient Amorphous Calcium Carbonate Phase. *Science.* **306**, 1161–1164 (2004).

30. Gower, L. B. Biomimetic Model Systems for Investigating the Amorphous Precursor Pathway and Its Role in Biomineralization. *Chem. Rev.* **108**, 4551–4627 (2008).

31. Weiner, S. & Addadi, L. Crystallization Pathways in Biomineralization. *Annu. Rev. Mater. Res.* **41**, 21–40 (2011).

32. Harris, J., Mey, I., Hajir, M., Mondeshki, M. & Wolf, S. E. Pseudomorphic transformation of amorphous calcium carbonate films follows spherulitic growth mechanisms and can give rise to crystal lattice tilting. *CrystEngComm* **17**, 6831–6837 (2015).

33. Killian, C. E. *et al.* Mechanism of calcite co-orientation in the sea urchin tooth. *J. Am. Chem. Soc.* **131**, 18404–18409 (2009).

34. Politi, Y. *et al.* Structural characterization of the transient amorphous calcium carbonate precursor phase in sea urchin embryos. *Adv. Funct. Mater.* **16**, 1289–1298 (2006).

35. Wolf, S. E. *et al.* Merging models of biomineralisation with concepts of nonclassical crystallisation: Is a liquid amorphous precursor involved in the formation of the prismatic layer of the Mediterranean Fan Mussel *Pinna nobilis*? *Faraday Discuss.* **159**, 433–448 (2012).

36. Wolf, S. E. *et al.* Single Nanogranules Preserve Intracrystalline Amorphicity in Biominerals. *Key Eng. Mater.* **672**, 47–59 (2016).

37. Jacob, D. E., Wirth, R., Soldati, A. L., Wehrmeister, U. & Schreiber, A. Amorphous calcium carbonate in the shells of adult *Unionoida*. *J. Struct. Biol.* **173**, 241–249 (2011).

38. Hovden, R. *et al.* Nanoscale assembly processes revealed in the nacroprismatic transition zone of *Pinna nobilis* mollusc shells. *Nat. Commun.* **6**, (2015).

39. Harris, J., Böhm, C. F. & Wolf, S. E. Universal structure motifs in biominerals: A lesson from nature for the efficient design of bioinspired functional materials. *Interface Focus* **7**, (2017).

40. Griffith, A. A. The Phenomena of Rupture and Flow in Solids. *Philos. Trans. R. Soc. London. Ser. A* **221**, 163–198 (1921).

41. Margolin, L. G. A Generalized Griffith Criterion for Crack Propagation. *Eng. Fract. Mech.* **19**, 539–543 (1984).

42. Gao, H., Ji, B., Jäger, I. L., Arzt, E. & Fratzl, P. Materials become insensitive to flaws at nanoscale: Lessons from nature. *Proc. Natl. Acad. Sci. U. S. A.* **100**, 5597–5600 (2003).

43. Barthelat, F., Li, C. M., Comi, C. & Espinosa, H. D. Mechanical properties of nacre constituents and their impact on mechanical performance. *J. Mater. Res.* **21**, 1977–1986 (2006).

44. Younis, S., Kauffmann, Y., Bloch, L. & Zolotoyabko, E. Inhomogeneity of nacre lamellae on the nanometer length scale. *Cryst. Growth Des.* **12**, 4574–4579 (2012).

45. Rodríguez-Navarro, C., Ruiz-Agudo, E., Harris, J. & Wolf, S. E. Nonclassical crystallization in vivo et in vitro (II): Nanogranular features in biomimetic minerals disclose a general colloid-mediated crystal growth mechanism. *J. Struct. Biol.* **196**, 260–287 (2016).

46. LaMer, V. K. & Dinegar, R. H. Theory, Production and Mechanism of Formation of Monodispersed Hydrosols. *J. Am. Chem. Soc.* **72**, 4847–4854 (1950).

47. Gower, L. A. & Tirrell, D. A. Calcium carbonate films and helices grown in solutions of poly(aspartate). *J. Cryst. Growth* **191**, 153–160 (1998).

48. Gower, L. B. & Odom, D. J. Deposition of calcium carbonate films by a polymer-induced liquid-precursor (PILP) process. *J. Cryst. Growth* **210**, 719–734 (2000).

49. Schenk, A. S. *et al.* Hierarchical calcite crystals with occlusions of a simple polyelectrolyte mimic complex biomineral structures. *Adv. Funct. Mater.* **22**, 4668–4676 (2012).

50. Harris, J. & Wolf, S. Desiccator Volume: A Vital Yet Ignored Parameter in $CaCO_3$ Crystallization by the Ammonium Carbonate Diffusion Method. *Minerals* **7**, 122 (2017).

51. Gordon, L. M. *et al.* Amorphous intergranular phases control the properties of rodent tooth enamel. *Science.* **347**, 746–750 (2015).

52. Amini, S. *et al.* Textured fluorapatite bonded to calcium sulphate strengthen stomatopod raptorial appendages. *Nat. Commun.* **5**, (2014).

53. ibidi. µ-Slide III 3in1. Available online: https://ibidi.com/img/cms/products/labware/channel_slides/S_8031X_Slide_III3in1/IN_8031X_III_3in1.pdf. *06.02.2019*

54. Schinzel, F. Powder Synthesis of Amorphous Calcium Carbonate with Inorganic and Organic Dopants. (2018).

55. Wiśniewska, M., Urban, T., Grządka, E., Zarko, V. I. & Gun'ko, V. M. Comparison of adsorption affinity of polyacrylic acid for surfaces of mixed silica-alumina. *Colloid Polym.*

Sci. **292**, 699–705 (2014).

56. Li, L., Ferng, L., Wei, Y., Yang, C. & Ji, H. F. Effects of acidity on the size of polyaniline-poly(sodium 4-styrenesulfonate) composite particles and the stability of corresponding colloids in water. *J. Colloid Interface Sci.* **381**, 11–16 (2012).

57. Rueden, C. T. *et al.* ImageJ2: ImageJ for the next generation of scientific image data. *BMC Bioinformatics* **18**, (2017).

58. Moore, J. K. *et al.* Quantitative identification of metastable magnesium carbonate minerals by solid-state ^{13}C NMR spectroscopy. *Environ. Sci. Technol.* **49**, 657–664 (2015).

59. Jäger, C. & Cölfen, H. Fine structure of nacre revealed by solid state ^{13}C and ^{1}H NMR. *CrystEngComm* **9**, 1237–1244 (2007).

60. Gitsas, A. *et al.* Control of peptide secondary structure and dynamics in poly(γ-benzyl-L-glutamate)-b-polyalanine peptides. *Macromolecules* **41**, 8072–8080 (2008).

61. Jochem, S. https://www.theresonance.com/cross-polarization-up-to-111-khz-mas-more/. 23.05.2019

62. Rodriguez-Blanco, J. D., Shaw, S. & Benning, L. G. The kinetics and mechanisms of amorphous calcium carbonate (ACC) crystallization to calcite, via vaterite. *Nanoscale* **3**, 265–271 (2011).

63. Korus, I. Heavy metals complexes of poly(sodium 4-styrenesulfonate) - Thermogravimetric studies. *Polimery* **57**, 290–295 (2012).

64. Khan, N., Dollimore, D., Alexander, K. & Wilburn, F. W. The origin of the exothermic peak in the thermal decomposition of basic magnesium carbonate. *Thermochim. Acta* **367**–**368**, 321–333 (2001).

65. Han, M. *et al.* A comparison of amorphous calcium carbonate crystallization in aqueous solutions of $MgCl_2$ and $MgSO_4$: implications for paleo-ocean chemistry. *Mineral. Petrol.* **112**, 229–244 (2018).

66. Jensen, A. C. S. *et al.* Hydrogen Bonding in Amorphous Calcium Carbonate and Molecular Reorientation Induced by Dehydration. *J. Phys. Chem. C* **122**, 3591–3598 (2018).

67. Andersen, F. A. & Brečević, L. Infrared spectra of amorphous and crystalline calcium carbonate. *Acta Chemica Scandinavica* **45**, 1018–1024 (1991).

68. Wang, Z.-S. *et al.* Self-Assembled Multilayers of Titania Nanoparticles and Nanosheets with Polyelectrolytes. *Chem. Mater.* **15**, 807–812 (2003).

69. Martins, C. R., Hallwass, F., De Almeida, Y. M. B. & De Paoli, M. A. Solid-State ^{13}C NMR Analysis of Sulfonated Polystyrene. *Ann. Magn. Reson* **6**, 46–55 (2007).

70. Fulmer, G. R. *et al.* NMR chemical shifts of trace impurities: Common laboratory solvents, organics, and gases in deuterated solvents relevant to the organometallic chemist. *Organometallics* **29**, 2176–2179 (2010).

71. Sen, S., Kaseman, D. C., Colas, B., Jacob, D. E. & Clark, S. M. Hydrogen bonding induced distortion of CO_3 units and kinetic stabilization of amorphous calcium carbonate: Results from 2D ^{13}C NMR spectroscopy. *Phys. Chem. Chem. Phys.* **18**, 20330–20337 (2016).

72. Nebel, H., Neumann, M., Mayer, C. & Epple, M. On the Structure of Amorphous Calcium Carbonate - A Detailed Study by Solid-State NMR Spectroscopy. *Inorg. Chem.* **47**, 7874–7879 (2008).

73. McNeill, I. C. & Sadeghi, S. M. T. Thermal Stability and Degradation Mechanisms of Poly(Acrylic Acid) and its Salts: Part 1-Poly(Acrylic Acid). *Polym. Degrad. Stab.* **29**, 233–246 (1990).

74. Brubach, J. B., Mermet, A., Filabozzi, A., Gerschel, A. & Roy, P. Signatures of the hydrogen bonding in the infrared bands of water. *J. Chem. Phys.* **122**, 184509 (2005).

75. Thijs, H. M. L. *et al.* Water uptake of hydrophilic polymers determined by a thermal gravimetric analyzer with a controlled humidity chamber. *J. Mater. Chem.* **17**, 4864–4871 (2007).

76. Leukel, S., Mondeshki, M. & Tremel, W. Hydrogen Bonding in Amorphous Alkaline Earth Carbonates. *Inorg. Chem.* **57**, 11289–11298 (2018).

77. Cantaert, B. *et al.* Use of Amorphous Calcium Carbonate for the Design of New Materials. *Chempluschem* **82**, 107–120 (2017).

6.7 Supplementary

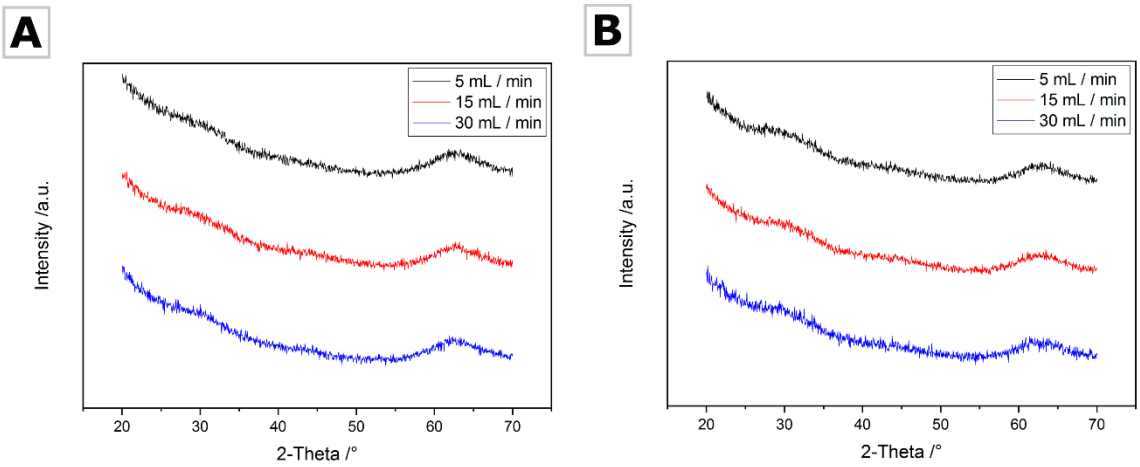

Supplementary Figure 6.1. X-ray diffractograms of Mg-doped ACC generated in the flow-chemistry setup in the presence of **(A)** PSS and **(B)** PAA.

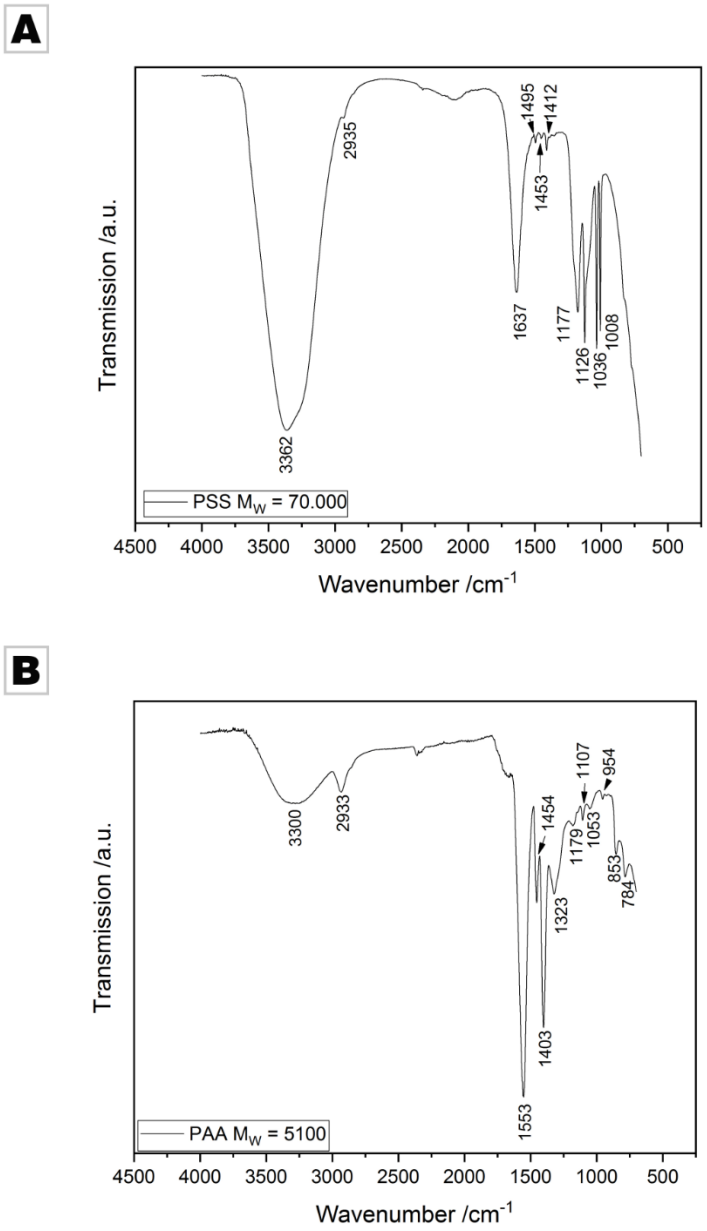

Supplementary Figure 6.2. ATR-FTIR spectra of the pure polymers **(A)** PSS and **(B)** PAA.

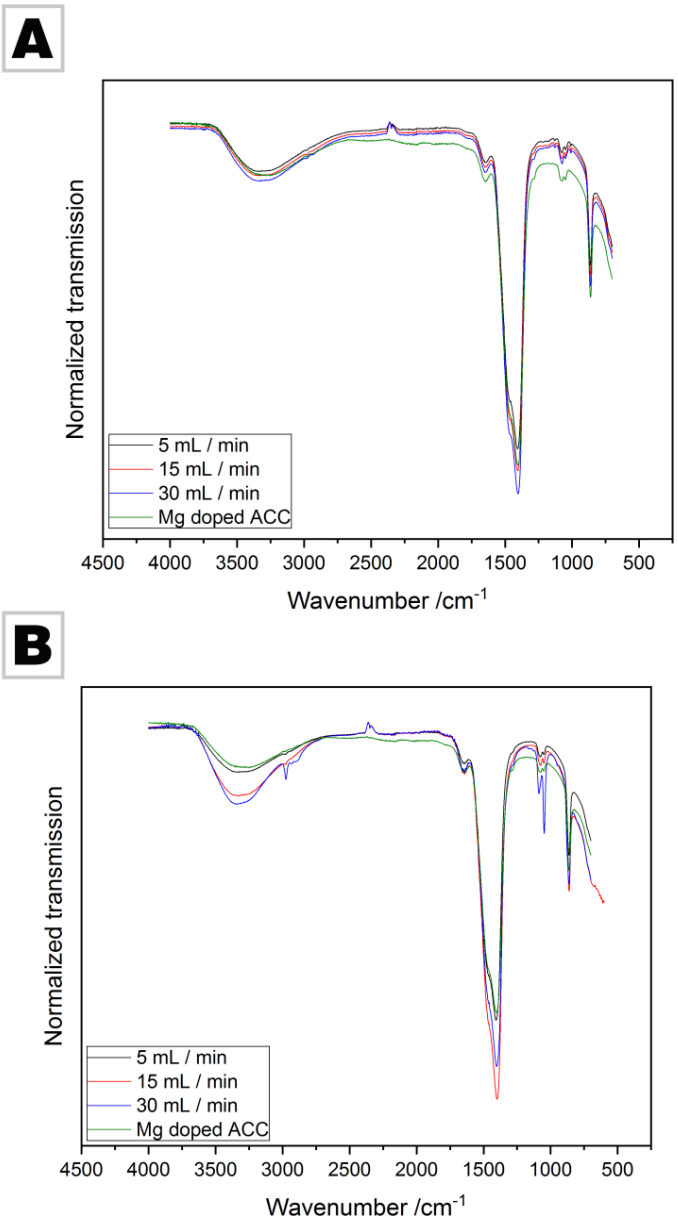

Supplementary Figure 6.3. ATR-FTIR spectra of **(A)** PSS-functionalised and **(B)** PAA-functionalised Mg-doped ACC, prepared at varying flow rates.

7. CONCLUSIONS AND OUTLOOK

7.1 Conclusion

While the influence of the solid-state transformation and dissolution-reprecipitation crystallisation on the chemical composition of ACC are known[1], the influence of the pseudomorphic transformation was as of yet unidentified. Therefore, this crystallisation pathway was investigated in Chapter 2, which revealed that the pseudomorphic transformation not only retains the morphology but also the partition coefficients, at least for the case of Sr-doped ACC. Furthermore, it was shown that the pseudomorphic transformation can be triggered by inorganic and organic additives such as phosphate, poly(acrylic acid) and polyaspartic acid. As these or similar additives are present in the environment of formation of biominerals, these findings may impact paleoclimatic reconstruction. The influence of the pseudomorphic transformation on oxygen isotope composition indicated that this crystallisation pathway is a quasi-solid-state transformation although this transformation takes place in an aqueous environment. Chapter 2 also demonstrated that the presence of additives in natural systems can promote the retention of the chemical composition of amorphous intermediates during crystallisation. This shows that the measured partition coefficients of a crystalline material, exploited as a proxy archive, describes one of two very different environmental conditions: Measured partition coefficients resulting from a dissolution-reprecipitation pathway reflect most closely the predicted equilibrium partition coefficients for the specific mineral phase and can serve to accurately reconstruct certain environmental parameters. In contrast, measured partition coefficients preserved via pseudomorphic transformation are only reflective of those of ACC.

As the properties of ACC intermediates can be retained during a pseudomorphic transformation, a thorough knowledge of the influence on synthesis conditions on the produced ACC is needed. Consequently, this thesis studied the influence of ACC synthesis on material properties and chemical composition in Chapter 3. Furthermore, Chapter 4 assesses the influence of mixing kinetics on the element partitioning and Chapter 5 determines the influence of synthesis condition on multi-doped ACC in artificial seawater.

To demonstrate how even simple changes in synthesis procedures impact on ACC composition and microstructure, a batch mixing synthesis and two flow-through syntheses were established and characterized in Chapter 3. It was demonstrated that the synthesis affects ACC material properties, as different particle sizes (between 32 ± 7 nm and 67 ± 20 nm), levels of hydration (between 12.2 % and 18.7 %), crystallisation temperatures (between 264 °C and 349 °C), and densities (1.63 g*cm^{-3} and 2.92 g·cm^{-3}) were found as a result of varying synthesis parameters. Notably, ACC synthesised via batch mixing method yielded in a lower average density (1.69 ± 0.06 g·cm^{-3}) compared to ACC synthesised via flow-

through methods, which possessed average densities between 2.42 ± 0.13 g·cm^{-3} and 2.63 ± 0.27 g·cm^{-3}. In contrast to these variations in material properties, the chemical composition of strontium and barium doped ACC were only slightly affected by changes in the synthesis parameters. However, a significant influence of the pH on barium incorporation was found.

Chapter 4 showed that changing flow rates alter particle size and chemical composition of ACC. While the particle size of Mg-doped ACC was not affected by the flow rate, decreasing particle sizes were measured for Sr- and Ba-doped ACC by increasing flow rates. The partition coefficients of Ba-doped ACC was not affected by flow rate alterations, whereas partition coefficients of strontium increased and those of Mg decreased. These findings demonstrate that element partitioning in ACC is flow rate dependent, and thus, kinetically controlled. As this effect is only rarely discussed in the current literature on ACC partitioning, these findings are crucial for paleoclimatology. This deviating behaviour can be rationalised when taking the coordination chemistry and preferred coordination ligands of the respective elements into account. Furthermore, different flow rate dependences of the dopants can be explained by the occurrence of prenucleation clusters as controlling “gate keepers” of dopant incorporation.

Precipitation of ACC in an environment which mimics the seawater composition resulted in the formation multiple-doped ACC (Chapter 5). Varying the synthesis conditions revealed an influence of the flow rate on the particle size (decreasing with increasing flow rate), on the level of hydration (decreasing with increasing flow rate), and on the magnesium and sulphur partition coefficients, which decrease for Mg and increase for sulphur by increasing flow rates. Changes in temperature affected the crystallisation temperature (occurrence of a secondary crystallisation peak) and yielded in increasing partition coefficients for magnesium and sulphur with increasing temperatures. Changing the pH affected the particle size (decreasing with increasing pH), the level of hydration (increasing with increasing pH), the crystallisation temperature (initially increasing with increasing pH, followed by a decrease), and the partition coefficients of all dopants (increasing partition coefficients with increasing pH). As PNCs exhibit an enhanced stability at higher pH[2,3], it is a reasonable to assume that PNCs exert a certain control over the element partitioning. Accordingly, a thorough understanding of PNCs and how experimental conditions affect their composition and constitution is necessary.

Ultimately, a reliable synthesis is needed which is capable of faithfully mimicking the formation of the fundamental building blocks of calcareous biominerals. As a first step in this direction, a feasibility study was presented in Chapter 6 which built on consecutive nanoparticle synthesis and surface functionalisation in a microfluidic setup. This study demonstrated that it is possible to successfully synthesise calcium carbonate nanograins coated with organic matrices which faithfully mimic the nanosized building units of biominerals.

7.2 Schlussfolgerungen

Während der Einfluss der Festphasenumwandlung sowie der klassischen Kristallisation auf die chemische Zusammensetzung von ACC bekannt ist[1], ist der Einfluss der pseudomorphen Umwandlung bislang ungeklärt. In dieser Arbeit wird in Kapitel 2 gezeigt, dass die pseudomorphe Umwandlung von ACC nicht nur die Morphologie während des Kristallisationsprozesses bewahrt – wie bislang angenommen – sondern zudem auch die Verteilungskoeffizienten, hier nachweislich für ACC, welches mit Strontium dotiert wurde. Weiterhin wurde gezeigt, dass diese pseudomorphe Umwandlung durch anorganische und organische Additive wie Phosphat, Polyacrylsäure oder auch Polyasparaginsäure ausgelöst werden kann. Da diese Additive in der Umgebung von Biomineralisationsprozessen auftreten oder den organischen Matrizes ähneln, können diese Ergebnisse von Bedeutung für paläoklimatische Studien sein. Der Einfluss der pseudomorphen Umwandlung auf die Sauerstoffisotopie deutet darauf hin, dass es sich bei diesem Kristallisationspfad um eine Pseudo-Festphasenumwandlung handelt, welche trotz der Lösungsumgebung stattfindet. Damit belegt Kapitel 2 erstmals, dass das Vorhandensein von Additiven in natürlichen Systemen zu einer Beibehaltung der chemischen Zusammensetzung von amorphen Zwischenphasen führen kann. Daher können verschiedene Umweltbedingungen die gemessenen Verteilungskoeffizienten, die in entsprechenden Biomineralen gefunden werden, verursacht haben. Während eine Kristallisation unter Umlösung die thermodynamisch vorhersagbaren Verteilungskoeffizienten der vorliegenden kristallinen Phase widerspiegelt, zeichnet die pseudomorphe Umwandlung im besten Falle die Verteilungskoeffizienten von ACC auf.

Da die Eigenschaften von amorphen Zwischenphasen während einer pseudomorphen Umwandlung beibehalten werden können, ist ein tiefergehendes Verständnis des Einflusses der Synthesebedingungen auf ACC notwendig. Dementsprechend wurde der Einfluss der Parameterwahl bei ACC-Synthesen auf Materialeigenschaften und chemische Zusammensetzung in Kapitel 3 untersucht. Zusätzlich wurde in Kapitel 4 der Einfluss der Kinetik auf die Einbauraten von Ionen untersucht, während in Kapitel 5 die Wirkung der Synthesebedingungen auf mehrfachdotiertes ACC untersucht wurde.

Um den Einfluss der Synthesen auf ACC zu bestimmen, wurde in Kapitel 3 ACC einerseits in einem Becherglas und andererseits in zwei Durchflusssynthesen hergestellt. Ein Einfluss der Synthesen auf die Materialeigenschaften wurde deutlich, da verschiedene Partikelgrößen (zwischen 32 ± 7 nm und 67 ± 20 nm), Hydratisierungen (zwischen 12.2 % und 18.7 %), Kristallisationstemperaturen (zwischen 264 °C und 349 °C) und Dichten (1.63 $g \cdot cm^{-3}$ und 2.92 $g \cdot cm^{-3}$) gemessen wurden. Beachtenswert war die geringere durchschnittliche Dichte (1.69 ± 0.06 $g \cdot cm^{-3}$) von ACC, welches im Becherglas hergestellt wurde, gegenüber von ACC welches mit Durchflusssynthesen hergestellt wurde (durchschnittliche Dichten zwischen

2.42 ± 0.13 g·cm^{-3} und 2.63 ± 0.27 g·cm^{-3}). Im Gegensatz zu den Materialeigenschaften wurde die chemische Zusammensetzung von mit Strontium und Barium dotiertem ACC nur geringfügig durch die Synthesen beeinflusst. Jedoch wurde ein deutlicher Einfluss des pH-Wertes auf den Einbau von Barium festgestellt.

In Kapitel 4 wurde festgestellt, dass eine Veränderung der Fließraten Auswirkungen auf die Partikelgröße und chemische Zusammensetzung von ACC hat. Während die Partikelgröße von Mg-dotiertem ACC nicht von der Fließrate beeinflusst wurde, wurden abnehmende Partikelgrößen bei steigenden Fließraten für Sr- und Ba-dotiertes ACC festgestellt. Für die Verteilungskoeffizienten von Ba-dotiertem ACC wurde kein Einfluss der Fließrate festgestellt, jedoch wurden mit steigenden Fließraten steigende Verteilungskoeffizienten für Sr-dotiertes ACC ermittelt, wohingegen geringere Verteilungskoeffizienten für Mg-dotiertes ACC berechnet wurden. Diese Ergebnisse verdeutlichen, dass der Einbau von Elementen in ACC von der Fließrate abhängt und somit kinetischer Kontrolle unterliegt. Da dieser Einfluss aktuell wenig in der Literatur betrachtet wird, sind diese Ergebnisse von Bedeutung für die Paläoklimatologie. Die unterschiedlichen Reaktionen der Dotierelemente auf die Fließrate können erklärt werden, wenn die Komplexchemie sowie die spezifischen Bindungen der Elemente miteinbezogen werden. Weiterhin können die verschiedenen Reaktionen auf eine Veränderung der Fließrate erklärt werden, wenn Pränukleationscluster als Pförtner des Einbaues von Dotierelementen betrachtet werden.

Die Synthese von ACC in künstlichem Meerwasser führte zur Bildung von mehrfachdotiertem ACC (Kapitel 5). Unter veränderten Synthesebedingungen wurde ein Einfluss der Fließrate auf die Partikelgröße (Abnahme dieser bei erhöhten Fließraten), auf die Hydratisierung (geringere Hydratisierung bei höheren Fließraten) und die Einbauraten von Magnesium und Schwefel festgestellt. Eine Erhöhung der Fließraten führte zu einem verringerten Einbau von Magnesium, im Gegensatz hierzu wurde Schwefel bei höheren Fließraten besser eingebaut. Die Temperatur hingegen beeinflusste die Kristallisationstemperatur (Auftreten eines zweiten Kristallisationspeaks) und führte, bei erhöhten Temperaturen, zu einem verstärkten Einbau von Magnesium und Schwefel. Durch eine Veränderung des pH-Wertes wurden die Partikelgröße (verringerte Partikelgröße bei erhöhtem pH-Wert), die Hydratisierung (Zunahme bei ansteigendem pH-Wert), die Kristallisationstemperatur (bei steigendem pH-Wert erhöhte sich diese zuerst, nahm anschließend jedoch wieder ab) und die Verteilungskoeffizienten (Anstieg aller Einbauraten bei erhöhten pH-Wert) beeinflusst. Aufgrund der Tatsache, dass PNCs eine höhere Stabilität bei höherem pH-Wert besitzen[2,3], ist es eine naheliegende Erklärung, dass PNCs ein gewisses Maß an Kontrolle über den Einbau von Fremdionen besitzen. Dementsprechend ist ein tiefgehendes Verständnis der PNCs und der Versuchsparameter, welche diese beeinflussen, notwendig.

Um fortgeschrittenere Modelle zur Beschreibung von Biomineralien zu entwickeln, ist es notwendig, eine verlässliche Synthese zu entwickeln, welche die fundamentalen Bausteine von kalkhaltigen Biomineralien nachbilden kann. Eine Machtbarkeitsstudie in Kapitel 6 offenbarte, dass es möglich ist, diese Bausteine durch mit Magnesium dotierte nanogranuläre ACC Partikel, welche mit Organik beschichtet sind, zu imitieren. Dies wurde durch die Serienschaltung von zwei Mikrofluidikbauteilen erreicht, welche eine konsekutive Synthese erlaubten: Im ersten Schritt wurden die Nanopartikel hergestellt, welche im zweiten Schritt mit einer entsprechenden organischen Beschichtung versehen wurden.

7.3 Outlook

The literature of ACC is often very confusing as many contrasting and therefore contradictory studies exist, such as the discussion of the existence of PNCs[2,4]. However, this work has laid the foundation for the identification of causes of contradiction and to remove, partially, some of the uncertainties. As shown in this work, the material properties and chemical composition of ACC are affected by the applied synthesis and the environmental conditions which were present. Accordingly, in contrast to the general assumption that ACC syntheses are interchangeable, ACC is “marked” by the synthesis used which impedes the comparability within the literature.

To remove the uncertainties caused by these findings, ACC syntheses have to be analysed in detail to determine how they influenced the precipitated ACC. However, this time-consuming research will yield in a better and more advanced understanding of ACC as it offers the possibility to consolidate contrasting results.

7.4 References

1. Giuffre, A. J., Gagnon, A. C., De Yoreo, J. J. & Dove, P. M. Isotopic tracer evidence for the amorphous calcium carbonate to calcite transformation by dissolution-reprecipitation. *Geochim. Cosmochim. Acta* **165**, 407–417 (2015).

2. Smeets, P. J. M. *et al.* A classical view on nonclassical nucleation. *Proc. Natl. Acad. Sci. U. S. A.* **114**, E7882–E7890 (2017).

3. Demichelis, R., Raiteri, P., Gale, J. D., Quigley, D. & Gebauer, D. Stable prenucleation mineral clusters are liquid-like ionic polymers. *Nat. Commun.* **2**, (2011).

4. Gebauer, D., Raiteri, P., Gale, J. D. & Cölfen, H. On classical and non-classical views on nucleation. *Am. J. Sci.* **318**, 969–988 (2018).